

**SPECTROSCOPY OF A MAGNESIUM ION CONFINED IN AN  
RF TRAP**

**THE LINEWIDTH AND HYPERFINE A  
CONSTANT OF THE  $^2P_{1/2}$  STATE OF A  
MAGNESIUM ION CONFINED IN A  
LINEAR PAUL TRAP**

By

JASON NGUYEN, B. Sc.

A Thesis  
Submitted to the School of Graduate Studies  
in Partial Fulfillment of the Requirements  
for the Degree  
Doctor of Philosophy

McMaster University  
©Copyright by Jason Nguyen, 2009.

DOCTOR OF PHILOSOPHY (2009)  
(Physics & Astronomy)

McMaster University  
Hamilton, Ontario

TITLE: The Linewidth and Hyperfine  $a$  Constant of the  ${}^2P_{\frac{1}{2}}$  State of a Magnesium Ion Confined in a Linear Paul Trap

AUTHOR: Jason Nguyen, B. Sc.(University of Guelph)

SUPERVISOR: Dr. Brian King

NUMBER OF PAGES: xxii, 357

# Abstract

We present and discuss results from a measurement of the hyperfine  $a$  constant of the  $1s^22s^22p^63p\ ^2P_{\frac{1}{2}}$  excited state in  $^{25}Mg^+$  and the linewidth of the same state in  $^{24}Mg^+$ . We trapped a single ion in a linear Paul trap and laser-cooled it using the  $^2S_{\frac{1}{2}} \rightarrow ^2P_{\frac{3}{2}}$  transition (in the case of  $^{25}Mg^+$ ) and the  $^2S_{\frac{1}{2}} \rightarrow ^2P_{\frac{1}{2}}$  transition (in the case of  $^{24}Mg^+$ ). We optically pumped the ion into the ( $F = 3, m_F = \pm 3$ ) ground states and weakly probed it with a tunable fibre laser that was scanned to drive the ion from the ground state to the  $F' = 3$  and  $F' = 2$  manifolds of the  $^2P_{\frac{1}{2}}$  state. The final state of the ion was determined by counting fluorescence (or the reduction therein) from the  $^2S_{\frac{1}{2}}(F = 3, m_F = \pm 3) \rightarrow ^2P_{\frac{3}{2}}(F'' = 4, m_F'' = \pm 4)$  cycling transition with a photomultiplier module. We determined that the hyperfine  $a$  constant is  $102.16 \pm 0.16\ MHz$  and the natural linewidth is  $42.4 \pm 1.2\ MHz$ .

# Acknowledgements

I have had the questionable fortune of taking a meandering path in my educational journey. It is a questionable fortune in that there are some who would argue that the shortest distance between two points is the most economical (emotionally, and financially). I, on the other hand, have *enjoyed* the scenic route.

Along my journey, I've met some amazing people who have helped to shape my development and I would like to take this opportunity to thank them. For those reading the acknowledgements to search for their name, I will place things in chronological order. Inevitably, I will miss some names, and for those people I apologize in advance.

From the beginning, my parents have continued to be an unwavering pillar of support – despite what I put them through. My father instilled within me a strong sense of honesty and willingness to work hard for the things you want. My mother taught me the importance of risk, and nurtured within me the instinct to try the things I think I cannot do. With adult eyes, I have been able to look back on the successes they have achieved and realized that without them as my base, I could not have taken advantage of the opportunities life has presented me.

Upon arriving in Canada, we were welcomed by the Mundels. Grossmama, Grosspapa, Aunt Mutti and their entire family made us feel at home. I will

never be able to thank them enough for their support. Growing up, a few teachers in particular stick out in my mind: Mr. Peters, Mr. Luongo, Mrs. Carlson, Mr. Hill, and Mr. Holobuff – you have all contributed, in often colorful ways.

Although I have lived in various different cities while growing up, I consider Langley as my “home” (yes Mike, I will admit that) since I spent the majority of my youth there. I am glad to have shared that time with friends who made it bearable. Andrea D., you still (and hopefully always will) hold the title of longest-term-friend. You are always in my thoughts – and I am not just saying that because you have the most embarrassing photos of me. Lisa, no matter how much time passes between our visits, it still feels just like back in the day, doesn't it? Katherine, no matter what I say about you, I know you will find some way to make it sound like a backhanded compliment – and that is why I love you. Mike, you're just awesome. I also have to mention my other Langley friends who still provide me with an ear to this day: Seb, Leslie, Jenni, Andrea J., Ilona, Mel, Mark, Brad, Laura and so many others.

My time at the University of Guelph marked my first venture out of the nest. I would like to thank Viet, Vien and their entire family for providing me with a home away from home. My time at Guelph was... interesting. Rob, Sarah, Becky and Laura – you helped me survive Guelph. I'd like to give a special thanks to Dr. Brooks, who I feel was the first person to properly

introduce me to the world of atomic physics. His teaching style and his investment in his students will always remain a highlight when I think back to my time spent at the University of Guelph. I also owe him a debt of gratitude for pointing me in the direction of McMaster University.

I could write an entire thesis about the things I've learned from being a graduate student. I'd like to begin by thanking the entire Physics and Astronomy department. From a graduate student's perspective, I've appreciated the accessibility of the staff and faculty in the department.

The experimental results and work I did in the lab would not have been possible without the help of many people. In particular, I'd like to thank the summer students who worked with us: Peter Klages, Swati Singh, John Oreopoulos, Jesse Gare, Agnes Skalski, Sarah Dyck, Daniel Goguen, James Kennedy, Ben Jackel, Katie Woods, Mike Collicutt, Nick Chisholm, Martin Horbanski, Vickram Lakhian, and Christian Karras. A special thanks also goes out to the following people who contributed advice, equipment, and time: Wayne Itano, Jim Bergquist, Henry Tiedje, Andy Duft, Rob Hughes, and Andy Duncan.

I consider myself lucky to have had Harold Haugen and Kari Dalnoki-Veress serve on my committee – thank you both for your advice and support throughout grad school.

Of course, my graduate life would not have been bearable without the

friends who helped me let off steam: Micah, Jordan, Randy, Gracie, Bruin, Aiden, Insyx, MB, Max and the whole gang. A special thanks to my good friend Greg – things just aren't the same without you around.

Erik, I could not have asked for a better friend. Sharing a space for as long as we have, we were bound to get into scuffles but, throughout it all, I've always known that I could count on your support when I needed it.

Thank you Jiajia and Laura for joining the group. Jiajia, you're one of the smartest people I know – but you've never made me feel intimidated by that. Laura, you are a riot. What always sticks out in my mind when I think of you is how you would dim the lights in the lab and declare to both me and Jiajia, "It's time to get romantic". I think I really lucked out in the co-worker/co-conspirator department with the two of you.

Finally, I want to express my gratitude and respect for my advisor, Brian King. Once, when we were at a talk you turned to me and whispered, "Now there is someone who lined up for seconds in the brains department". Afterwards, I told Jiajia and Laura and of course we all laughed because we're convinced *you* went for at least thirds, or fourths. Not only are you one of the brightest people I've had the pleasure of knowing, you are also one of the most compassionate and understanding. Your investment into your student's well-being (both personal and professional) was instrumental to my success. You've taught me so, *so* much – thank you.



# Contents

<b>1</b>	<b>Introduction</b>	<b>1</b>
<b>2</b>	<b>Ion Trapping and Laser Cooling</b>	<b>13</b>
2.1	Atomic Structure of Magnesium . . . . .	14
2.2	Ion Trapping . . . . .	22
2.2.1	Pseudo-Potential Approximation . . . . .	23
2.2.2	Mathieu Equation . . . . .	26
2.2.3	Sidebands From Ion Motion . . . . .	30
2.3	Laser Cooling . . . . .	36
2.3.1	Two-Level Rabi Problem . . . . .	39
2.3.2	Optical Bloch Equations . . . . .	43
2.3.3	Modelling Laser Cooling . . . . .	44
<b>3</b>	<b>Apparatus</b>	<b>53</b>
3.1	Introduction to the Apparatus . . . . .	53

3.2	Vacuum Chamber . . . . .	54
3.2.1	Ion Trap . . . . .	60
3.2.2	Mg Source . . . . .	63
3.2.3	Electron Guns . . . . .	64
3.2.4	Helical Resonator . . . . .	66
3.3	Lasers . . . . .	69
3.3.1	Fibre Laser . . . . .	71
3.3.2	Dye Laser . . . . .	72
3.4	Optics . . . . .	75
3.4.1	The Optical Beamlines . . . . .	75
3.4.2	Cyclor Beamline . . . . .	75
3.4.3	Probe Beamline . . . . .	85
3.4.4	Photoionization Beamline . . . . .	87
3.4.5	Frequency Doubling with the WaveTrain® . . . . .	89
3.5	Iodine Spectroscopy . . . . .	92
3.5.1	Saturated Absorption Spectroscopy . . . . .	94
3.5.2	Bennet Holes . . . . .	96
3.6	Imaging System . . . . .	99
3.7	Experiment Control and Data Acquisition . . . . .	106
3.7.1	Individual Trap Control . . . . .	107
3.7.2	Experiment Control . . . . .	108

3.7.3	Data Acquisition . . . . .	111
<b>4</b>	<b>Frequency Doubling</b>	<b>115</b>
4.1	Introduction . . . . .	115
4.2	Frequency Doubling Parameters . . . . .	117
4.2.1	Second Harmonic Generation . . . . .	117
4.2.2	Crystal Selection . . . . .	123
4.2.3	Boyd Kleinman Focusing Parameter . . . . .	127
4.3	Cavity Design . . . . .	130
4.3.1	General Comments . . . . .	130
4.3.2	Geometric Stability . . . . .	136
4.3.3	ABCD Matricies and Gaussian Beams . . . . .	139
4.3.4	Cavity Eigenmodes and Astigmatic Compensation . . . . .	143
4.3.5	Cavity Equations . . . . .	145
4.3.6	Maple Worksheet Example . . . . .	146
4.3.7	Cavity Locking Scheme . . . . .	150
4.3.8	Cavity Assembly . . . . .	152
4.4	LBO Performance . . . . .	153
4.5	BBO Performance . . . . .	157
<b>5</b>	<b>Spectroscopy of <math>^{25}\text{Mg}^+</math></b>	<b>163</b>
5.1	Overview . . . . .	163
5.2	Interaction of the Nucleus with Atomic Fields . . . . .	165

5.3	Atoms in External Fields . . . . .	168
5.3.1	Weak-Field Limit . . . . .	170
5.3.2	Intermediate Field . . . . .	173
5.3.3	Strong Field Limit . . . . .	175
5.4	Electric Quadrupole Interaction . . . . .	177
5.5	Detailed Atomic Structure of $^{25}\text{Mg}^+$ . . . . .	178
5.6	Population Dynamics in $^{25}\text{Mg}^+$ . . . . .	181
<b>6</b>	<b>Experimental Technique and Data Analysis</b>	<b>189</b>
6.1	Experimental Technique . . . . .	190
6.1.1	Initial Preparation and Loading . . . . .	190
6.1.2	Characterizing Micromotion . . . . .	196
6.1.3	Power Saturation Parameter . . . . .	201
6.1.4	Determining Probe Time . . . . .	207
6.1.5	Determining Detection Time . . . . .	212
6.1.6	Determining Molecular Iodine Hyperfine Frequency Sep- aration . . . . .	215
6.1.7	Taking Data Curves . . . . .	220
6.2	Hyperfine $a$ Constant Of The $^2P_{\frac{1}{2}}$ State . . . . .	224
6.2.1	Constrained Slope Method . . . . .	228
6.2.2	Constrained Slope and Zero-Field Method . . . . .	231
6.2.3	Average Polarization Method . . . . .	232

<i>CONTENTS</i>	xiii
6.2.4 Summary of Analysis Methods . . . . .	235
6.3 Linewidth of $Mg^+$ . . . . .	239
6.3.1 Contributions to Line Broadening . . . . .	239
6.3.2 Measurement of the Linewidth of $Mg^+$ . . . . .	255
<b>7 Conclusions</b>	<b>265</b>
7.1 Hyperfine $a$ Constant . . . . .	266
7.2 Linewidth of $^{24}Mg^+$ . . . . .	268
7.3 Improvements on the Measurements . . . . .	271
7.4 Measuring the $^2P_{\frac{3}{2}}$ Hyperfine Constants . . . . .	274
<b>A Cavity Design Worksheet</b>	<b>277</b>
<b>B Population Dynamics Worksheet</b>	<b>281</b>



# List of Figures

2.1	Simplified energy-level diagram . . . . .	20
2.2	Cyclor laser transitions . . . . .	20
2.3	Simplified energy-level diagram for photoionization of neutral magnesium . . . . .	21
2.4	Ion motion along the x-axis . . . . .	25
2.5	Stability diagram for the Mathieu differential equation . . . . .	29
2.6	Simplified picture of laser cooling . . . . .	37
2.7	Simulated linewidth curve including Doppler effects . . . . .	51
3.1	Side view of the vacuum chamber . . . . .	56
3.2	Side-view schematic of the vacuum chamber as seen looking along the trap axis . . . . .	57
3.3	Top-view schematic of the vacuum chamber . . . . .	58
3.4	Ion trap photo and schematics . . . . .	62
3.5	Photograph of the magnesium oven . . . . .	64

3.6	Photograph of the helical resonator . . . . .	68
3.7	Dye laser schematic . . . . .	73
3.8	Schematic for the Cyclor LBO beam line . . . . .	79
3.9	Schematic for Cyclor iodine . . . . .	81
3.10	Schematic for double-pass AOM . . . . .	82
3.11	Schematic for UV Cyclor beam line . . . . .	85
3.12	Schematic for $I_2$ Probe beamline . . . . .	88
3.13	Schematic for the WaveTrain® . . . . .	90
3.14	Screen capture showing the fluorescence from the neutral mag- nesium beam . . . . .	93
3.15	Schematic of the imaging system . . . . .	105
3.16	Screenshot of VI for Trap Control . . . . .	109
3.17	Timing diagram for an experiment . . . . .	111
3.18	Screenshot of VI for Experiment Control . . . . .	112
3.19	Data acquisition screenshot . . . . .	114
4.1	Propagation of ordinary and extraordinary rays relative to the crystal axis . . . . .	120
4.2	Plot of the angular dependence of the index of refraction . . . . .	121
4.3	Brewster cut crystals . . . . .	127
4.4	Boyd-Kleinmann peak efficiency vs. focusing parameter . . . . .	131
4.5	Boyd-Kleinmann peak efficiency vs. double-refraction parameter	131

4.6	Simple ring resonator geometry . . . . .	132
4.7	Multiple Pass Oscillation Pattern . . . . .	137
4.8	Stability Plot . . . . .	138
4.9	Intensity and field distribution of a Gaussian beam . . . . .	140
4.10	Gaussian beam profile along the direction of propagation . . . . .	141
4.11	Schematic for bowtie and $\mathcal{Z}$ cavity . . . . .	148
4.12	Cavity stability plot for the LBO cavity . . . . .	149
4.13	Cavity stability plot for the LBO cavity . . . . .	150
5.1	Vector model for a weak external field . . . . .	172
5.2	Vector model for a strong external field . . . . .	176
5.3	$^{25}\text{Mg}^+$ energy-levels diagram . . . . .	180
5.4	$^{25}\text{Mg}^+$ simplified energy-level diagram . . . . .	182
6.1	Schematic of pushing the ion along the radial direction to minimize micromotion . . . . .	200
6.2	Absorption sidebands due to micromotion . . . . .	201
6.3	Background Counts vs. Probe Laser Power . . . . .	203
6.4	Lineshape broadening of $^{24}\text{Mg}^+$ . . . . .	205
6.5	Plot of ratio of counts vs. laser power . . . . .	207
6.6	Plot of data determining the overall detection quantum efficiency	208
6.7	Probe-time and ion-resonance curves for the $3 \rightarrow 3'$ transition .	209
6.8	Probe-time and ion-resonance curves for the $3 \rightarrow 2'$ transition .	210

6.9	Bright- and dark-state histograms used to determine optimal detection time . . . . .	213
6.10	Uncalibrated iodine feature . . . . .	216
6.11	Schematic of the apparatus for the measurement of the separation between iodine hyperfine features $n$ and $r$ . . . . .	217
6.12	Iodine spectrum used to determine frequency separation of features $n$ and $r$ . . . . .	218
6.13	Plot of line centre vs. Quantization-Coil current for the $F = 3 \rightarrow F' = 3$ transition and the $F = 3 \rightarrow F' = 2$ transition . . . . .	227
6.14	Plot of data using the constrained-slope method . . . . .	230
6.15	Plot of data using the constrained-slope and constrained-zero-field crossing method . . . . .	233
6.16	Plot of data using average method . . . . .	234
6.17	A plot of the time-dependent fluorescence for different initial ion energies . . . . .	243
6.18	An oscilloscope plot of a cavity fringe used to characterize the laser linewidth . . . . .	251
6.19	Calibration of the linear portion of the iodine signal . . . . .	255
6.20	A plot of the noise power spectral density using a two-mirror cavity as a frequency discriminator . . . . .	256

6.21 A plot of the noise power spectral density using iodine feature  
    *b* as a frequency discriminator . . . . . 256

6.22 Low Laser Power: Total Counts vs. UV Frequency . . . . . 258

6.23 High Laser Power: Total Counts vs. UV Frequency . . . . . 259

6.24 Fit to Extrapolate the Natural Linewidth of  $Mg^+$  . . . . . 263



# List of Tables

3.1	Ion Trap: Summary of Trap Dimensions . . . . .	63
3.2	Helical Resonator: Summary of Resonator Dimensions . . . . .	69
3.3	Imaging System: Summary of Optical Components and Detection Efficiency . . . . .	104
4.1	LBO Cavity: Summary of LBO Cavity Dimensions . . . . .	151
4.2	BBO Cavity: Summary of BBO Cavity Dimensions . . . . .	151
4.3	Cavity Components: Summary of Required Optical Components	153
4.4	LBO Cavities: Typical Optimized Performance . . . . .	161
4.5	BBO Cavities: Typical Optimized Performance . . . . .	161
6.1	Fitting results from the constrained-slope method . . . . .	229
6.2	Fitting results from the constrained-slope and zero-field coil current . . . . .	232
6.3	Weighted average and fitting results from the average-polarization method . . . . .	235

6.4	Hyperfine $a$ Constant for ${}^2P_{\frac{1}{2}}$ : Summary of Analysis . . . . .	240
6.5	Error Budget: factors contributing to the magnesium linewidth measurement . . . . .	262

# Chapter 1

## Introduction

Spectroscopy has a rich history in physics [1], with broad-ranging implications. It was in 1814 that Joseph von Fraunhofer first noticed dark absorption bands in the solar spectrum, but it wasn't until 1859 that these bands were explained as atomic absorption lines by Gustav Kirchoff and Robert Bunsen. This led to the realization that, by analysing the absorption spectrum, one could determine the Sun's chemical composition. As the field of spectroscopy developed, the spectra of different atoms were collected and analysed. In 1885 Johann Balmer noticed a regularity in the spectra of hydrogen, now called the Balmer series. This description was later extended by Johannes Rydberg who extended this more generally to other lines of hydrogen.

With the introduction of quantum theory [2] (originally proposed by Planck in his consideration of blackbody radiation) these regularities were explained

first by Neils Bohr. He postulated that the electron's angular momentum is quantized, resulting in discrete orbits around the nucleus, and that light is emitted when the electron makes a transition from a higher orbital into a lower one. The discrete nature of the orbits explained the regularity in the observed spectra. In this manner, spectroscopic measurements were inextricably connected to quantum mechanics.

Prior to Bohr, Einstein had explained the photoelectric effect (in which electrons are ejected from matter after the absorption of light above a specific frequency) using the idea of quanta of light (which we now call photons). In 1916, Einstein also proposed three coefficients describing absorption, spontaneous emission and stimulated emission (which is integral to the understanding and development of lasers that would follow). The key point to stress is that historically, there has been an interplay between our understanding of quantum mechanics, atomic structure, and spectroscopy.

Quantum mechanics continued to develop, through the work of Schrödinger, Heisenberg and Dirac (to name a few). Experimental results also continued to push the theory. For example, in 1916 Sommerfeld introduced the fine structure constant and explained the observed fine structure splitting (which was absent in Bohr's model). In 1922, Stern and Gerlach observed the quantization of angular momentum in silver atoms, in which a beam of silver atoms was deflected into distinct components (using a magnetic field), indicative of

the quantization of angular momentum. (Paradoxically, the beam split into two components, indicating a half-integer value for the spin.) In 1924, Pauli first postulated that nuclear angular momentum was responsible for the observed splitting of spectral lines into so-called “hyperfine” components. A year later, Pauli proposed what is now called “the Pauli Exclusion Principle”, which states that no two electrons may occupy the same quantum state – Pauli formalized this spin theory in 1927. This furthered the understanding of atomic structure and is an example of correlation between electrons. Finally, in 1928 Dirac’s theory of relativistic hydrogen gave a complete explanation of quantum angular momentum.

As quantum theory evolved, our understanding of atomic structure grew, as did our ability to interpret spectra. Unfortunately, optical spectroscopy was limited in its ability to probe the finer splitting of spectral lines, since often this structure was buried within a broad spectrum resulting from Doppler broadening. A simple example of the Doppler effect is how a car’s horn changes pitch as it passes you by. As the car approaches, the frequency of the sound wave is shifted to a higher frequency, and as the car passes by, the frequency is shifted to a lower frequency in the observer’s reference frame. Atomic samples of gas travel at high velocities (even at room temperature), resulting in a shift in the frequency of light. This frequency shift results in broadening of absorption profiles. Even though the velocities of atoms in a gas are high,

they are still much lower than the speed of light. In this limit, the Doppler broadening can be treated as being linearly proportional to the frequency of radiation. This fact led to a significant tool – RF spectroscopy.

Radio waves ( $MHz$ ) have lower frequencies than light ( $THz$ ), and so the Doppler shift is much smaller – this resulted in RF spectroscopy being the most precise form of spectroscopy for many years. Rabi and Breit studied nuclear structure using beam deflection techniques similar to those of Stern and Gerlach. A key difference in their apparatus was the replacement of a single deflecting magnetic field with three (one strong, and two weak) which separated the atomic beam into distinct components. Using their beam-deflection technique, they studied the nuclear spin of different atoms: the first atom studied was sodium [3]. Ramsey, who had worked with Rabi, also worked with atomic beams and developed an oscillatory field method [4] that improved the resolution by reducing broadening associated with the transit time through the apparatus. One particular experiment that demonstrated the power of RF techniques was that of Lamb and Retherford. They measured a shift between the  $^2S_{\frac{1}{2}}$  level and the  $^2P_{\frac{1}{2}}$  level of hydrogen of about  $1000 MHz$  [5]. This finding provided evidence that contradicted Dirac’s calculation of the energy spectrum of hydrogen (which had predicted the two levels to be degenerate). Dirac did not account for vacuum fluctuations that perturb the energy levels – this was resolved by the work of Bethe. Previous attempts to

compare experimental measurements of hydrogen with Dirac’s calculation had been inconclusive, primarily because such measurements had been dominated by Doppler broadening.

The next significant tool in spectroscopy was the laser. The first ruby laser was demonstrated in 1960 by Maiman [6]. The further development of lasers and of nonlinear optics (such as frequency doubling, first demonstrated by Franken *et al.* [7]) quickly extended the wavelength range of lasers. Laser physics opened up new possibilities in spectroscopic measurements because of lasers’ narrow spectral width, high intensity, and phase coherence – these allowed one to address particular transitions to further understand atomic structure. Also, new techniques such as saturated absorption spectroscopy [8] allowed one to observe spectra free of Doppler broadening – and finally resolve transitions that were previously buried within a Doppler-broadened profile.

The development of atom trapping and laser cooling provided spectroscopists with another tool in precision spectroscopy. While other techniques (such as saturation absorption spectroscopy) allow us to observe spectra free of Doppler broadening, trapping and laser-cooling atoms reduces first-order (since the motion averages to zero) and second-order (since we reduce the ion’s speed) Doppler shifts, and transit-time broadening. Furthermore, it was realized in the fifties that a particle confined to a region smaller than the wavelength of the interrogating radiation would be free of Doppler broadening

[9]. Ion traps, in particular, provide strong enough confinement to realize this regime for microwave – and even optical – transitions.

Ion traps were proposed in the late fifties [10], [11], [12], along with the Penning trap [13] (which uses static electric fields and a static magnetic field to confine ions). Both of these techniques use quadrupole fields to confine the ion. Many significant spectroscopic results have been obtained using both RF traps and Penning traps. For example, Major and Werth measured a hyperfine transition frequency in  $^{199}\text{Hg}^+$  to a part in  $10^9$  using an RF trap [14] (more recently, the fractional uncertainty has been reduced to less than  $10^{-17}$  [15]). One of the earlier measurements of the anomalous magnetic dipole moment was performed using a Penning trap [16] and, in the sixties, a significant amount of progress in spectroscopy of trapped ions was achieved by Dehmelt *et al.* [17] [13] using Penning traps.

Laser cooling was first proposed by Wineland and Dehmelt [18] (for trapped ions) and Hänsch and Schawlow [19] (for neutral atoms). In 1978, the first demonstration of laser cooling trapped ions occurred with magnesium [20] and barium [21]. This was followed by cooling of neutral sodium atoms [22] in 1982. Trapping and cooling of ions and atoms have found use in a broad variety of other areas. In particular, spectroscopy of laser-cooled trapped ions has implications in astrophysics, nuclear physics, atomic physics, and frequency standards. The ions, held in traps under vacuum, are relatively free from per-

turbations from the environment and are perfect candidates for high-precision spectroscopic measurements.

Improvements in spectroscopy are still significant, since spectroscopy still plays an important role in many branches of physics. Shifts in atomic-transition frequencies in quasar absorption systems can be used to detect changes in the fine structure constant [23] [24]. In nuclear physics, spectroscopic measurements of isotope shifts can be used to extract nuclear charge radii for halo nuclei studies [25]. This requires an accuracy of better than 1%. Theoretical calculations of atomic properties require accurate calculation of the wavefunctions and spectroscopic measurements of properties such as hyperfine constants provide a test against current atomic models [26] [27].

Spectroscopy is also the basis for the best-realized standard of measurement. We define the second by an accurate measurement of the frequency of a particular transition: currently, the SI second is defined in terms of a microwave transition between two ground-state hyperfine levels of neutral cesium [28]. The NRC FCs1 cesium clock [29] and the NIST-F1 cesium clock [30] are two examples of atomic frequency standards; the latter is accurate to within one second in sixty million years. With progress in laser physics, trapping, and laser cooling of ions and atoms, it seems likely that the second will be redefined. Several atomic clocks based on optical transitions have been demonstrated, using  $^{199}\text{Hg}^+$  [15],  $^{26}\text{Al}^+$  [31], and  $\text{Sr}$  [32]. The mercury ion

clock, for example, is stable to within one second every four-hundred million years. The ratio of the frequencies of different clocks can also be used to detect changes in the fine structure constant [33].

For comparison to theoretical atomic calculations, even lower-precision spectroscopic measurements can be relevant. In our lab, we trapped  $^{24,25}\text{Mg}^+$  ions in a linear Paul trap and laser cooled them. The levels relevant to our experiment were the  $1s^22s^22p^63s\ ^2S_{\frac{1}{2}}$  level, the  $1s^22s^22p^63p\ ^2P_{\frac{1}{2}}$  level, and the  $1s^22s^22p^63p\ ^2P_{\frac{3}{2}}$  level. For our initial experiments, we measured the lifetime of the  $^2S_{\frac{1}{2}} \rightarrow ^2P_{\frac{1}{2}}$  transition in  $^{24}\text{Mg}^+$ , which has been measured previously by different groups [34] [35] [36] [37]. We also measured the hyperfine  $a$  constant of the  $^2P_{\frac{1}{2}}$  state, which has never before been measured. Our value for the hyperfine  $a$  constant serves as a comparison to theoretical calculations of atomic properties [26] [27].

In this thesis we will describe the apparatus and laser systems required to trap and cool ions. We will also discuss the specifics of the measurements of the hyperfine  $a$  constant and the linewidth of the excited state in magnesium.

In our experiment we used a linear Paul trap that provides radial confinement with RF electric fields and axial confinement with DC electric fields. By laser cooling the ion we reduce its motional energy. This reduces the Doppler broadening normally associated with an ion in motion, allowing for a precise measurement of the linewidth and hyperfine  $a$  constant. In Chapter 2 we

present a simple discussion of atomic theory, ion trapping and laser cooling.

In Chapter 3 we discuss the apparatus used in the experiment. To achieve long trapped-ion lifetimes, we placed the ion trap, neutral Mg sources, and associated parts into a vacuum chamber. This allowed us to maintain a low vacuum ( $\sim 10^{-11}$  Torr) to minimize collisions between the trapped ion and background gases. For laser cooling, photoionization, and addressing other transitions relevant to our measurement we used a total of three different laser systems. Laser cooling of  $^{25}\text{Mg}^+$  was done using the  $^2S_{\frac{1}{2}} \rightarrow ^2P_{\frac{3}{2}}$  transition, while the  $^2S_{\frac{1}{2}} \rightarrow ^2P_{\frac{1}{2}}$  transition was used to laser cool  $^{24}\text{Mg}^+$  and as a probe transition for the hyperfine  $a$  constant. A significant amount of optics and diagnostic tools was required to ensure that we were at the correct frequency to drive these transitions and so a significant section of Chapter 3 is devoted to discussing the various optical setups. Since lasers at the wavelengths we required were not readily available (and were not economically viable even once they were) we opted instead to purchase two fibre lasers (centred at 1120 nm) and a dye laser (centred at 560 nm) and used frequency doubling to convert to 280 nm.

In Chapter 4 we will discuss frequency doubling in more detail. Although it is possible to frequency quadruple from the IR to the UV, we opted instead to do two separate stages of doubling. This allowed us to optimize each stage of the conversion process, resulting in a higher overall conversion efficiency than

quadrupling. The total power of the frequency-doubled beam is proportional to the square of the power in the fundamental beam, and so a high-finesse cavity was built around the doubling crystal to enhance the laser power. We also include a discussion of the optimal cavity design parameters and typical performance of the cavities. Specifically, we obtain an overall conversion efficiency of approximately  $25 \frac{\%}{W}$  in doubling from the IR to the visible, and an overall conversion efficiency of up to  $9 \frac{\%}{W}$  from the visible to the UV. The low conversion efficiency from the visible to the UV is due to crystal quality, as discussed in Section (4.5). A similar frequency doubling scheme was concurrently implemented by Friedenauer *et al.* [38] for the purpose of detection and cooling of  $Mg^+$ . They obtained conversion efficiencies of approximately  $30 \frac{\%}{W}$  for both doubling stages. In fact, their crystals were longer: 18 *mm* in the case of LBO, and 11 *mm* in the case of BBO. Scaling for crystal length, we determined that our LBO cavity out-performs theirs by  $2.5\times$ , whereas their best BBO cavity out-performs our worst by  $6.2\times$ . Our laser systems (as well as those of Friedenauer *et al.*) represent the first realization of a fibre-based system to address transitions near 280 *nm*.

In Chapter 5 we expand on the atomic theory discussed in Chapter 2. We discuss the hyperfine structure that results from the interaction between the nuclear magnetic moment and the magnetic field generated by the orbiting electrons. The nuclear magnetic moment also interacts with external magnetic

fields, causing a further shift in the hyperfine energy levels (Zeeman splitting). This additional shift in energy levels can introduce broadening and pulling of lines in the transitions in which we are interested, and so this effect is modelled before we discuss the experiments performed.

In Chapter 6 we treat the measurement of the hyperfine  $a$  constant of the  $^2P_{\frac{1}{2}}$  state, and the measurement of the linewidth. Of course, it is rarely the case that one walks into a lab and performs an intended measurement immediately, so we begin the Chapter by discussing the required preparatory steps. These can primarily be broken up into two parts: steps performed daily, and steps required to determine optimal operation parameters.

In Chapter 7 we summarize the details of both measurements, discussing improvements to the experiment as well as possible near-future directions for our apparatus.



## Chapter 2

# Ion Trapping and Laser Cooling

The first significant results to come out of our lab were a measurement of the linewidth and the hyperfine  $a$  constant of the excited state of magnesium. To understand the spectroscopy, we need to discuss a bit about atomic structure and so we begin with such a discussion. Spectroscopic measurements are further complicated by Doppler effects that result both in an increase in the linewidth and pulling of line centre. These Doppler effects can be reduced by ion trapping and laser cooling. After introducing the relevant transitions in our section on atomic structure, we continue with a discussion on ion trapping and laser cooling.

## 2.1 Atomic Structure of Magnesium

The energy-level structure of an atom results from interactions between the electrons and an internal or external field. To describe the gross structure we treat the nucleus as a positively charged point source and calculate the shift in energy resulting from the electrostatic interaction between the orbiting electrons and the nucleus. From there, we treat successively smaller shifts in the energy levels as perturbations to the gross structure. In particular, we will discuss the fine structure here, leaving the hyperfine structure to Chapter 5. In this treatment, the full Hamiltonian is:

$$H_T = H_0 + H_{fs} + H_{hfs} \quad (2.1)$$

where  $H_0$  is the gross structure,  $H_{fs}$  is the fine structure, and  $H_{hfs}$  is the hyperfine structure. A perturbative approach allows us to deal with each contribution to the total energy separately.

We begin by treating the nucleus as a point source. We can write the Schrödinger equation as [39]:

$$\left\{ -\sum_i^N \frac{\hbar^2}{2m} \nabla_i^2 + \frac{Ze^2}{4\pi\epsilon_0 r_i} + \sum_{i>j} \frac{e^2}{4\pi\epsilon_0 r_{ij}} \right\} \Psi = E\Psi \quad (2.2)$$

where  $\hbar$  is Planck's constant,  $m$  is the reduced mass,  $Z$  is the atomic number,  $e$  is the electronic charge,  $\epsilon_0$  is the permittivity of free space,  $r_i$  is the distance

between the  $i^{\text{th}}$  electron and the nucleus, and  $r_{ij}$  is the distance between the  $i^{\text{th}}$  and the  $j^{\text{th}}$  electron.

In order to solve the Schrödinger equation we recast it in a form that simplifies the description of the interactions. In particular, the second term of Equation (2.2) consists of an electrostatic attraction between the orbiting electrons and the nucleus whereas the third term consists of an electrostatic repulsion between different electrons. The net effect is that the orbiting electrons that are close to the nucleus partially screen the nucleus from the outer electrons. Using this fact we choose to rewrite the Hamiltonian of Equation (2.2) as [39]:

$$\mathcal{H} = \mathcal{H}_0 + \mathcal{H}_1, \quad (2.3)$$

where

$$\mathcal{H}_0 = - \sum_i^N \frac{\hbar^2}{2m} \nabla_i^2 + U(r_i), \quad (2.4)$$

and

$$\mathcal{H}_1 = \sum_{i>j} \frac{e^2}{4\pi\epsilon_0 r_{ij}} - \left\{ \sum_i^N \frac{Ze^2}{4\pi\epsilon_0 r_i} + U(r_i) \right\}. \quad (2.5)$$

Here we have introduced an undetermined central *effective* potential  $U(r_i)$ , accounting for the screening effect of the inner electrons.

By separating the Hamiltonian in Equation (2.2) into two parts, we can now apply the central-field approximation in which we assume that  $\mathcal{H}_1 \ll \mathcal{H}_0$ . This allows us to neglect the contribution of  $\mathcal{H}_1$ , consisting of the residual electron-

electron interactions. We can now approximately rewrite the Schrödinger equation as[39]:

$$-\sum_i^N \left( \frac{\hbar^2}{2m} \nabla_i^2 + U(r_i) \right) \Psi = E\Psi \quad (2.6)$$

By solving Equation (2.6) we can calculate the energies associated with the gross structure, although the calculation is non-trivial. We note that the form of Equation (2.6) is similar to that of the hydrogen atom, except that here we are summing over  $N$  electrons and that the exact form of  $U(r_i)$  and  $\Psi$  are not known.

A first approximation is known as the Hartree-Fock method [39], in which a reasonable “guess” of the potential  $U(r_i)$  is made. To determine the form of  $U(r_i)$  it is assumed that every electron moves around in a potential created by the nucleus and the average potential of all the other electrons. The Schrödinger equation is then solved iteratively, in a self-consistent manner. The wavefunctions are expressed in terms of Slater determinants of single orbital wavefunctions. When written as a Slater determinant, the wavefunction must be antisymmetric (otherwise it is zero). This accounts for the Pauli Exclusion Principle (no two identical fermions can occupy the same quantum state).

The main problem with this approach is that we entirely ignore some electron correlations. Since electrons only interact with the average potential of all the other electrons, no direct Coulomb repulsion between electrons is consid-

ered. Several methods exist [40] [26] [27] which include electron correlation by treating it as a correction to the Hartree-Fock method. While we will not go into depth on these different methods, we will discuss some of the key points to gain a better understanding into the complexity of the problem.

The starting point for these methods is the fact that the exact wavefunction can be expressed as a linear combination of all the possible Slater determinants that can be formed from the Hartree-Fock orbitals. The difference between the methods is the choice of coefficients forming the linear combination. The difficulty in the problem lies in the fact that the number of Hartree-Fock orbitals is large and so even with modern computers, approximation methods are required. One such method is the “Configuration Interaction” (CI) method [40], in which the linear combination is truncated, to determine an approximate solution. Another method, similar to the CI method, is the “Coupled Cluster Theory” method. In particular Safranov *et al.* [26] and Sur *et al.* [27] both use a Coupled Cluster Theory method, and calculate the hyperfine ground and excited states for  $^{25}\text{Mg}^+$  (Safranov *et al.* also consider other sodium-like ions whereas Sur *et al.* concentrate on magnesium). While we have introduced different methods used to determine approximate solutions to the Schrödinger equation for multi-electron atoms, this is in no way a full treatment of the topic. The key point is merely that electron correlation makes these calculations difficult and so we must appeal to different approximation methods to

obtain a solution. Note that magnesium has twelve electrons and so clearly an approximation method is required to obtain a solution for the energy levels. Since all of these methods are approximations to the exact solution, spectroscopic measurements in the lab allow us to compare different theoretical models against one another and to test the validity of their approximations.

The energy levels are further split by the fine structure that results from interactions between the magnetic moment of the electron (its spin) and the internal magnetic field of the atom. Physically, if we consider an electron orbiting a nucleus, the electron’s motion results in a magnetic field. The interaction between this field and the electron’s spin results in a further splitting of the energy levels known as the fine structure splitting [39]. Including the fine structure splitting, we can label the different energy levels by the quantum numbers  $L$ ,  $S$ , and  $J$  where  $L$  is the angular momentum,  $S$  is the spin, and  $J$  is the total angular momentum.

In Figure (2.1) we show a simplified energy diagram of magnesium (excluding hyperfine structure). The levels relevant to our experiment were the  $1s^2 2s^2 2p^6 3s \ ^2S_{\frac{1}{2}}$  level, the  $1s^2 2s^2 2p^6 3p \ ^2P_{\frac{1}{2}}$  level, and the  $1s^2 2s^2 2p^6 3p \ ^2P_{\frac{3}{2}}$  level. In particular, we drove the  $^2S_{\frac{1}{2}} \rightarrow ^2P_{\frac{1}{2}}$  transition that was addressed by what we call the “Probe” laser (discussed in Section (3.4.3)) and the  $^2S_{\frac{1}{2}} \rightarrow ^2P_{\frac{3}{2}}$  transition that was addressed by what we call the “Cycler” laser (discussed in Section (3.4.2)).

In Figure (2.2) we have included the hyperfine splitting (see Section (5.2)) in the  $^2S_{\frac{1}{2}}$  level. The Cyclor laser is actually split into two beams whose frequency difference is chosen to be the same amount as the hyperfine splitting. We call one of these beams the “Cyclor” beam ( $\sigma^{+(-)}$  polarized) since it drives the cycling transition  $(3, \pm 3) \rightarrow (4', \pm 4')$ . From the excited state  $(4', \pm 4')$  the atom can only decay back into the  $(3, \pm 3)$  state, and the “cycle” repeats. We call the other beam the “Repumper” beam ( $\sigma^{+(-)}$  polarized) since it drives transitions out of the  $F = 2$  manifold. This beam is used for optical pumping and laser cooling. (Optical pumping assures us that we start out in a single ground state hyperfine sublevel – in our case either the  $(3, \pm 3)$  state).

As discussed in Section (3.2.2), we used an oven of natural-abundance magnesium for all of the experiments described in this thesis. By heating the oven, a beam of magnesium atoms was directed at the trap. To obtain magnesium ions we photoionized the neutral atoms. The relevant levels for photoionization are the  $1s^2 2s^2 2p^6 3s^2 \ ^1S_0$  level and the  $1s^2 2s^2 2p^6 3s 3p \ ^1P_0$  level. In particular, the  $^1S_0 \rightarrow ^1P_0$  transition (which is also a cycling transition) was addressed by what we call the “Photoionization” laser (discussed in Section (3.4.4)). By driving the  $^1S_0 \rightarrow ^1P_0$ , it is possible for a two-photon transition to occur – in which case a single electron is promoted into the continuum [41]. In Figure (2.3) we show a simplified energy diagram showing the possible paths resulting in ionization.

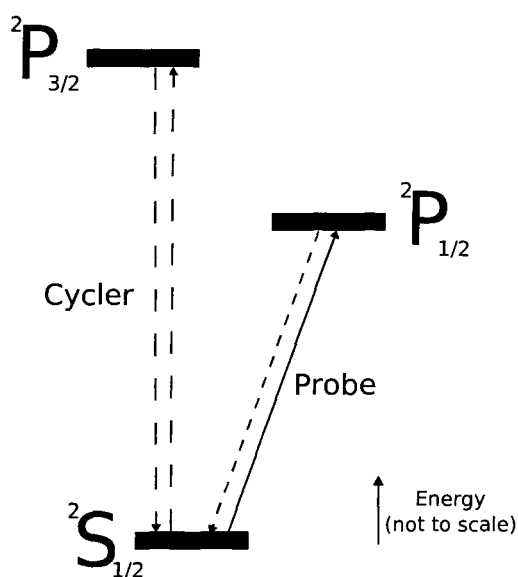


Figure 2.1: Simplified energy-level diagram. The  ${}^2S_{1/2} \rightarrow {}^2P_{1/2}$  transition is addressed by the Probe laser (discussed in Section (3.4.3)) and the  ${}^2S_{1/2} \rightarrow {}^2P_{3/2}$  transition is addressed by the Cycler laser (discussed in Section (3.4.2)). The cycler laser is actually split into two beams, whose frequencies are chosen to differ by the hyperfine structure splitting (discussed in Section (5.2)). Decay from the excited state is shown in dashed lines.

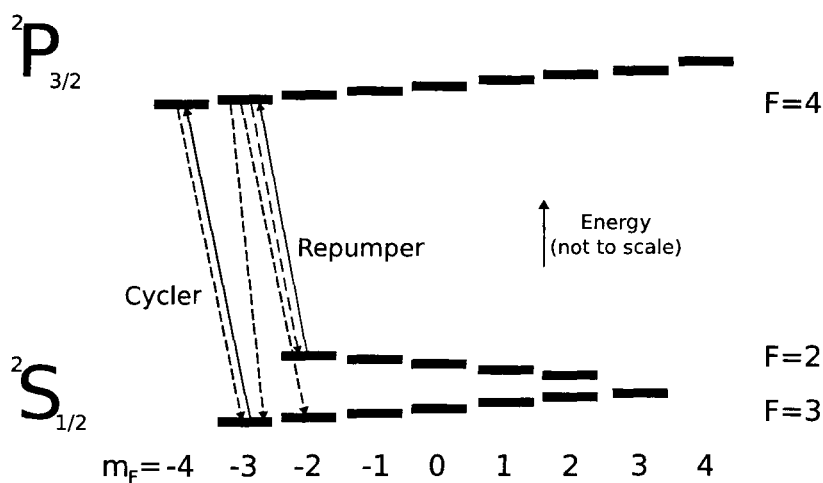
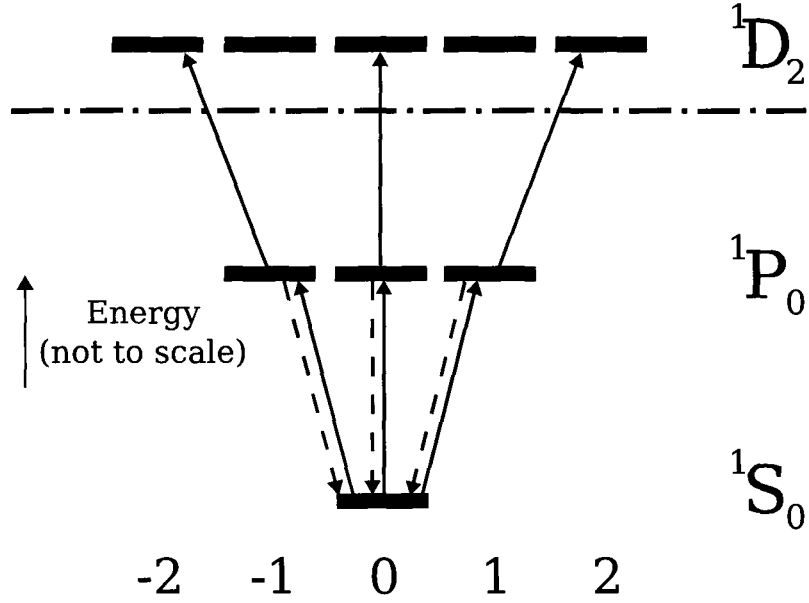
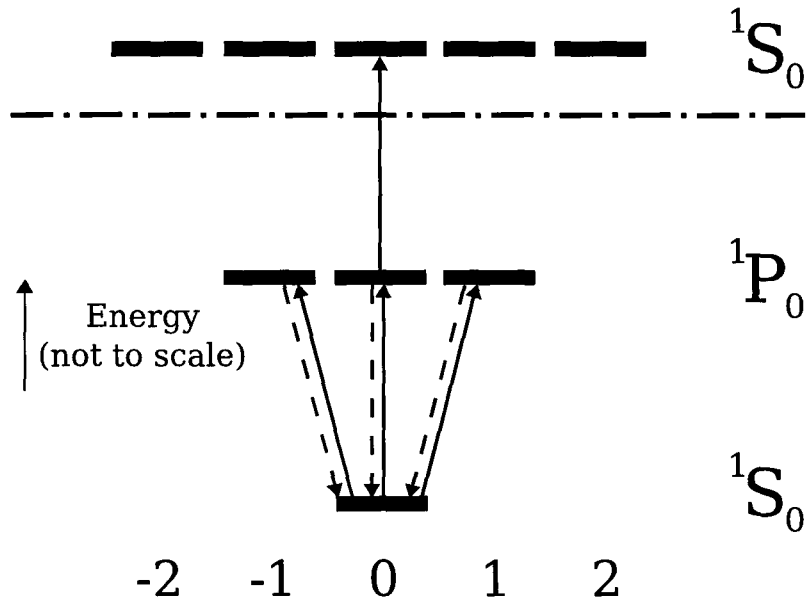


Figure 2.2: Simplified energy-level diagram showing the hyperfine structure pertinent to our experiments. The Cycler laser is actually split into two beams, whose frequencies are chosen to differ by the hyperfine structure splitting (discussed in Section (5.2)). Decay from the excited state is shown in dashed lines.



(a) Level diagram showing the possible paths to the  $^1D_2$  continuum state.



(b) Level diagram showing the possible path to the  $^1S_0$  continuum state.

Figure 2.3: Simplified energy-level diagram for photoionization of neutral magnesium. In both figures bound levels and levels in the continuum are separated by a dot-dashed line. From the  $^1P_0$  state the electron either decays back into the  $^1S_0$  state or is promoted into the continuum.

## 2.2 Ion Trapping

As mentioned previously, a linear Paul trap uses RF fields to confine the ion in the radial direction and DC fields to confine the ion in the axial direction.

To understand how this works, consider only the radial directions.

The force on a charged particle due to an electric field  $E(x, y)$  is given by  $F = qE(x, y)$ , where  $q$  is the charge of the particle. It might seem that the simplest way to confine a particle would be to use a parabolic potential such as:

$$\Phi(x, y) = \frac{V_{DC}}{2}(\alpha x^2 + \beta y^2) \quad (2.7)$$

where  $V_{DC}$  is the externally applied field, and  $\alpha$  and  $\beta$  describe the trap geometry. The problem with the potential in Equation (2.7) is that it only provides trapping along one direction and anti-traps along the other. This comes naturally out of Laplace's Equation,  $\nabla^2\Phi(x, y) = 0$ , which implies that  $\alpha = -\beta$  in two dimensions (the equivalent trapping/anti-trapping problem arises in three dimensions).

Instead of the static field of Equation (2.7), we can instead use a sinusoidally varying field:

$$\Phi(x, y, t) = \frac{V_{RF} \cos(\Omega_T t)}{2}(\alpha x^2 + \beta y^2). \quad (2.8)$$

Changing from a constant external field to a sinusoidally varying external field results in the trapping/anti-trapping direction alternating at a frequency of

$\Omega_T$ . The equations of motion for the potential of Equation (2.8) are given by:

$$\ddot{x} = \frac{eV_{RF}\alpha}{m} \cos(\Omega_T t)x \quad (2.9)$$

$$\ddot{y} = -\frac{eV_{RF}\beta}{m} \cos(\Omega_T t)y. \quad (2.10)$$

Here  $e$ , is the electric charge, and  $m$ , the particle mass. These allow for a time-averaged, stable trapping potential. It is possible to transform the pair of differential equations into two Mathieu differential equations that have well-known solutions [42]. Before discussing the solutions to the Mathieu equation we will first look at the pseudo-potential approximation [43].

### 2.2.1 Pseudo-Potential Approximation

The ion motion described in Equation (2.9) can be separated into two components: the secular motion ( $x_s$ ) that varies slowly in time, and the micromotion ( $x_m$ ) that varies rapidly in time. To see how this occurs, we rewrite Equation (2.9) as:

$$\ddot{x}_s + \ddot{x}_m = \frac{eV_{RF}\alpha}{m} \cos(\Omega_T t)[x_s + x_m], \quad (2.11)$$

where we've expanded the total motion  $x$  into the secular motion and the micromotion. If we assume that  $x_s \gg x_m$  and that  $\ddot{x}_s \ll \ddot{x}_m$ , we may neglect

$x_m$  and  $\ddot{x}_s$  in equation (2.11):

$$\ddot{x}_m = \frac{eV_{RF}\alpha}{m} \cos(\Omega_T t) x_s. \quad (2.12)$$

Since we've assumed that  $\ddot{x}_s \ll \ddot{x}_m$ , we integrate Equation (2.12), treating  $x_s(t)$  as constant, to obtain:

$$x_m = -\frac{eV_{RF}\alpha}{m\Omega_T^2} \cos(\Omega_T t) x_s. \quad (2.13)$$

Two important things to note here are that the micromotion is proportional to the secular motion and that the micromotion oscillates at the RF drive frequency,  $\Omega_T$ . Note that in this derivation we've implicitly ignored any background DC fields that can push the ion away from RF trap centre, resulting in additional micromotion [44] [45]. In Section (2.2.3) we will discuss how the excess micromotion affects the lineshape, and in Section (6.1.2) we will discuss our method of minimizing micromotion by nulling out background fields. For the purposes of the current discussion, the additional micromotion is ignored.

To obtain an expression for the secular motion, we can substitute equation (2.12) and equation (2.13) into equation (2.11):

$$\ddot{x}_s = -\left(\frac{eV_{RF}\alpha}{m\Omega_T}\right)^2 \cos^2(\Omega_T t) x_s \quad (2.14)$$

$$\ddot{x}_s = -\left(\frac{eV_{RF}\alpha}{\sqrt{2}m\Omega_T}\right)^2 x_s \quad (2.15)$$

where in the last step we've averaged over one period of the RF drive. This is the equation of motion of a harmonic oscillator whose frequency is given by

$$\omega_x = \frac{eV_{RF}\alpha}{\sqrt{2}m\Omega_T}.$$

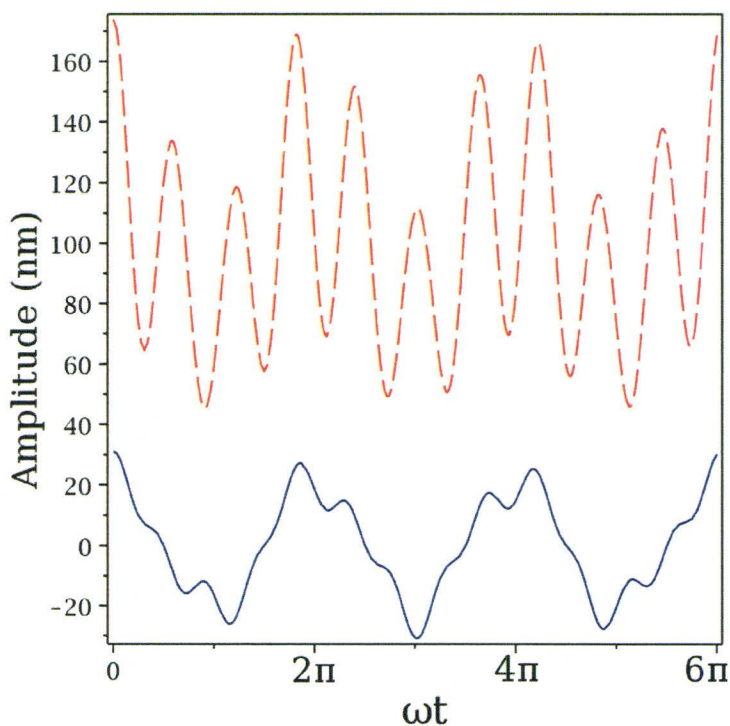


Figure 2.4: Ion motion along the x-axis. The amplitude of motion is plotted as a function of secular period (assuming an ion temperature  $\approx 1$  mK). In the solid plot we see the ion motion oscillates at the secular frequency ( $\omega_x$ ). Imposed on top of the slow oscillations we see small amplitude oscillations that occur at the trap frequency ( $\Omega_t$ ). In the dashed plot we have simulated a background field that has pushed the ion 100 nm away from trap centre. The secular oscillations are still present; however, the amplitude of the micromotion has increased.

Figure (2.4) shows how the ion motion changes in time. The ion exhibits harmonic motion, oscillating about  $x = 0$  at a frequency of  $\omega_x$ . As the ion moves away from  $x = 0$ , the micromotion grows and is largest at the anti-nodes

of the secular motion. The dashed line shows a more general case where the ion has additional micromotion because its mean position is shifted from trap centre by 100 nm. In the experiment, we nulled the DC fields, with residual shifts of up to a hundred nanometres (see Section (6.1.2)).

### 2.2.2 Mathieu Equation

In the previous sections we considered a two-dimensional parabolic potential that oscillated in time. This allowed us to concentrate on the dynamics of an ion in a RF trapping field without worrying about the effect of a DC field to confine the ion along the axial direction. In practice however, we need to confine the ion in three dimensions, which we accomplished by including a static potential:

$$\Phi(x, y, z, t) = \frac{V_{DC}}{2}(\alpha'x^2 + \beta'y^2 + \gamma'z^2) - \frac{V_{RF}}{2} \cos(\Omega t)(\alpha x^2 + \beta y^2 + \gamma z^2) \quad (2.16)$$

By defining  $a_x = \frac{4eV_{DC}\alpha'}{m\Omega_T^2}$ ,  $\zeta = \frac{\Omega_T t}{2}$ , and  $q_x = \frac{2eV_{RF}\alpha}{m\Omega_T^2}$  we write the equation of motion along the x-direction as a Mathieu differential equation given by:

$$\frac{\partial^2 x}{\partial \zeta^2} + [a_x - 2q_x \cos(2\zeta)]x = 0 \quad (2.17)$$

and similarly for the  $y, z$ -direction. The solutions to the Mathieu differential equation can be found in mathematical textbooks such as Abramowitz and

Stegun [42]. Depending on the values of  $a_x$  and  $q_x$  we obtain stable, or unstable solutions to Equation (2.17). Figure (2.5) shows a plot of the stability zones. For traps that operate with  $a_x$  and  $q_x^2 \ll 1$ , the trap frequency (to lowest order) is given by:

$$\omega_x = \frac{\Omega_T}{2} \sqrt{\frac{q_x^2}{2} + a_x} \quad (2.18)$$

and similarly for the  $y$  and  $z$ -directions. For larger values of  $a_x$  and  $q_x$ , the Mathieu equation must be solved to determine the trap frequency, and from the solution we may determine the amplitude of motion. Since our trap operated with  $q_x = 0.783$  and  $q_y = 0.747$ , we will briefly discuss a method of solving the Mathieu equation.

The coefficients of Equation (2.17) are periodic, and so we can write the solution in terms of two independent Floquet solutions given by [42]:

$$F_1 = e^{i\beta\zeta} P_1(\zeta), \quad (2.19)$$

$$F_2 = e^{-i\beta\zeta} P_2(\zeta), \quad (2.20)$$

where  $\beta$  is the characteristic frequency and  $P_1(\zeta)$  and  $P_2(\zeta)$  are periodic functions of  $\zeta$  with the same periodicity as the coefficient in the Mathieu equation. By making a Fourier expansion of  $P_1(\zeta)$  and  $P_2(\zeta)$ , and using Euler's theorem we may write the most general (stable) solution of the Mathieu equation as

[42]:

$$x(\zeta) = A_0 \sum_{n=-\infty}^{\infty} C_{2n} \cos([2n + \beta]\zeta) + iB_0 \sum_{n=-\infty}^{\infty} C_{2n} \sin([2n + \beta]\zeta). \quad (2.21)$$

Here,  $A_0$  and  $B_0$  are constants which depend on the initial conditions and  $C_{2n}$  are the Fourier coefficients of  $P_1(\zeta)$  and  $P_2(\zeta)$ .

If the Fourier coefficients are known, the amplitude of motion can be calculated to arbitrary order in  $n$ . To determine the Fourier coefficients, we substitute Equation (2.21) into Equation (2.17) and define  $D_{2n} \equiv \frac{a_x - (2n + \beta)^2}{q_x}$ , obtaining the following recursion relationship:

$$D_{2n}C_{2n} = C_{2n-2} + C_{2n+2}. \quad (2.22)$$

From the recursion relationship and the definition of  $D_{2n}$  in terms of  $a_x$  and  $q_x$  we have:

$$\beta = \sqrt{a_x - q_x \left( \frac{C_{-2} + C_2}{C_0} \right)}, \quad (2.23)$$

$$\frac{C_{2n}}{C_{2n+2}} = \frac{1}{D_{2n} - \frac{1}{D_{2n-2} - \frac{1}{\dots}}}, \quad (2.24)$$

$$\frac{C_{2n}}{C_{2n-2}} = \frac{1}{D_{2n} - \frac{1}{D_{2n+2} - \frac{1}{\dots}}}. \quad (2.25)$$

Thus, from Equations (2.23), (2.24), and (2.25) we can determine the trap frequencies and Fourier coefficients to arbitrary order in  $n$  (see Leibfried *et al.*

[46] for further discussion).

In our experiment, our geometric factors are:  $|\alpha| = 2.64 \text{ mm}^{-2}$ ,  $|\beta| = 2.52 \text{ mm}^{-2}$ ,  $|\gamma| = 0.12$ ,  $|\alpha'| = |\beta'| = 0.12 \text{ mm}^{-2}$ , and  $|\gamma'| = 0.24 \text{ mm}^{-2}$ . We operated with  $V_{RF} = 283 \text{ V}$  and  $V_{DC} = 6 \text{ V}$  so  $\omega_x = 4.65 \text{ MHz}$ ,  $\omega_y = 4.32 \text{ MHz}$ , and  $\omega_z = 421 \text{ kHz}$ .

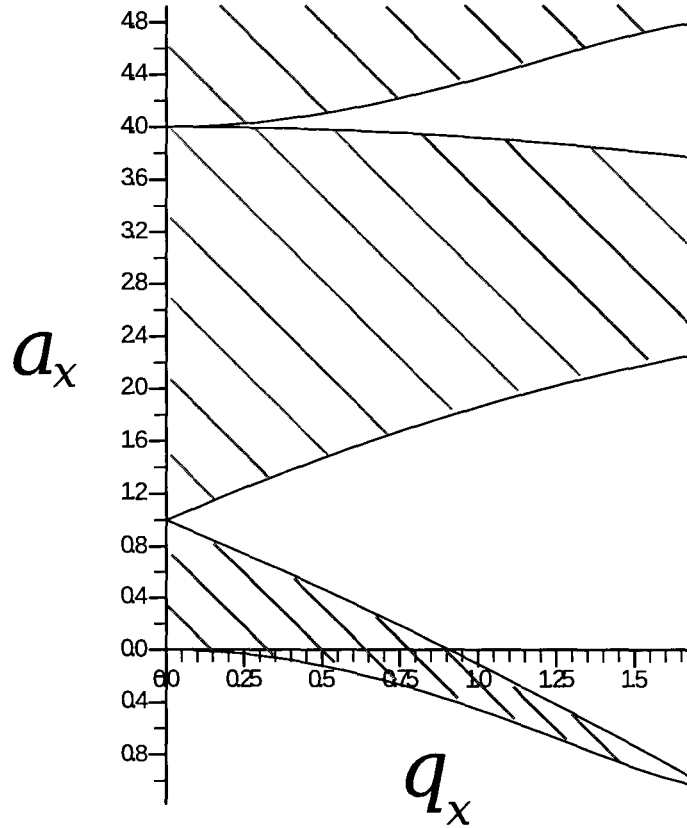


Figure 2.5: Stability diagram for the Mathieu differential equation. The hatched areas correspond to regions where the ion's motion is stable. The trap in this experiment operates in the lowest stability region. [Image courtesy of Jiajia Zhou.]

### 2.2.3 Sidebands From Ion Motion

Since a significant portion of this thesis will be devoted to spectroscopy of  $Mg^+$ , we need to consider how the ion motion changes the observed spectra. Qualitatively, the effect of micromotion and secular motion is the same. In the ion's reference frame, the laser frequency is modulated due to Doppler effects, resulting in sidebands separated by the frequency of motion. If we are in the resolved-sideband limit, then the observed absorption spectrum consists of distinct peaks separated by the frequency of motion. However, if we are not in the resolved-sideband limit, then the effect of ion motion is to broaden the lineshape. We begin by considering the resolved-sideband limit, to build an intuition for how the ion motion affects the lineshape.

If we treat the laser as purely monochromatic, we may write the electric field of the laser as a plane wave given by:

$$\mathcal{E}(x, t) = \mathcal{E}_0 \cos(\omega_L t + kx(t) + \phi) \quad (2.26)$$

where  $\mathcal{E}_0$  is the peak field amplitude,  $\omega_L$  is the laser frequency,  $k$  is the laser wave-vector,  $x(t)$  is the ion displacement from its equilibrium position, and  $\phi$  is an arbitrary phase. To simplify things, we will only consider the secular motion of the ion and in one dimension. In this case, we may write the ion

displacement as:

$$x(t) = x_0 \cos(\omega_x t) \quad (2.27)$$

where  $x_0$  is the total ion displacement from trap centre. By substituting equation (2.27) into equation (2.26), expanding the exponentials, and setting  $\phi = 0$  we obtain:

$$\mathcal{E}(x, t) = \mathcal{E}_0 \cos(\omega_L t + kx_0 \cos(\omega_x t)) \quad (2.28)$$

which looks just like a frequency-modulated wave with modulation index  $kx_0$ .

We can re-write equation (2.28) in terms of Bessel functions [42]:

$$\mathcal{E}(x, t) = \mathcal{E}_0 \left( J_0 \cos(\omega_L t) + \sum_{n=1}^{\infty} J_n [\cos(\omega_L + n\omega_x) + (-1)^n \cos(\omega_L - n\omega_x)] \right) \quad (2.29)$$

In the reference frame of the ion, the laser has been frequency-modulated about the carrier frequency  $\omega_L$ . The absorption spectrum now has frequency components separated by  $\omega_x$ . The amplitude of the different frequency components are determined by the modulation index,  $kx_0$ .

If we start with the laser detuned far red (lower frequency) of resonance and tune the laser blue (to higher frequency), we bring the different frequency components closer to (or further from) resonance. If the fluorescence is monitored, the observed spectrum (in the Lamb-Dicke limit) consists of a peak at resonance with equally spaced sidebands, separated by  $\omega_x$ . A similar analysis can be done for both the normal micromotion and excess micromotion. Again,

such an analysis shows that the micromotion also results in sidebands in the absorption spectrum, separated by  $\Omega_T$ .

For the experiments discussed in this thesis, we are in the unresolved-sideband limit ( $\Gamma > \Omega_T > \omega_{x,y} > \omega_z$ ) and so we do not observe distinct peaks. The effect of motion in the unresolved-sideband limit is to broaden the lineshape. In this limit, we can determine how the lineshape is broadened by convolving a Doppler-shifted Lorentzian with the appropriate velocity distribution.

In Section (6.3.1) we discuss how we determine an upper limit for the ion's average equilibrium energy. Using the equilibrium energy, we determine the effect on the lineshape. In this case, the broadening due to the secular and normal micromotion results in a Voigt profile (see Section (6.3.1)), since the equilibrium energy (and hence velocity due to secular motion) has a Maxwell-Boltzmann probability distribution. Since the normal micromotion is proportional to the secular motion, the micromotion velocity also has a Maxwell-Boltzmann probability distribution.

The velocity distribution of the excess micromotion (resulting from the ion being pushed away from RF null) is not thermal, since in this case the ion's motion is coherently driven. Thus, we need to determine the velocity distribution which can then be used to determine the effect of excess motion on the lineshape. Let us begin by considering what happens to the ion as it

is pushed away from trap centre by a background DC field. In particular, consider a DC electric field that pushes the ion along the x-direction. We can calculate the new equilibrium position by noting that this occurs when the force due to the DC electric field is equal to the restoring force due to the trap:

$$x_D = \frac{qE}{m\omega_x^2}. \quad (2.30)$$

Here  $q$  is the charge,  $E$  is the magnitude of the DC electric field,  $m$  is the ion mass, and  $\omega_x$  is the trap frequency. In the ion's new equilibrium position (which is displaced from RF null) the ion samples the AC electric field. The electric field changes direction with a frequency  $\Omega_T$ , pushing and pulling the ion back and forth. Thus, the ion exhibits harmonic motion with a frequency of  $\Omega_T$  (see Figure (2.4)). To calculate the probability distribution for the velocity we begin by noting that [47]:

$$P(x)dx = \left(\frac{2}{T}\right) dt \quad (2.31)$$

where  $x$  is the ion position,  $t$  is time, and  $T$  is the period of motion. Using the chain rule, we obtain:

$$P(v)dv = \left(\frac{2}{T}\right) \left(\frac{dt}{dx}\right) \left(\frac{dx}{dv}\right) dv \quad (2.32)$$

$$= \left(\frac{2}{T}\right) \left(\frac{1}{v}\right) \left(\frac{dx}{dv}\right) dv \quad (2.33)$$

where  $v$  is the velocity. Using conservation of energy for a harmonic oscillator, we obtain an expression for the velocity and position:

$$x = \sqrt{x_\mu^2 - \left(\frac{v}{\Omega_T}\right)^2} \quad (2.34)$$

$$v = \Omega_T \sqrt{x_\mu^2 - x^2} \quad (2.35)$$

where  $x_\mu$  is the maximum amplitude of motion (proportional to the ion displacement from trap centre). Using Equation (2.34) we obtain  $\frac{dx}{dv}$ , and substituting this, as well as Equation (2.35), into Equation (2.33) we obtain:

$$P(v)dv = \frac{1}{\pi} \frac{1}{\sqrt{(\Omega_T x_\mu)^2 - v^2}} dv, \quad (2.36)$$

where we have also used the fact that  $T = \frac{2\pi}{\Omega_T}$ .

The broadening of the lineshape due to excess micromotion is calculated by taking the convolution of a Doppler-shifted Lorentzian and the probability distribution given by Equation (2.36):

$$\mathcal{L} = \int_{-\Omega_T x_\mu}^{\Omega_T x_\mu} \frac{1}{\pi^2} \left( \frac{2\Gamma}{(\Delta_L - kv)^2 + \Gamma^2} \right) \left( \frac{1}{\sqrt{(\Omega_T x_\mu)^2 - v^2}} \right) dv \quad (2.37)$$

where  $\Gamma$  is the natural linewidth,  $\Delta_L$  is the laser detuning from ion resonance, and  $k$  is the laser wavevector. Simply put, Equation (2.37) tells us that the broadened lineshape is a sum of Doppler-shifted Lorentzians weighted by the

probability of the ion having a particular velocity. Wesenberg *et al.* considered the temporal dynamics of laser cooling and they obtained an analytic solution similar in form to Equation (2.37) [48]. Using Maple [49], we found an expression in terms of natural logarithms (which is long and will not be shown here).

In Section (6.1.2) we use Equation (2.37) to fit the data obtained when the ion was intentionally pushed from trap centre along the radial direction. From the fit, we determined the contribution of micromotion to the overall measured lineshape.

Before going into a discussion of laser cooling (required for Section (6.3.1) in which we discuss the Voigt profile), we note some of the subtler points about the lineshape due to excess micromotion. In particular, we can re-express the maximum amplitude of excess micromotion in terms of the displacement from trap centre [45]:

$$x_\mu = \sqrt{2} \frac{\omega_x}{\Omega_T} x_D \quad (2.38)$$

Naively, one would assume that by choosing a larger drive frequency  $\Omega_T$  we would reduce the micromotion (since  $x_\mu \propto \frac{1}{\Omega_T}$ ). In fact, substituting Equation (2.38) into Equation (2.37) we see that  $\Omega_T$  cancels out in the expression, and the relevant frequency is  $\omega_x$ . Furthermore, as we increase  $\omega_x$ , we reduce the displacement from trap centre (since  $x_D \propto \frac{1}{\omega_x^2}$ ), which in turn reduces the broadening due to excess micromotion. Increasing  $\Omega_T$  allows us to increase  $\omega_x$

since we must have  $\omega_x \leq \frac{\Omega_x}{2}$  for stable trapping (see Equation (2.18) and Figure (2.5)), although this also requires an increase in voltage. In our experiment we chose to use a lower drive frequency since we were voltage-limited (at higher voltages we noticed a voltage-correlated rise in the pressure). Lower drive frequencies resulted in higher trap frequencies for the maximum voltage we could apply to the trap.

## 2.3 Laser Cooling

Laser cooling of trapped ions has been treated in several sources [18] [19] [48] [50]. Our treatment will follow the previous work of the NIST group [48], in which the dynamics of laser cooling was considered when the ion was in the hot regime (initial stages of cooling) as well as the cold regime (final stages of cooling). By considering both cases we can later put an upper limit on the trap heating rate (see Section (6.3.1)), and subsequently an upper limit on the final ion temperature during our spectroscopic measurements. This is the case since the steady-state temperature results from an equilibrium between the trap heating, the ion recoil heating, and the laser cooling rates.

We use a one-dimensional semiclassical model of Doppler cooling for a weakly-trapped, single ion, which sufficiently encapsulates the physical processes involved. We assume the ion is trapped in a harmonic potential, as discussed in Section (2.2). The secular frequency of our trap is  $\omega_x$ , and we will

ignore any effects due to micromotion.

We will also assume a single laser beam is used for cooling. When trapping  $^{24}\text{Mg}^+$ , which has no hyperfine structure, a single laser beam is sufficient. However, in the case of  $^{25}\text{Mg}^+$  two laser beams are necessary for cooling, since there are two hyperfine manifolds into which the ion can decay from the excited  $^2P_{3/2}$  state.

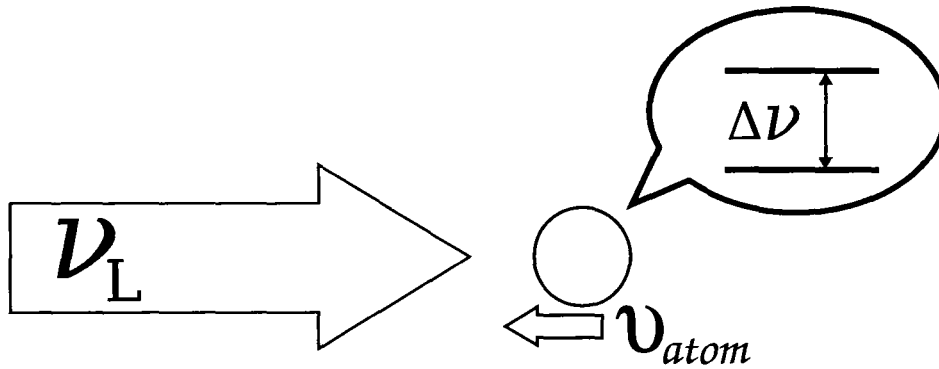


Figure 2.6: Simplified picture of laser cooling. A cartoon diagram of a simple two level atom in the presence of a laser beam (laser frequency  $\nu_L$ ). The atom is shown as moving in the opposite direction to the laser beam at a velocity,  $\nu_{atom}$  which results in a Doppler-shifted frequency in the reference frame of the ion. The atomic energy levels are separated by  $E = h\Delta\nu$ .

The simplest way to think of laser cooling is through conservation of energy. A moving atom will absorb light that has been Doppler-shifted into resonance while (on average) emitting light at the natural resonant frequency. Conservation of energy results in the atom losing some motional energy to compensate for the difference in average energy of the absorbed and emitted light.

Consider the two level atom in the presence of a laser beam from Figure (2.6). The atom is moving with some velocity,  $\nu_{atom}$ , and has a transition

energy,  $\Delta E = h\Delta\nu$ , associated with the internal energy levels.

Since the ion is moving, the frequency of the laser beam is Doppler shifted (to first order) according to:

$$\nu'_L = \nu_L - \frac{\vec{k} \cdot \vec{v}_{atom}}{2\pi} \quad (2.39)$$

where  $\nu_L$  is the laser frequency in the lab frame,  $\vec{k}$  is the laser wave-vector, and  $\vec{v}_{atom}$  is the velocity of the atom.

If the ion is moving opposite to the laser direction then the laser frequency in the atom's reference frame is shifted blue. By tuning the laser red of resonance, the atom can absorb a photon from the laser with energy  $h\nu_L < h\Delta\nu$  but will still emit (on average) a photon of frequency  $h\Delta\nu$ . The difference in energy between the absorbed and emitted photon comes from the motional energy of the atom. The atom is then subsequently cooled over many scattering events (each taking  $\sim ns$ ). This ignores the RMS spread in energy due to atom recoil.

For a more quantitative description, we consider the weak-binding regime,  $\Gamma \gg \omega_x$ , which is the case in all of our experiments. In this limit, the spontaneous decay from the excited state occurs on a much faster time scale than the period of oscillation and so the treatment of a trapped ion is similar to the treatment of a free atom.

The net cooling rate is determined by the laser cooling rate, the recoil

heating rate (the recoil experienced by the atom as it emits a photon) and any background heating rate (eg. due to anomalous heating[51]). In order to calculate these different rates we need an expression for the scatter rate. To this end, we need solve the optical Bloch equations[50], from which we obtain a scatter rate that is used to calculate the cooling rate.

The optical Bloch Equations describe the time dynamics of the excited-state and ground-state populations. They are obtained by using a density-matrix approach but, before discussing this approach, we will first look at the Rabi two-level problem. This sets up the problem, since we can relate the solutions from the Rabi two-level problem to the solution of the Bloch equations.

### 2.3.1 Two-Level Rabi Problem

We want to determine an expression for the photon scatter rate, which can be used to calculate the ion cooling rate (since  $\Delta E \propto \hbar\Gamma$ ). To solve this, we begin by considering the two-level Rabi problem. Recall that we are treating the ion as a two-level system that is addressed by a laser as shown in Figure (2.6). In general, we want to solve the time-dependent Schrödinger equation [50]:

$$\mathcal{H}(t)\Psi(x, t) = i\hbar \frac{\partial \Psi(x, t)}{\partial t} \quad (2.40)$$

where  $\mathcal{H}(t)$  is the Hamiltonian of the system,  $\Psi(x, t)$  is the wavefunction, and  $\hbar$  is Planck's constant.

The Hamiltonian can be written in terms of the field-free, time-independent atomic Hamiltonian ( $\mathcal{H}_0$ ) and an interaction Hamiltonian ( $\mathcal{H}'(t)$ ), describing the interaction between the laser field and the atom. The interaction Hamiltonian will be expanded upon later. For now, we'll note that the eigenvalues of the atomic Hamiltonian are given by  $E_n = \hbar\omega_n$  where, in our two level system,  $n = \{e, g\}$ . The corresponding eigenfunctions are denoted by  $\phi_n(x)$ .

The wavefunction for the full dynamics can be expanded in terms of the orthonormal atomic eigenfunctions  $\phi_n(x)$ , giving  $\Psi(x, t) = \sum_n c_n(t)\phi_n e^{-i\omega_n t}$  where  $|c_n t|^2$  is the probability of being in state  $n$  at time  $t$ . This can be substituted back into the Schrödinger equation to give:

$$[\mathcal{H}_0 + \mathcal{H}'(t)] \sum_n c_n(t) |\phi_n\rangle e^{-i\omega_n t} = i\hbar \frac{\partial}{\partial t} \sum_n c_n(t) |\phi_n\rangle e^{-i\omega_n t} \quad (2.41)$$

Moving into the interaction picture [52] (which can be thought of as an intermediate between the Schrödinger and Heisenberg picture), multiplying both sides of Equation (2.41) by  $\langle\phi_e|$ , and integrating over  $x$  we can obtain a coupled differential equation for  $c_e(t)$ , and likewise for  $c_g(t)$ . Explicitly, we

have:

$$i\hbar\dot{c}_e(t) = \langle\phi_e|\mathcal{H}'(t)|\phi_g\rangle c_g(t)e^{i\omega_{ge}t} \quad (2.42)$$

$$i\hbar\dot{c}_g(t) = \langle\phi_g|\mathcal{H}'(t)|\phi_e\rangle c_e(t)e^{-i\omega_{ge}t} \quad (2.43)$$

The interaction Hamiltonian,  $\mathcal{H}'$ , can be evaluated using the electric dipole approximation, in which the spatial variation of the electric field is ignored, since the wavelength is much larger than the spatial extent of the electron wavefunction. This yields [50]:

$$\langle\phi_e|\mathcal{H}'(t)|\phi_g\rangle = -eE_0 \cos(k_x x - \omega_L t) \langle e|x|g\rangle \quad (2.44)$$

$$= \hbar\Omega \cos(k_x x - \omega_L t), \quad (2.45)$$

where  $e$  is the electric charge,  $E_0$  is the electric field amplitude and in the second step we've defined the Rabi frequency to be  $\Omega = -\frac{eE_0}{\hbar} \langle e|x|g\rangle$ .

We will now substitute equation (2.45) into the coupled differential equations (2.42) and (2.43). To simplify the expansion, we re-write the cosine term of equation (2.45) as a sum of exponentials and obtain:

$$\dot{c}_e(t) = -\frac{i\Omega}{2} c_g(t) e^{i\omega_{ge}t} [e^{i(k_x x - \omega_L t)} + e^{-i(k_x x - \omega_L t)}] \quad (2.46)$$

$$= -\frac{i\Omega}{2} c_g(t) [e^{ik_x x} e^{-i(\omega_L - \omega_{ge})t} + e^{-ik_x x} e^{i(\omega_L + \omega_{ge})t}] \quad (2.47)$$

$$= -\frac{i\Omega}{2} c_g(t) e^{-i\Delta_L t}. \quad (2.48)$$

In going from equation (2.47) to equation (2.48) we used the rotating-wave approximation [53], neglecting terms that oscillate rapidly at  $\omega_L + \omega_{ge}$ , and defined  $\Delta_L = \omega_L - \omega_{ge}$ . We also assumed that we were in the Lamb-Dicke regime, so that  $k_x x \ll 1$ . In actuality, this is only true as we approach the Doppler limit.

Similarly, for the ground state we get:

$$\dot{c}_g(t) = -\frac{i\Omega^*}{2}c_e(t)e^{i\Delta_L t} \quad (2.49)$$

We can decouple the equations by differentiating them, and substituting one into the other to obtain a second-order differential equation for each population coefficient:

$$\ddot{c}_e(t) + i\Delta_L \dot{c}_e(t) + \frac{\Omega^2}{4}c_e(t) = 0 \quad (2.50)$$

$$\ddot{c}_g(t) - i\Delta_L \dot{c}_g(t) + \frac{\Omega^2}{4}c_g(t) = 0 \quad (2.51)$$

These equations can be solved analytically, given a set of initial conditions. In particular, with  $c_g(0) = 1$   $c_e(t) = 0$  we obtain:

$$c_g(t) = \left[ \cos\left(\frac{\Omega't}{2}\right) - i\frac{\delta}{\Omega'} \sin\left(\frac{\Omega't}{2}\right) \right] e^{i\frac{\Delta_L t}{2}} \quad (2.52)$$

$$c_e(t) = -i\frac{\Omega}{\Omega'} \sin\left(\frac{\Omega't}{2}\right) e^{-i\frac{\Delta_L t}{2}} \quad (2.53)$$

where  $\Omega' = \sqrt{\Omega^2 + \Delta_L^2}$ . Note that spontaneous emission has been ignored. In solving the optical Bloch equations, we can phenomenologically include spontaneous emission. By doing this, we obtain an expression for the photon scatter rate, and hence the ion cooling rate.

### 2.3.2 Optical Bloch Equations

The density matrix describing the two-level Rabi problem previous discussed is given by [50]:

$$\begin{pmatrix} \rho_{ee} & \rho_{eg} \\ \rho_{ge} & \rho_{gg} \end{pmatrix} = \begin{pmatrix} c_e c_e^* & c_e c_g^* \\ c_g c_e^* & c_g c_g^* \end{pmatrix} \quad (2.54)$$

which is the density matrix of a pure state. While the Schrödinger approach was useful for describing a pure state, spontaneous emission is an incoherent process and so in practice we must solve the optical Bloch equations to phenomenologically include the effect of spontaneous emission. By comparing the components of the two matrices we may obtain equations for the different elements of the density matrix. To obtain the optical Bloch equations we differentiate both sides of Equation (2.54) and phenomenologically include the

effect of spontaneous decay[50]:

$$\dot{\rho}_{gg} = \Gamma\rho_{ee} + \frac{i}{2}(\Omega^*\tilde{\rho}_{eg} - \Omega\tilde{\rho}_{ge}) \quad (2.55)$$

$$\dot{\rho}_{ee} = -\Gamma\rho_{ee} + \frac{i}{2}(\Omega\tilde{\rho}_{ge} - \Omega^*\tilde{\rho}_{eg}) \quad (2.56)$$

$$\dot{\tilde{\rho}}_{ge} = -\left(\frac{\Gamma}{2} + i\Delta_L\right)\tilde{\rho}_{ge} + \frac{i}{2}\Omega^*(\rho_{ee} - \rho_{gg}) \quad (2.57)$$

$$\dot{\tilde{\rho}}_{eg} = -\left(\frac{\Gamma}{2} - i\Delta_L\right)\tilde{\rho}_{eg} + \frac{i}{2}\Omega(\rho_{gg} - \rho_{ee}). \quad (2.58)$$

where the time dependent exponential  $e^{-i\Delta_L t}$  has been absorbed into  $\rho_{ge}$  by defining  $\tilde{\rho}_{ge} = \rho_{ge}e^{-i\Delta_L t}$  and similarly for  $\rho_{eg}$ . A particularly relevant case of the optical Bloch equations are the steady-state solutions, which will be used in the following section in modelling laser cooling.

### 2.3.3 Modelling Laser Cooling

Recall that the ion undergoes harmonic oscillations in the trap at the secular trap frequency (ignoring micromotion, which is small). What we want to do is to calculate the total change in mechanical energy of the ion averaged over a secular oscillation, taking into account the different cooling and heating mechanisms involved.

After the ion absorbs a photon from the laser, it will spontaneously emit a photon in a random direction. Both the absorption and spontaneous emission of a photon result in a momentum kick. Since the emission is in a random

direction, over many absorption-emission events the momentum kicks due to spontaneous emission average to zero (although the RMS spread is nonzero). The momentum kicks due to absorption however, do not average to zero since the ion absorbs a photon from the laser beam that is travelling in a well-defined direction. The ion experiences a velocity-dependent force due to the absorption given by:

$$F_x(v_x) = \hbar k_x \Gamma \rho_{ee}(v_x) \quad (2.59)$$

where  $v_x$  is the velocity of the ion,  $\hbar$  is Planck's constant,  $\Gamma$  is the excited state decay rate, and  $\rho_{ee}$  is the excited state population.

The right-hand side of Equation (2.59) is simply the change in momentum due to an absorption of a photon by the ion which is more evident if we note that the scatter rate is given by  $\frac{dN}{dt} = \Gamma \rho_{ee}(v_z)$ . While the force is small for a single event, over many scattering events this results in appreciable cooling of the ion.

In the weak-binding regime (which is the case for all of our experiments), the time it takes the ion to spontaneously decay from the excited state is much smaller than the period of oscillation in the trap and so we can treat the ion as though it equilibrates to its steady state population immediately after it absorbs a photon. From the steady-state solutions, we may write the

population of the excited state for a given effective detuning as [50]:

$$\rho_{ee}(v_x) = \frac{\frac{s}{2}}{1 + s + \left(\frac{2\Delta_{eff}}{\Gamma}\right)^2}. \quad (2.60)$$

Here  $v_x$  is the velocity along the  $x$ -direction,  $s = \frac{I}{I_{sat}}$  is the saturation parameter, and  $\Delta_{eff}$  is the effective detuning and is defined as  $\Delta_{eff} = \Delta_L - k_x v_x$ .

This latter parameter takes into account the first-order Doppler shift.

We can obtain an expression for the rate of change in mechanical energy, given by [48]:

$$\left(\frac{dE}{dt}\right)_{cooling} = \langle v_x F_x(v_x) \rangle, \quad (2.61)$$

where the brackets correspond to averaging over one motional cycle. We will expand on Equation (2.61) by using Equations (2.59) and (2.60) but first we re-visit the force due to spontaneous emission.

Recall that the ion will spontaneously emit a photon after each absorption, and that the momentum kicks associated with the emission will average to zero over many cycles. As we approach the cooling limit, however, the recoil force due to the RMS value of the momentum kicks is no longer negligible. Assuming the emission is isotropic, the photon recoil results in a heating rate given by [48]:

$$\frac{\hbar\Gamma}{2} \sqrt{1+s} \left(\frac{dE}{dt}\right)_{recoil} = \frac{4}{3} \frac{(\hbar k_x)^2}{2m} \frac{dN}{dt} \quad (2.62)$$

where  $m$  is the ion mass and  $s = \frac{I}{I_{sat}}$  is the saturation parameter.

The total change in mechanical energy is simply the difference between the cooling rate and the recoil heating rate, when other effects that can lead to heating of the ion have been ignored. In previous analysis by Wesenberg et al. [48] the effect of recoil heating was also neglected since they were primarily concerned with ion fluorescence in the hot-regime. Here we will take the recoil heating rate into account.

Following the analysis of the NIST group we rescale the energies by  $\frac{\hbar\Gamma}{2}\sqrt{1+s}$  where  $\frac{\Gamma}{2}\sqrt{1+s}$  is the power broadened linewidth, and time by the resonant scattering rate. Explicitly, we define [48]:

$$\varepsilon = \frac{E}{\frac{\hbar\Gamma}{2}\sqrt{1+s}} \quad (2.63)$$

$$\delta = \frac{\hbar\Delta}{\frac{\hbar\Gamma}{2}\sqrt{1+s}} \quad (2.64)$$

$$r = \frac{\frac{(\hbar k_x)^2}{2m}}{\frac{\hbar\Gamma}{2}\sqrt{1+s}} \quad (2.65)$$

$$\tau = \frac{t}{\Gamma \frac{s}{2(1+s)}} \quad (2.66)$$

where  $\varepsilon$  is the scaled energy of the ion,  $E$  is the energy of the ion,  $\hbar$  is Planck's constant,  $\Gamma$  is the natural linewidth,  $s = \frac{I}{I_{sat}}$  is the saturation parameter,  $\delta$  is the scaled laser detuning from ion resonance,  $\Delta$  is the laser detuning from ion resonance,  $r$  is the scaled recoil energy,  $k_x$  is the laser vector,  $m$  is the ion mass,  $\tau$  is the scaled time, and  $t$  is the time.

Since the ion is undergoing harmonic oscillations in the trap, the probability

distribution of the instantaneous Doppler shift is [48] (see Section (2.2.3)):

$$P_D(\delta_M, \delta_D) = \begin{cases} \frac{1}{\pi\sqrt{\delta_M^2 - \delta_D^2}}, & \text{if } |\delta_D| < \delta_M \\ 0 & \text{otherwise} \end{cases} \quad (2.67)$$

where  $\delta_M$  is the maximal Doppler shift and  $\delta_D$  is the instantaneous Doppler shift. Using the distribution of Equation (2.67), we may rewrite Equation (2.61) in scaled units as [48]:

$$\left(\frac{d\varepsilon}{d\tau}\right)_{cooling} = \int -\delta_D P_D(\delta_M, \delta_D) \frac{1}{1 + (\delta + \delta_D)^2} d\delta_D \quad (2.68)$$

$$= \frac{1}{2\sqrt{\varepsilon r}} (\text{Re}(Z) + \delta \text{Im}(Z)) \quad (2.69)$$

where:

$$Z = \frac{i}{\sqrt{1 - \frac{(\delta+i)^2}{4\varepsilon r}}} \quad (2.70)$$

and we have substituted  $\delta_M = 2\sqrt{\varepsilon r}$  into Equation (2.68). Note that Equation (2.68) is similar to the integral of Equation (2.37) aside from the  $\delta_D$  in the numerator of the integrand and the fact that they are considering the secular motion instead of the excess micromotion. Following their analysis, we could have obtained an analytic expression for the integral; however, in fitting, we obtained an analytic form for Equation (2.37) using Maple [49].

The scattering rate, in their analysis, is given (in scaled units) by [48]:

$$\frac{dN}{d\tau} = \frac{Im(Z)}{\sqrt{\varepsilon r}}. \quad (2.71)$$

Equation (2.69) gives us an expression for the average change in mechanical energy over one trap oscillation, and Equation (2.71) gives the average scattering rate over one trap oscillation. In the hot regime, we can use Equation (2.69) to calculate the energy as a function of time, given that the ion starts with some initial energy,  $\varepsilon_0$ . To calculate the ion's motional energy as we move into the cold regime, we need to include the effects of recoil heating, since the motional energy approaches the recoil energy.

To account for the recoil energy, we rewrite Equation (2.62) in the scaled units as:

$$\left(\frac{d\varepsilon}{d\tau}\right)_{recoil} = \frac{2}{3}\sqrt{\frac{r}{\varepsilon}}Im(Z). \quad (2.72)$$

Combining the two rates we obtain an expression for the total change in mechanical energy given by:

$$\frac{d\varepsilon}{d\tau} = \frac{1}{2\sqrt{\varepsilon r}}(Re(Z) + \delta Im(Z)) + \frac{2}{3}\sqrt{\frac{r}{\varepsilon}}Im(Z). \quad (2.73)$$

In one of the experiments done in the lab, we measured the linewidth of  $^{24}Mg^+$  using a single laser beam that laser-cooled the ion using the  $^2S_{\frac{1}{2}} \rightarrow ^2P_{\frac{1}{2}}$  transition. As we tuned towards resonance, the steady-state temperature the

ion reached at each different detuning was different, due to Doppler effects.

To model this effect it is possible to numerically integrate Equation (2.73); however, this model neglects background heating (eg. anomalous heating [51]) that causes the ion to equilibrate at a higher mechanical energy. We have also assumed that the emission is isotropic, which is not true for dipole radiation. Alternatively, it is possible to obtain an analytic form for the steady-state mechanical energy, as has been done by Itano and Wineland [54]. In their treatment, they considered a more general case, accounting for the angular distribution of emitted photons. In Section (6.3.1) we will use their analysis to obtain an analytic form for the lineshape.

While Equation (2.73) does not fully encompass all of the physics involved in the experiment we performed, we can still use it to qualitatively understand what occurs. To this end, we numerically integrated Equation (2.73) in Maple [49], and determined the steady-state energy for a number of different laser detunings. From the steady-state energy, we calculated the scattering rate using Equation (2.71). In Figure (2.7) we plotted the calculated normalized scatter rate for different detunings from resonance. As resonance is approached, the ion is appreciably heated, resulting in a loss of fluorescence. In practice, we could typically recover the ion by tuning red of resonance. The solid curve corresponds to a power-broadened Lorentzian, showing good agreement between the calculated data points and the Lorentzian curve to as close as 5 *MHz* from

ion resonance.

To reiterate, we have ignored background heating in this model and we have also assumed that the emission pattern is isotropic and so we do not expect numerical agreement between this model and our experiment but rather, we used this model to qualitatively understand how the lineshape changes. In Section (6.3.1) we obtain an analytic form for the lineshape, and in Section (6.3.2) we compare and discuss the results obtained from fitting to the analytic solution as well as fitting to a power-broadened Lorentzian.

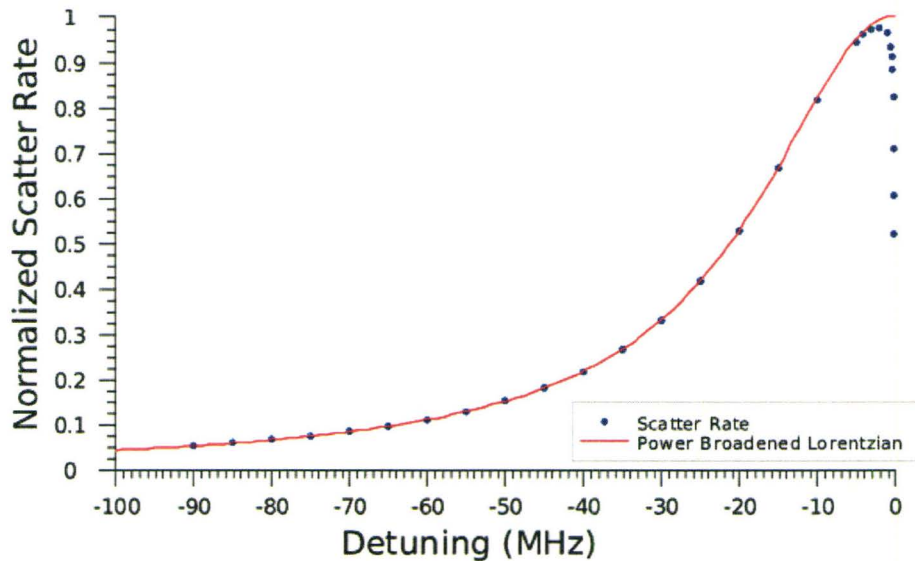


Figure 2.7: Simulated linewidth curve including Doppler effects. The steady-state energy was calculated for a series of different laser detunings to determine the steady-state scattering rate according to Equation (2.71). The normalized scattering rate was plotted as a function of laser detuning to demonstrate that the Doppler effects do not significantly change the lineshape for laser detunings larger than 5 MHz from ion resonance.



# Chapter 3

## Apparatus

### 3.1 Introduction to the Apparatus

The requirements for ion trapping are not simple. Ion traps are not “off-the-shelf equipment” and the components of the apparatus come from various fields. For long trapping lifetimes, a high vacuum ( $10^{-11}$  Torr) must be maintained to prevent ion loss due to collisions with background gasses. Thus, we place the ion trap, along with magnesium sources, inside of a vacuum chamber which can be evacuated to the low pressures required.

To address our ions we require laser systems to cool and interact with the ions. A significant amount of beam shaping and frequency shifting is required. Also, numerous optics to monitor and stabilize the frequency are necessary, as discussed in Section (3.3). Numerous synthesizers as well as

function generators are used in order to drive the various optical components (such as acousto-optic modulators), and we will include a description of these in the discussion where relevant.

In addition to apparatus for cooling and containment, we also need a detection system. We used an Andor™ EMCCD camera to image the ion and a Hamamatsu photomultiplier tube to count photons using an electron shelving method [55]. A full discussion of the imaging system and the electron shelving technique used to determine the state of the ion is included in Section (3.6).

A majority of the experiment was run by computer control since we needed to rapidly turn on and off different pulse sequences. This required an RF switchbox made up of TTL-controlled RF switches. To generate the different pulses, we used a PulseBlaster (a TTL pulse generator), that allowed us to rapidly turn on and off different pulse sequences for the experiment. Labview VIs were written to give us a user interface that allowed us to control most of the equipment from a single computer (see Section (3.7)).

## 3.2 Vacuum Chamber

To maintain long ion lifetimes, the trap, source, and associated parts are all placed into a vacuum chamber (see Figure (3.1)) at low pressure ( $\sim 10^{-11}$  Torr). The vacuum chamber (*MFC600 – SO200800 – A*) was purchased from Kimball Physics. A schematic of the chamber from the side, as well as from the top

looking down (without the imaging system in place), is shown in Figure (3.2) and Figure (3.3). At sufficiently low pressure, elastic collisions between the trapped ion and background gas that can cause ion heating become infrequent ( $\sim 1$  every 10 minutes at  $10^{-11}$  Torr) [56]. Their frequency is much lower than the time for a typical experiment ( $< 1$  ms), and so collisions between trapped ion and background gas should not affect most measurements. Inelastic collisions, resulting in ion loss, occur less frequently. This is supported by the fact we typically keep a trapped ion for a minimum of several hours.

To reduce the pressure to this level a lot of preparation is required: cleaning, and baking of the vacuum parts, the trap, the electron guns, the oven, and associated connectors and wires. The bulk of this work was performed by Jiajia Zhou and detailed information on the cleaning as well as preparation can be found in his thesis [57].

To summarize his work, many of the smaller pieces were first cleansed by immersing them in a beaker filled with warm water and detergent and agitating for 30 minutes in an ultrasonic cleaner. The parts were rinsed and then placed in a large beaker partially filled with acetone and agitated for an additional 10 minutes before being rinsed off and allowed to air dry.

This process was followed by methanol-vapour degreasing, in which the parts were held in a basket placed above a beaker of heated methanol. The beaker of methanol was heated on a hot plate (without boiling the methanol)

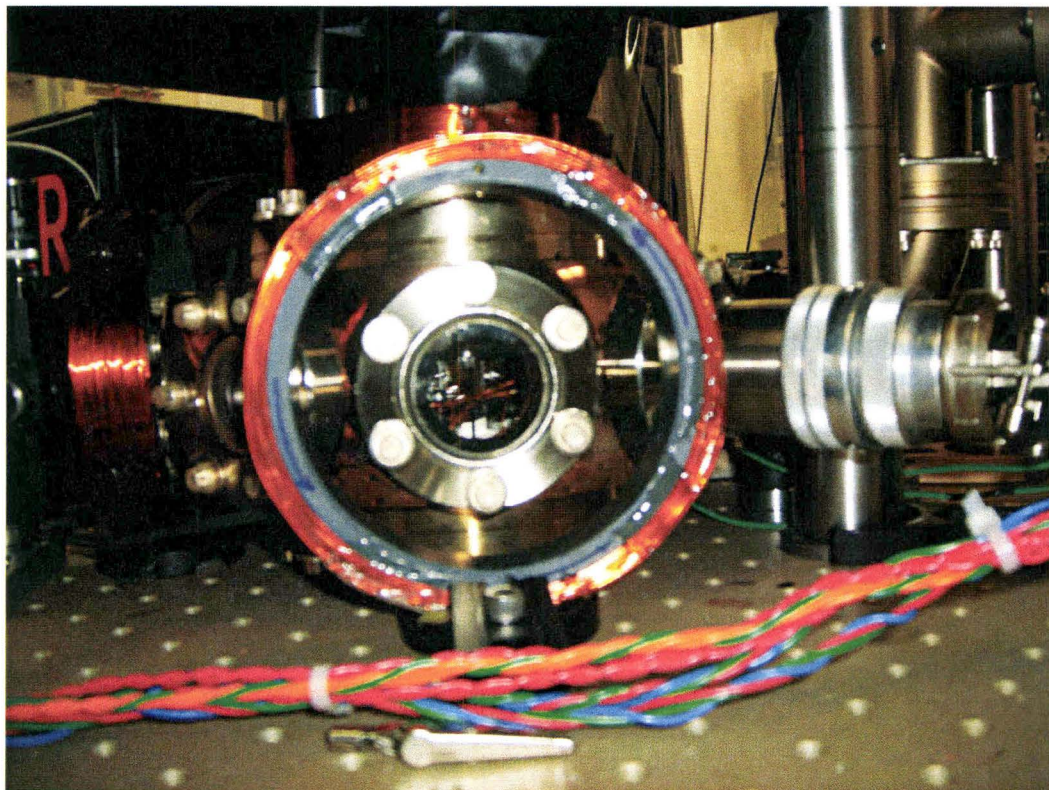


Figure 3.1: Side view of the vacuum chamber. Also seen in the figure are the magnetic-field coils. The coil in the centre of the photograph is the Perpendicular Coil. Laser access to the ion is blocked in this vacuum chamber window because of a bolt protruding down from the top of the chamber. The Quantization Coil can be seen on the left side of the photograph. All of the laser beams go through the vacuum chamber window (not depicted) from the left with the exception of the Photoionization beam, which goes through the vacuum chamber window from the right (also not depicted).

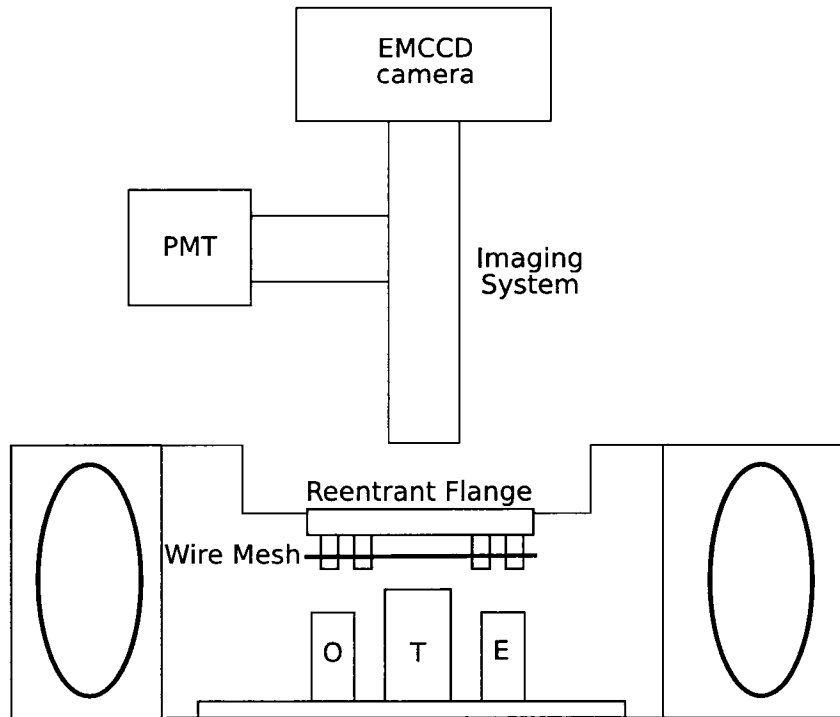


Figure 3.2: Side-view schematic of the vacuum chamber as seen looking along the trap axis (not to scale). Attached to the bolts of the re-entrant flange is a wire mesh that was used to shield the trap from static charge buildup on the dielectric window. Also shown inside of the vacuum chamber is the trap (see Section (3.2.1)), the natural abundance magnesium oven (see Section (3.2.2)) and one of the electron guns (see Section (3.2.3)). Unfortunately, one of the bolts attaching the re-entrant flange to the vacuum chamber prevented laser light access through the rightmost window shown in the figure. This prevented us from being able to send purely  $\pi$ -polarized light into the vacuum chamber; given our need for  $\sigma^{+/-}$ -polarized light to drive the  $^{25}\text{Mg}^+$  cycling transition. For detailed information on the imaging system, including the EMCCD and PMT, see Section (3.6). [Definition of labels used in the figure: O = magnesium oven; T = trap; E = electron gun]

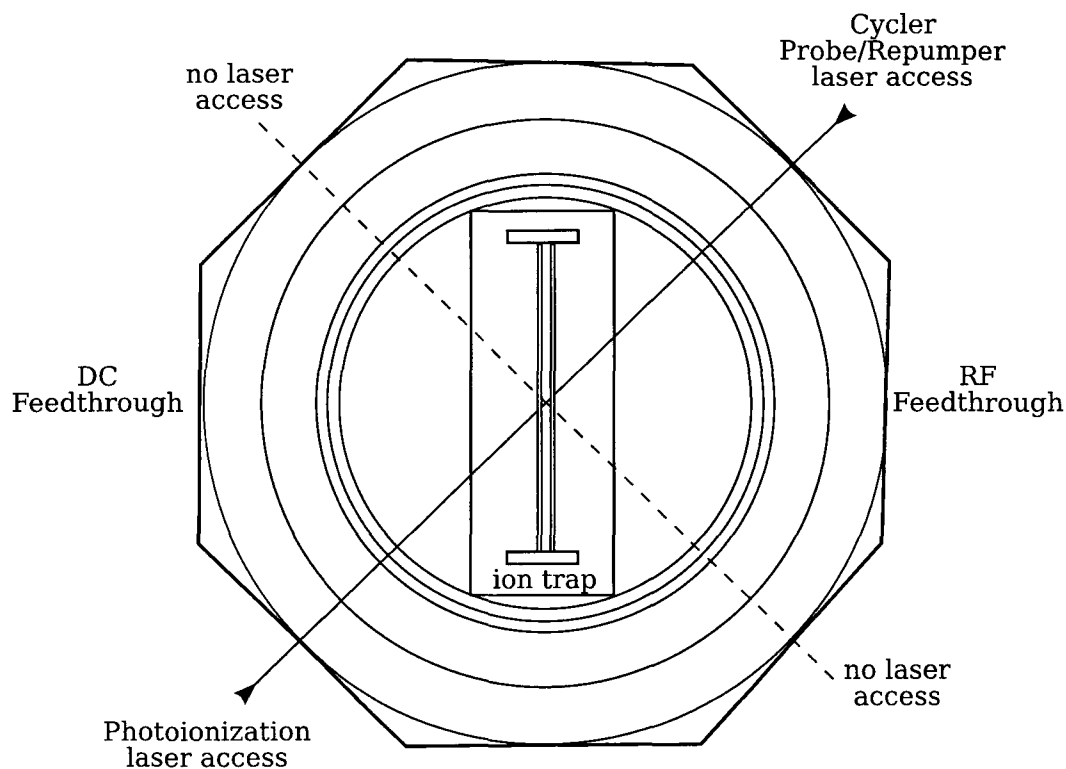


Figure 3.3: Top-view schematic of the vacuum chamber (not to scale). The trap (see Section (3.2.1)) is shown centrally in the image. The RF and DC feedthroughs are labelled in the figure, along with the laser access viewports for all of the laser beams. Also shown in a dashed line is the beam path that is blocked by bolts attaching the re-entrant flange to the vacuum chamber.

until droplets formed on both the parts and the basket. As droplets fell from the parts held in the basket, they pulled off any residual grease that remained on the pieces. The degreasing was continued for approximately 20 minutes before the parts were rinsed off with tap water and placed into a beaker of deionized water that was agitated using an ultrasonic cleaner.

The trap electrodes were also electropolished to smooth the surface of the electrodes and thus reduce vacuum electrical discharges. For the electrodes that were not kept at a high voltage, a chemical cleaning of the stainless steel parts was deemed sufficient.

Many of the larger stainless steel parts were cleaned with acetone using Kimwipes and pre-baked in an oven at  $400^{\circ}\text{C}$  for 2 – 3 days, producing a chromium-oxide layer that is said to reduce water diffusion and hydrogen desorption from the stainless steel [58] [59] [60].

Once the pre-baking and cleaning of parts was finished, the trap, vacuum chamber and all of the electrical connections were assembled and placed inside a home-built oven. The chamber was connected to a turbo-pump station used to do the initial pumping. The oven was sealed, and the temperature was slowly ramped to  $200^{\circ}\text{C}$  and monitored via thermocouples until the pressure reached equilibrium (typically occurring at  $10^{-7}$  Torr). Once equilibrium was reached, the oven temperature was reduced to allow us to close the valve to the turbo-pump and turn the ion pump on. With the ion pump on, a second bake

was performed, again ramping the temperature to  $200^{\circ}\text{C}$  and waiting until the pressure reached equilibrium.

When baking was complete, the electrical connections to all of the parts were checked for continuity and the vacuum chamber was moved onto the optical table. The pressure was monitored using a nude ion gauge, which can measure pressures as low as  $2 \times 10^{-11}$  Torr (although measurements of the pressure at the low end are not reliable). By one week after baking, the indicated pressure typically ranged from  $2.2 - 2.5 \times 10^{-11}$  Torr. In addition to the ion pump (suitable for pumping background helium and hydrogen), we also had a titanium sublimation pump that we would periodically fire off to reduce the pressure. The TSP is suitable for chemically reactive gases such as hydrogen and nitrogen but is not suitable for the chemically inert noble gases.

Unfortunately, when the vacuum chamber was assembled, one of the bolts connecting the re-entrant flange and the vacuum chamber blocked laser access through two of the windows. This prevented us from driving transitions with  $\pi$ -polarized light if we also wanted to drive with  $\sigma^{+/-}$ -polarized light.

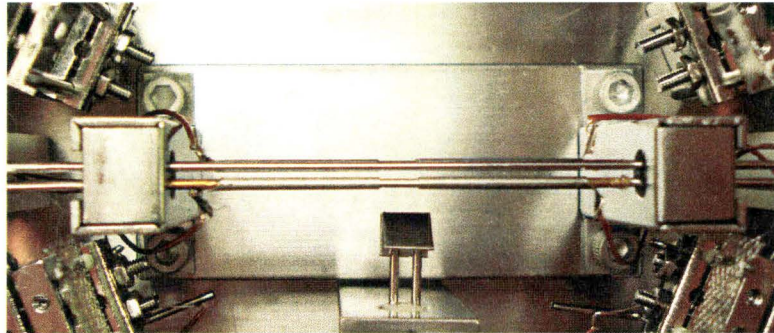
### 3.2.1 Ion Trap

The ion trap used in the experiments was a linear Paul trap built by Jiajia Zhou, roughly following the design in Ref. [61]. High-voltage RF fields provide confinement along the radial direction and DC fields provide confinement along

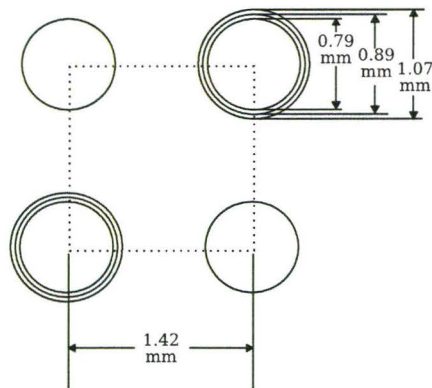
the axial direction, as discussed in Chapter 2. For typical voltages used in the experiments discussed in this thesis ( $V_{RF} \approx 283 \text{ V}$ ,  $\Omega_T \approx 2\pi \cdot 14 \text{ MHz}$ ,  $V_{DC} \approx 6 \text{ V}$ ), the trap frequencies were  $\omega_x = 2\pi \cdot 4.65 \text{ MHz}$ ,  $\omega_y = 2\pi \cdot 4.32 \text{ MHz}$ , and  $\omega_z = 2\pi \cdot 421 \text{ kHz}$ . Table (3.1) gives a summary of the trap dimensions.

The trap consists of four electrodes as shown in Figure (3.4). Two of the electrodes are held at RF high and two held at RF ground. Two tube electrodes are slid around each of the two RF ground electrodes to provide DC voltages for confinement along the axial direction. A polyimide tube ( $25 \mu\text{m}$  thickness) between the tube electrodes and the RF ground rod is used to provide insulation between DC tube electrodes and the RF ground rods and to mechanically fix the tube electrodes in place. The geometric factors corresponding to our trap design are:  $|\alpha| = 2.64 \text{ mm}^{-2}$ ,  $|\beta| = 2.52 \text{ mm}^{-2}$ ,  $|\gamma| = 0.12$ ,  $|\alpha'| = |\beta'| = 0.12 \text{ mm}^{-2}$ , and  $|\gamma'| = 0.24 \text{ mm}^{-2}$ .

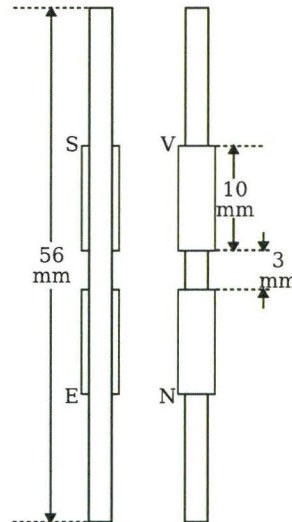
RF voltages are applied to the trap electrodes using a helical resonator as discussed in Section (3.2.4). A static voltage is applied to the DC electrodes using a DC voltage supply (*HP6227A* in the experiments discussed here) that is connected to an electrical feedthrough on the vacuum chamber. The DC voltages can be adjusted using a Labview VI that allows for separate adjustment of each of the DC tube electrode voltages (see Section (3.7.1)).



(a) Ion trap photo. The ion trap is shown in the vacuum chamber looking from the top down. Visible in the photo is one of the RF rods held at high voltage (nearest to the top of the photograph), an RF ground rod (nearest to the bottom of the photograph), and all four of the DC tube electrodes (surrounding the RF ground rods). The tube electrodes are separated by  $3\text{ mm}$  along the trap axis. The edges of the other two tube electrodes are also visible beneath the rod kept at high voltage, though the RF ground rod is not. Also shown in the photo is the compensation electrode (used to push the ion between the RF ground rods) as well as the the bracket supports for the electron guns and magnesium ovens. (Photo courtesy of Jiajia Zhou.)



(b) A schematic for the trap looking along the trap axis (not to scale).



(c) A schematic for the trap looking down from above (not to scale).

Figure 3.4: Ion trap photo and schematics. The RF rods are centred  $1.42\text{ mm}$  apart with a diameter of  $0.79\text{ mm}$ . Polyimide tubing ( $OD = 0.89\text{ mm}$ ) surrounds the RF ground electrodes to provide electrical isolation between RF ground and the DC tube electrodes ( $OD = 1.07\text{ mm}$ ). The RF rods are  $56\text{ mm}$  long. The tube electrodes are  $10\text{ mm}$  long and are separated by  $3\text{ mm}$  along the trap axis. Trap dimensions are listed in Table (3.1). [Definition of labels used in the figure: E = Eva; S = Snake; N = Naomi; V = Vamp]

Table 3.1: Ion Trap: Summary of Trap Dimensions

rod diameter	0.79 <i>mm</i>
distance between RF rods (centre to centre)	2 <i>mm</i>
rod length	60 <i>mm</i>
inner diameter of tube electrode	0.88 <i>mm</i>
outer diameter of tube electrode	1.05 <i>mm</i>
distance between tube electrodes (end to end)	3 <i>mm</i>
length of tube electrodes	10 <i>mm</i>

### 3.2.2 Mg Source

An oven of natural-abundance magnesium was placed in the vacuum chamber, as well as a  $^{25}\text{Mg}$ -isotopically enriched oven. For the experiments described in this thesis, only the natural-abundance oven was used. Both were built in-house by Laura Toppozini, based on a design from the NIST Ion Storage Group [62].

The ovens, shown in Figure (3.5), were constructed from a 10 *mm* long alumina spacer whose diameter was 4 *mm*. The spacer had four holes in it, each with a diameter of 0.80 *mm*. One hole was cemented closed at one end and filled with magnesium foil to serve as the atom source.

A second hole was threaded with a Type K thermocouple and used to monitor the temperature of the oven. To heat the oven, the outer diameter of the alumina spacer was tightly wound with 0.015" diameter tungsten wire. One end of the wire was grounded, and the other end connected to a DC feedthrough. Typically, a current of 1.5 – 1.8 *A* is used to bring the oven to a steady state temperature of 150° *C*.

To provide approximate collimation of the neutral atom beam, a stainless steel shim with a 1.5 mm diameter hole was placed in front of the oven.

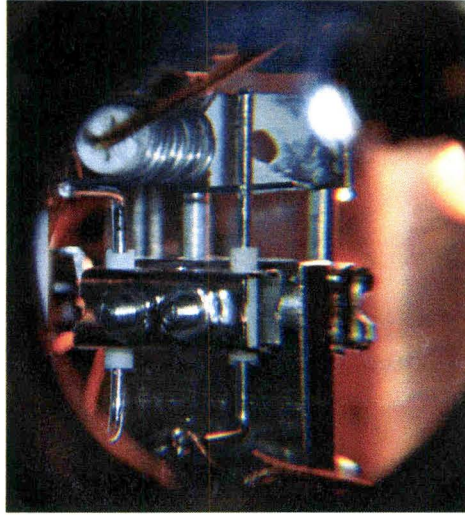


Figure 3.5: A photograph of the magnesium oven as seen through one of the vacuum-chamber windows. The oven is constructed from a 10 mm long alumina spacer whose diameter was 4 mm. One of the four holes in the spacer had one end cemented closed and was filled with magnesium foil. This served as the atom source. A second hole was threaded with a Type K thermocouple that was used to monitor the temperature. One of the lead wires for the thermocouple can be seen in the image, protruding from the back of the alumina spacer. Two empty holes are also visible in the image. The alumina spacer was wound with tungsten wire that was spot-welded to either end to two L-brackets. Wires were spot-welded to the other end of the L-bracket, and connected to the DC feedthrough. A stainless steel shim with a 1.5 mm diameter hole was placed in front of the oven to provide approximate collimation. Typically a current of 1.5 – 1.8 A is used to bring the oven to an equilibrium temperature of 150°C. Magnesium plating on the stainless steel shim can be seen in the photograph. [Photograph courtesy of Brian King.]

### 3.2.3 Electron Guns

Two electron guns, built by Laura Topozini, were included in the vacuum chamber, although neither was used for the present work. We opted to install

them into the vacuum chamber as an option if problems arose with photoionization. The electron guns consisted of a 0.25 mm diameter thoriated tungsten wire wound into a cylindrical coil, with the ends of the wire spot welded to separate stainless steel rods that were  $\frac{1}{32}$ '' in diameter. The rods were then spot welded to wires with one rod grounded and the other rod connected to a DC feedthrough.

A stainless steel grid, with each side spot-welded to a stainless steel rod, was placed in front of the electron gun. Applying a voltage to the grid would accelerate and direct electrons emitted from the thoriated tungsten towards trap centre.

The disadvantage of using an electron gun is that as it heats up it causes outgassing in the chamber, producing contaminants that can potentially collide with a trapped ion and reduce the ion lifetime. Additionally, emitted electrons can charge dielectric surfaces, resulting in potentials that can affect the trapping fields. In particular, we were concerned about charge potentially building up on the viewport window (see Figure (3.15)). We opted to install a wire mesh (59.1% open area) that hung just below the viewport window. The mesh was held in place using the vacuum chamber bolts screwed into the re-entrant flange. This gave emitted electrons near the viewport window an alternate path to ground (through the wire mesh) at the cost of a reduction in transmitted light (59.1% transmission). The mesh also shielded the trap from

static buildup on the dielectric window.

### 3.2.4 Helical Resonator

The linear Paul trap uses high RF voltages ( $\sim 400\text{ V}, 13\text{ MHz}$ ) for the RF trapping field. This provides a radial trap frequency of  $4.2\text{ MHz}$ . A helical resonator [63] was built to deliver high voltages at RF frequencies to the trap electrodes. Although the fields in a helical resonator are not  $TEM_{00}$ , the resonator can be approximately treated as if it were a simple transmission line. At these frequencies the wavelength of the electrical signal is a significant fraction of the physical length of the transmission line and so its spatial variation along the line must be treated.

From transmission line theory [64], for an open-circuited load (or purely reactive load), a maximum of the voltage occurs at the load location. A quarter-wavelength away, the voltage is a minimum, while the current is a maximum. We place the trap at the load and couple into the resonator where the voltage is a minimum so that we can use the voltage amplification to deliver high voltages to the trap electrodes. The peak voltage at the load can be calculated from the power delivered to the resonator, and the  $Q$  of the resonator. Specifically, the voltage is given by [65]:

$$V_{RF} = \zeta \sqrt{P_I Q_L} \quad (3.1)$$

where  $\zeta$  is a geometric factor, dependent on the resonator design parameters [65],  $P_I$  is the power coupled into the resonator, and  $Q_L$  is the loaded  $Q$  of the resonator (the measured  $Q$  when the resonator is attached to a load) which depends on the resistive losses.

The advantage of using a helical resonator as opposed to a traditional transmission line is that a helical resonator is much more compact. For example, at 14 MHz, a quarter-wavelength is 5.4 m whereas the equivalent helical resonator is only 19.8 cm long.

The resonator, shown in Figure (3.6), consists of a wound copper coil with one end soldered to an outer conductor (copper cylinder) held at ground. The other end of the coil is soldered to an MHV connector that can be attached to an RF feedthrough on the vacuum chamber. The dimensions of the resonators used are given in Table (3.2). For the experiments described in this thesis, resonator  $\mathcal{A}$  was used.

The RF source for the helical resonator is a signal generator (*Agilent 33120A*) that is connected to a high power amplifier (for resonator  $\mathcal{B}$  the *HP 8656A* was used). The output of the amplifier is connected to a circular loop soldered to the stripped end of a BNC cable. This loop inductively couples power into the resonator. Coupling into the resonator was optimized by monitoring the forward and reflected voltages with a bi-directional coupler attached to the output of the amplifier and iteratively adjusting the resonant frequency and

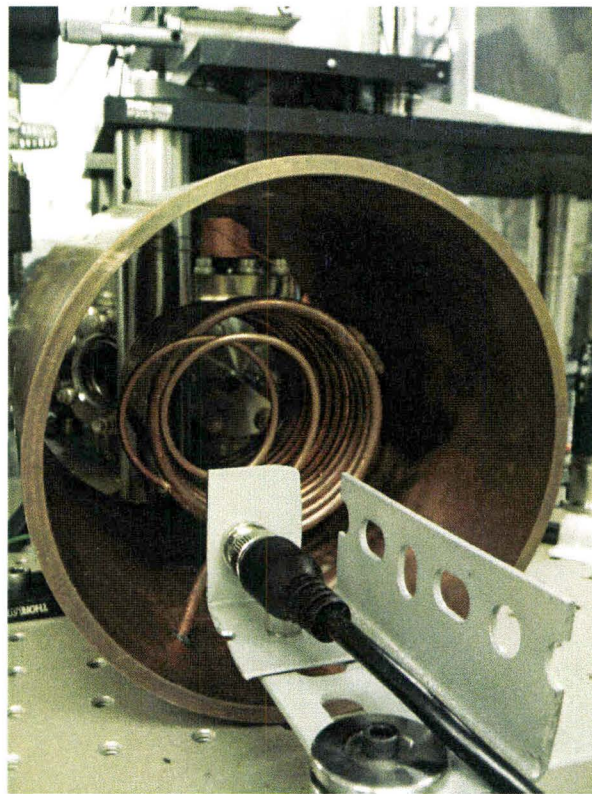


Figure 3.6: A photograph of resonator  $\mathcal{A}$  connected to the RF feedthrough of the vacuum chamber. The coupling loop (seen in the foreground) consists of two turns of copper wire, soldered to a stripped BNC cable.

loop position to minimize the reflected voltage.

Table 3.2: Helical Resonator: Summary of Resonator Dimensions

Resonator Label	$\mathcal{A}$	$\mathcal{B}$
$D$ (outer conductor diameter)	14.58 <i>cm</i>	9.22 <i>cm</i>
$d$ (coil diameter)	8.02 <i>cm</i>	4.67 <i>cm</i>
$L$ (outer conductor length)	19.81 <i>cm</i>	15.06 <i>cm</i>
$l$ (coil length)	12.04 <i>cm</i>	8.38 <i>cm</i>
$d_0$ (wire diameter)	0.41 <i>cm</i>	0.32 <i>cm</i>
$N$ (number of turns)	13	10
$Q_L$ (loaded Q)	500	341
$\zeta$ (geometric factor)	10	10
$f_0$ (resonant frequency)	13.9379 <i>MHz</i>	22.5476 <i>MHz</i>

### 3.3 Lasers

The invention of the laser had wide-ranging applications. We use lasers in medicine, entertainment, and modern electronics, to name a few applications. In spectroscopy, lasers provide us with a source of high power, narrowband coherent light. This allows us to coherently drive particular atomic transitions. In order to drive the transitions introduced in Section (2.1) we set up three different laser systems.

To load ions into the trap, we photoionized a neutral beam of magnesium by driving the  $Mg I \ ^1S_0 \rightarrow \ ^1P_0$  transition. From the  $\ ^1P_0$  state it is possible for the neutral atom to absorb another photon (see Section (2.1)), giving the electron enough energy to excite into the continuum [41].

We laser cooled the ion using the  $\ ^2S_{\frac{1}{2}} \rightarrow \ ^2P_{\frac{1}{2}}$  transition for  $\ ^{24}Mg^+$  and the

${}^2S_{\frac{1}{2}} \rightarrow {}^2P_{\frac{3}{2}}$  transition for  ${}^{25}\text{Mg}^+$ . To measure the linewidth and the hyperfine  $a$  constant of the  ${}^2P_{\frac{1}{2}}$  we probed the  ${}^2S_{\frac{1}{2}} \rightarrow {}^2P_{\frac{1}{2}}$  transition.

These latter two transitions lie at approximately 280 *nm*, whereas the photoionization transition lies at 285 *nm*. At the time when we began building the lab, lasers in the UV were not readily available at the required wavelengths. The solution was to purchase lasers at longer wavelengths and use frequency conversion techniques in order to bring us to the appropriate wavelength. After looking at our options we decided to purchase a used dye laser and two fibre lasers. The tuning range of the dye laser was large ( $\approx 20$  *nm* without switching laser dye type), and so it would be suitable for driving photoionization as well as Raman transitions (which require high laser power). The two fibre lasers had a smaller tuning range ( $\approx 0.3$  *nm*) and so we placed an order with a specified centre frequency suitable for the Cyclor and Probe beam lines, respectively.

An advantage of the dye laser is its large tuning range so that it could technically be used to replace the Cyclor or the Probe beamlines. The main disadvantage of the dye laser is that its linewidth is significantly larger than the fibre lasers and would be a limiting factor in the precision of our measurements. The fibre lasers have a smaller linewidth. The lasers are also much simpler to use. They are turned on by the switch of a key and do not require the constant alignment or constant dye changes that the dye laser does.

A commercial solution was chosen in order to frequency-double the visible

output of the dye laser. We purchased a WaveTrain®(Spectra-Physics), which is an interesting ring cavity employing two mirrors and a prism mounted on a piezo stack to close the cavity.

For the fibre laser systems a home-built system was designed. The output of the fibre lasers are IR and so doubling the frequency from the IR into the UV required two separate doubling cavities to quadruple the frequency. A more thorough discussion of the design of these frequency doubling systems is included in Chapter 4.

### 3.3.1 Fibre Laser

Both fibre lasers are Koheras A/S Boostik fibre lasers consisting of a ytterbium-doped inner core that serves as the gain medium. A Bragg grating is etched onto the fibre. The fibre laser is pumped by a 980 nm diode laser, and the output of the fibre laser is amplified by an internal amplifier.

The “Probe” laser, used to drive the  ${}^2S_{\frac{1}{2}} \rightarrow {}^2P_{\frac{1}{2}}$  transition, has a maximum output of 1.3 W, centered at 1121.41 nm and the “Cycler” laser, used to drive the  ${}^2S_{\frac{1}{2}} \rightarrow {}^2P_{\frac{3}{2}}$  transition, has a maximum output of 2.0 W centered at 1118.54 nm. The factory specified linewidth of both lasers is  $< 40$  kHz ( $< 160$  kHz in the UV). We measured a linewidth of  $122 \pm 4$  kHz (in the UV), as discussed in Section (6.3.1). Both fibre lasers are tunable by temperature tuning ( $\Delta\lambda \approx 0.3$  nm), which changes the index of refraction, and voltage

tuning ( $\Delta\lambda \approx 0.1 \frac{pm}{V}$ ), which changes the period of the Bragg grating by stretching the fibre. The maximum voltage that can be applied to the fibre is 200 V, corresponding to a total of  $\Delta\lambda \approx 20 pm$ . The factory specified bandwidth of voltage-tuning input is 20 kHz.

Temperature tuning is adjusted by a knob located on the front panel. Voltage tuning is adjusted by applying voltage to a LEMO plug on the back of the laser, thus moving a PZT internal to the laser. This stretches the laser fibre, changing the wavelength because of changes in the length as well as stress-induced changes in the index of refraction [66].

Although the factory-specified laser linewidth is  $< 40 kHz$ , there is also a broad background of 100 nm width. This is due to spontaneous emission in the fibre laser that is also amplified by the internal amplifier. This results in a broadband unpolarized background that is  $\approx 30\%$  of the total power in the 1.3 W laser and  $\approx 10\%$  of the total power in the 2.0 W laser. The bandwidth of the ASE is well outside the bandwidth of the doubling cavities, and so the ASE does not contribute significantly to the frequency doubled light.

### 3.3.2 Dye Laser

The dye laser is a Coherent CR – 699 – 21 ring dye laser pumped by a solid state Verdi laser (V10 – A1616) that has a maximum power output of 10 W. The lasing medium is 400 mg of Rhodamine-19 dissolved in 50 mL of benzyl

alcohol and mixed with approximately 2 L of ethelene glycol. The laser cavity is a four mirror ring cavity, with additional intracavity optics for single-mode, unidirectional operation as shown in Figure (3.7).

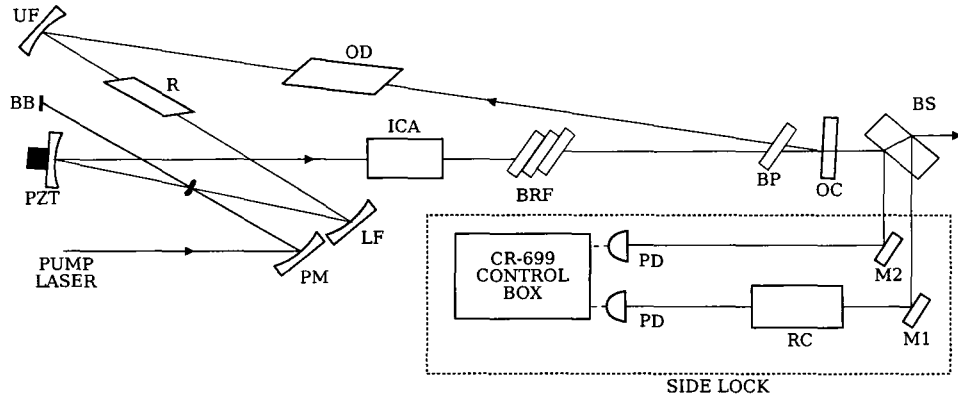


Figure 3.7: Schematic of the dye laser (*CR – 699 – 21*). The image is not to scale. [Definition of the labels used in the figure: PM = pump mirror; BB = pump laser beam block; PZT = piezo-mounted mirror; ICA = intracavity assembly (thin etalon and thick etalon); BRF = birefringent filter; BP = Brewster plate; OC = output coupler; OD = optical diode; UF = upper fold mirror; R = astigmatic compensation rhomb; LF = lower fold mirror; BS = beamsplitter; M1 and M2 = beam steering mirrors; RC = temperature stabilized reference cavity for side lock; PD = photodetector]

The pump beam is focussed into the dye jet using the pump mirror. Part of the  $4\pi$ -steradian fluorescence from the dye is collected by the PZT and LF mirrors and is sent through the laser cavity in a bow-tie configuration. In the counter-clockwise direction, the nearly-collimated fluorescence bounces off the PZT mirror and is directed through the intracavity assembly (ICA) and birefringent plate (BRF), which are frequency selective components.

Since the mirrors and the fluorescence from the dye jet are broadband, the dye laser will tend to operate multi-mode. The BRF and the ICA prevent this

from occurring, by introducing loss to the undesirable modes. This allows us to tune the dye laser, as well as obtain single-mode operation of the dye laser.

The least frequency-selective component of the dye laser is the birefringent filter, which has a free spectral range (FSR) of 1 THz. This is followed by the thin etalon, which has a FSR of 100 GHz and the thick etalon, which has a FSR of 10 GHz. The most frequency selective component is the laser cavity itself, with a FSR of  $\approx 75$  MHz. Only the wavelength for which the different passbands overlap can lase resulting in single-mode operation.

After the BRF, the beam passes through a Brewster plate before being directed by the output coupler (OC) through an optical diode (OD), whose purpose is to prevent bi-directional lasing from occurring. The optical diode consists of a Faraday rotator and a quartz plate, both of which introduce a rotation in the polarization of the laser. The difference between the two elements is that the quartz plate introduces the same rotation to the polarization regardless of which direction the beam is travelling whereas the Faraday rotator introduces a rotation to the polarization that is directionally dependent, due to the Faraday effect.

In the counter-clockwise direction, the polarization of the laser beam is unchanged. The quartz plate rotates the polarization by an angle  $\theta$ , whereas the Faraday rotator introduces a rotation of  $-\theta$ . In the clockwise direction, the Faraday rotator introduces an additional rotation of  $\theta$ , and so the beam

acquires a net rotation in its polarization. This introduces loss in the clockwise-travelling beam since a number of optical elements (the astigmatic compensation rhomb, the dye jet, the birefringent filter) are Brewster-angled surfaces.

## **3.4 Optics**

### **3.4.1 The Optical Beamlines**

A significant amount of beam reshaping and manipulation is required before the laser beams pass into the vacuum-chamber windows. All of our beams undergo one or more stages of frequency doubling in resonant power-buildup cavities and so care has to be taken to properly match the incoming beam to each cavity mode for optimal coupling. Diagnostic beams are also required to keep the various cavities locked as well as to monitor the wavelength of the lasers. The following sections are broken up by beamline. We use the well-known hyperfine lines of molecular iodine as frequency standards and to stabilize the frequency of our laser systems, so we complete the discussion of beamlines with a section of iodine spectroscopy.

### **3.4.2 Cycler Beamline**

The 2 W Koheras Boostik fibre laser is used for the Cycler beamline. The output of the fibre laser is centered at 1118.5 nm and so two frequency-doubling

stages are required in order to bring it down to the UV.

The output of the laser is highly divergent. An aspheric lens is used at the fibre output to collimate the beam. Back reflections into the laser can be amplified, damaging the unit. While the system has an auto-shutdown mechanism in place we opted to also include an optical isolator to prevent back reflections from occurring.

A commercial optical isolator was purchased from ConOptics for our experimental setup. The optical isolator consisted of two polarizers, one at the input and one at the output, with a Faraday rotator between them. The Faraday rotator is similar in operation to the one discussed in Section (3.3.2), except that it induces a larger rotation of the laser polarization. The Faraday rotator rotates the polarization of the linearly polarized input beam by  $45^\circ$ , so that the plane of polarization coincides with the optical plane of the output polarizing beamsplitter, allowing light to pass through it. If a stray beam is reflected back through the optical system, then the Faraday rotator rotates the beam by an additional  $45^\circ$  so that its plane of polarization is perpendicular to the optical plane of the input polarizer, and so the beam reflects off the input polarizing beamsplitter. This prevents back-reflections into the fibre laser.

Before entering the optical isolator, the collimated beam is sent through a quarter-wave and a half-wave plate to transform the laser polarization to that required for the optical isolator input. The polarizers allow for day to

day adjustment of the input polarization since the laser output fibre is not a polarization maintaining fibre.

After the optical isolator, the beam passes through a half-wave plate used to rotate the polarization of the beam. This wave plate is used to set the amplitude of the error signal for the 1120 nm to 560 nm doubling cavity.

### Cyclor LBO Cavity

The first-stage doubling cavity is a four-mirror ring cavity built around a temperature-controlled lithium borate (LBO) crystal. The crystal is encased in a brass housing with an embedded heater and a RTD probe. The RTD probe and heater are connected to the same controller (*Fuji Electric PXR – 4*). The temperature measured by the probe is used to derive an error signal used to keep the temperature constant. For optimal conversion efficiency, the LBO crystal is kept at 106° C. The cavity beamline and its associated optics are shown in Figure (3.8).

Light is coupled into the cavity using a pair of mirrors and two lenses that take the collimated output from the fibre laser and match it to the mode of the doubling cavity. A typical efficiency for coupling into the cavity is 85 – 90% (measured by taking a ratio of the measured power when the cavity is unlocked and far from resonance to when the cavity is locked).

The cavity is locked using a Hansch-Coulliaud stabilization scheme [67] that compares the phase shift between the light reflected from the cavity and

the light circulating inside of the cavity through polarization techniques. The light is measured on a pair of photodiodes which monitor the components of horizontally and vertically polarized light. The difference between the photodiode outputs is used to derive an error signal. The error signal drives a piezo-mounted mirror that adjusts the length of the cavity, keeping it resonant. A thorough discussion of the frequency doubling system can be found in Chapter 4.

The output of the doubling cavity is sent through a polarizing beamsplitter that sends off 70 *mW* of light to the cyclotron diagnostics and the remaining 290 *mW* to a second doubling cavity.

### **Cyclotron Diagnostic Beamline**

The diagnostic beam is split in two. One of these beams is itself split into two and sent to a Wavemeter (*WA – 1000*), used for coarse calibration of the wavelength, and a spectrum analyzer. For the experiments described, the spectrum analyzer was not used. The second beam is sent through an iodine spectroscopy setup for fine calibration of the wavelength. A full discussion of iodine spectroscopy is included in Section (3.5.1); however, the specifics of the beamline will be discussed below.

The iodine setup (Figure (3.9)) in this beamline consists of an acousto-optic modulator (AOM) in a double-pass configuration (Figure (3.10)), a frequency-modulated acousto-optic modulator, an iodine cell, and various optics for beam

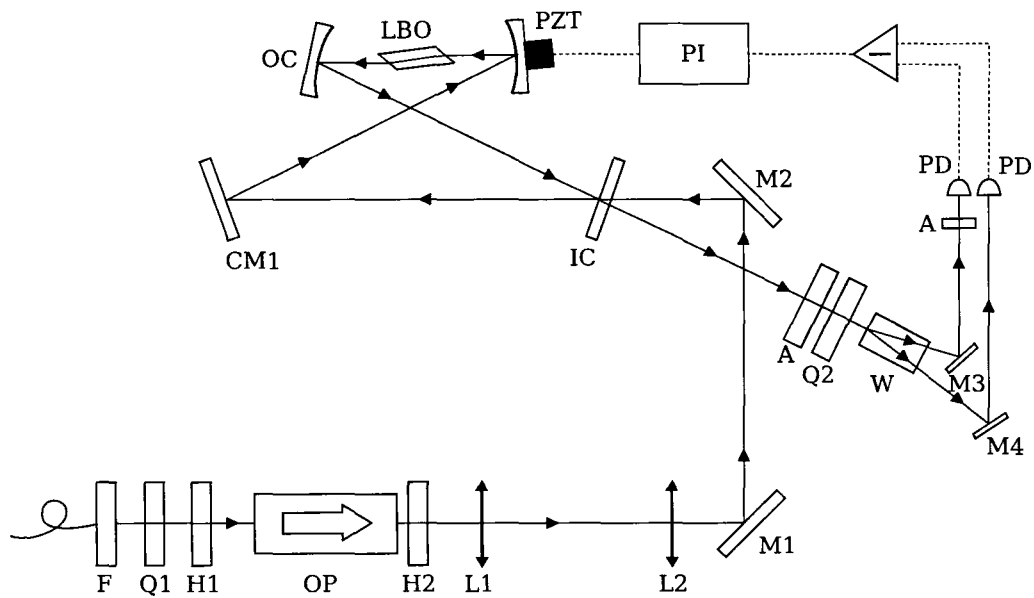


Figure 3.8: Schematic for the Cyclor LBO beam line (not to scale). [Definition of labels used in the figure: F = fibre collimator and mount; Q1,Q2 =  $\frac{\lambda}{4}$  waveplate; H1,H2 =  $\frac{\lambda}{2}$  waveplate; OP = optical isolator; L1,L2 = mode-matching lenses; M1,M2,M3,M4 = beam steering mirrors; IC = input coupler; CM1 = cavity mirror; PZT = piezostack and mounted mirror; LBO = LBO nonlinear crystal; OC = output coupler; A = optical attenuator; W = wollaston prism; PD = photodiode; PI = proportional and integral gain]

shaping and electronics for signal processing.

The double-pass AOM (*IntraAction ATM 801A1*) is used to shift the frequency of the laser. The AOM is connected to a signal generator (*HP 8656A*) which provides the RF drive. The RF signal drives a piezo stack connected to a birefringent crystal ( $TeO_2$ ) internal to the AOM. The piezo stack generates an acoustic wave inside of the crystal, and the compression and rarefactions of the sound wave result in a periodic change of the index of refraction. The input beam is diffracted off this acoustic grating, resulting in multiple diffracted orders separated by multiples of the RF drive frequency. The amount of power diffracted into each higher order depends on the RF amplitude and the angle between the input beam and the sound wave (according to the Bragg condition). The AOM centre frequency is 80 MHz with a bandwidth of  $\pm 15$  MHz.

The double-pass AOM setup is shown in Figure (3.10). The first lens in the AOM setup focuses the beam into the AOM. In order to separate the incoming and outgoing beams, the AOM setup was first aligned on the optical axis, ensuring the beam retro-reflected. The beam height on the first lens was then dropped by  $\frac{1}{8}$ ". Upon being retro-reflected through the system, the beam exiting the double-pass AOM setup came out  $\frac{1}{8}$ " above the optic axis and was separated from the input beam by using a pick-off mirror and an aperture to block the other-order beams.

In the first pass of of the double-pass AOM, the first order diffracted beam

(shifted by  $-80$  MHz) is selected using two knife-edges to block the other orders. Typically, 80% of the laser power input to the AOM is diffracted into the first order beam. The beam is then retro-reflected back through the AOM and again the first-order beam is selected, picking up an additional frequency shift. The overall efficiency of the double-pass AOM setup is 60–64% including reflection losses from the various optical surfaces.

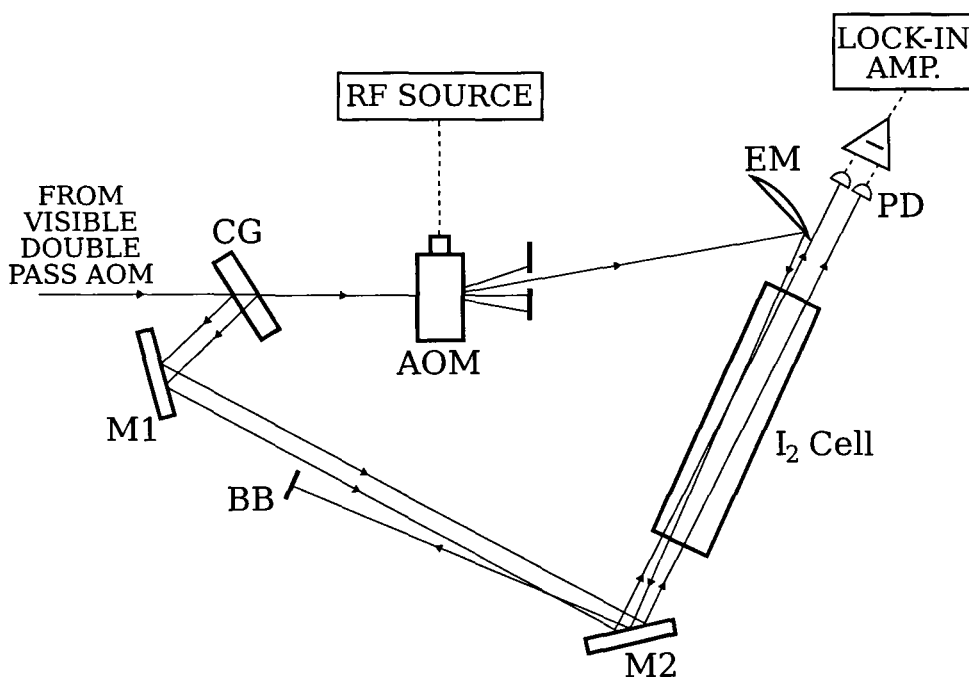


Figure 3.9: Schematic for the Cyclor iodine setup (not to scale). The modulating AOM shown in the figure is driven by a 75 MHz source (*FLUKE 6061A*) and externally modulated with a peak frequency deviation of 99 kHz. [Definition of labels: M1,M2 = beam steering mirrors; BB = beam block; CG = coated glass; EM = elliptical edge mirror; PD = photodiode]

The double-passed beam is sent to the iodine setup shown in Figure (3.9).

Details of FM saturated absorption spectroscopy are given in Section (3.5).

The beam is split into three, using a coated piece of glass. The two weaker

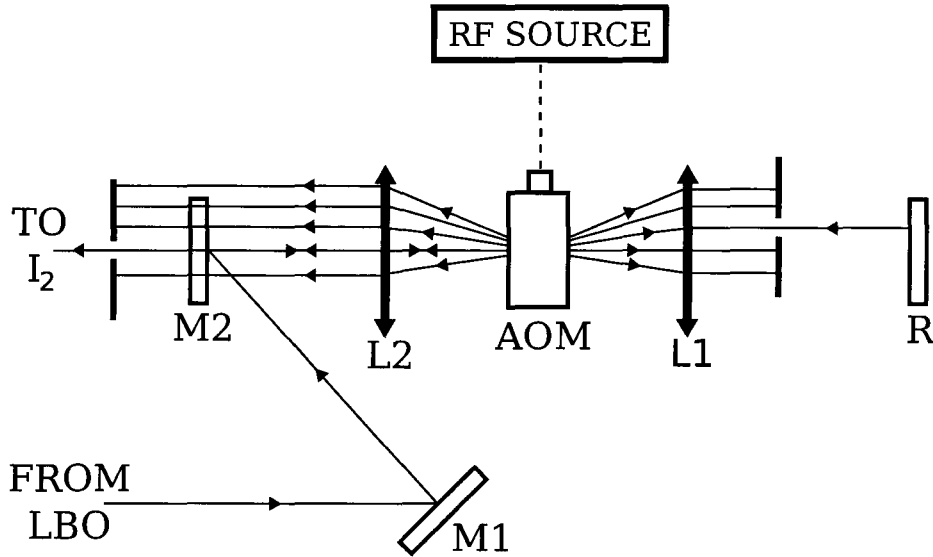


Figure 3.10: Schematic for the double-pass AOM (not to scale). A top view is shown. The beam is also displaced along the vertical direction so that the second pass exits L2 above the first pass. [Definition of labels: M1, M2 = beam steering mirrors; L1, L2 = lenses; R = retro-reflector]

beams, reflected off each face of the glass, are used as probe and reference beams for the molecular iodine gas cell. The beam passing through the glass is used as the pump beam.

The pump beam is passed through a frequency-modulated AOM (*IntraAction ATM 801A1*). The AOM is driven by a signal generator (*Fluke 6061A*) with a centre frequency of  $75\text{ MHz}$ . The signal generator is externally frequency-modulated by applying  $2 V_{pp}$  at a modulation frequency of  $78\text{ kHz}$ , corresponding to a maximum frequency deviation of  $99\text{ kHz}$  and a modulation index of  $0.0013$ . The source of the modulation is a function generator (*HP 33120A*).

The probe beam is overlapped with the counter-propagating pump beam in the molecular iodine gas cell and the probe and reference beams are focused

onto a pair of photodiodes. The output from the photodetector is sent to a lock-in amplifier to obtain a derivative signal used to lock the laser to a hyperfine component of molecular iodine.

### Cyclor BBO Cavity and Further Optics

The BBO cavity is a four-mirror enhancement cavity built around a  $\beta$ -barium borate (BBO) crystal to frequency-double the 560 nm input light to 280 nm. Detailed information on the cavity is included in Chapter 4. Typically, of the 290 mW from the LBO doubling cavity, a total of 9 mW of UV light is obtained at the BBO cavity output.

The energy levels of the  $^2S_{\frac{1}{2}} \rightarrow ^2P_{\frac{1}{2}}$  transition are split due to hyperfine interactions (see Section (5.2)). In order to drive transitions from the ground state to excited state, we need two lasers beams whose frequency difference corresponds to the hyperfine splitting ( $\approx 1.729$  GHz). In order to derive these two beams from the same source, we take the output from BBO cavity and split it using a polarizing beamsplitter (PBS). Each output of the PBS is sent to a different double-pass AOM setup as shown in Figure (3.11). All the AOMs (*IntraAction ASM 445ILA45*) in the two UV double-pass setups are driven at 432.25 MHz by the same signal generator (*HP 8656B*); however, one arm has a positive frequency shift and the other has a negative frequency shift, giving the desired frequency difference between the two beams.

After the UV double-pass setups, both beams are sent through separate

200 MHz AOMs (*ASM 200.8LA45*) that are used to switch the beams on and off. Since the different-order diffracted beams are spatially separated from one another, we can set up an aperture to only pass the first-order beam, blocking all the other-order beams. When RF power is applied to the AOM, the transmitted beam is shifted by +200 MHz, and passes through the aperture. When no RF power is applied, only the zeroth-order beam remains, but it is blocked by the aperture and so the laser is effectively “off”. For the experiments described in this experiment, the 200 MHz AOMs were not used to turn the beams on(off). Instead, the RF power applied to the UV double-pass AOMs was used.

Accounting for all of the frequency shifts due to the various AOMs, the laser frequency measured relative to iodine is:

$$\nu'_L = 2\nu'_{I_2} + 4\nu'_{DP} - \nu_{MOD} \pm 2\nu_{UVDP} + \nu_{200} \quad (3.2)$$

where  $\nu'_L$  is the UV laser frequency,  $\nu'_{I_2}$  is the frequency of the iodine transition (in the visible),  $\nu'_{DP}$  is the visible double-pass AOM drive frequency,  $\nu_{MOD}$  is the modulating AOM drive frequency,  $\nu_{UVDP}$  is the UV double-pass AOM drive frequency (positive for the Cyclor, and negative for the Repumper), and  $\nu_{200}$  is the drive frequency of the 200 MHz AOM.

After the 200 MHz AOM, the Cyclor beam is combined with the Probe beam (discussed in Section (3.4.3)) on a polarizing beamsplitting cube (PBS)

and then both are recombined with the Repumper on a 50/50 beamsplitting cube (BS).

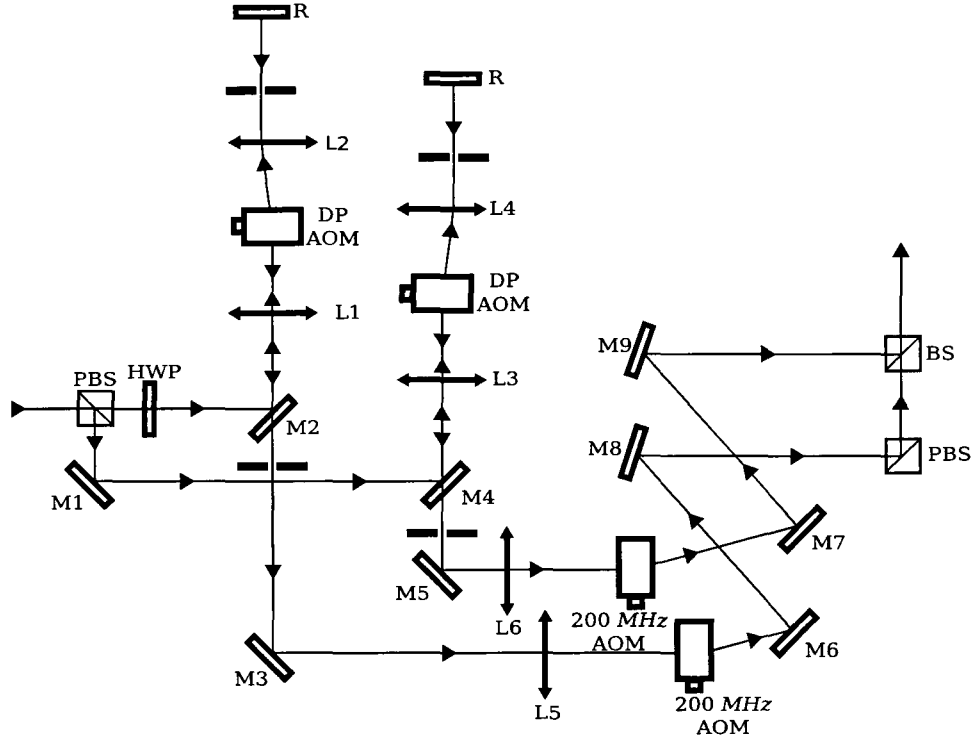


Figure 3.11: Schematic for the UV Cycler beam line (not to scale). Omitted from the image are the blocked diffracted beams in the all the AOMs. Also excluded are the power sources driving the AOMs. The two double-passed AOMs (DP AOM) are driven by the same signal generator (*HP 8656B*) and the two 200 MHz AOMs are driven by the same 200 MHz source (*IntraAction ME-2002*). [Definition of labels: PBS = polarization beam splitter cube; HWP =  $\frac{\lambda}{2}$  wave plate; M1–M9 = beam steering mirrors; L1–L6 = lenses; R = retro-reflector; BS = 50/50 beam splitter cube]

### 3.4.3 Probe Beamline

The 1 W Koheras Boostik fibre laser is used to drive  ${}^2S_{\frac{1}{2}} \rightarrow {}^2P_{\frac{1}{2}}$  transitions.

The setup of the Probe beamline is similar to that of the Cycler beamline.

An optical isolator prevents back-reflections into the laser, and two doubling cavities are used to frequency double the IR to the UV. Typically, 170 *mW* of green light is generated, and from that 800  $\mu W$  of UV is generated.

The main differences between the Cyclor and Probe beamlines are that the iodine diagnostics of the Probe beamline have one additional AOM, used to tune the laser frequency across the transitions we are probing, and that there are no double-pass AOMs in the UV for the Probe since we do not need to derive a second beam from the Probe laser. Instead, the output from the BBO cavity is sent through a single on/off AOM that is used to switch the light on and off, as well as to provide a 200 *MHz* shift to the laser frequency. After the on/off AOM the beam is combined on a PBS near the vacuum chamber with the Cyclor and Repumper beams.

### **Probe Diagnostic Beamline**

The output of the Probe LBO cavity is passed through a PBS, with 50 *mW* of light sent to the iodine beamline, and the remainder sent to the BBO doubling cavity. The Probe iodine beamline, shown in Figure (3.12), is essentially the same as the Cyclor beamline except for the addition of a second double-pass AOM. Both AOMs (*IntraAction ATM 801A1*) in the Probe beamline are driven by the same source (*HP 8662A*). The drive frequency typically varies from 65–95 *MHz*, with the geometry chosen to give a negative frequency shift from both AOMs.

The output from the second AOM is sent on through beam steering and shaping optics before being split into a probe, reference and pump beam on a plate beamsplitter. Typical powers are 14 *mW* in the pump beam and 300  $\mu W$  in the probe and reference beams. The pump beam is sent through a modulating AOM (*IntraAction ATM 801A1*), driven by the same RF source as the modulating AOM in the Cyclor beamline (*FLUKE 6061A*).

Including all of the frequency shifts from the AOMs, the laser frequency measured relative to iodine is:

$$\nu_L = 2\nu_{I_2} + 8\nu_{DP} - \nu_{MOD} + \nu_{200}. \quad (3.3)$$

Here  $\nu_L$  is the UV laser frequency,  $\nu_{I_2}$  is frequency of the iodine feature (in the visible),  $\nu_{DP}$  is the visible double-pass AOM drive frequency,  $\nu_{MOD}$  is the modulating AOM drive frequency, and  $\nu_{200}$  is the drive frequency of the 200 *MHz* AOM (*IntraAction ASM 200.8LA45*).

### 3.4.4 Photoionization Beamline

A beam of neutral magnesium atoms is ionized to obtain our ions. Two possible ways of ionizing are by electron impact or by photoionization. A beamline from the dye laser was set up for the sole purpose of photoionization. The dye laser is tuned to 570.592 *nm* and coupled onto the main optical table with a single-mode fibre using a Thorlabs (*KT 110*) fibre launching system. Typically we

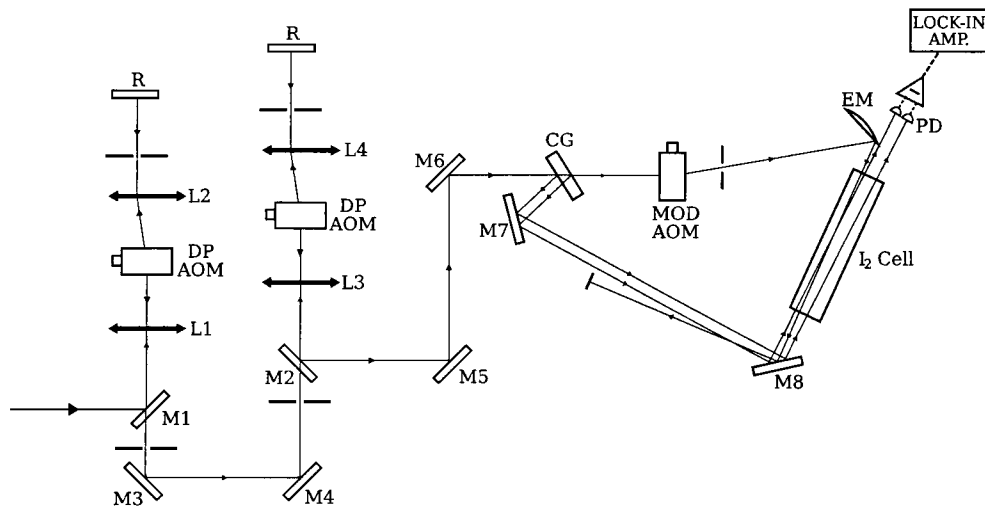


Figure 3.12: Schematic of the Probe  $I_2$  beamline (not to scale). Omitted from the schematic are the signal generators driving the three AOMs. Both of the AOMs are in a double-pass arrangement (DP AOM) and are driven by the same signal generator (*HP 8662A*). The third AOM (MOD AOM) is driven by a *FLUKE 6061A*. [Definition of the labels: M1–M8 = beam steering mirrors; L1–L4 = lenses; R = retro-reflector; CG = coated glass; EM = edge mirror; PD = photodiode]

couple 65 – 70% of the light through the fibre.

The single-mode fibre is coiled on three paddles that are used to change the polarization of the dye-laser beam, and then collimated using an aspheric lens at the output of the fibre. The light is split using a PBS, sending off a fraction of the light to the Wavemeter and an iodine cell and the remaining light to the WaveTrain (see Section (3.4.5)). Using the Wavemeter, we coarsely set the wavelength and then tune to a nearby feature of iodine. Since the photoionization transition is Doppler-broadened ( $\sim 1$  GHz) we find that we can successfully ionize using the Wavemeter to calibrate the wavelength and iodine cell as a visual cue (by tuning 500 MHz blue of where the cell is brightest).

### 3.4.5 Frequency Doubling with the WaveTrain®

The output of the fibre lasers is frequency doubled using the cavities discussed in Chapter 4. The dye-laser output is frequency doubled using a commercially purchased WaveTrain®, from Coherent, Inc. Figure (3.13) shows all of the associated optics.

The actual cavity of the WaveTrain® is enclosed inside the resonator block (RB) and is sealed from the external environment to extend the lifetime of the mildly hygroscopic BBO crystal.

The cavity consists of curved mirrors M1 and M2, a BBO crystal (for Type II frequency doubling), and a prism (P) that is mounted to a PZT. The cavity

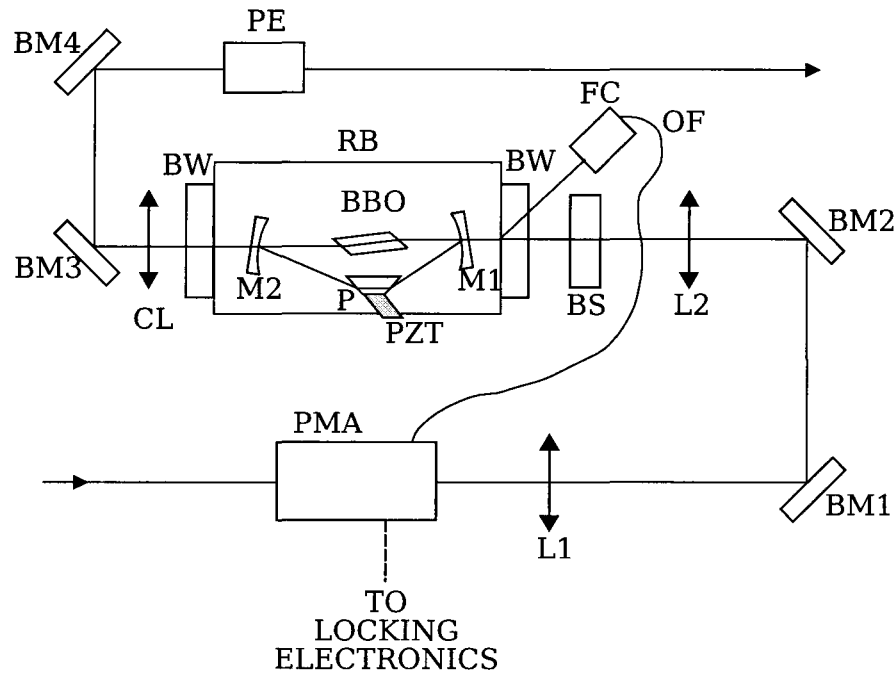


Figure 3.13: Schematic of the WaveTrain<sup>®</sup> used to frequency double the dye-laser output to the UV (not to scale). [Definitions of labels: PMA = phase modulation assembly (for Pound-Drever-Hall locking scheme); L1 and L2 = mode-matching lenses; BM1-4 = beam steering mirrors; BS = beam shifter; BW = Brewster window; FC = fibre coupler; OF = optical fibre; M1 and M2 = cavity mirrors; P = prism; PZT = piezo; CL = cylindrical lens; PE = prism expander]

length is adjusted (keeping the cavity locked) by applying a voltage to the PZT. This voltage is derived from an error signal using the Pound-Drever-Hall technique [68]. By moving the prism position, the optical path length of light travelling through the crystal is changed, resulting in a change of the cavity path length. The advantage of using a prism in this configuration over a traditional ring cavity is that the cavity is much more compact and less susceptible to vibrations. Also, fewer cavity optics are required, reducing the cavity losses and leading to an increase in harmonic generated light. The remaining optics in Figure (3.13) are required for coupling into the cavity, locking the cavity, and re-shaping the elliptical output.

Before entering the resonator block, light first passes through the phase modulator assembly (PMA), an electro-optic phase modulator. Mirrors BM1 and BM2 are used to couple the light into the cavity. Lenses L1 and L2 and the beam-shifter (BS) are required to match the input-beam mode with the cavity mode. Light reflected from the cavity is coupled into an optical fibre (OF) with the fibre coupler (FC) and is sent to photodiodes, whose output is used by the electronics to derive a lock signal.

The second-harmonic output from the cavity is coupled out of the cavity through M2 and bounces off BM3 and BM4. The output is elliptical due to walk-off that occurs during harmonic generation. Due to the birefringent nature of the crystal, harmonic light “walks off” at an angle relative

to the fundamental beam and so travels a different optical path length than the fundamental light (see Section (4.2.3)). Interference between harmonic light generated at different points in the crystal results in a harmonic beam that is well-collimated along one direction, and highly divergent along the other. A cylindrical lens (CL) is used to collimate the beam followed by a prism expander (PE) to circularize it. The frequency-doubled output from the wavetrain is then sent to the vacuum chamber through a  $f = 15 \text{ cm}$  lens that focuses the beam at the centre of the trap.

To align the PI beam, the magnesium oven is turned on and left to equilibrate at  $\sim 200^\circ \text{ C}$  so that the neutral beam is visible (although for loading ions we let the oven equilibrate at  $\sim 150^\circ \text{ C}$ ). With the Andor™ EMCCD camera on (discussed in Section (3.6)), the  $f = 15 \text{ cm}$  lens is carefully adjusted by hand while watching for fluorescence from the neutral beam, although for day to day adjustment of the beam, a mirror upstream of the lens is used to adjust the beam. Figure (3.14) is a screen capture from the EMCCD camera, showing the neutral beam.

## 3.5 Iodine Spectroscopy

Frequency-modulated saturation absorption spectroscopy of molecular iodine was used to provide a frequency reference. By locking the laser to a hyperfine iodine absorption feature of line #1599 from the Iodine Atlas [69] and tun-

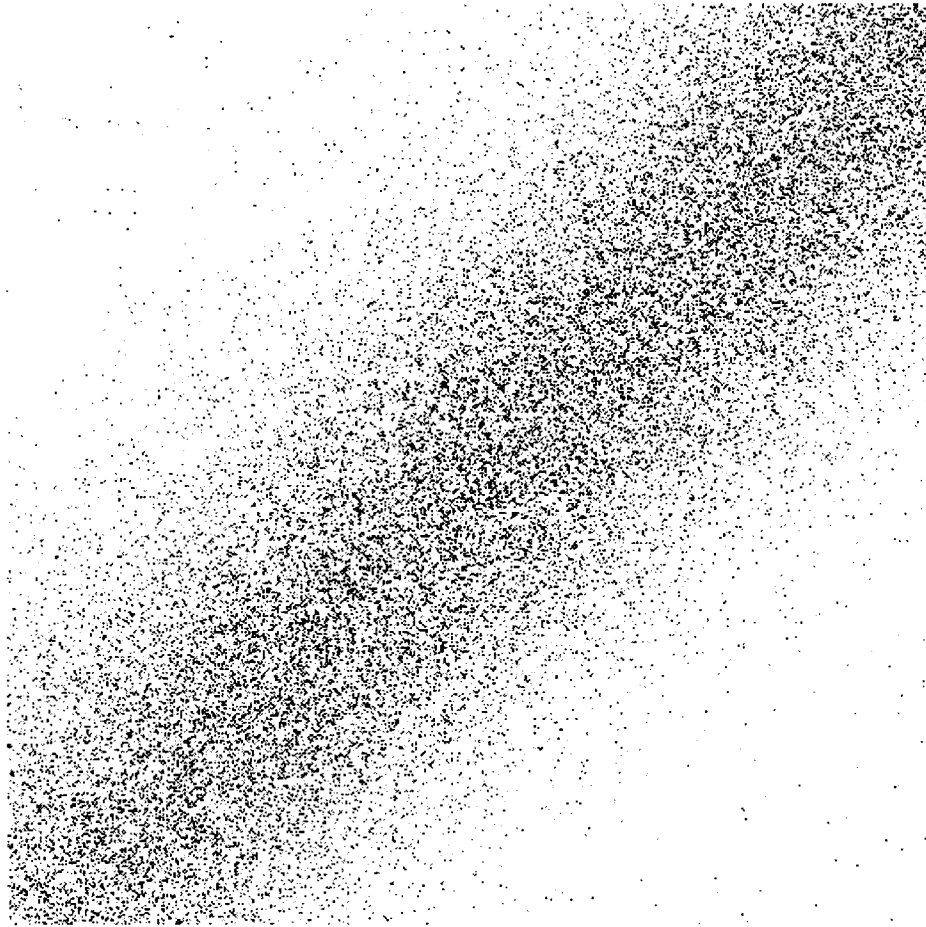


Figure 3.14: A screen capture showing the fluorescence from the neutral magnesium beam. For typical powers in the PI beam ( $\sim 1 \text{ mW}$ ) we can observe fluorescence from the neutral magnesium atoms on the EMCCD camera once the oven has reached  $\sim 200^\circ\text{C}$ . The trap electrodes are parallel to the sides of the image, with trap centre centered on the image. (Trap centre was determined earlier by centering a single trapped ion in the image). The image has been graphically enhanced in the Gimp to enhance the contrast between the background and counts due to the neutral beam.

ing the signal generator driving the visible double-pass AOMs in the iodine beamline, we swept the probe laser through the  ${}^2S_{\frac{1}{2}} \rightarrow {}^2P_{\frac{1}{2}}$  transition. For detection and laser cooling we locked to a hyperfine feature of line #1833 [69].

In previous Sections we discussed the specifics of the apparatus used for the diagnostic beamlines; Section (6.1.6) contains an overview of the iodine features used to lock and scan the probe laser. Here we will go over the theoretical background of saturated absorption spectroscopy. In this technique, a strong pump beam is used to saturate an iodine transition, resulting in a Bennet hole [70]. A weak probe beam is used to detect the Bennet hole.

### 3.5.1 Saturated Absorption Spectroscopy

The molecular transitions in iodine are inhomogeneously broadened by the Doppler shifts due to the molecules' Maxwellian velocity distribution. Recall from Chapter 2 that an atom in motion (or molecule in this case) experiences a Doppler shift. The effective frequency is given (to first order) by:

$$\omega'_L = \omega_L - \vec{k} \cdot \vec{v}_{atom} \quad (3.4)$$

where  $\omega'_L$  is the laser frequency (in the molecule's reference frame),  $\omega_L$  is the laser frequency (in the lab's reference frame),  $\vec{k}$  is the laser wavevector, and  $\vec{v}$  is the velocity of the molecule.

If the laser of frequency  $\omega_L$  is tuned near the resonance frequency  $\omega_{12}$  of

a transition, then molecules of a particular velocity class will absorb photons while others will not. This results in inhomogeneous broadening of the line-shape, since molecules of different velocity classes interact differently with the laser. The absorption coefficient is given by [8]:

$$\alpha(\omega_L) = \alpha^0(\omega_0)e^{-\left(\frac{\omega_L - \omega_0}{0.6 \delta\omega_D}\right)^2} \quad (3.5)$$

where  $\alpha^0(\omega_0)$  is the on-resonance absorption coefficient and  $\delta\omega_D$  is the Doppler width. At room temperature, a typical Doppler width is about 1 *GHz*.

The linewidth of magnesium is 42.4 *MHz*, and a transition that is 1 *GHz* wide would not be suitable as a frequency reference since the resulting resolution of the error signal would be too coarse. To detect narrow transitions within the Doppler-broadened spectrum we saturate the narrow transition with a strong pump beam. A sufficiently intense beam saturates the molecules belonging to the velocity class that satisfies Equation (3.4) resulting in a dip in the absorption spectrum within a small velocity bandwidth. The resultant dip, called a Bennett hole, cannot be detected by a single laser beam, as will be shown in Section (3.5.2). However, its effects can be detected in the absorption spectrum of a second, weak beam. By using this technique, we can obtain an iodine signal that is sufficiently narrow to be used as a frequency reference.

### 3.5.2 Bennet Holes

To simplify the discussion we will consider a gas of molecules with a Maxwell velocity distribution that is being irradiated by a laser beam traveling along the  $z$ -direction. We will treat the molecules as an open two level system whose energy difference is given by  $\hbar\omega_{12}$ .

The population of the ground and excited state is given by [8]:

$$N_1(\omega_L, v_z) = N_1^0(v_z) - \frac{\Delta N^0}{\gamma_1} \left( \frac{s(\frac{\gamma}{2})^2}{(\omega_L - \omega_{12} - k_z v_z)^2 + (\frac{\gamma_s}{2})^2} \right) \quad (3.6)$$

$$N_2(\omega_L, v_z) = N_2^0(v_z) + \frac{\Delta N^0}{\gamma_2} \left( \frac{s(\frac{\gamma}{2})^2}{(\omega_L - \omega_{12} - k_z v_z)^2 + (\frac{\gamma_s}{2})^2} \right). \quad (3.7)$$

Here,  $\omega_L$  is the laser frequency,  $v_z$  is the velocity satisfying Equation (3.4),  $N_i^0$  is the unsaturated population of the  $i^{\text{th}}$  level,  $\Delta N^0$  is the unsaturated population difference,  $\gamma_i$  is the relaxation rate out of the  $i^{\text{th}}$  level,  $s$  is the saturation parameter (dependent on laser intensity),  $\gamma$  is the natural transition linewidth, and  $\gamma_s$  is the power-broadened linewidth.

By taking the difference of Equations (3.6) and (3.7) we obtain the population difference [8]:

$$\Delta N(\omega_L, v_z) = \Delta N^0(v_z) \left( 1 - \frac{s(\frac{\gamma}{2})^2}{(\omega_L - \omega_{12} - k v_z)^2 + (\frac{\gamma_s}{2})^2} \right). \quad (3.8)$$

The second term in the brackets is commonly referred to as a ‘‘Bennet hole’’, and represents a power-broadened Lorentzian whose minimum is at  $v_z =$

$$\frac{(\omega_L - \omega_{12})}{k}.$$

The total absorption coefficient, however, is still given by [8]:

$$\alpha_s(\omega_L) = \frac{\alpha^0(\omega_{12})}{\sqrt{1+s}} e^{-\left(\frac{\omega_L - \omega_{12}}{0.6 \delta\omega_D}\right)^2} \quad (3.9)$$

where  $\alpha^0(\omega_{12})$  is the resonant unsaturated absorption coefficient and  $\delta\omega_D$  is the Doppler width. Despite the laser burning a Bennet hole as it is tuned through the transition, the hole cannot be observed in the absorption spectrum with a single laser beam. As we tune through the Doppler-broadened transition, we saturate distinct velocity classes and so the Bennet hole is located at a different frequency for each different laser detuning. The net result is a broad absorption spectrum whose overall amplitude has been decreased. To observe the Bennet hole we need to introduce a second laser beam that is sufficiently weak to cause no significant additional saturation of the population.

The strong pump beam, with wavevector  $k_1$ , burns a Bennet hole in the population difference. A weak probe beam, with wavevector  $k_2$  is overlapped with the pump beam, and frequency tuned through the Doppler-broadened profile. The resulting absorption profile is given by [8]:

$$\alpha_s(\omega_L, \omega_1) = \alpha^0(\omega_L) \left( 1 - \frac{s}{\sqrt{1+s}} \frac{\left(\frac{\gamma}{2}\right)^2}{(\omega_L - \omega')^2 + \left(\frac{\gamma s}{2}\right)^2} \right) \quad (3.10)$$

where  $\alpha^0(\omega_L)$  is the unsaturated absorption profile,  $s$  the saturation parameter

of the strong beam,  $\gamma$  is the natural linewidth,  $\omega_L$  is the probe laser frequency,  $\omega_1$  is the pump laser frequency,  $\omega'$  is the minimum of the Bennet hole, and  $\gamma_s$  is the linewidth of the Bennet hole.

From Equation (3.10) we can see that by using two laser beams we can observe the Bennet hole, although it is located on a broad background due to Doppler broadening. During the experiment, we use a third beam that serves as a reference beam. The reference beam is not overlapped with the strong pump beam, and so by monitoring the probe and reference beams on two separate photodiodes we can subtract the broad Doppler spectrum, leaving only peaks due to the Bennet holes.

In practice, we also frequency-modulate the pump beam to obtain an error signal. An additional advantage of using frequency modulation is that the output of the photodiode is sent to a lock-in amplifier, which uses a homodyne technique to amplify the frequency-modulated iodine signal, resulting in a reduction of technical noise. To understand how this works, we will consider the basic operation of a lock-in amplifier.

The signal input to the lock-in amplifier is first amplified, and then mixed with the reference signal (obtained from the signal generator modulating the AOM). The product of the input signal and the reference signal has frequency components that are sums and differences of the two signals. The net result is that the frequency-modulated iodine signal is mixed down to low frequency

(corresponding to the difference between the two signals). A low-pass filter internal to the lock-in amplifier passes the low frequency components of the mixed signal while blocking the high frequency components. By choosing a high modulation frequency (78 kHz in our case) we move away from the technical noise which is primarily at low frequencies. A representative iodine trace is shown in Figure (6.10).

### 3.6 Imaging System

Imaging of the ion and detection of its electronic state is done by collecting fluorescence from the  ${}^2S_{\frac{1}{2}}|F = 3, m_F = \pm 3\rangle \leftrightarrow {}^2P_{\frac{3}{2}}|F'' = 4, m''_F = \pm 4\rangle$  transition (see Section (2.1)), where a positive (negative)  $m_F$  corresponds to using  $\sigma^{+(-)}$  polarized light to optically pump and to drive the cycling transition.

In order to detect the state of the ion, we use an electron-shelving technique [55]. If the ion is in the  $(3, -3)$  state, then when we turn the Cyclor laser on we drive the  $(3, -3) \leftrightarrow (4, -4)$  transition. Since this is a closed transition, we detect many photons with the photomultiplier tube (PMT) and so we call  $(3, -3)$  the bright state.

If the ion is in the  $F = 2$  manifold, then the Cyclor laser is not resonant with any transition and so we do not detect any photons – we call this the dark state. In practice, we actually do detect photons in the dark state [71] [72] since it is possible to off-resonantly pump the ion out of the dark state

with the Cyclor laser (see Section (6.1.5)). Nonetheless, we do see a significant reduction in the number of detected photons.

To understand how pumping out of the dark state works, we consider a few of the more subtle points. Recall that the Cyclor beam drives transitions from  $(3, -3)$  to  $(4, -4)$  (the cycling transition). In actuality, the nonzero linewidth ( $\approx 2\pi \cdot 42 \text{ MHz}$ ) and the finite ground-state hyperfine splitting ( $\approx 1.78 \text{ GHz}$ ) results in 1 scattering event from the dark state (due to the Cyclor beam) for every 6917 scattering events from the bright state. Thus, the dark state is not truly dark. Now, consider an experiment where we prepare the ion in a dark state, and then turn on the Cyclor beam for some time  $t_{det}$ . After some time  $\tau$ , the ion, which started out in a dark state at  $t = 0$ , is *off-resonantly* driven to the excited state by the Cyclor beam. From the excited state, the ion can either fall into the  $F = 3$  manifold or the  $F = 2$  manifold (with the final state of the ion dependent on the branching ratios from the excited state). If the ion falls into the bright state, then for the remainder of the detection gate ( $t_{det} - \tau$ ) the ion scatters photons just as a bright state does. Thus in the dark state, we detect *fewer* photons than we do in the bright state, but not zero photons. Typical bright and dark state histograms are shown in Figure (6.9).

Figure (3.15) shows a diagram of the imaging system designed by Jiajia Zhou and Table (3.3) lists the optical components and the transmittance through each element. Fluorescence from the ion passes through the AR-coated

viewport window (*special – 11466 – 01 – CF*, Ceramaseal) that is mounted to a custom-built re-entrant flange (Drawing No. *MCF600 – SO200800 ASSY*, Ceramaseal)<sup>1</sup>. The re-entrant flange is required because the working distance of the objective is 15 *mm*. Approximately 2.6% of the light is collimated by a Mitutoyo M Plan UV 20× objective (*OBJ*) with a numerical aperture of 0.36, a focal length of 10 *mm*, and a working distance of 15 *mm*. The fraction of fluorescence collected by the Mitutoyo is set by the dipole radiation pattern of fluorescence and the collection angle.

The collimated light from the Mitutoyo objective passes through a second lens (*L1*),  $f = 50$  *mm*, that focuses the light to form a magnified image. The magnification is 5× for this first stage. An adjustable aperture is placed at the focus of the second lens to filter out background light and laser light scattered from the trap electrodes.

A doublet (*(L2 and L3)*,  $f = 75$  *mm*) is placed upstream of the magnified image to focus it onto either the Andor™ iXon electron-multiplying charge-coupled device (EMCCD) camera or the Hamamatsu PMT (*H8259 – 01*) module. The doublet consists of two  $f = 150$  *mm* plano-convex lenses with the curved surfaces facing each other. A mirror after the doublet is put in place when we want to direct the fluorescence onto the PMT and removed when we want to image the ion. The magnification of the doublet is expected to be 8×

---

<sup>1</sup>A viewport window is attached to the re-entrant flange with the normally air-side facing into the vacuum chamber (as are the stainless-steel bolts connecting it). Despite these parts not necessarily being UHV compatible, we are still able to attain low pressures.

for a total magnification of  $40\times$ .

The EMCCD is a silicon-based semiconductor chip with a two-dimensional matrix of photo-sensors (pixels). It is similar to a CCD chip, except that an additional section (the gain register) is included, which effectively reduces readout noise by using electron impact ionization. This effectively reduces the significance in readout-amplifier noise, resulting in an increase in signal to noise (as explained below). This makes the EMCCD suitable for low light applications. In a traditional CCD chip, an image is captured on the two dimensional matrix, consisting of a number of rows and columns ( $512 \times 512$  for our EMCCD chip). Below the lowest row is the shift register, consisting of a row of pixels that are used during readout. The shift register transfer the charge to the output amplifier.

When light falls onto the photo-sensors, electrons are produced, and these electrons are confined to their respective pixels. Upon readout, the charge from the pixels in each row are shifted down into the shift register and then transferred to the output amplifier. The shift register moves the charge sequentially to the readout amplifier. The amplifier introduces noise in both CCD chips and in EMCCD chips. For large photoelectric signals, this is negligible. If only a few photoelectrons are produced in a pixel, however, the readout noise dwarfs the signal.

In the case of EMCCD chips, an additional register (the gain register) is

placed after the shift register but before the output amplifier. Charge moves from the shift register into the gain register, one element at a time. Each electrode in the gain register is replaced with two electrodes (one held at high voltage, and the other clocked). As an electron moves along the gain register, impact ionization generates new electrons (due to the high electric field generated between the electrodes) so that by the end of the gain register, the signal has been amplified without significantly increasing the readout noise.

When setting up the imaging system, the camera was placed at a fixed distance from trap centre and the position of  $L3$  was adjusted to form an image on the camera. Due to lack of space, we did not place the camera far enough away to obtain the expected magnification. To measure the actual overall magnification, we imaged the trap electrodes and measured the pixel separation between two trap electrodes. Using the physical distance between trap electrodes ( $630 \mu m$ ) we determined one pixel length corresponded to  $0.88 \mu m$  at trap centre. The actual length of a single pixel at the camera is  $16 \mu m$  and so the measured overall magnification is  $18\times$ .

Although the EMCCD camera is great for imaging, we used a Hamamatsu PMT module for photon counting. With PMTs, light excites electrons in the photocathode so that electrons are emitted and subsequently accelerated through a series of dynodes. Each dynode is at a higher voltage than the previous one. Amplification of the signal occurs through electron impact ionization,

which converts the single photoelectrons into multiple electrons at each dynode. By the time the signal reaches the anode it has been sufficiently amplified so that an appreciable current can be measured. This requires high voltages (thousands of volts). The Hamamatsu PMT module that we used has an internal high-voltage power supply circuit, and voltage-divider circuit to supply voltage to each dynode. The module requires only a 5 V DC input to operate it. The PMT also has a built-in preset discriminator that sets a threshold voltage, below which no photon is counted and above which a photon is counted. This produces a TTL signal from the PMT output that is suitable for direct counting.

Table 3.3: Imaging System: Summary of Optical Components and Detection Efficiency

Collection Angle and Dipole Radiation Pattern	2.6%
Wire Mesh	59.1%
Viewport Transmission	99.0%
Objective Transmission	60.0%
L2 (two surfaces)	99.5%
L3 (four surfaces)	99.0%
Expected EMCCD QE (PMT QE)	35% (20%)
Expected Total QE for EMCCD (PMT)	0.315% (0.180%)

The total quantum efficiency using the PMT was determined experimentally by measuring the fluorescence as a function of laser detuning for  $^{24}\text{Mg}^+$  as discussed in Section (6.1.3).

While the EMCCD allowed us to image the ion, we used a PMT for photon counting during all of our experiments.

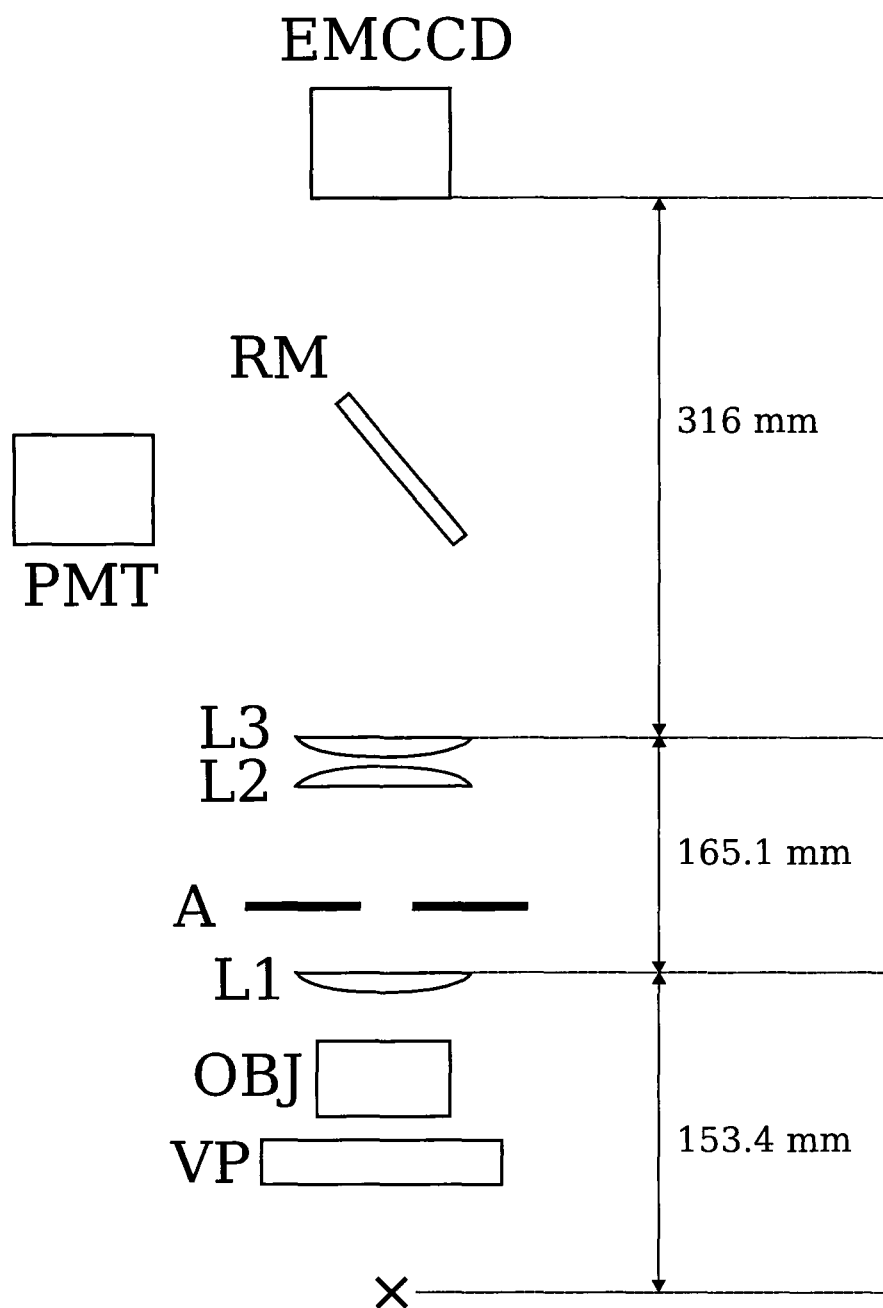


Figure 3.15: Schematic of the imaging system (not to scale). The entire system is wrapped in black fabric to keep the out room light. A removable mirror is used to direct fluorescence to the PMT. [Description of labels:  $\times$  = trap centre; VP = viewport (vacuum chamber window,  $13.5\text{ mm}$  thickness); OBJ = Mitutoyo objective ( $f = 10\text{ mm}$ ); L1 = lens ( $f = 50\text{ mm}$ ); L2 and L3 together form a doublet ( $f = 75\text{ mm}$ ); RM = removable mirror]

### 3.7 Experiment Control and Data Acquisition

Control of the apparatus and data collection was primarily performed using a series of Labview interfaces. We required the ability to program rapid pulse sequences to switch between different laser beams and to gate the PMT on timescales faster than the computer can reliably process. To accomplish this we used a PulseBlaster (SpinCore Technologies), which is a TTL pulse generator with 24 output channels. The PulseBlaster’s outputs were connected to an RF switchbox to drive the different AOMs.

Typical pulse times are on the order of one microsecond to a few hundred hundred microseconds and so a typical experiment takes several hundred microseconds. The detection efficiency is low and so less than 10 photons are detected in a single experiment. To obtain sufficient statistics for a single data point, we repeat each experiment a few thousand times. In a typical curve, such as when probing the  ${}^2S_{\frac{1}{2}} \rightarrow {}^2P_{\frac{1}{2}}$ , 200 data points were taken, requiring us to be able to change the double-pass AOM frequency every few milliseconds.

A total of three Labview interfaces were written to facilitate the experiment control and data acquisition requirements: `Individual_Trap_Control.vi`, `Experiment-control.vi`, and `Histo_taking.vi`.

### 3.7.1 Individual Trap Control

Background fields push the ion away from RF null. This leads to micromotion sidebands similar to the secular motion sidebands described in Section (2.2.3), and this broadens the spectral line. To minimize the effects of micromotion, we applied different voltages to the DC tube electrodes to push the ion to RF null. The details of the procedure are discussed in Section (6.1.2).

Individual\_Trap\_Control.vi (written by Brian King) allows us to control the DC voltages on each tube electrode separately by communicating via GPIB with the DC power supply (*HP 6627A*) connected to each tube electrode. The *HP 6627A* is negatively biased using a second DC power supply (*Agilent E3631*) that can also be controlled from the VI through GPIB. In nulling out background fields, we maintained zero DC voltage and trapped with the RF voltage alone – this allowed us to determine the location of RF null. Biasing the power supply increased the voltage range over which we could push the ion while keeping the mean voltage zero. During operation, the mean voltage was kept positive by maintaining a voltage on the tube electrodes that was larger than the bias voltage. A screen capture of the interface is shown in Figure (3.16). The tube electrodes are named Naomi, Eva, Vamp and Snake with their locations shown in Figure (3.16) and in Figure (3.4).

Voltages for each tube electrode can be entered manually, or using the slider to incrementally change the voltage. The VI allows us to simultaneously

change the voltage on selected tube electrodes. It also allows us to invert the direction in which the voltage would increment on selected tube electrodes to push the ion around. For example, by inverting the increment voltage on Naomi and Eva we can push the ion along the axial direction. Similarly we can invert the voltage increment on Naomi and Vamp to push the ion along one of the radial directions.

### **3.7.2 Experiment Control**

As mentioned previously, we need to be able to program rapid pulse sequences to switch different lasers on and off. To do this, we use an RF switchbox made up of TTL-controlled RF switches. As discussed earlier, in order to generate the different TTL pulses, we use a PulseBlaster. A Labview VI (Experiment-control.vi) was written by Martin Horbanski (the VI is shown in Figure (3.18)) to program different pulse sequences into the PulseBlaster, whose outputs are connected to the TTL input of the RF switchbox.

The RF switchbox is made up of Mini-Circuits ZYSWA and GSWA TTL-controlled RF switches. The ZYSWA switch has two RF inputs, one RF output, and a TTL control input. The GSWA is a four-input version of the ZYSWA. The GSWA allows us to perform more complex RF pulses, although for the pulse sequences used in all of the experiments the ZYSWA was sufficient and only three of the outputs of the RF switchbox were used. Only one of

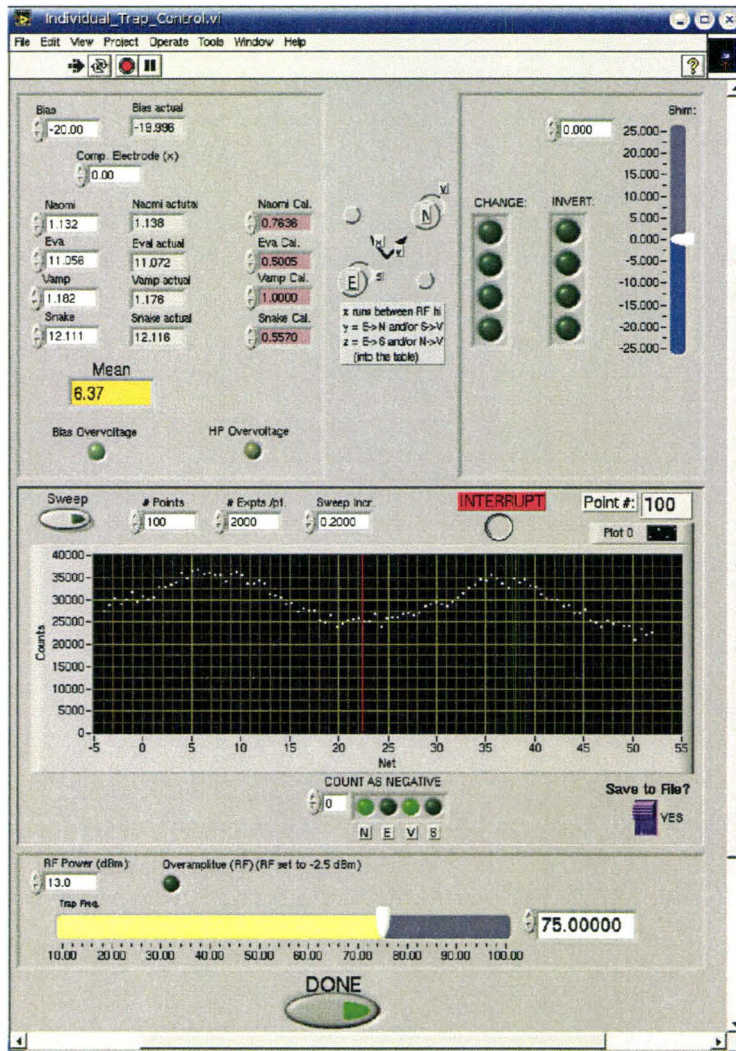


Figure 3.16: VI for Trap Control. To minimize the effect of micromotion we adjusted the DC tube electrode voltages to push the ion to the location of RF null (see Section (6.1.2)). The program allowed us to either vary the voltages in real-time, or to sweep a voltage range determined by the number of points and voltage increment. The VI controlled both the *HP 6627A* and the *Agilent E3631* via GPIB. The VI was also capable of communicating with a signal generator (*HP 8656A*) that had, in the past, been used as a RF power supply for the trap.

the inputs of the ZYSWA was connected to an RF supply and so each of RF switchbox outputs functions as a TTL-controlled on/off switch.

As a specific example, consider the experiment where we probe the  ${}^2S_{\frac{1}{2}} \rightarrow {}^2P_{\frac{1}{2}}$  transition (see Section (6.1.7)). We begin with optical pumping for  $50 \mu s$  to prepare the ion in the ( $F = 3, m_F = -3$ ) ground state using the Cyclor and Repumper beams. This is followed by  $1 \mu s$  of probing with the Probe beam and then  $250 \mu s$  of detection, consisting of the Cyclor beam and photon counting using the PMT. A timing diagram is shown in Figure (3.17).

To turn the Probe laser on/off, the output of the signal generator (*IntraAction ME – 2000*) is connected to one of the inputs of the RF switchbox. The output of the RF switchbox is connected to the on/off AOM in the Probe beamline. The output of the PulseBlaster corresponding to the probe pulse is connected to the TTL switch of the RF switchbox, which can then be rapidly switched on/off by the PulseBlaster. A similar configuration was also used for the Cyclor and Repumper beamlines.

We repeat the experiment a total of 5000 times for each data point and tune the probe laser (by changing the frequency of the AOM while the laser is locked to iodine) to sweep through the  ${}^2S_{\frac{1}{2}} \rightarrow {}^2P_{\frac{1}{2}}$  transition. The total time for the above experiment is  $301 \mu s$ , and a single data point (5000 experiments) takes 1.5 s. To obtain a full curve (ie. trace through the transition) we also change the frequency of the laser from data point to data point. A total of

125-150 data points are typically collected and so a full curve typically takes less than five minutes.

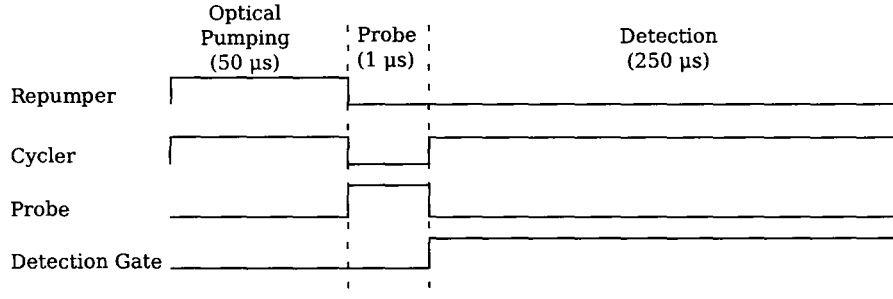


Figure 3.17: Timing diagram for an experiment in which we probe the  ${}^2S_{\frac{1}{2}} \rightarrow {}^2P_{\frac{1}{2}}$  transition. First we optically pump the ion into the  $(3, -3)$  state using the Cyclers and Repumper beams for  $50 \mu s$ . Then we probe the transition with the Probe laser for  $1 \mu s$  and detect the state of the ion using the Cyclers beam and the PMT for  $250 \mu s$ . These are typical pulse lengths, although the probe time varies for different Probe laser intensities.

### 3.7.3 Data Acquisition

A separate Labview interface written by Brian King is used for data acquisition. This interface is shown in Figure (3.19). The VI allows us to set the number of times to repeat the experiment, and to adjust other experimental parameters (via GPIB control) such as sweeping through a laser voltage range (to change the laser frequency) or sweeping through the frequency driving the visible double-pass AOM in the Probe beamline. After each data point, the interface updates with the number of photons detected and a histogram of the number of photons per experiment. The histogram is particularly useful in adjusting the polarization of the laser and the current applied to the magnetic

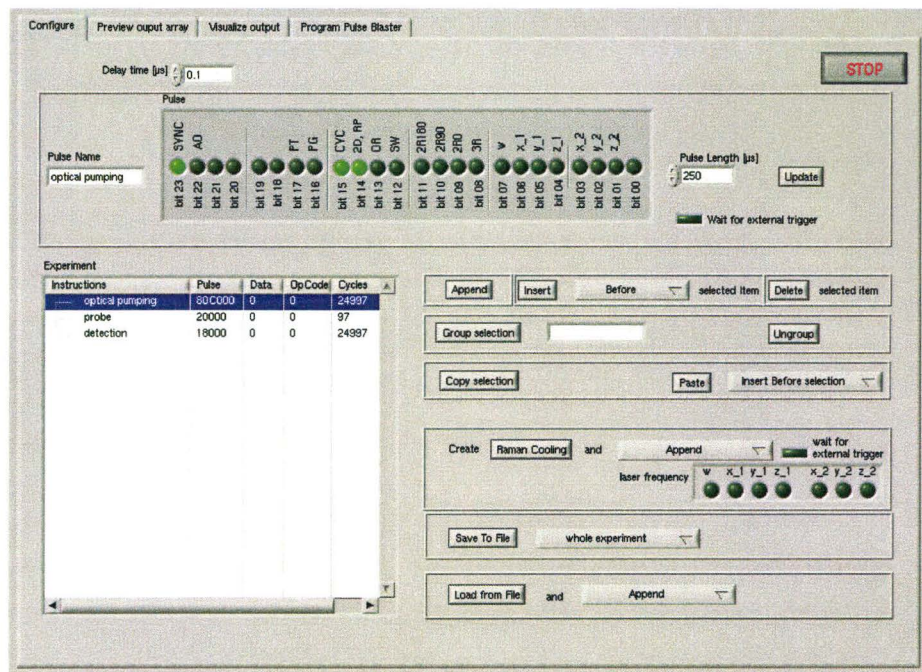


Figure 3.18: Screenshot of VI for Experiment Control. The interface allows us to program in different pulses by entering in pulse times and choosing which bits to include. It also allows us to preview the pulse sequences in a timing diagram similar to Figure (3.17) before programming the PulseBlaster.

field coils since it gives a real-time update on the success of optical pumping process (see Section (6.1.1)).

A single data point takes roughly 1.5 s; however, we also need to count the number of photons detected in each experiment (for histograms). The data is acquired using a National Instruments DAQ board (*NIPCI – 6036E*) that (with a minor modification) allows us to do buffered-gated counting. The benefit of buffered-gated counting is that buffered counting stores the photon counts using direct memory access (DMA). The advantage of this is that the number of photon counts is written into memory without tying up the computer CPU. However, we also want to gate the counting, so that photons are only counted during the detection pulse. To realize this, the DAQ board has two inputs: one for photon counting, and the second input for the Detection Gate. The board takes in photon counts which are logically AND-ed with the Detection Gate obtained from the PulseBlaster. This is performed using a home-built digital logic circuit housed inside of the DAQ-cable breakout box.

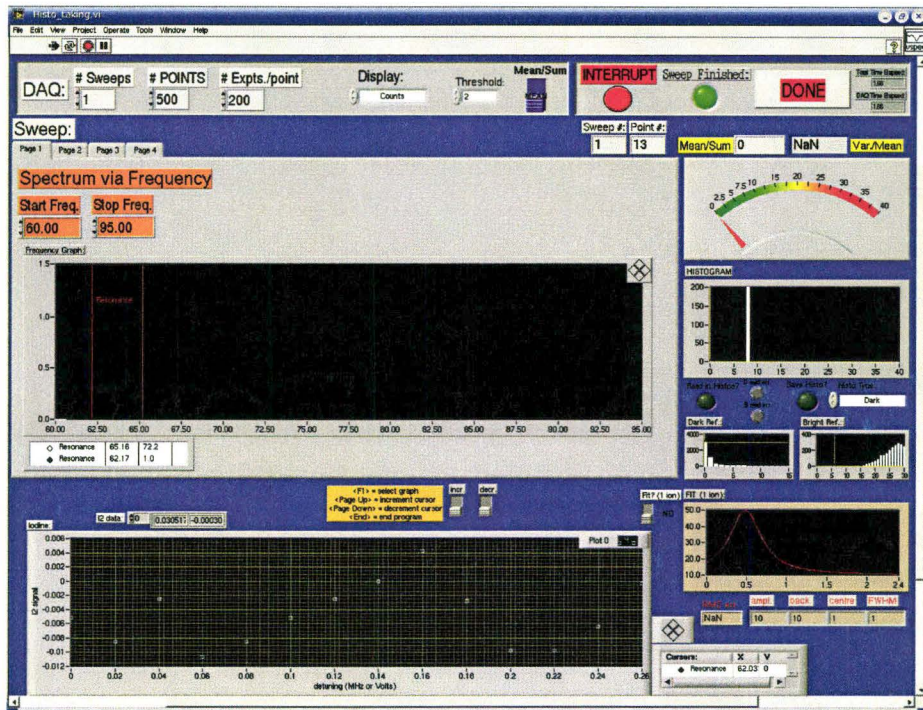


Figure 3.19: Data acquisition screenshot. This interface was used for data collection. Using the different tabs we were able to sweep the laser voltage, visible DP AOM frequency, or sweep the length of a pulse (which required the additional use of a pulse generator (*DG535*) (Stanford)). After a scan was completed, the VI would continue to update the photon histogram and displayed counts.

# Chapter 4

## Frequency Doubling

### 4.1 Introduction

The  $Mg^+$  transitions relevant to our experiments are all in the UV near  $280\text{ nm}$ . Specifically, we addressed the  ${}^2S_{\frac{1}{2}} \rightarrow {}^2P_{\frac{1}{2}}$  and  ${}^2S_{\frac{1}{2}} \rightarrow {}^2P_{\frac{3}{2}}$  transitions which are roughly separated by  $0.718\text{ nm}$  in the UV. This is larger than the tuning range of the fibre lasers discussed in Chapter 3 and so a separate laser system was used to address each transition.

CW UV lasers at the wavelengths in which we were interested ( $280\text{ nm}$ ) were not readily available at the time when we were building the apparatus (more recently, a diode-based UV laser system has been available from Toptica Inc.). While it is possible to build a dye-laser based UV source, the linewidths are typically on the order of a few  $MHz$ , and for high-resolution spectroscopy

we require narrow laser linewidths. As a solution, we purchased two fibre lasers, both operating at approximately 1120 nm. Each laser was frequency doubled in two stages: first to the visible, then to the UV. These systems (along with the ones concurrently constructed by Friedenauer *et al.* [38]) were the first fibre-based systems at 280 nm.

Frequency doubling was first demonstrated in a quartz crystal with a ruby laser in 1961 [7] by Franken *et al.* This opened the field of spectroscopy by increasing the range of transitions that were addressable by lasers. Frequency doubling occurs when a dielectric medium, such as a nonlinear crystal, is subjected to an intense electric field. For a sufficiently intense field, higher-order (nonlinear) terms in the electric susceptibility become non-negligible and it is these higher order terms that are responsible for frequency doubling (see Section (4.2.1)).

In this chapter second harmonic generation will be discussed in detail, paying particular attention to the parameters that can be optimized to maximize the production of frequency-doubled light. We will also discuss the crystal itself. In particular, we want to choose a crystal that has a large nonlinear coefficient (to maximize the harmonic light generated), and low absorption at the fundamental wavelength as well as at the harmonic wavelength. Generally speaking, optimization of second harmonic generation is a compromise between maximizing the intensity inside of the crystal and keeping the intensity

constant throughout the length of the crystal. We will explore this trade-off in what follows. To satisfy these requirements, we used lithium borate (LBO) to frequency double from the infrared to visible, and  $\beta$ -barium borate (BBO) to frequency double from the visible to the ultraviolet.

Even with optimal crystal choice and focusing within the crystal, the typical conversion efficiency of frequency doubling crystals is on the order of  $10^{-4} W^{-1}$ . Our fibre lasers output  $1 - 2 W$ . To increase the amount of harmonic light generated we enclosed the crystals in cavities to take advantage of the high circulating power inside of the cavity. We will discuss the cavity design, the parameters chosen and how these parameters were chosen to optimize the harmonic generation process. We will finish the chapter by discussing the performance of the four cavities.

## 4.2 Frequency Doubling Parameters

### 4.2.1 Second Harmonic Generation

If a dielectric medium is subjected to an external electric field then the atoms in the medium become polarized. This is typically accounted for in Maxwell's Equations by defining:

$$\vec{P} = \chi \vec{E} \tag{4.1}$$

where  $\vec{P}$  is the induced polarization,  $\chi$  is the linear susceptibility coefficient, and  $\vec{E}$  is the applied electric field.

The assumption made is that the electric field is weak and so a linear characterization of the polarization is accurate. If the intensity of the electric field is stronger, as often is the case with lasers, then we need to consider an expansion of the induced polarization:

$$\vec{P} = \chi^{(1)}\vec{E} + \vec{E}\chi^{(2)}\vec{E} + O(|E|^3) \quad (4.2)$$

The higher-order, nonlinear terms are no longer negligible. The second-order term is responsible for second harmonic generation. Substitution of this induced polarization back into Maxwell's Equations results in a differential equation for the second-harmonic field. A derivation (in which the incident wave is treated as a plane wave) can be found in Yariv. The resultant equation is [73]:

$$P_{2\omega} = \frac{2}{\pi cn^2} \left( \frac{\mu_0}{\epsilon_0} \right)^{\frac{3}{2}} \omega^3 d_{eff}^2 l \left( \frac{\sin(\frac{\Delta kl}{2})}{\frac{\Delta kl}{2}} P_{\omega} \right)^2, \quad (4.3)$$

where  $c$  is the speed of light,  $n$  is the index of refraction of the fundamental light,  $\mu_0$  is the permeability of free space,  $\epsilon_0$  is the permittivity of free space,  $\omega$  is the frequency of the fundamental light,  $d_{eff}$  is the nonlinear coefficient (a property of the material),  $l$  is the crystal length,  $\Delta k$  is the wave-vector difference between the fundamental light and the second harmonic (which will

be explained in further detail later) and  $P_\omega$  is the input power.

The important results of the derivation are two-fold. First, if the wave-vector difference is zero, then as we increase the length of the non-linear crystal, and hence the interaction length, there is a linear increase of the harmonic output (neglecting absorption). Second, the harmonic output can be increased by phase matching. In Equation (4.3) there is a sinc function, which is maximized when the argument is zero. The argument consists of two terms: the crystal length, and the wave-vector difference between the fundamental and second harmonic. Obviously, for the argument to be zero we want the wave-vector difference to be zero.

Physically speaking, a wave-vector difference results in a phase mismatch. If we look at a cross-section of the crystal in the direction of propagation, we notice that the second harmonic field generated at any given cross-section is in phase with the fundamental field at that location. As the second harmonic propagates, it gets out of phase relative to the fundamental if the wavevectors are not integer multiples of each other. The generated harmonic field will not be in phase with the propagating harmonic field, leading to destructive interference. To circumvent this problem, we must match the indices of refraction at the two frequencies.

In a non-symmetric crystal the index of refraction depends on the laser polarization (see Figure (4.2)) as well as the crystal temperature and so we

can use either property to match the phase of the fundamental and harmonic light. The different methods to achieve this can be classified as either critical or non-critical phase matching. In critical phase matching, we exploit the angular dependence of the index of refraction for the extraordinary ray; with non-critical phase matching, we use the temperature dependence of the index of refraction.

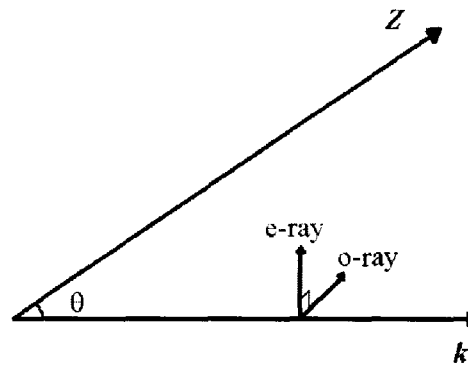


Figure 4.1: The crystal axis,  $\vec{Z}$ , is indicated along with the direction of propagation,  $\vec{k}$ . The plane created by these two vectors is the principal plane. Extraordinary rays have polarization in this plane, and ordinary rays have polarization perpendicular to this plane.

For critical phase matching, we phase match using the angular dependence of the index of refraction. In Figure (4.1) we have designated the crystal axis as  $\vec{Z}$ , and the direction of propagation of the laser beam as  $\vec{k}$ . The polarization of the ordinary and extraordinary rays is also shown. For uniaxial crystals (crystals in which double refraction is absent) the principal plane is the plane defined by  $\vec{Z}$  and  $\vec{k}$ . The ordinary ray has a polarization that is perpendicular to the principal plane, and the extraordinary ray has a polarization in the

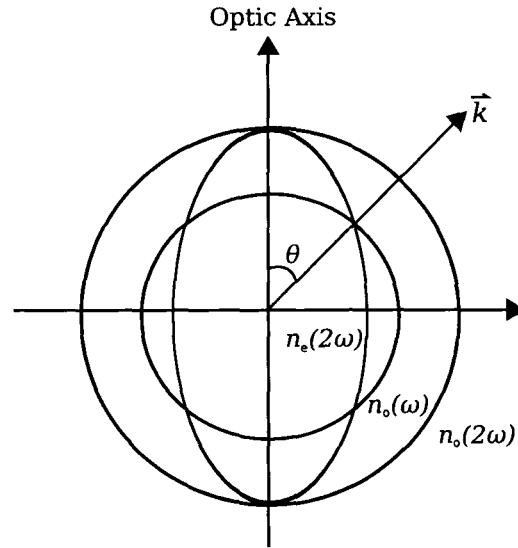


Figure 4.2: Plot of the angular dependence of the index of refraction. By tilting the crystal so that its optic axis is at an angle  $\theta$  relative to the direction of beam propagation we can match the indices of refraction for the fundamental ( $n_o(\omega)$ ) and harmonic light ( $n_e(2\omega)$ ).

principal plane. For the ordinary ray, the index of refraction is independent of the angle between the crystal axis and the direction of laser propagation,  $\theta$ , so a polar plot of  $n_o(\theta)$  traces out a circle. The extraordinary ray has an index of refraction which varies as a function of  $\theta$  so a plot of  $n_e(\theta)$  traces out an ellipse. To satisfy the phase-matching condition, we select crystals which match the indices of refraction of the fundamental and second harmonic at some critical angle,  $\theta_c$ .

An unfortunate downside to critical phase matching is that walkoff occurs in the generated second harmonic. The field generated at one plane inside of the crystal propagates at an angle  $\rho$  from the fundamental due to birefringence

and so it is not in phase with the field generated at a different plane inside of the crystal. At the observer plane, we have a peak intensity that is less than if walkoff had not occurred [74] [75]. The beam also appears elliptical due to the elongation that occurs in the plane with walkoff.

Non-critical phase matching (using temperature tuning) can be used in some cases where the critical angle required for phase matching is small, since the index of refraction has a slight temperature dependence. If non-critical phase matching is used, then the problems associated with critical phase matching, such as walk-off, can be avoided. This leads to a higher conversion efficiency.

Both critical and non-critical phase matching can be divided into Type I phase matching, and Type II phase matching. In Type I phase matching, the fundamental light is an ordinary (extraordinary) ray, and the second harmonic is an extraordinary (ordinary) ray for negative (positive) uniaxial crystals. For Type II phase matching, the fundamental light is a superposition of an ordinary and an extraordinary ray, with the second harmonic being an ordinary ray for positive uniaxial crystals and an extraordinary ray for negative uniaxial crystals. The choice of phase matching depends on which phase matching type results in a larger effective nonlinear coefficient ( $d_{eff}$ ) and is entirely a crystal property.

As we will see in Section (4.2.2), we can reduce cavity losses by cutting

the crystal at Brewster's angle. By reducing cavity losses, we increase the overall cavity gain (since less light is lost in the cavity per pass). When we cut a crystal at Brewster's angle, light which is P-polarized (polarized in the plane of incidence) is fully transmitted while light that is S-polarized (polarized perpendicularly to the plane of incidence) is partially transmitted. In order to take full advantage of Brewster's angle to reduce optical losses, we use Type I phase matching where the input beam is of only one type of polarization. Input light in Type II phase matching will suffer from reflection losses of S-polarized light. For Type I phase matching, we must also be careful to orient the crystal in such a way that the ordinary ray corresponds to P-polarization or else the input beam will suffer from reflection losses.

In either case, the phase matching angle or the temperature to which one must tune is calculable. Manufacturers give plots of angle, or temperature as a function of operating frequency for the crystals they carry. Programs also exist which readily calculate all of these parameters. One such standard program is SNLO [76].

### **4.2.2 Crystal Selection**

We considered several candidate crystals for frequency doubling. For doubling from 1120 nm to 560 nm, we considered using lithium borate (LBO) and periodically-poled lithium niobate (ppLN). In the case of LBO, we could use

non-critical phase matching, in which the temperature of LBO is tuned in order to match the indices of refraction of the fundamental and harmonic light. In periodically poled materials such as ppLN, the crystal consists of a number of domains, each being the mirror image of the one that it precedes. Domain inversion, as it is called, results in the phase mismatch alternating sign as it passes through the domains. Since the average phase mismatch is zero, destructive interference in the generated second harmonic light is reduced.

For doubling from 560 nm to 280 nm, we considered using  $\beta$ -barium borate (BBO), potassium dihydrogen phosphate (KDP), and cesium lithium borate (CLBO). Phase matching for the aforementioned crystals is accomplished using angle-tuning. We also looked at other crystals – however these are the choices that stood out.

Of the possible candidates, there is no clear preferred choice. Each has their own benefits and drawbacks. For doubling from IR to VIS, neither LBO nor ppLN suffers from walk-off. The advantage of ppLN is that it has a much higher single-pass conversion efficiency, due to the different manner in which phase matching is achieved. The drawback, however, is that it is much more expensive and at the time it was determined ppLN would not have resulted in a significant increase in the overall conversion efficiency.

A cheaper alternative is LBO. Temperature tuning in the IR is possible with LBO, and so the second-harmonic generated output does not suffer from walk-

off. This gives a single-pass conversion efficiency that is large enough to yield an appreciable amount of output light when the crystal is placed in a resonant cavity, and for a fraction of the cost of ppLN. The optimal temperature for phase matching is  $106^\circ C$ . This gives a single-pass conversion efficiency of  $1.4 \cdot 10^{-4} / W$  for a  $7 \text{ mm}$  long crystal.

For conversion from VIS to UV, BBO is the best choice. None of the crystals we considered (mentioned below) are temperature tunable at this wavelength, and so they all have to be angle tuned. As a result, they all give rise to walk-off: BBO, CLBO, then KDP in descending order. Although CLBO has a low walk-off angle, its effective non-linear coefficient,  $d_{eff}$ , is low, and CLBO is very hygroscopic: it must be heated to  $150^\circ C$  to avoid crystal damage.

KDP is also fairly hygroscopic whereas BBO is mildly hygroscopic. Although KDP suffers from less walk-off than BBO, its non-linear coefficient is smaller. Nielsen [77] has shown that KDP can result in more harmonic generated light than BBO, in the case of long crystals. This is because KDP has a smaller absorption coefficient than BBO at  $560 \text{ nm}$ , and so longer KDP crystals can be used. Despite this, we determined that BBO is the better choice since it is less hygroscopic and we have to go to unreasonable crystal lengths ( $> 50 \text{ mm}$ ) before KDP outperforms BBO. The critical angle for phase matching is  $44^\circ$ . This gives a single-pass conversion efficiency of  $1.6 \cdot 10^{-4} / W$  for a  $7 \text{ mm}$  long crystal of BBO.

In addition to absorption losses, we need to consider reflection losses at the crystal surfaces. To minimize reflection losses we cut the crystal at Brewster's angle, resulting in negligible reflection losses of the fundamental light since it is P-polarized. The second-harmonic light is S-polarized and so it suffers from reflection losses at the exit interface.

In Figure (4.3), three different examples of a Brewster cut crystal are shown. In Figure (4.3(a)), the beam will propagate at an angle  $\alpha$  from the normal of the crystal surface where  $\alpha$  corresponds to Brewster's angle going from a crystal with an index of refraction  $n$  to air. In this case, the crystal thickness should be large enough to allow passage of the beam without clipping. In Figure (4.3(b)) the beam is incident at an angle  $\beta - \alpha$  from a line parallel to the direction of propagation inside of the crystal, where  $\beta$  corresponds to Brewster's angle going from air to a medium of index  $n$ . The crystal mount should accommodate this by allowing passage of the beam in and out of the mount. A so-called B-cut corresponds to that of Figure (4.3(b)).

The cut in Figure (4.3(c)) is similar to the previous one. However in this case, it is possible to build a two mirror traveling wave resonator, which is both interesting and compact. The resonator would offer the advantages of a traditional ring resonator, such as uni-directional harmonic generation and no back reflections, while maintaining a short round trip path length. A closer examination of this design, however, reveals that it is overly restrictive. The

incidence angle on the crystal fixes the incidence angle on the mirror. If we want to compensate for astigmatism [78], then the crystal length fixes the mirror radius of curvature. For both LBO and BBO we would have to use a mirror with a radius of curvature of 4.4 cm for a crystal length of 7 mm. This would either require a custom mirror, or accepting partial compensation of astigmatism. It would also be difficult to couple light into such a cavity since the input coupler would also have to serve as the piezo mounted mirror (to keep the cavity locked). It is possible to use a tube PZT, although this would require the use of high-voltages to drive the PZT. We chose to order B-cut crystals for the cavities we built.

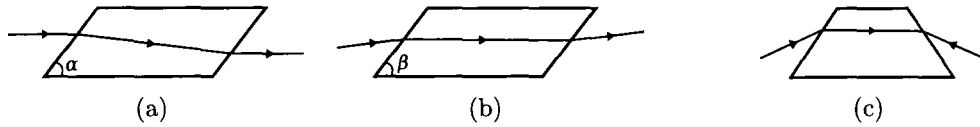


Figure 4.3: In example (a) we see that propagation occurs at an angle inside of the crystal.  $\alpha$  is Brewster’s angle going from medium index  $n$  to air, and  $\beta$  is going from air to medium index  $n$ . In (b) the crystal is cut so that propagation inside of the crystal occurs parallel to the crystal sides. This is commonly referred to as a “ $\beta$ -cut” crystal. The same can be said for (c). However with (c) it is possible to build a more compact cavity with fewer mirrors.

### 4.2.3 Boyd Kleinman Focusing Parameter

The earlier treatment assumed that the incident field could be treated as a plane wave; however, for lasers the intensity of the beam generally has a Gaussian profile in the coordinates transverse to beam propagation. A more accu-

rate derivation of the generated second harmonic light was performed by Boyd and Kleinman [74], in which they used solutions to the paraxial wave equation for the incident field and accounted for walkoff within the crystal.

Two results follow from the analysis. First, a slight mismatch in the indices of refraction between the fundamental and harmonic is actually desirable. This is due to the Guoy Effect [79], in which a Gaussian beam acquires a phase shift in passing through a focus that is different compared to a plane wave with the same frequency. Second, for a given crystal length, there is an optimal waist size which maximizes the harmonic output in the presence of walkoff.

We know that the generated harmonic intensity is quadratic in the incident intensity. This suggests that a tight focus is desirable, since a tight focus results in higher peak intensity. A tightly focused beam however, corresponds to a larger divergence angle, and hence a smaller Rayleigh range (or confocal parameter), beyond which the peak intensity rapidly drops off. Considering these two factors, it is clear that we want a tightly focused beam, whose spot size does not change appreciably over the extent of the crystal.

From a practical perspective, it is simple to extract from the paper [74] an estimation of the confocal parameter, and hence waist size, which maximizes the harmonic output. From this, we can estimate the single-pass conversion efficiency using Equation (4.4). As an example, we will consider  $\beta$ -Barium

Borate (BBO). The second-harmonic power is given in the paper [74] as:

$$P_{2\omega} = \frac{4\omega^2 n^3}{\lambda \epsilon_0 c^3} d_{eff}^2 l h e^{-l(\alpha_\omega + \frac{1}{2}\alpha_{2\omega})} P_\omega^2 \quad (4.4)$$

where  $\omega$  is the fundamental frequency,  $n$  is the index of refraction,  $\lambda$  is the fundamental wavelength,  $\epsilon_0$  is the permittivity of free space,  $c$  is the speed of light,  $d_{eff}$  is the crystal's non-linear coefficient,  $l$  is the crystal length,  $\alpha$  is the absorption,  $h$  is a numerical value representing peak efficiency, obtained from the Boyd and Kleinmann paper, and  $P_\omega$  is the incident power.

For example, the walkoff angle for BBO is 84 *mrad* if the fundamental wavelength is 560 *nm* [76]. From the Boyd-Kleinman paper, we may calculate the so-called double refraction parameter,  $B$ :

$$B = \rho n \sqrt{\frac{l\pi}{2\lambda}} \quad (4.5)$$

where  $\lambda$  is the fundamental wavelength,  $l$  is the crystal length,  $\rho$  is the walkoff angle, and  $n$  is the index of refraction at the fundamental frequency.

The double refraction parameter is a measure of walkoff occurring in the crystal. Second-harmonic light that is generated at one point in the crystal moves at an angle  $\rho$  relative to the fundamental beam. Since it travels a different optical path length through the crystal than the fundamental beam does, it is no longer in phase with harmonic light generated at another point

inside of the crystal. This results in less harmonic light being generated due to destructive interference between light generated at different points in the crystal.

In this case,  $B$  is 20 *rad* for a 7 *mm* long crystal (corresponding to the crystal length we used for our doubling systems). From this information we can estimate the optimal waist and calculate the single-pass conversion efficiency.

From Figure (4.4) we can estimate that the function  $h \approx 0.035$  for  $B = 20$  *rad*. From Figure (4.5) we also see that for large double refraction parameter, the optimal focusing parameter is 1.39. This corresponds to a waist of approximately 20  $\mu\text{m}$ . From Equation (4.4), the second harmonic output power is approximately  $1.6 \cdot 10^{-4}/W$ .

## 4.3 Cavity Design

### 4.3.1 General Comments

Since single-pass conversion efficiencies are small, we need to look at cavity designs which will increase the obtainable harmonic output. We will consider ring-resonator geometries, consisting of two curved mirrors and two flat mirrors (shown in Figure (4.6)). In our cavity (which has a bowtie configuration), one of the flat mirrors is used as an input coupler, and one of the curved mirrors is attached to a piezoelectric transducer to keep the cavity resonant.

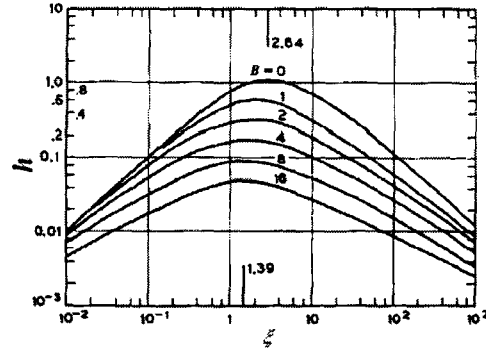


Figure 4.4: The peak efficiency  $h$  is plotted as a function of the optimal focusing parameter,  $\xi$ , for different values of the double refraction parameter. As the double refraction parameter is increased, the optimal focusing parameter decreases from its maximum value of 2.84 to 1.39. This plot can be used to estimate the conversion efficiency for waist values other than the optimal value. The image is reproduced with permission from the Boyd and Kleinman paper [74].

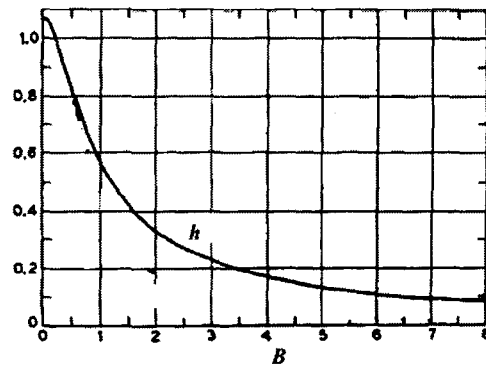


Figure 4.5: The peak efficiency  $h$  is plotted as a function of the double refraction parameter. In particular, if temperature-tuned LBO is used, then  $B = 0$ , and, from Figure (4.4), the optimal focusing parameter is 2.84. In the case of BBO, which will be used to double from VIS to UV,  $B = 20$ . For large values of  $B$  we may use  $\xi = 1.39$  [74]. In both cases, for a 7 mm long crystal this happens to correspond to a waist of 21  $\mu\text{m}$ . The image is reproduced with permission from the Boyd and Kleinman paper [74].

Although standing wave cavity geometries are possible, we opted against this. The problems with standing-wave cavities are threefold. First, there is light back-reflected into the laser cavity, which can damage the laser. Second, the harmonic generation occurs in two directions and so the output power in a given beam is less than if it only occurred in one direction. Third, since we have a standing wave cavity, there are nodes and anti-nodes within the crystal which reduces the average harmonic output.

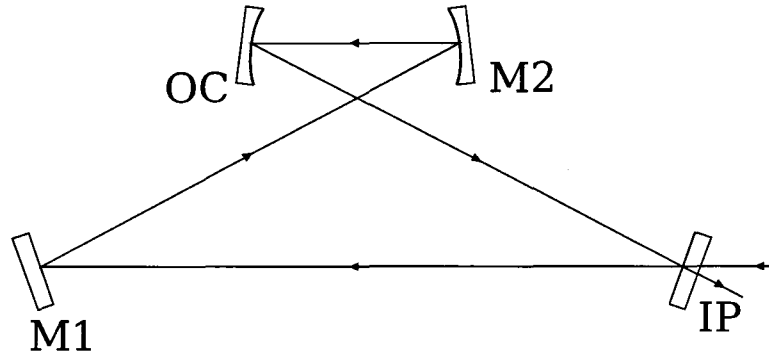


Figure 4.6: Simple ring resonator geometry. The cavity consists of four mirrors arranged in a ring. Light enters the cavity through mirror IP and is directed around the cavity in a bow-tie configuration (IP → M1 → M2 → OC → IP).

Since the circulating light is not normally incident on the curved mirrors, astigmatism is introduced upon reflection. If we use a Brewster-cut crystal, then we may use the astigmatism introduced by reflection off the mirrors to compensate for the astigmatism introduced by propagation through the crystal [78]. Using the ABCD matrix formalism [79], we may account for the astigmatism by assigning a different effective mirror radius of curvature for each plane, and treating the planes separately.

Optical elements and propagation in media may be represented by  $2 \times 2$  matrices. Cascading them, from right to left in the order that the beam encounters the elements results in an overall  $2 \times 2$  matrix that is used to calculate the complex beam parameter,  $q$ , which is related to the beam spot size and radius of curvature [79].

Before going into details, let us start by considering general requirements that one would expect of a stable resonator. First, the beam size should not appreciably change after a single pass through the resonator. Second, we should not be sensitive to small beam misalignments, and third, we need to keep the cavity resonant.

Assuming that we begin with some complex beam parameter,  $q$ , at some arbitrary reference plane within the resonator, we expect that after a full round trip through the resonator, the  $q$  parameter should return to its initial starting value. This is just to say that, regardless of where we want to measure the beam radius of curvature and spot size, it should remain constant in that cross-sectional slice after an arbitrary number of passes. This requirement is equivalent to stating that the geometry of the resonator fixes the lowest order transverse mode it can support.

The requirement that the complex beam parameter periodically repeats itself as it passes around the cavity is also equivalent to stability against small beam misalignments. Thus our first two operational requirements amount to

the same criterion. This is evident if we consider what happens to the beam after a single pass through the cavity. If the beam is misaligned then it will not overlap the first pass on the second pass through the cavity. After multiple passes, the effect of the misalignment can be grossly exaggerated if the cavity design is sensitive to beam misalignment.

This is a rather rigid requirement and one would expect that in practice, any resonator would suffer from mild beam misalignment, or lateral displacement from an optimal value. Stability against these types of perturbations is considered in Section (4.3.2). We also would like the cavity to consist of as few optical elements as possible. Every additional optical element we add will contribute to linear losses in the cavity, which will deplete the fundamental light.

Our third requirement is that the cavity be resonant at the frequency of the fundamental light. Hence, we need to compensate (servo) for vibrations that may move the cavity away from resonance. We do this by mounting one of the cavity mirrors on a piezoelectric transducer (PZT) that allows us to change the cavity length in response to an error signal. Two common methods of deriving a cavity error signal are the Pound-Drever-Hall technique [68] and the Hänsch-Couillaud technique [67]. In the Pound-Drever-Hall technique the input beam is sent through a phase modulator, which adds RF-sidebands to the input signal. At the input coupler the reflected wave – a superposition

between the modulated signal and the transmitted signal from inside the cavity – is monitored. The resulting signal is used to derive the electrical signal that drives the PZT. In the Hänsch-Couillaud technique, the polarization of the reflected beam at the input coupler is monitored and used to derive an electrical signal that drives the PZT. For our cavities, we chose the Hänsch-Couillaud technique which is cheaper and requires less and simpler electronics.

As mentioned earlier, the cavity supports certain transverse modes, determined by the optical elements and propagation distances. In order to input light into the cavity, we must match the input beam to the cavity mode. This is generally accomplished with two lenses, whose parameters may be determined by ABCD matrix analysis. It is interesting to note here that astigmatism will be introduced as a result of propagation through the input coupler, which cannot be compensated for within the cavity. However, it is possible to tilt one of the mode-matching lenses slightly for compensation.

As it turns out, calculation of the cavity mode and determination of the stability of the cavity against beam misalignments are intimately related to the ABCD ray matrix formulation for geometric stability [79]. In Section (4.3.2) we consider the general formulation of geometric stability in the context of rays, which is then connected to Gaussian beams in Section (4.3.3). By relating the Gaussian beam analysis to the ray analysis, we can determine optimal cavity parameters as discussed in Section (4.3.5).

Finally, we should consider cavity size in our analysis. That is, we should choose our parameters in such a way that the cavity is of reasonable dimensions to avoid obscuring the beam at any point, or taking up too much of the optical table. Although this may appear obvious, one can easily fall into the trap of forgetting about practical physical constraints.

A treatment of many of these considerations can be found in Siegman [79], which deals with generalized paraxial resonator theory. This, along with mode matching, is also discussed in Kogelnik and Li [80].

### 4.3.2 Geometric Stability

An obvious consideration is how sensitive the cavity will be to perturbations whether they be from mode-mismatch or from slight misalignment of the beam. This ends up being intimately related to ray stability in periodic focusing systems.

Consider what happens to a ray, characterized by its distance  $r$  from the optical axis and slope  $r'$ , as it travels through a resonator. Here, the optic axis is defined by a line parallel to the symmetry axis of a curved element such as a lens. Cavity misalignments (such as hitting a curved mirror off centre) are not accounted for in this treatment; however, they can be handled by treating the tangential and sagittal planes separately [79]. The round-trip matrix is determined by cascading the matrices for each element and multiplying them.

This results in the  $A$ ,  $B$ ,  $C$ , and  $D$  elements that are also used in calculating the resonator eigenmodes in Section (4.3.3). In the case of ray optics, we obtain the following eigenvalue equation:

$$\begin{pmatrix} A & B \\ C & D \end{pmatrix} \begin{pmatrix} r \\ r' \end{pmatrix} = \lambda \begin{pmatrix} r \\ r' \end{pmatrix} \quad (4.6)$$

Siegman [79] shows that the eigenvalues and the eigenrays of Equation (4.6) can be grouped as describing stable and unstable periodic focusing systems. For stable periodic focusing systems, we find that the displacement of the ray oscillates, as shown in Figure (4.7).

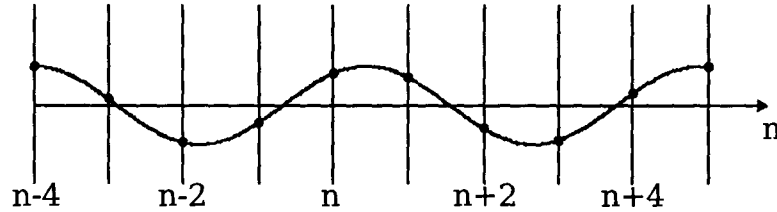


Figure 4.7: After multiple passes through a resonator we can see that the ray height will oscillate for a stable periodic focusing system. For unstable systems, the displacement continues to grow.

We also find that there is a region of geometric stability defined by resonator  $g$ -parameters, as shown in Figure (4.8). The  $g$ -parameters are essentially a coordinate transformation, determined from the physical distances in the cavity. They are given as:

$$g_{1s,t} = 1 - \frac{2(L + \frac{L}{2n})}{R_{s,t}} \quad (4.7)$$

$$g_{2s,2t} = 1 - \frac{2X}{R_{s,t}} \quad (4.8)$$

where  $s$  and  $t$  correspond to the sagittal and tangential planes.  $X$  is the distance between the spherical mirror and the secondary waist,  $R$  is the mirror radius of curvature, and  $L$  is the distance between the spherical mirror and the crystal face. Although Figure (4.8) is generally shown in the context of two mirror resonators, it applies to the four mirror resonator case as well with the  $g$ -parameters redefined according to Equations (4.7) and (4.8).

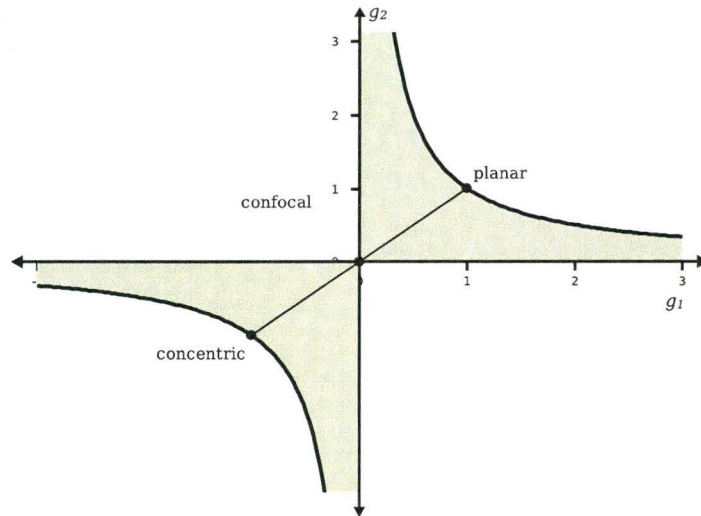


Figure 4.8: A plot of resonator stability. We will be operating in the bottom left quadrant, to the right of the straight line denoting  $g_1 = g_2$ . The shaded region corresponds to stable regions.

In general, our resonator will lie in a region to the right of  $g_1 = g_2$ , in the lower left quadrant. Geometries which do not have  $g$ -parameters lying in this quadrant will have ray heights which oscillate as discussed earlier, and shown in Figure (4.7).

### 4.3.3 ABCD Matrices and Gaussian Beams

So far, we have considered propagation of rays. The beam is in fact Gaussian, although its propagation through optical elements can still be described using the same ABCD matrix formalism introduced in the previous section.

The ray picture is intimately related to what happens with real Gaussian beams. If our resonator lies within the region of stability shown in Figure (4.8) then it will be stable against minor beam perturbations such as misalignment and over or under-coupling. If we were to sit at a reference plane, and observe the spot size after each pass, the size would oscillate around the lowest-order transverse cavity mode. It would do so because at that reference plane, the transverse profile consists of the lowest-order allowed mode, plus higher-order modes. After multiple passes, these higher-order modes do not stay in phase since the phase difference due to the Guoy effect is larger for higher order modes. This results in destructive interference and only the lowest-order transverse mode supported by the cavity survives.

In-depth discussions of ABCD matrices and Gaussian beams can be found in various texts and papers [79], [80], [81]. The ABCD matrices are obtained from ray tracing and have the form:

$$\begin{pmatrix} A & B \\ C & D \end{pmatrix} \quad (4.9)$$

In no way is this section a full treatment of the topic. Instead, we will only look at how this approach can be applied to our resonator design.

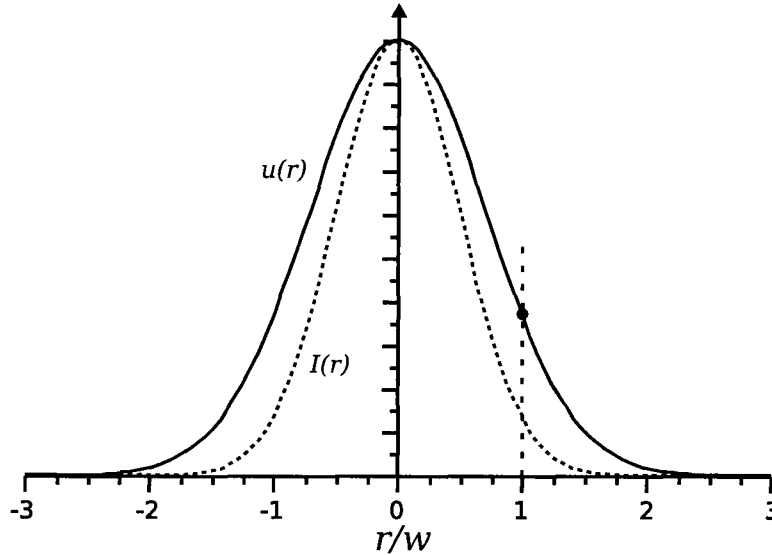


Figure 4.9: Intensity and field distribution of a Gaussian beam. The field is denoted  $u(r)$  and the intensity is  $I(r)$ . The spot size,  $w(z)$  is defined to be the point where the field strength falls by  $\frac{1}{e}$ . The beam diameter is twice the beam waist.

A laser beam propagating along the  $z$ -direction has a Gaussian intensity distribution in the transverse plane, as shown in Figure (4.9). The spot size,  $w(z)$ , is defined to be the point where the field strength falls by  $\frac{1}{e}$  in the transverse direction.

We have chosen  $z = 0$  as the location where the beam has its smallest size,  $\omega_0$ . At this waist location the beam radius of curvature is infinite and the on-axis beam intensity is maximized.

The other important property of Gaussian beams is the Rayleigh range:

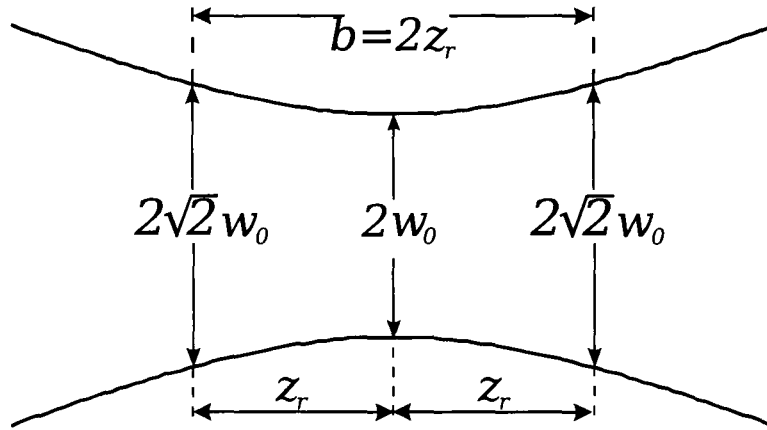


Figure 4.10: Gaussian beam profile along the direction of propagation. The Rayleigh range ( $z_r$ ) as well as the confocal parameter ( $b$ ) are labelled in the figure. The spot size  $w(z)$  is a minimum at the waist ( $w_0$ ).

how far along the  $z$ -direction we must go before the spot size increases by a factor of  $\sqrt{2}$ . The full distance between Rayleigh ranges on other side of the waist location is termed the confocal parameter.

We need to know how the beam evolves as it propagates and passes through various focusing elements, mirrors, or through the crystal itself. To determine the effect of multiple optical elements and propagation distances, we can cascade the ABCD matrices together, and use the overall matrix to determine the resultant complex beam parameter,  $q_f$ , from the formula:

$$q_f = \frac{Aq_i + B}{Cq_i + D} \quad (4.10)$$

The complex beam parameter  $q$  is defined by:

$$\frac{1}{q(z)} = \frac{1}{R(z)} + i \frac{\lambda}{n\pi w(z)^2} \quad (4.11)$$

where  $R$  and  $w$  correspond to the beam radius of curvature and spot size respectively.

We can determine the total round-trip matrix, starting at some reference plane. The choice of reference plane is arbitrary, and any choice is valid. However, there are two reasons to choose one of the cavity waists as the reference plane. First, the initial  $q$  parameter, and final  $q$  parameter are *strictly* complex, since at a waist the radius of curvature is infinite. Second, as we shall see, this choice of starting location also simplifies the calculations when we determine the resonator eigenmodes.

A final property of the cavity is that the total round trip ABCD matrix is different for the tangential and saggital planes. This is because the curved mirror has differing effective curvatures for the two planes, and the Brewster-cut crystal, if used, has differing effective lengths. In general, this means that the cavity eigenmodes are astigmatic; however, it is possible to compensate for this astigmatism [78] by choosing the angle of the mirrors in such a way that they introduce astigmatism in the opposite sense to that introduced by the Brewster-cut crystal.

### 4.3.4 Cavity Eigenmodes and Astigmatic Compensation

Thus, in general, the eigenmodes of the cavity will be astigmatic and so we must calculate the eigenmodes for each plane separately. Earlier, we commented that the eigenmodes are calculated by requiring a self consistent  $q$  value after a roundtrip in the resonator.

From Equation (4.10), setting the initial and final  $q$  parameters to be equal, we can obtain the condition for a self-consistent solution:

$$q = \frac{A - D}{2C} \pm \sqrt{\frac{(A - D)^2}{4C^2} + \frac{B}{C}} \quad (4.12)$$

where we have the eigenmodes expressed in terms of the round trip matrix elements,  $A$ ,  $B$ ,  $C$  and  $D$ . The eigenmodes can thus be determined from the saggital and tangential round trip matrix elements.

If we compare Equation (4.12) to Equation (4.11), we can note that two things must be true. First, since our round-trip matrix elements are derived by starting at a waist, the  $q$  parameter must be entirely complex. From Equation (4.12), this means  $A$  must equal  $D$ . Second, either  $B$  or  $C$  must be negative.

If the eigenmodes are astigmatic, then obviously coupling into the cavity becomes difficult, since our input beam is  $TEM_{00}$ . As a result, we will be over-coupled or under-coupled in one of the two planes, or possibly both, and so we may be stable in one plane, but unstable in the other. Even if the beam

happens to be stable in both planes, the beam may be focused the centre of the crystal in one plane, but outside of the crystal in the other. This leads to suboptimal harmonic output.

A solution to this problem is to use the astigmatism introduced by the mirrors to compensate for the astigmatism introduced by the B-cut crystal. As mentioned earlier, the effect of the angled mirror is that the effective radius of curvature is different in the two planes. Specifically, the focal point in the tangential plane occurs at a distance that is closer to the mirror than the focal point in the saggital plane. The B-cut crystal effectively has a longer path length in the saggital plane than in the tangential plane, for the same physical distance traversed. In addition, if the focal point is inside of the crystal, then the waist in the tangential plane is approximately a factor of  $n$  larger than the saggital plane, where  $n$  is the crystal's index of refraction[78]. The combined effect is that, although the focal point in the two planes would be displaced from one another due to the off-axis spherical mirrors, the effect of the crystal is to bring the focal point back to the same physical position due to the laser beam's different effective path lengths in each plane.

A complete description, and derivation is treated by various authors: Kogelnik *et al.* [78], Ferguson and Dunn [82], and Hanna [83]; the paper by Ferguson and Dunn [82] gives the astigmatic compensation formula but concentrates on compensation of coma. To summarize, the astigmatic compensa-

tion formula is:

$$R \sin \theta \tan \theta = l \frac{(n^2 - 1)}{n^3} \quad (4.13)$$

where  $R$  is the mirror radius of curvature,  $\theta$  the mirror incidence angle,  $l$  the crystal length, and  $n$  is the crystal index of refraction. Although it is theoretically possible to compensate for coma [82], this requires an unreasonable mirror radius of curvature and so it is not considered here.

### 4.3.5 Cavity Equations

We are now in a position to summarize the results of the analysis for a four mirror ring resonator. Although these equations can be found in a Maple worksheet “brewstercrystalcavity.mw” that I wrote (see Appendix A), they are included here for reference. In terms of saggital and tangential  $g$  parameters, using Equation (4.12), we have:

$$w_{cs} = \sqrt{\frac{\lambda R_s}{2n\pi} \sqrt{\frac{g_{1s}g_{2s}(1 - g_{1s}g_{2s})}{g_{2s}^2}}} \quad (4.14)$$

$$w_{ct} = n \sqrt{\frac{\lambda R_t}{2n\pi} \sqrt{\frac{g_{1t}g_{2t}(1 - g_{1t}g_{2t})}{g_{2t}^2}}} \quad (4.15)$$

$$w_{as} = \sqrt{\frac{\lambda R_s}{2\pi} \sqrt{\frac{g_{1s}g_{2s}(1 - g_{1s}g_{2s})}{g_{1s}^2}}} \quad (4.16)$$

$$w_{at} = \sqrt{\frac{\lambda R_t}{2\pi} \sqrt{\frac{g_{1t}g_{2t}(1 - g_{1t}g_{2t})}{g_{1t}^2}}} \quad (4.17)$$

where Equations (4.14) and (4.15) correspond to the waist in the crystal, and the other two correspond to the secondary waist in air. Subscripts  $s$  and  $t$  correspond to saggital and tangential and  $g$ -parameters that were defined earlier. Armed with these equations, we may now determine the cavity parameters.

### 4.3.6 Maple Worksheet Example

The cavity parameters can be calculated using the Maple worksheet mentioned in the previous section. The worksheet is fairly simple to follow, and requires some user input; the crystal parameters, mirror radius of curvature, etc., must be entered manually.

The worksheet assumes that a B-cut crystal and curved mirrors with equal radius of curvature will be used. From the user's input, it returns a plot of the cavity waist as a function of  $L$ , the distance from the curved mirror to the crystal face. This plot defines a region of stability. A stability plot for the LBO cavity is shown in Figure (4.12). Outside of the stability region ( $L < 36 \text{ mm}$  or  $L > 38.4 \text{ mm}$ ), the crystal waist is not defined, since multiple passes do not overlap and so no waist is formed inside of the cavity. Inside the stability region ( $36 \text{ mm} < L < 38.4 \text{ mm}$ ), a waist inside of the crystal is formed. The size of the crystal waist increases with increasing  $L$  to a maximum at

approximately  $L = 37 \text{ mm}$  before decreasing with increasing  $L$ . The cavity is most stable against perturbations when  $L \simeq 37 \text{ mm}$ , since the crystal waist is least sensitive to changes in  $L$  at this value.

Once an optimal value of  $L$  has been determined, the worksheet also calculates and returns the crystal waist, secondary waist (which will be used to determine mode-matching parameters), and the waist size on the curved mirrors. It also returns the distance between the two flat mirrors, assuming a symmetric ring design. In actual practice, it may be desirable to stray from this design to partially compensate for coma, in which case the remaining cavity distance (outside of the two curved mirrors containing the crystal) is defined as  $2X$ .

As specific examples, we will first look at using an LBO crystal, temperature tuned to satisfy the phase-matching criterion for  $1120 \text{ nm}$  to  $560 \text{ nm}$ . Then we will examine the case of a BBO crystal, angle tuned for phase-matching for  $560 \text{ nm}$  to  $280 \text{ nm}$ . In the case of temperature tuning, there is no walk-off, and hence the Boyd-Kleinman paper [74] gives the optimal waist as:

$$w_0 = \sqrt{\frac{\lambda l}{5.68\pi}} \quad (4.18)$$

where  $l$  is the crystal length, and  $\lambda$  is the free-space wavelength. Since, in our case, the crystal is  $7 \text{ mm}$  long, this corresponds to a waist of  $20.96 \mu\text{m}$ . As a side note, since the crystal is  $7 \text{ mm}$  long, and the operating wavelength is

1120 nm we expect the temperature bandwidth (3 dB point) to be approximately 6.7°C [76]. The geometry of the resonator is shown in Figure (4.11(a)).

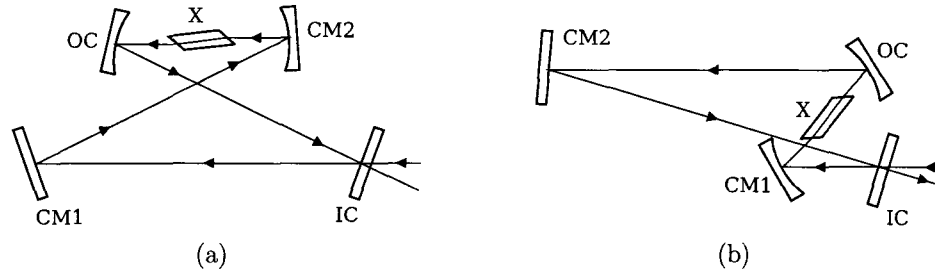


Figure 4.11: Figure (a) shows a typical ring cavity. It is possible to use this cavity to compensate for astigmatism, but not coma. Figure (b) shows a  $Z$  cavity, which can potentially compensate both for coma and astigmatism.

Entering appropriate parameters into the maple worksheet, and using a radius of curvature of 7.5 cm, we obtain the stability diagram shown in Figure (4.12). From this figure, we see that we would like to operate with  $L$  being close to 37.4 mm. Using this value, we calculated the other cavity parameters shown in Table (4.1).

In the case of BBO, for a mirror radius of curvature of 7.5 cm, we obtain the stability diagram in Figure (4.13). From Figure (4.13) we see that we would like to operate with  $L$  being close to 38.6 mm. Using this value, we calculated the other cavity parameters shown in Table (4.2).

Using these cavity parameters, the cavities were assembled on the optics table.

Brewster Cut LBO, mirror ROC = 7.5cm, theta = 10.77 degrees

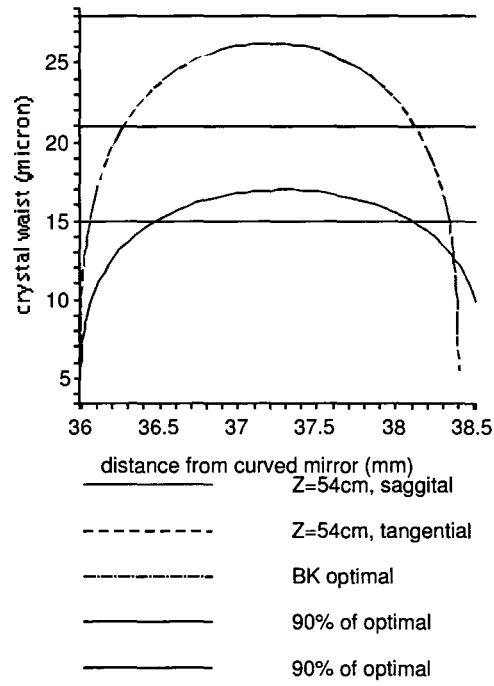


Figure 4.12: Stability plot for the LBO cavity ( $R = 7.5 \text{ cm}$ ). In this case, we require a incidence angle of  $10.77^\circ$  to compensate for astigmatism.

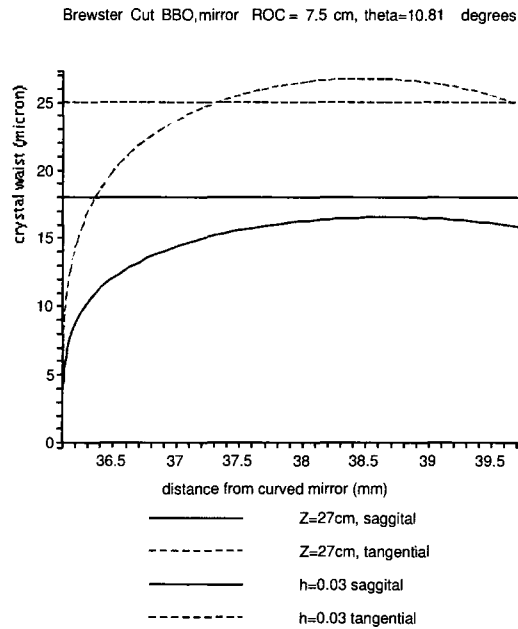


Figure 4.13: Stability plot for the BBO cavity ( $R = 7.5 \text{ cm}$ ). In this case, we require a incidence angle of  $10.81^\circ$  to compensate for astigmatism.

### 4.3.7 Cavity Locking Scheme

In order to keep the cavity locked we decided to employ the Hänsch-Coulliaud [67] technique, as discussed in Section (4.3.1). This technique uses polarization spectroscopy to obtain the error signal that is fed back to the cavity mirror to keep the doubling cavities resonant. To derive the error signal a fixed attenuator ( $OD = 3$ ), a quarter-waveplate, a Wollaston prism, a variable attenuator and a photodetector are used.

The light sent to the input of the cavity is linearly polarized. Light reflecting off the cavity input passes through the fixed attenuator (which prevents saturation of the photodiode) and then through a quarter-waveplate set to  $45^\circ$ .

Table 4.1: LBO Cavity: Summary of LBO Cavity Dimensions

$L$ (distance from crystal face to mirror)	37.4 <i>mm</i>
$R$ (mirror radius of curvature)	7.5 <i>cm</i>
$\theta$ (mirror angle of incidence)	10.77°
$w_{ct}$ (tangential waist size at crystal focus)	26.25 $\mu m$
$w_{cs}$ (sagittal waist size at crystal focus)	16.96 $\mu m$
$w_{at}$ (tangential waist size at secondary focus)	0.45 <i>mm</i>
$w_{as}$ (sagittal waist size at secondary focus)	0.46 <i>mm</i>
$w_{mt}$ (tangential spot size at curved mirror surface)	0.65 <i>mm</i>
$w_{ms}$ (sagittal spot size at curved mirror surface)	0.65 <i>mm</i>
$Z$ (distance between flat mirrors)	53.6 <i>cm</i>

Table 4.2: BBO Cavity: Summary of BBO Cavity Dimensions

$L$ (distance from crystal face to mirror)	38.6 <i>mm</i>
$R$ (mirror radius of curvature)	7.5 <i>cm</i>
$\theta$ (mirror angle of incidence)	10.81°
$w_{ct}$ (tangential waist size at crystal focus)	26.80 $\mu m$
$w_{cs}$ (sagittal waist size at crystal focus)	16.53 $\mu m$
$w_{at}$ (tangential waist size at secondary focus)	0.22 <i>mm</i>
$w_{as}$ (sagittal waist size at secondary focus)	0.23 <i>mm</i>
$w_{mt}$ (tangential spot size at curved mirror surface)	0.34 <i>mm</i>
$w_{ms}$ (sagittal spot size at curved mirror surface)	0.34 <i>mm</i>
$Z$ (distance between flat mirrors)	26.5 <i>cm</i>

If an index card is placed inside of the cavity to prevent light from circulating, then the light that is reflected off the input coupler is circularly polarized after passing through the quarter-waveplate.

The Wollaston prism acts as a polarization analyser: circularly polarized light is split into horizontally and vertically polarized components that are spatially separated at the exit port of the Wollaston prism. The two beams are then sent to a photodetector that subtracts the two photocurrents. A variable attenuator is placed in one of the beams to account for variations in

the photodiodes that result in different photocurrents for the same amount of light.

If light is allowed to circulate inside of the cavity then the light passing through the quarter-waveplate consists of the light directly reflected off the input coupler as well as light from the cavity that passes back out through the input coupler. If the cavity is resonant then the light circulating inside of the cavity is in phase with the light input to the cavity. As the cavity length increases (decreases) then the phase of the circulating light leads (lags) the phase of the circulating light. This phase difference results in elliptically polarized light after passing through the quarter-waveplate. After passing through the Wollaston prism, the power in each beam depends on whether the cavity was too short or too long, resulting in a dispersion signal when the photocurrent from each beam is subtracted.

The voltage signal obtained from the photodetector is sent to a lock box (built in-house) that uses proportional and integral gain on the input signal to drive the PZT connected to a cavity mirror, keeping the cavity resonant.

### **4.3.8 Cavity Assembly**

The cavities were assembled directly on the optical table, leaving an appropriate amount of space for the optics coupling into the cavity as well as the optics required for the locking scheme. It should be noted that in the first

iteration of the cavity design, we used mirrors with a lower quality reflection coating ( $R > 99\%$ ) for the cavity. In the second iteration, we purchased the substrates and had them coated separately ( $R > 99.9\%$ ). This resulted in approximately a factor of 2 increase for each doubling stage. Table (4.3) summarizes the optics components used in the cavity design and associated optics for the locking scheme. Excluded from the list are optics for mode-matching and beam steering.

Table 4.3: Cavity Components: Summary of Required Optical Components

Total	Part Name and Manufacturer
2	Flat Mirror Substrate (BK7, $R > 99.9\%$ ) – CVI
2	Flat Mirror Substrate (Fused Silica, $R > 99.9\%$ ) – CVI
2	Curved Mirror ( $ROC = 75 \text{ mm}$ , BK7, $R > 99.9\%$ ) – CVI
2	Curved Mirror ( $ROC = 75 \text{ mm}$ , Fused Silica, $R > 99.9\%$ ) – CVI
2	Piezo-Electric Actuator (PZT) – Thorlabs ( <i>AE0505D08F</i> )
1	Wollaston Prism (AR coated for $1120 \text{ nm}$ ) – Karl Lambrecht
1	Wollaston Prism (AR coated for $560 \text{ nm}$ ) – Karl Lambrecht
1	$\frac{\lambda}{4}$ waveplate (AR coated for $1120 \text{ nm}$ ) – Karl Lambrecht
1	$\frac{\lambda}{4}$ waveplate (AR coated for $560 \text{ nm}$ ) – Karl Lambrecht
1	$\frac{\lambda}{2}$ waveplate (AR coated for $1120 \text{ nm}$ ) – Karl Lambrecht
1	$\frac{\lambda}{2}$ waveplate (AR coated for $560 \text{ nm}$ ) – Karl Lambrecht
1	Reflection Coating ( $HR@560 \text{ nm}$ , $HT@280 \text{ nm}$ ) – Advanced Thin Films
1	Reflection Coating ( $HR@1120 \text{ nm}$ , $HT@560 \text{ nm}$ ) – Precision Photonics

## 4.4 LBO Performance

The LBO cavities frequency double from  $1120 \text{ nm}$  to  $560 \text{ nm}$ . Rough alignment was done by using an IR card and following the beam path around the cavity, adjusting the mirrors to steer the beam to the central region of each

subsequent mirror. Once the first pass around the cavity was roughly aligned using the IR card, the cavity output and input couplers were iteratively adjusted to overlap the multiple passes of the beam inside of the cavity. The beam overlap was optimized by monitoring the reflected signal with a photodiode and an oscilloscope while the cavity length was scanned by sending a sawtooth waveform to the PZT, maximizing the dip of the  $TEM_{00}$  mode while minimizing higher order modes.

Fine adjustment of the coupling into the cavity was performed with a pair of dog-leg mirrors while monitoring the signal reflected from the cavity with a photodiode and an oscilloscope. The beam from the fibre laser was mode-matched into the LBO cavity using two lenses to match the beam to the cavity mode. One of the lenses was placed on a linear translation mount to allow for adjustment of the beam size for optimal mode matching.

The cavity crystal was encased in a copper housing to keep the crystal at a fixed temperature, as discussed in Section (4.3.8). The temperature of the crystal was adjusted to phase-match the fundamental and second-harmonic light generated in the crystal. In order to optimize the temperature, the cavity output power was monitored while the temperature was adjusted by small increments, allowing the crystal to equilibrate at each temperature step.

Localized heating inside of the crystal due to the high circulating power inside of the cavity (when locked) results in thermal lensing [84], [85], [86].

Evidence of this effect was observed when we were locking the cavity: we could only approach resonance from one direction. As resonance was approached, the crystal would heat, changing the index of refraction and hence the optical path length through the crystal. As the optical path length changed, the optimal cavity length changed. If the piezo was swept in phase with the change in cavity length then the cavity could be locked. If the PZT was swept out of phase with the change in cavity length then the locking electronics could not respond fast enough to the temperature-dependent change in cavity resonance and the cavity could not be locked.

Once the cavity was locked, the crystal temperature would quickly equilibrate. The temperature-dependent changes of the focus inside of the crystal results in a different cavity mode when the cavity is locked or unlocked. Coupling into the cavity had to be optimized by iteratively moving the lenses while the cavity was locked, maximizing the measured harmonic generated light.

Typical optimal cavity performances for both LBO cavities are summarized in Table (4.4). With the 2 W fibre laser we obtained an overall conversion efficiency of  $24.2 \frac{\%}{W}$  and with the 1 W fibre laser we obtained an overall conversion efficiency of  $26.4 \frac{\%}{W}$ . In both cases, we obtained a single-pass conversion efficiency  $\approx 1 \cdot 10^{-4} \frac{1}{W}$ . The single-pass conversion efficiency is approximately 65% of the expected conversion efficiency of  $1.6 \cdot 10^{-4} \frac{1}{W}$  (see Section(4.2.2)).

A possible cause for the reduction in conversion efficiency is thermal lensing

[84], [85], [86]. A tight focus within the crystal results in localized heating (since the circulating power is high) and so the index of refraction is no longer constant throughout the crystal. This can result in defocusing within the crystal and subsequently, less frequency-doubled light would be generated since focusing within the crystal is no longer optimal. One solution is to intentionally form a tighter focus within the crystal (so that defocused beamsizes are optimal). The difficulty with this solution is that the “hot” cavity mode (when the cavity is locked) is different from the “cold” cavity mode (when the cavity length is scanned) and so optimization of the cavity must be done when it is hot. If the hot cavity mode is much different from the cold cavity mode, then coupling into the cold cavity may not be sufficient to obtain a suitable error signal to lock the cavity – this would result in having to re-optimize the cavity every time it went out of lock.

A similar doubling scheme was implemented by Friedenauer *et al.* [38] at approximately the same time as we were building our laser system. They also had a Koheras fibre laser that they frequency doubled for detection and laser cooling of  $Mg^+$ . They also chose to use two separate doubling stages, the first with temperature-tuned LBO to frequency-double from the IR to the visible, and the second with angle-tuned BBO to frequency-double from the visible to the UV. For their LBO cavity they obtained a conversion efficiency of  $29.3 \frac{\%}{W}$ , which is approximately 10% better than our cavity. They used an 18 mm

long crystal, and since  $P_{2\omega} \propto l$  (see Section (4.2.3)), one would expect their conversion efficiency to be  $2.5\times$  higher than ours (since our crystal is 7 mm long); in this sense, our LBO cavity out-performed their LBO cavity. The discrepancy may be due to absorption dominating at longer crystal lengths so that the linear relationship is no longer valid. One advantage of using a longer crystal however, is that the optimal waist inside of a longer crystal is larger than the optimal waist inside of a shorter crystal – this leads to a reduction of thermal lensing. In fact, Friedenauer *et al.* did not observe thermal lensing in their cavities [38]. This might not be a cost-effective solution since it does not appear to result in a significant increase in harmonic-generated light and since we found we were able to optimize with the cavity hot, obtaining a conversion efficiency that was within 10% of theirs (for a much shorter crystal).

## 4.5 BBO Performance

The BBO cavities were used to frequency-double the green output from the LBO cavity. Thermal lensing inside of the LBO cavity results in a slightly astigmatic beam since the index of refraction is not uniform throughout the crystal. To correct for this, the collimating lens at the output of the LBO cavity was tilted slightly to achieve a circular beam as monitored at multiple points far downstream of the collimating lens.

Rough alignment into the cavities was much easier to do in the BBO cavities

than in the LBO cavities since the light was visible. Using an index card, the light could be traced around the interior of the cavity and roughly aligned in the central region of all four mirrors. By using the output coupler and the input coupler, the beam was overlapped with itself and then the mode was optimized by monitoring the reflected signal from the input coupler with a photodiode and an oscilloscope. As with the LBO cavity, the cavity length was scanned by applying a sawtooth voltage signal to the piezo-mounted mirror, and the dip in the reflected signal corresponding to the  $TEM_{00}$  mode was minimized.

Mode matching into the BBO cavity was done using a pair of lenses after the collimating lens. The position of the first lens was fixed while the second lens was placed on a magnetic base to allow for fine adjustment of the waist size.

An angle-tuned BBO crystal was used for harmonic generation. Since BBO crystals are mildly hygroscopic, a desiccant was placed inside of the cavity enclosure to extend the crystal lifetime. Angle tuning results in walk-off, discussed earlier, and so the highly astigmatic output was collimated using a cylindrical lens, with a focal length of  $f = 10 \text{ cm}$ . Table (4.5) summarizes typical cavity performance.

The single-pass conversion efficiencies (up to  $3.43 \cdot 10^{-5} \frac{1}{W}$ ) for both cavities were significantly less than the expected conversion efficiency ( $1.6 \cdot 10^{-4} \frac{1}{W}$ ). Furthermore, the conversion efficiencies between the two cavities were not

consistent. The Cyclor BBO cavity conversion efficiency was  $2.5\times$  larger than the Probe BBO cavity. We believe that this is primarily due to crystal quality. In particular, we had noticed that by translating the crystal perpendicular to the beam, we could locate a better spot in the crystal.

It is also possible that the crystal quality degraded over time, due to hygroscopic effects. Although we did place desiccant near the crystal, the enclosure was not air-tight and so it is possible that crystal degradation over time reduced the conversion efficiency. In fact, it was observed in the Probe BBO cavity that the amount of frequency-doubled light did reduce over time. A similar observation was made in the Cyclor BBO cavity. Alternatively, we could have also housed the crystal in an oven (similar to the LBO crystal), and kept the crystal at constant temperature to prevent the absorption of moisture. Friedenauer *et al.* also used an angle-tuned BBO crystal for their second doubling stage [38]. In their design, they chose to use a 10 mm long crystal, and obtained an overall conversion efficiency of  $30 \frac{\%}{W}$ . Again, their crystal was longer (by a factor of  $1.4\times$ ) and so to compare the two conversion efficiencies, we scale theirs down to  $21 \frac{\%}{W}$ . Thus, they obtained a conversion efficiency that was  $6.2\times$  better than our Repumper BBO cavity and  $2.1\times$  better than our Cyclor BBO cavity. They chose to house their BBO crystal inside of an oven that was heated to  $50^\circ C$ , to minimize hygroscopic effects. When we originally purchased the crystals, we opted to not heat the crystals since BBO

is listed as being mildly hygroscopic. In the future, we might chose to place the crystals inside of an oven, especially since the summers can be particularly humid.

We conclude by reiterating that at the time our cavities were built there were no commercially available sources of UV light at the wavelengths we required for our experiment. As a solution, we built one of the first fibre-based UV lasers. At the same time, Friedenauer *et al.* [38] had also built their own fibre-based laser to address magnesium ions. While our overall efficiency (from the IR to the UV) was lower than theirs, our LBO doubling stage outperformed theirs on a per-crystal-length basis.

As mentioned previously, it is possible to build a dye-laser based UV source and in fact we did frequency double our dye laser for photoionization. The advantages of a fibre based system are stability (both power and frequency), a narrow linewidth, and ease of use. More recently, Toptica Inc. has produced a diode-based laser system operating at 280 *nm*. Their system consists of a grating-stabilized diode laser followed by a semiconductor amplifier. The output from the diode laser is first amplified and then sent through two doubling stages. Their specified output at 280 *nm* is up to 100 *mW*. For their doubling stages, they also use a four mirror ring cavity although their resonator is manufactured from a solid metal block which provides better stability against vibrations and acoustic noise.

Table 4.4: LBO Cavities: Typical Optimized Performance

	Probe LBO Cavity	Cyclor LBO Cavity
Total Input Power (W)	1.33	1.60
ASE (W)	0.386	0.166
Input Coupling (%)	85 – 90	85 – 90
Harmonic Output (mW)	170	360
Single-Pass Conversion ( $W^{-1}$ )	$1.06 \times 10^{-4}$	$0.97 \times 10^{-4}$
Overall Conversion ( $W^{-1}$ )	0.264	0.242

Table 4.5: BBO Cavities: Typical Optimized Performance

	Probe BBO Cavity	Cyclor BBO Cavity
Total Input Power (mW)	170	360
Input Coupling (%)	90 – 95	90 – 95
Harmonic Output (mW)	0.8	9
Single-Pass Conversion ( $W^{-1}$ )	$1.36 \times 10^{-5}$	$3.43 \times 10^{-5}$
Overall Conversion ( $W^{-1}$ )	0.0342	0.0857



# Chapter 5

## Spectroscopy of $^{25}\text{Mg}^+$

### 5.1 Overview

The energy-level structure of an atom results from the interaction between the electron and an internal or external field. In the case of hydrogen, the structure is exactly solvable [39]; however, calculations of the energy structure for complex atoms are challenging because of the interactions between the electrons of many-electron systems.

In Section (2.1) we discussed the difficulties inherent in calculating the energy structure resulting from electron correlation. Recall that, in order to solve the Schrödinger equation, we need to appeal to approximation methods such as the Configuration Interaction method and the Coupled Cluster Theory method. In particular, the Coupled Cluster Theory method is considered one

of the foremost accurate theoretical models, although even it is still only an approximation. By measuring spectroscopic quantities such as the hyperfine  $a$  constant (see Section (5.2)), we provide experimental values that theorists can use as benchmarks to compare against *ab initio* calculations of hyperfine constants.

Previously, we considered the gross structure of an atom and treated the nucleus as a charged point source [39] [87] [88]. Successive interactions of smaller magnitude can be treated as perturbations which shift the energy levels. Here, we will consider the magnetic dipole interaction and the electric quadrupole interaction in order to provide a theoretical background for the measurement of the hyperfine  $a$  constant in Chapter 6.

The magnetic dipole interaction is between the nuclear magnetic moment and a magnetic field. The magnetic field arising from the orbiting electrons results in hyperfine structure, and an external field results in further Zeeman splitting of the levels. The case of zero external field will be considered first and then we will consider how external fields further shift the energy levels.

The next-highest-order perturbation is the electric quadrupole interaction, resulting from the electrostatic interaction between orbiting electrons and the nucleus when the nucleus is no longer treated as a point source. We will include the effects of the electric quadrupole interaction in the discussion for completeness. However, in the case of  $J = \frac{1}{2}$  this interaction vanishes [39] and

so the  $^2P_{\frac{1}{2}}$  level, whose hyperfine splitting was measured, experiences no shift due to the quadrupole interaction.

Ideally, we would like to measure the energy separation between the excited state hyperfine manifolds by driving transitions with the Probe laser from the ground state to specific states within the hyperfine manifolds, since this directly gives us the hyperfine  $a$  constant. Unfortunately, the situation is more complicated. Zeeman splitting of the  $m_F$  sublevels (see Section (5.3)) adds nearly degenerate levels that can be also driven by the Probe laser and so we need to consider population dynamics (Section (5.6)) in order to quantify this effect on the linewidth and hyperfine  $a$  constant measurements.

## 5.2 Interaction of the Nucleus with Atomic Fields

An atom with nonzero nuclear spin  $I$  has a magnetic moment that interacts with the magnetic field generated by the angular momentum of the orbiting electrons and with any external magnetic fields. As pointed out above, this gives rise to hyperfine structure. The total angular momentum is the sum of the electronic angular momentum and the nuclear spin:

$$\vec{F} = \vec{J} + \vec{I} \quad (5.1)$$

and the allowed values are  $\{I + J, I + J - 1, I + J - 2, \dots, |I - J|\}$ . The Hamiltonian describing the magnetic dipole interaction is given by [88]:

$$\mathcal{H} = -\vec{\mu}_I \cdot (\vec{B}_J + \vec{B}_0) \quad (5.2)$$

where  $\vec{\mu}_I$  is the nuclear magnetic moment,  $\vec{B}_J$  is the magnetic field due to the electrons, and  $\vec{B}_0$  is the external magnetic field. We can also re-express the nuclear magnetic moment in terms of the nuclear spin. Explicitly, we have [88]:

$$\vec{\mu}_I = \frac{\mu_I}{I} \vec{I} \quad (5.3)$$

$$= \gamma_I \hbar \vec{I} \quad (5.4)$$

$$= g_I \mu_N \vec{I} \quad (5.5)$$

where  $\gamma_I$  and  $g_I$  are gyromagnetic ratio and nuclear  $g$ -factor and are analogous to their electronic counterparts [88]. In the absence of an applied magnetic field the second term in the Hamiltonian (Equation (5.2)) vanishes leaving only the field due to the electronic structure. The field due to the electronic structure results in hyperfine splitting.

By rewriting Equation (5.2) in terms of the electronic angular momentum,  $\vec{J}$ , and assuming no external field we obtain an equation for the Hamiltonian

of the form [88]:

$$\mathcal{H} = -\frac{\mu_I B_J}{I J} \vec{I} \cdot \vec{J} \quad (5.6)$$

$$= ha \vec{I} \cdot \vec{J} \quad (5.7)$$

where  $ha = -\frac{\mu_I B_J}{I J}$ . The hyperfine  $A$  constant is defined as [88]:

$$A = ha \quad (5.8)$$

although it is often quoted in frequency units. We will more accurately quote the  $a$  constant. The important point is that the hyperfine  $a$  constant is proportional to the magnetic field produced by the orbiting electrons, and is proportional to  $\langle \frac{1}{r_i^3} \rangle$  where  $r_i$  is the distance of the  $i^{\text{th}}$  electron from the nucleus. The radial wavefunctions for the hydrogen atom are exactly solvable; however, the radial wavefunctions for complex atoms are not. By measuring the hyperfine  $a$  constant, we provide a benchmark value that can be used to compare different theoretical approaches to solving the radial wavefunctions.

The Hamiltonian of Equation (5.7) is now diagonal in the  $(F, m_F)$  basis. This becomes more apparent when we evaluate the product of the total angular momentum with itself:

$$\langle \vec{F} \cdot \vec{F} \rangle = \vec{I}^2 + \vec{J}^2 + 2\vec{I} \cdot \vec{J}. \quad (5.9)$$

By isolating  $\vec{I} \cdot \vec{J}$  from Equation (5.9) and substituting it into equation (5.7) we obtain:

$$\mathcal{H} = \frac{A}{2}[\vec{F}^2 - \vec{J}^2 - \vec{I}^2]. \quad (5.10)$$

In calculating the energy eigenvalues we need only note that the angular momentum vectors are actually operators and we obtain [88]:

$$E = \frac{A}{2}[F(F+1) - I(I+1) - J(J+1)]. \quad (5.11)$$

Physically, the orbital electrons generate a magnetic field with which the nucleus interacts analogous to the way the electronic spin interacts with the orbital angular momentum. In the latter case, the result is fine structure splitting, whereas in the former case, the interaction results in hyperfine splitting.

Thus far we have ignored the effect of an external magnetic field. The interaction between the nuclear magnetic moment and an externally applied magnetic field lifts the degeneracy of the  $m_F$  sublevels. In the following section Equation (5.2) will be revisited assuming a non-zero external field.

### 5.3 Atoms in External Fields

If we now include the effect of an external magnetic field we need add to our Hamiltonian terms involving both the nuclear magnetic moment and the electronic magnetic moment. The Hamiltonian is now [88]:

$$\mathcal{H} = A\vec{I} \cdot \vec{J} - \vec{\mu}_I \cdot \vec{B}_0 - \vec{\mu}_J \cdot \vec{B}_0 \quad (5.12)$$

$$= A\vec{I} \cdot \vec{J} - \frac{\mu_I}{I} \vec{I} \cdot \vec{B}_0 - \frac{\mu_J}{J} \vec{J} \cdot \vec{B}_0 \quad (5.13)$$

$$= A\vec{I} \cdot \vec{J} - g_I \mu_N \vec{I} \cdot \vec{B}_0 - g_J \mu_B \vec{J} \cdot \vec{B}_0 \quad (5.14)$$

where  $g_J$  is the electronic  $g$ -factor,  $\mu_J$  is the electronic magnetic moment and  $B_0$  is an externally applied magnetic field. In the last line we have expressed the Hamiltonian in terms of the nuclear and electronic  $g$ -factors and the nuclear and Bohr magnetons.

The Hamiltonian of Equation (5.14) is not diagonal in any *single* angular-momentum basis for *all* nonzero magnetic fields. Since no particular choice of common basis simplifies the calculation, we proceed by choosing an arbitrary basis and solving the equation. This was done by Laura Topozini in her Master's thesis [89]. In the following sections we will look at how the energy is shifted in different limits, where a *single* angular-momentum basis *does* simplify the calculation.

In the weak-field limit the Zeeman effect is observed. The external magnetic field is small relative to the internal magnetic field,  $B_J$  and so the  $\vec{I} \cdot \vec{J}$  term dominates. In this case it is more sensible to work in the  $(F, m_F)$  basis, whereas in the strong field limit the  $\vec{J} \cdot \vec{B}_0$  and the  $\vec{I} \cdot \vec{B}_0$  terms dominate and the  $(m_I, m_J)$

basis becomes the preferred basis. This gives us the Paschen-Bach regime. The intermediate regime becomes more complicated, but is easily calculable using a computer.

### 5.3.1 Weak-Field Limit

Before discussing the weak-field limit it is helpful to estimate the magnitude of the electronic magnetic field. For a hydrogenic atom the order of magnitude of the field can be estimated by [39]:

$$B_{el} \approx \frac{\mu_0}{4\pi} \frac{Z\mu_B}{\left(\frac{a_0}{Z}\right)^3} \quad (5.15)$$

where  $B_{el}$  is the field at the nucleus due to the orbiting electrons,  $\mu_0$  is the permeability of free space,  $Z$  is the atomic number,  $\mu_B$  is the Bohr magneton, and  $a_0$  is the Bohr radius. We may also write the field at the orbiting electrons due to the nucleus as:

$$B_{nuc} \approx \frac{\mu_0}{4\pi} \frac{Z\mu_N}{\left(\frac{a_0}{Z}\right)^3}. \quad (5.16)$$

Here,  $\mu_N$  is the nuclear magnetic moment. Thus, the electronic dipole magnetic field at the nucleus is on the order of  $10^5$  T. Since  $\mu_B = 1836\mu_N$ , due to the mass difference between a proton and an electron, the nuclear dipole magnetic field at the orbiting electrons is  $\frac{B_{el}}{1836} \approx 55$  T.

The hyperfine splitting results from a dipole-dipole interaction between the

nuclear and the electronic magnetic moment. In writing the interaction energy (ie.  $\vec{\mu} \cdot \vec{B}$ ) we note that the interaction energy for the hyperfine splitting can be equivalently be written as  $\mu_N B_{el}$  or  $\mu_B B_{nuc}$ . The difference in magnetic moments is cancelled out by the difference in field strengths; however, the nuclear and electronic magnetic moment also interact with any externally applied magnetic field. For all of the experiments discussed in this thesis, the externally applied field was kept below below  $0.6 \text{ mT}$  ( $6 \text{ G}$ ). Thus, the experiments discussed in this thesis were all performed in the weak-field limit.

Of course, the actual calculation of  $B_{el}$  is not as straight forward as Equation (5.16) since it actually involves calculations of  $\langle \frac{1}{r_i^3} \rangle$  for the particular multi-electron atom in question [39] and so equation (5.16) serves as an order of magnitude estimate.

If the external field is sufficiently weak then we know that  $\vec{I}$  and  $\vec{J}$  are strongly coupled to one another. The total angular momentum is given by  $\vec{F} = \vec{I} + \vec{J}$  and so in a vector-model picture, as shown in Figure (5.1), the projection of  $\vec{F}$  onto  $\vec{B}_0$  is well-defined whereas  $\vec{I}$  and  $\vec{J}$  precess about  $\vec{F}$ . This implies that one should work in the  $(F, m_F)$  basis.

Rewriting Equation (5.14) we have [88]:

$$\mathcal{H} = A\vec{I} \cdot \vec{J} - g_I \mu_N \frac{(\vec{I} \cdot \vec{F})(\vec{F} \cdot \vec{B}_0)}{\vec{F}^2} - g_J \mu_B \frac{(\vec{J} \cdot \vec{F})(\vec{F} \cdot \vec{B}_0)}{\vec{F}^2} \quad (5.17)$$

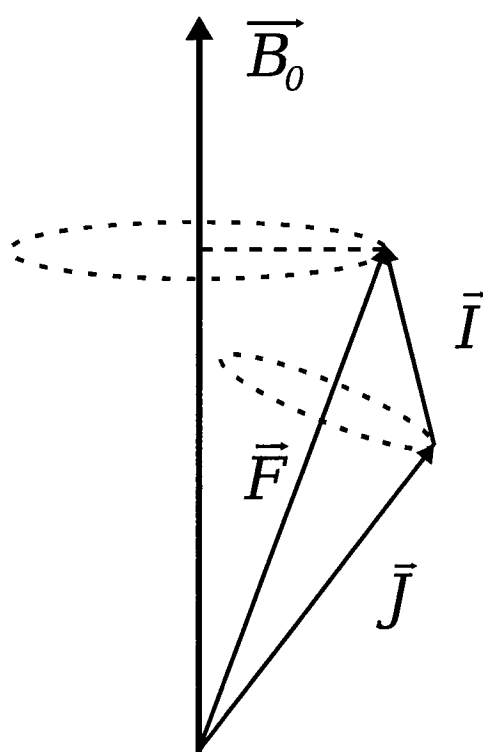


Figure 5.1: In the vector-model picture, the projection of  $\vec{F}$  onto  $\vec{B}_0$  is well-defined whereas  $\vec{I}$  and  $\vec{J}$  precess about  $\vec{F}$  (for a weak external field).

And from the total angular momentum  $\vec{F} = \vec{I} + \vec{J}$  we have that:

$$\vec{J} \cdot \vec{F} = \frac{1}{2}[\vec{F}^2 + \vec{J}^2 - \vec{I}^2] \quad (5.18)$$

$$\vec{I} \cdot \vec{F} = \frac{1}{2}[\vec{F}^2 + \vec{I}^2 - \vec{J}^2] \quad (5.19)$$

By substituting Equation (5.19) into Equation (5.17) and noting that the angular momentum vectors are operators we obtain the shift in energy [88]:

$$\Delta E = \frac{A}{2}[F(F+1) - I(I+1) - J(J+1)] - g_F \mu_B m_F B_0 \quad (5.20)$$

where the allowed values of  $m_F$  are  $\{-F, -F+1, \dots, F-1, F\}$  and similarly for  $I$  and  $J$ . We have defined:

$$g_F = g_J \frac{F(F+1) + J(J+1) - I(I+1)}{2F(F+1)} + g_I \frac{\mu_N}{\mu_B} \frac{F(F+1) + I(I+1) - J(J+1)}{2F(F+1)} \quad (5.21)$$

For zero applied magnetic field the different Zeeman sublevels, denoted by  $m_F$ , are degenerate. For small applied magnetic fields, the splitting grows linearly with field.

### 5.3.2 Intermediate Field

In the intermediate field, Equation (5.14) must be solved exactly to determine the shift in energy for arbitrary magnetic field. A specific case of this calcula-

tion relevant to the measurement of the hyperfine  $a$  constant of the  $^2P_{\frac{1}{2}}$  is the case where  $J = \frac{1}{2}$ . An analytic form of the energy splitting can be obtained in this case and is valid at any externally applied magnetic field [88].

If we take the externally applied magnetic to be along the z-axis then equation (5.14) becomes [88]:

$$\mathcal{H} = A(I_x J_x + I_y J_y + I_z J_z) - g_I \mu_N I_z B_0 - g_J \mu_B J_z B_0. \quad (5.22)$$

As before, in a quantum mechanical formulation the angular momentum vectors are actually vector operators. To evaluate the operators we make the following definitions valid for a general angular momentum operator  $S = S_x + S_y + S_z$ :

$$S_+ = S_x + iS_y \quad (5.23)$$

$$S_- = S_x - iS_y \quad (5.24)$$

$$S_x = \frac{S_+ + S_-}{2} \quad (5.25)$$

$$S_y = \frac{S_+ - S_-}{2i} \quad (5.26)$$

By substituting Equations (5.25) and (5.26) into Equation (5.22) we obtain:

$$H = AI_z J_z + \frac{A}{2}(I_+ J_- + I_- J_+) - g_I \mu_N I_z B_0 - g_J \mu_B J_z B_0. \quad (5.27)$$

The matrix elements of the Hamiltonian in equation (5.27) are straightforward to evaluate.

The form of the Hamiltonian implies a choice of  $(m_I, m_J)$  basis states. In the  $(m_I, m_J)$  basis there are a total of  $2J + 1$  possible  $m_J$  states and  $2I + 1$  possible  $m_I$  states, giving a total of  $2(J + I + 1)$  possible combinations of  $(m_I, m_J)$ . The dimension of the matrix is  $(2(J + I + 1))^2$ . We can instead choose to work in the  $(F, m_F)$  basis, but this choice makes the calculation of the energy eigenvalues more tedious.

If we specifically look at  $J = \frac{1}{2}$  we obtain an interaction Hamiltonian matrix consisting of  $2 \times 2$  matrices. Each submatrix can be solved to obtain a general expression for the shift in energy [88]:

$$\Delta E = \frac{A}{4} - g_I \mu_N m_F B_0 \pm \frac{A}{2} (2I + 1) \sqrt{1 + \frac{4m_F}{2I + 1} x + x^2} \quad (5.28)$$

$$x = \frac{(g_I \mu_N - g_J \mu_B) B_0}{A(2I + 1)} \quad (5.29)$$

where  $+$  is used for  $F = I + \frac{1}{2}$  and  $-$  is used for  $F = I - \frac{1}{2}$ . When there is no externally applied magnetic field we obtain the hyperfine splitting in the absence of Zeeman effects.

### 5.3.3 Strong Field Limit

In the strong field limit  $\vec{I}$  and  $\vec{J}$  are no longer strongly coupled. For a sufficiently intense external magnetic field  $\vec{I}$  and  $\vec{J}$  strongly couple to the external

field and so the latter two terms in equation (5.14) are dominant. In a vector picture model of figure (5.2)  $\vec{I}$  and  $\vec{J}$  rapidly precess about  $B_0$  with their projections onto the magnetic field being well-defined. In this case the preferred basis is the  $(m_I, m_J)$  basis.

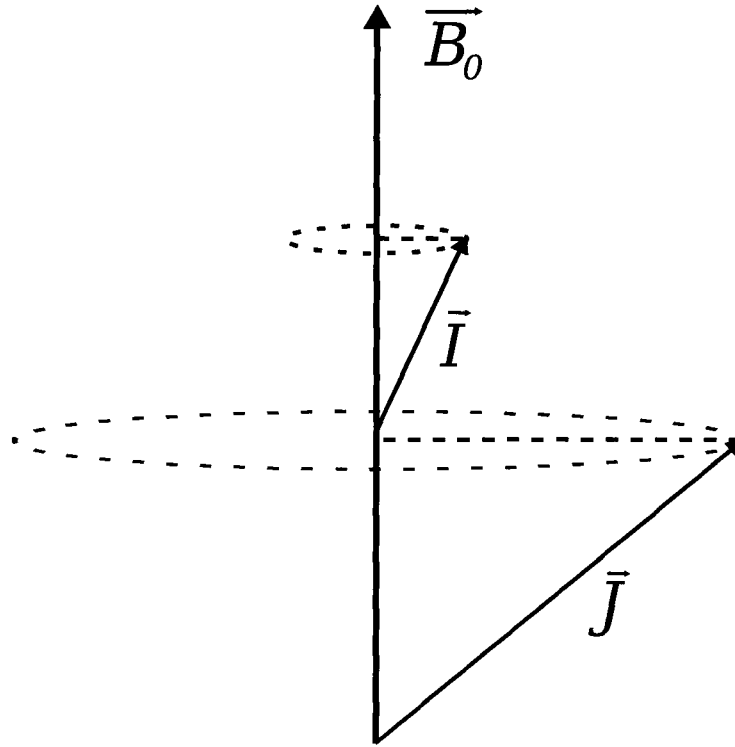


Figure 5.2: In the presence of a strong external field,  $H_0$ , angular momenta  $\vec{I}$ ,  $\vec{J}$  strongly couple to the external field.

In this limit the energy is given by:

$$E = \hbar a m_I m_J - (\mu_B g_B m_J + \mu_N g_I m_I) H_0 \quad (5.30)$$

where  $m_I$  has allowed values of  $\{-I, -I + 1, \dots, I - 1, I\}$  and similarly  $m_J$  ranges from  $\{-J, -J + 1, \dots, J - 1, J\}$ .

## 5.4 Electric Quadrupole Interaction

The next-highest-order perturbation to the energy level of an atom is the electric quadrupole interaction. Until now we have been treating the nucleus of the atom as a point charge. By ignoring its spatial extent we have implicitly taken a multipole expansion of the general expression for the electrostatic energy and ignored higher-order effects. Explicitly we have [39] [87]:

$$\frac{-e^2}{4\pi\epsilon_0|\vec{r}_e - \vec{r}_n|} = \frac{-e^2}{4\pi\epsilon_0} \sum_k \frac{r_n^k}{r_e^{k+1}} P_k(\cos\theta) \quad (5.31)$$

where the subscripts  $\vec{r}_e$ ,  $\vec{r}_n$  are electronic and nuclear coordinates respectively,  $\epsilon_0$  is the vacuum permittivity and  $P_k$  are Legendre polynomials of order  $k$ . The angle  $\theta$  corresponds to the angle between  $\vec{r}_e$  and  $\vec{r}_n$ .

The  $0^{th}$ -order term of the series in equation (5.31) is the electrostatic potential for an electron a distance  $r_e$  away from a point charge. The  $1^{st}$ -order term is zero since the nuclear electric dipole moment is zero [39] [87]. The next non-zero term is the quadrupole moment.

Equation (5.31) involves a single proton and a single electron: to calculate the complete quadrupole interaction a sum over all protons and electrons needs to be done. In terms of angular momentum operators, the Hamiltonian for the

quadrupole interaction is given by [39]:

$$\mathcal{H} = B \frac{3(\vec{I} \cdot \vec{J})^2 + \frac{3}{2}\vec{I} \cdot \vec{J} - I(I+1)J(J+1)}{2I(2I-1)J(2J-1)} \quad (5.32)$$

$$B = eQ \left\langle \frac{\partial^2 V_e}{\partial z^2} \right\rangle \quad (5.33)$$

where the Hyperfine  $B$  constant is a product of the nuclear quadrupole moment,  $Q$ , and the average gradient of the electric field produced by the electrons at the nucleus,  $\left\langle \frac{\partial^2 V_e}{\partial z^2} \right\rangle$ .

Since the quadrupole interaction is proportional to the average gradient of the electric field, it is zero for a spherically symmetrical electron distribution ( $I, J \geq 1$ ), and so the  ${}^2S_{\frac{1}{2}}$  and  ${}^2P_{\frac{1}{2}}$  both have no quadrupole interaction since they both have a spherically symmetric electron distribution [90]. The shift in energy due to this interaction is given by [39] [87]:

$$E = \frac{B \frac{3}{2}K(K+1) - 2I(I+1)J(J+1)}{4 I(2I-1)J(2J-1)} \quad (5.34)$$

$$K = F(F+1) - J(J+1) - I(I+1) \quad (5.35)$$

## 5.5 Detailed Atomic Structure of ${}^{25}\text{Mg}^+$

The nuclear spin of  ${}^{25}\text{Mg}^+$  is  $I = \frac{5}{2}$  and so its energy levels are separated by hyperfine splitting. The possible values of  $m_I$  are  $m_I = \{-\frac{5}{2}, -\frac{3}{2}, -\frac{1}{2}, \frac{1}{2}, \frac{3}{2}, \frac{5}{2}\}$ .

The energy levels relevant to the experiment are the  ${}^2S_{\frac{1}{2}}$ ,  ${}^2P_{\frac{1}{2}}$ , and  ${}^2P_{\frac{3}{2}}$  lev-

els. Both the  ${}^2S_{\frac{1}{2}}$  and  ${}^2P_{\frac{1}{2}}$  levels lack any further splitting due to the electric quadrupole interaction. The  ${}^2P_{\frac{3}{2}}$  level is more complicated since the quadrupole moment is nonzero. A discussion of the  ${}^2P_{\frac{3}{2}}$  is required since we use this state for detection (however, only a rough estimation of the splitting is needed).

Since all of the measurements done in the laboratory were in the low-field limit we can approximate the shift in the energy levels using equation (5.20). In this limit we can label the sublevels by their  $(F, m_F)$  values. Figure 5.3 shows all three levels. In the case where  $J = \frac{1}{2}$ , the total angular momentum has allowed values  $F = \{2, 3\}$ . When  $J = \frac{3}{2}$  the total angular momentum can be  $F = \{1, 2, 3, 4\}$ . In all cases  $m_F = \{-F, -F + 1, \dots, F - 1, F\}$ .

The hyperfine  $a$  constant for the  ${}^2P_{\frac{1}{2}}$  level was determined by measuring the difference in transition energies of the  ${}^2S_{\frac{1}{2}}|F = 3, m_F = -3\rangle \rightarrow {}^2P_{\frac{1}{2}}|F' = 3, m_{F'} = -2\rangle$  and  ${}^2S_{\frac{1}{2}}|F = 3, m_F = -3\rangle \rightarrow {}^2P_{\frac{1}{2}}|F' = 2, m_{F'} = -2\rangle$  transitions at varying magnetic fields and extrapolating to zero-field.

To drive these transitions, we first optically pumped the ion into the  $(3, \pm 3)$  state using the Cyclor and Repumper beams with  $\sigma^{+/-}$ -polarized light. This was followed by a pulse from the Probe laser (using  $\sigma^{-/+}$ -polarized light) which was tuned through each transition separately. The final state of the ion was detected using the electron shelving technique discussed in Sections (2.1), (3.6), and (6.1.5). If the ion was in the  $(3, \pm 3)$  state we would detect many

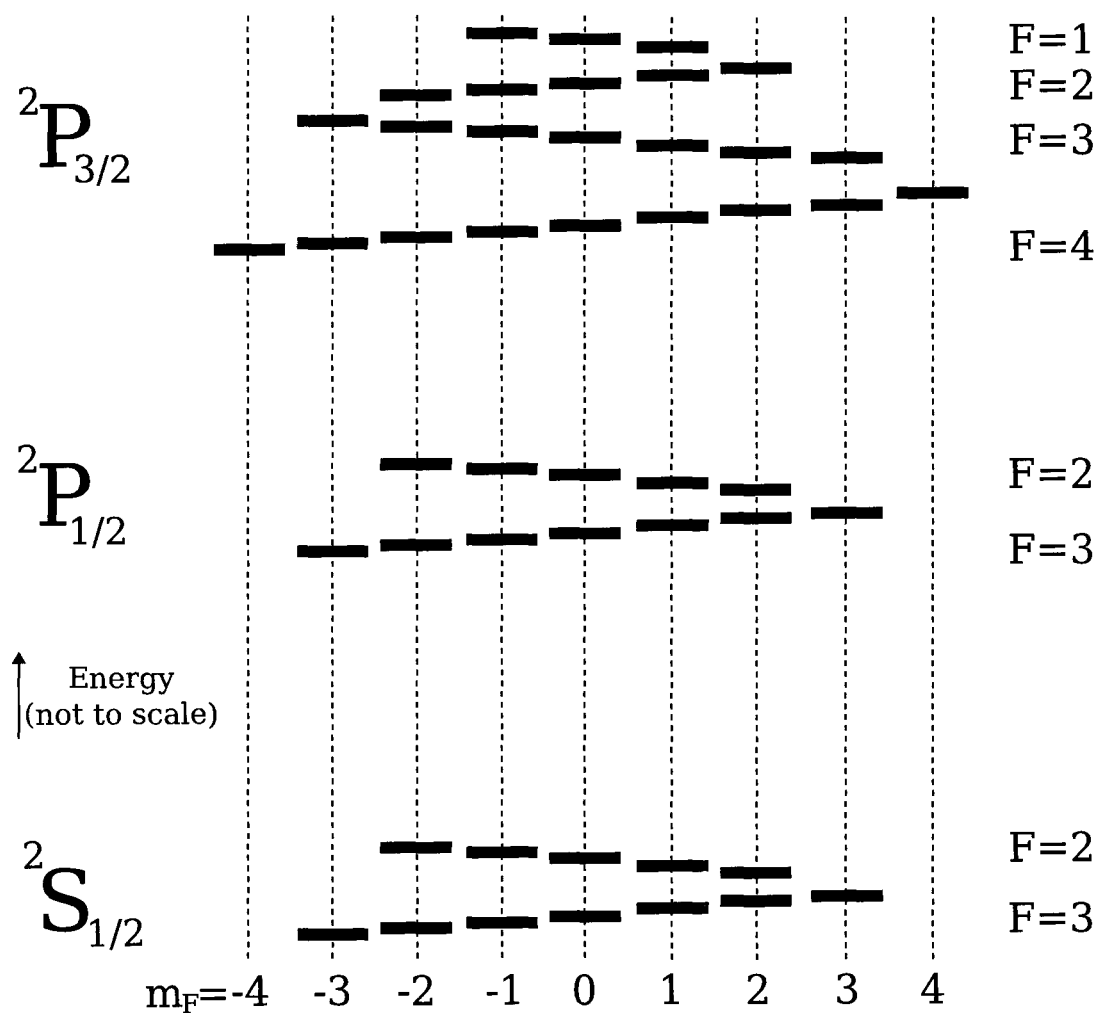


Figure 5.3:  $^{25}\text{Mg}^+$  energy-level diagram. The relevant energy levels to the experiment are the  $^2S_{1/2}$ , the  $^2P_{1/2}$ , and the  $^2P_{3/2}$  levels. The hyperfine splitting and the Zeeman sublevels have been included in the figure.

photons when driving the cycling transition, and if the ion was in the  $F = 2$  manifold, we would see a reduced number of detected photons.

Ideally, if the ion was driven by the Probe laser from the  $(3, \pm 3)$  state into the excited state, it would only decay into the  $F = 2$  manifold. In actuality, the ion can decay from the excited state into one of the other Zeeman sublevels in the  $F = 3$  manifold and subsequently be driven back into the excited state, broadening the line and pulling line centre (due to the different Zeeman shifts). The effect of population dynamics on the spectroscopic measurements will be discussed in the following section. However, in the data analysis, we used techniques that mitigated the effects of line pulling, as discussed in Section (6.2).

## 5.6 Population Dynamics in $^{25}\text{Mg}^+$

For the  $^2P_{\frac{1}{2}}$  state, the only allowed values of the total angular momentum are  $F = 2$  and  $F = 3$ . In the laboratory the transition between hyperfine manifolds of the excited state was not measured directly. Instead, the transition energies from the ground state,  $^2S_{\frac{1}{2}}(F = 3)$  to the excited states,  $^2P_{\frac{1}{2}}(F = 2)$  and  $^2P_{\frac{1}{2}}(F = 3)$ , were measured separately, and the  $^2P_{\frac{1}{2}}$  hyperfine separation was determined from that information.

The addition of an externally applied field complicates matters since it lifts the degeneracy between different Zeeman sublevels; however, the background

magnetic fields at the ion are unknown and the addition of a varying externally applied field allows us to extrapolate to the field-free line centre. A simplified energy diagram, including only the  $^2S_{1/2}$  and  $^2P_{1/2}$  levels, is shown in Figure (5.4).

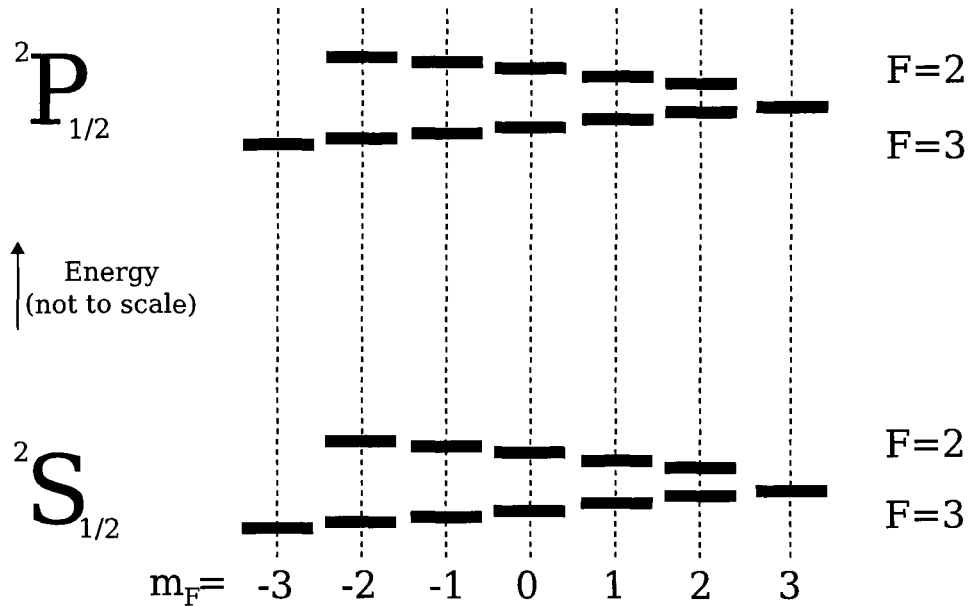


Figure 5.4:  $^{25}\text{Mg}^+$  simplified energy-levels diagram. An energy level diagram showing the  $^2S_{1/2}$  level, and the  $^2P_{1/2}$  level. The Probe laser is tuned to drive the  $(3, -3) \rightarrow (3, -2)$  transition or the  $(3, -3) \rightarrow (2, -2)$  transition although inadvertent population of the other ground state Zeeman sublevels can occur by driving to the excited state by the Probe laser.

To simplify the discussion we will only consider transitions driven from the ground to the excited state that add a unit of angular momentum ( $\sigma^+$  – polarized) but we will consider all the possible decay channels from the excited state. We will also use the convention where excited-state quantum numbers are primed.

An ion starting in the  $(3, -3)$  state can be driven to either the  $(3', -2')$  state or the  $(2', -2')$  state with  $\sigma^+$ -polarized light. We will only describe driving to the  $(3', -2')$  state since the physics involved in the two processes are qualitatively similar.

From the  $(3', -2')$  state the ion can decay into either  $(3, -3)$ ,  $(3, -2)$ ,  $(3, -1)$ ,  $(2, -2)$ , or  $(2, -1)$ . If the ion ends up in the  $F = 2$  manifold then it can no longer be driven by the Probe laser since the  $F = 3$  and  $F = 2$  manifolds are well-separated ( $1.79 \text{ GHz}, \Gamma = 2\pi \cdot 42 \text{ MHz}$ ). An ion that decays back into the  $F = 3$  manifold can continue to be driven by the Probe laser.

If the ion decays back into the  $(3, -3)$  state then nothing has changed. If instead it falls into the  $(3, -2)$  state, it can be driven into the  $(3', -1')$  state and subsequently decay into one of the six possible ground states:  $(3, -2)$ ,  $(3, -1)$ ,  $(3, 0)$ ,  $(2, -2)$ ,  $(2, -1)$ , or  $(2, 0)$ . This process will continue until the ion is either in a dark state ( $F = 2$ ), or has pumped over to the  $(3, 3)$  state, which cannot be driven by the Probe laser. Each transition going from  $(3, m_F) \rightarrow (3', (m_F + 1)')$  is centered at a different frequency because of differences in the g-factors for the ground and excited states. A similar process occurs when we drive to the  $(2', -2)$  state from the  $(3, -3)$  state except with different probabilities for decaying from the excited state due to the different Clebsch-Gordan coefficients. Additionally, neither the  $(3, 2)$  state nor the  $(3, 3)$  state can be driven into the  $2'$  excited state with  $\sigma^+$ -polarized light.

A rate-equation approach, neglecting coherence effects, was used to model the population dynamics of the multi-level system. This approach is valid under the assumption that the Probe laser power is not saturating the ion, which is true for the experiments described in this thesis (see Section (6.1.3)). The excited state was eliminated by calculating the probability of driving transitions from one Zeeman sublevel to another, connected by a rapidly decaying excited state. This results in a system of linear differential equations given by:

$$\dot{p}_{(3,-3)} = -a_1 p_{(3,-3)} \quad (5.36)$$

$$\dot{p}_{(3,-2)} = -a_2 p_{(3,-2)} + b_1 p_{(3,-3)} \quad (5.37)$$

$$\dot{p}_{(3,-1)} = -a_3 p_{(3,-1)} + b_2 p_{(3,-3)} + c_1 p_{(3,-2)} \quad (5.38)$$

$$\dot{p}_{(3,0)} = -a_4 p_{(3,0)} + c_2 p_{(3,-2)} + d_1 p_{(3,-1)} \quad (5.39)$$

$$\dot{p}_{(3,1)} = -a_5 p_{(3,1)} + d_2 p_{(3,-1)} + e_1 p_{(3,0)} \quad (5.40)$$

$$\dot{p}_{(3,2)} = e_2 p_{(3,0)} + f_1 p_{(3,1)} \quad (5.41)$$

$$\dot{p}_{(3,3)} = f_2 p_{(3,1)} \quad (5.42)$$

where  $a_n, b_n, c_n, d_n, e_n, f_n$  are the probabilities of driving in or out of a given sub-level,  $p_{ij}$ . Specifically, these probabilities are the product of the Clebsch-Gordan coefficients squared for the upwards and downwards transitions. The aforementioned system of equations only considers the dynamics of driving from the ground state  $(3, -3)$  to one of the excited states. What we want to

determine is the net effect of population dynamics on our observed spectrum. To do this, we also need to include the effect of off-resonantly driving transitions. In particular, it is possible to off-resonantly drive transitions during the probe pulse as well as the detection pulse.

The excited states of the  $^2P_{\frac{1}{2}}$  level are separated by approximately 306 MHz. On average, one scattering event from the ground state to the  $F = 2'$  manifold occurs for every 200 scattering events from the ground state to the  $F = 3'$  manifold when the laser is tuned to drive transitions to the  $F = 3'$  manifold (and similarly if the laser is tuned to drive transitions to the  $F = 2'$  manifold). To account for this, we included the probability of off-resonantly driving transitions into our model by adding it into the calculation of the probability of driving out of a given Zeeman sublevel and into another Zeeman sublevel.

We have also thus far neglected the effect of state detection on the lineshape. After the probe laser is turned off, the ion has some nonzero probability of being in any of the Zeeman sublevels. We can calculate this, using the rate-equation approach discussed above. When we turn on the Cyclor laser, the average number of photons the ion emits will be different, depending on its final state after being probed.

We have already discussed some of the Cyclor dynamics in Section (3.6) and will expand on that now. Recall that if the ion is in the  $(3, -3)$  state, then the ion is bright and we will detect many photons, whereas if the ion is

in the  $F = 2$  manifold then the ion is in a dark state and so we see a reduction in the number of detected photons. To determine the average number of photons detected when the Cyclor laser is turned on, we used a rate equation approach similar to the one discussed for the Probe laser. The key difference is that we considered transitions driven by the Cyclor laser ( $\sigma^-$ -polarized light) for a given state distribution after probing (calculated from the Probe laser dynamics). The full system of equations (including probe and cyclor dynamics) was solved using Maple [49] and the solution is included in Appendix (B).

The results from the Maple [49] worksheet were fit to a Lorentzian with a quadratic background (to determine line centre) using Gnuplot [91]. The fit to the simulated data indicated that the maximum shift in line centre is  $0.41 \pm 0.02$  MHz when driving to the  $F = 3'$  manifold, and the maximum shift in line centre is  $0.22 \pm 0.03$  MHz when driving to the  $F = 2'$  manifold. In both cases, the maximum shift corresponded to inputting the largest magnetic field and the longest probe times used in the experiment, into the simulation.

The net shift in line centre can be thought of as resulting from two different processes. The first we will call “nearly-resonant” effects. The pulling of line centre results from populating the different Zeeman sublevels that are split by an externally applied field. The second we will call “off-resonant” effects. The pulling of line centre results from off-resonantly driving to the other excited level by the Probe laser.

The near-resonant effects pull line centre in different directions depending on the driving laser polarization. In this discussion, we treated the Probe laser as having  $\sigma^+$ -polarized light. During the experiment we took data with *both* polarizations separately. Since the Zeeman sublevels tune symmetrically (see Section (5.3.1)) at the magnetic fields we used, line centre is pulled in opposite directions but with the same magnitude (for a given probe time and magnetic field). By taking the average value of line centre for the two polarizations we average out the near-resonant effects (see Section (6.2.3)).

The off-resonant effects pull line centre in different directions depending on which transition is being addressed. When driving transitions from the ground state to the  $F = 3'$  manifold, we off-resonantly drive transitions to the  $F = 2'$  manifold. Transitions from the ground state to the  $F = 2'$  manifold are blue of those to the  $F = 3'$  manifold and this results in line centre being pulled to higher frequency. Similarly, line centre is pulled red when we consider transitions from the ground state to the  $F = 2'$  manifold. However, the wings of the other Lorentzian contribute less than 1% to the amplitude, and the corresponding shift in line centre is less than 0.005% – thus, the shift contributes negligibly to the uncertainty in the hyperfine  $a$  constant (0.16%).



## Chapter 6

# Experimental Technique and Data Analysis

A lot of preparation was required prior to measuring the hyperfine  $a$  constant (see Section(6.2)) and the linewidth (see Section (6.3)) of the  $^2P_{\frac{1}{2}}$  level. First, we needed to load a single ion (see Section (6.1.1)) and minimize the micro-motion (see Section (6.1.2)).

In addition to these steps (which we did once per day), we also needed to determine optimal parameters and to characterize our system. We determined the power saturation parameter for the laser beams so that we could characterize any power broadening introduced into the lineshape (see Section (6.1.3)).

An optimal probe time was chosen (see Section (6.1.4)) to minimize line

broadening and line pulling due to the population dynamics discussed in Section (5.6). An optimal detection time was chosen to minimize the overlap between dark and bright states (see Section (6.1.5)).

The frequency separation between the two molecular iodine hyperfine features to which the laser was locked had to be measured, since we used iodine as a frequency reference to determine the hyperfine separation (see Section (6.1.6)). Also, for the magnesium linewidth measurement we measured the laser linewidth and placed an upper limit on the ion temperature (both of which are discussed in Section (6.3.1)) since the measured linewidth is a convolution of the natural linewidth, the laser linewidth, and any additional Doppler width due to the ion's finite temperature.

We begin with a discussion of the daily steps required for our experiment, and then continue to discuss the different methods used to characterize our system.

## 6.1 Experimental Technique

### 6.1.1 Initial Preparation and Loading

In order to load an ion we photoionized a neutral magnesium atom through its  $^1P_0$  level (see Section (2.1)). The Photoionization beam was threaded through trap centre and could be adjusted independently of the Cyclor and

Repumper beams using a mirror. Adjustment was not typically necessary since successful single ion loading was not a strong function of the beam position. The Photoionization beam was tuned approximately 500 *MHz* blue of the peak count rate for the neutral beam. This was found to maximize the likelihood of ionizing  $^{25}\text{Mg}$ . The laser beam was tuned to maximize the peak count rate for the neutral beam when loading  $^{24}\text{Mg}^+$ . This corresponded to the maximizing the fluorescence of the iodine cell.

The Cyclor and Repumper beams were combined on a 50/50 beamsplitter and aligned to overlap the Photoionization beam using mirrors to roughly overlap the beams, and a lens for fine adjustment of both the Cyclor and Repumper beams, together. The lens used to adjust the beam position was mounted on a precision mount from Thorlabs (*ST1XY – D*) that made possible fine adjustment of the beam position along the horizontal and vertical directions. Both the Cyclor and Red Doppler beams were detuned by approximately 500 *MHz* from ion resonance.

All three laser beams were left on continuously while the oven was heated to an equilibrium temperature of 150°C, with the trap on. Once the oven equilibrated, the combined Cyclor and Repumper beam positions were scanned horizontally and vertically while fluorescence was monitored on an Andor EMCCD camera. Typical loading times varied from 30–60 seconds. For typical voltages used in all of the experiments ( $V_{RF} \approx 283\text{ V}$ ,  $\Omega_T \approx 2\pi \cdot 14\text{ MHz}$ ,  $V_{DC} \approx 6\text{ V}$ ),

the trap frequencies are  $\omega_x = 2\pi \cdot 4.65 \text{ MHz}$ ,  $\omega_y = 2\pi \cdot 4.32 \text{ MHz}$ , and  $\omega_z = 2\pi \cdot 421 \text{ kHz}$ .

Once an ion was observed, the Photoionization beam was manually blocked with an index card and the oven was turned off to prevent any further ion loading. The oven was allowed to cool and the Cyclor and Red Doppler beams were tuned out to 1 GHz red of ion resonance, keeping the count rate low to minimize the likelihood of photon-assisted chemical reactions between the ion and background gas.

The camera count rate was monitored while the oven cooled and the laser beam position was adjusted using the coarse adjustment of the Thorlabs (*ST1XY – D*) translation mount. The lens was adjusted to maximize the camera count rate. Five minutes was sufficient to allow the oven to cool and to visually confirm that only a single ion was loaded; however, visual confirmation did not guarantee that other isotopes of magnesium were not also trapped since other isotopes would not be resonant with either laser beam. A few different techniques were employed to look for other ions that could have been trapped but that were not resonant with the laser beam.

By tuning the laser frequency it was possible to look for fluorescence due to  $^{24}\text{Mg}^+$ . Since resonance of  $^{26}\text{Mg}^+$  is blue of  $^{25}\text{Mg}^+$ , direct observation of fluorescence due to this isotope resulted in potentially losing  $^{25}\text{Mg}^+$  due to heating. Instead, the RF power driving the trap was lowered while keeping the

DC electrode voltages fixed. At sufficiently low RF power, confinement along the trap axis became stronger than in the radial direction and, if multiple ions were present, hopping of the fluorescing ion was observed as it exchanged axial position with the dark ion.

Next we reduced micromotion. Recall from Section (2.2) that micromotion is caused by background electric fields pushing the ion away from RF null. The micromotion was minimized along the axial and radial directions separately. The RF power driving the trap was lowered while ion position was monitored on the EMCCD camera. As we lowered the RF power, we reduced the trap depth. If a background field was present, then the ion moved to a new equilibrium position. We would then adjust the DC voltages to compensate for ion drift, and repeat this iteratively until the ion did not appreciably move. Since it was not possible to observe how the ion moved in and out of the plane of the camera, minimization of micromotion in this plane was done by monitoring the photon count on a photomultiplier tube while the ion was pushed along the radial direction at a fixed laser detuning, as described in Section (6.1.2).

Once micromotion along the axial direction had been minimized, a mirror was placed in the path to the EMCCD camera to steer the ion fluorescence onto the photomultiplier tube (PMT) so that we could count photons. The mirror angle was adjusted to maximize the number of photons falling on the PMT entry window by monitoring the observed count rate. The laser power

for both beams was attenuated so that  $\frac{I}{I_s} \simeq \frac{1}{20}$ . While monitoring the number of photons detected, the micrometer was adjusted to maximize the overlap between the combined laser beams and the ion.

The magnetic fields and laser polarization were also optimized at this point using the following procedure. A pulse sequence consisting of 200  $\mu s$  of optical pumping (to prepare the ion in the  $(3, -3)$  state) and 250  $\mu s$  of detection was programmed into the PulseBlaster using the Experiment-control.vi LabView interface (see Section (3.7.2)).

Both the Cyclor (driving transitions out of the  $F = 3$  manifold) and the Repumper (driving transitions out of the  $F = 2$  manifold) were turned on to optically pump the ion into the  $(3, -3)$  state. During the detection pulse, the Cyclor and Detection Gate were turned on (see Section (3.7.2)). If the magnetic field was aligned with the direction of laser propagation and the laser polarization was circular then optical pumping drove the ion into the cycling transition ( $F = 3, m_F = -3 \rightarrow F = 4, m_F = -4$ ). If the magnetic field or polarization was not optimized then the ion could fall into the  $F = 2$  manifold, resulting in fewer photons being counted during the detection gate.

The magnetic field was controlled by three coils oriented perpendicular to one another. Each coil was made from insulated copper wire that was wound around a tubular form. The diameters of the coils were 0.05875 m and they consisted of 200 turns. One of the coils was oriented with its magnetic field

vector along the direction of propagation of the laser beam. We called this the “Quantization Coil” since it was used to set the quantization axis. The coil on top the vacuum chamber was called the “Vertical Coil”, while the remaining coil was called the “Perpendicular Coil”. The purpose of the latter two coils was to null out ambient fields. From the diameter, number of turns, and distance from trap centre the magnetic field due to each of these coils is  $B_Q \approx B_P \approx 2.014I \cdot 10^{-4} \frac{T}{A}$  and  $B_V \approx 5.683I_c \cdot 10^{-4} \frac{T}{A}$  where  $I_c$  is the current in the coil. The magnitude of the field due to the Vertical Coil is higher for a given current since the coil is closer to trap centre than the other two coils.

The magnetic field and polarization could be optimized by monitoring the photon count as well as by monitoring the photon histogram. By averaging over 1000 experiments the mean count was maximized and the number of experiments with zero counts was minimized by iteratively adjusting the waveplates and magnetic field direction (by adjusting the current driving each coil). This process was repeated with successively lower power (up to 20 dB attenuation) in the Repumper beam. By lowering the power in the Repumper beam, we reduced the probability of driving transitions out of the  $F = 2$  manifold, which increased the sensitivity of optical pumping to imperfect polarization and magnetic fields. Repeating the process with successively lower laser power allowed us to finely adjust the polarization and magnetic fields. Typical histograms, for a detection time of 250  $\mu s$ , are shown in Figure (6.9).

### 6.1.2 Characterizing Micromotion

Once the magnetic fields and polarization were set by following the aforementioned procedure, we minimized micromotion along the radial direction. In Section (2.2.3) we discussed the effect of excess micromotion on the lineshape. Recall that the ion is trapped along the radial direction by an electric field that is rapidly oscillating at  $\Omega_T$ . If we push the ion away from where the RF field is zero, then as the field oscillates it pulls the ion back and forth at the RF frequency, since the ion samples the change in the electric field away from RF null. Any background field can push the ion away from RF null, resulting in additional micromotion. We can use the DC tube electrodes to push the ion towards RF null to minimize this micromotion. By determining an upper limit for the displacement from trap centre, we can subsequently determine the associated maximum Doppler shift to put an upper limit on the contribution to the lineshape due to excess micromotion.

To minimize micromotion along the axial direction, the tube electrodes were adjusted while the ion position was monitored on-screen, as discussed in Section (6.1.1). The procedure was performed at low trap frequencies, ( $0.092 \times$  nominal), and it was observed, using the EMCCD camera, that the ion moved by less than 2 pixels. This corresponds to an upper limit of  $1.8 \mu m$  (see Section (3.6)). Scaling back up to nominal trap frequencies of  $421 kHz$ , this displacement corresponds to an upper limit of  $15 nm$  (since the displacement

from trap centre is inversely proportional to the square of the trap frequency).

Minimizing micromotion along the radial direction is a bit more difficult since we cannot see how the ion moves in and out of the plane of the camera. To minimize micromotion along this direction, we intentionally pushed the ion along the radial direction while monitoring the number of photons counted at a fixed laser detuning. To push the ion along the radial direction, IndividualTrapControl.vi (see Section (3.7.1)) was used. By inverting the voltages on tube electrodes Naomi and Vamp, we were able to increment the voltages so that the ion was pulled along the radial direction by Naomi and Vamp and pushed along the radial direction by Eva and Snake (see Figure (6.1)). This prevented inadvertent pushing of the ion along the axial direction. (Recall that micromotion along the axial direction was minimized by following the procedure outlined in Section (6.1.1).)

We should note here that ion movement along the radial direction (a line connecting the DC tube electrodes) can be broken up into vertical and horizontal components. Along the vertical direction, the ion is pulled side to side by the RF trapping fields and along the horizontal direction, the ion is pulled up and down by RF trapping fields. During the experiment, the laser beam was oriented so that its  $k$  vector had an equal component along the axial direction and the horizontal direction and so we were only sensitive to motion along these two directions (since  $\vec{k} \cdot \vec{v} = 0$  for motion along the vertical di-

rection). We did not compensate for micromotion along the vertical direction since motion along the vertical axis is perpendicular to the beam and so we are not sensitive to motion along this direction. A typical curve is shown in Figure (6.2).

During the experiment, the DC voltages were chosen so that the fluorescence was at a minimum, between the two peaks (corresponding to trap centre). To do this, we adjusted the DC tube electrodes so that the voltages corresponded to sitting on the steepest part of the slope (see Figure (6.2)), on either side of the minimum, corresponding to  $V_a$  and  $V_b$ . We estimated that we could determine each of these voltages to within  $50 \text{ mV}$ , which was limited by the fluctuations in each data point. We determined the location of the minimum by averaging these two voltages, and so an upper limit on the uncertainty is  $\frac{\sqrt{50^2+50^2}}{2} = 35 \text{ mV}$ . To determine an upper limit on the ion displacement from the uncertainty in the voltage, we fit the data to a convolution of a Doppler-shifted Lorentzian and the harmonic velocity distribution (see Section (2.2.3)):

$$\mathcal{L}(V) = N \int_{-4\omega_x\Lambda V}^{4\omega_x\Lambda V} \frac{1}{\pi^2} \left( \frac{2\Gamma}{(\Delta_L - kv)^2 + \Gamma^2} \right) \left( \frac{1}{\sqrt{(4\omega_x\Lambda V)^2 - v^2}} \right) dv. \quad (6.1)$$

Here,  $N$  is an overall scaling,  $\omega_x$  is the trap frequency,  $\Lambda$  is the conversion between ion displacement and voltage,  $V$  is the applied voltage to one tube

electrode,  $\Delta_L$  is the laser detuning from resonance,  $k$  is the laser wavevector, and  $\Gamma$  is the natural linewidth. We fit the data to Equation (6.1), keeping the trap frequency (4.32 MHz) and linewidth (42 MHz) fixed. From the fit we obtained an upper limit of  $\Lambda < 46 \frac{nm}{V}$ . We also varied the value of the trap frequency and linewidth and found that the fit value for  $\Lambda$  did not vary significantly. Thus, using the lower trap frequency along the radial direction serves as a conservative upper limit. By multiplying our uncertainty in voltage and our conversion factor  $\Lambda$  we obtained an upper limit of 1.6 nm at 4.32 MHz. The resultant upper limit for the Doppler shift due to the radial and axial displacements is  $\frac{\vec{k} \cdot \vec{v}}{2\pi}$ . Since  $q_x = 0.783$  and  $q_y = 0.747$  along the radial directions, we need to include up to  $n = \pm 6$  for the Fourier components of the velocity. Along the axial direction, the higher order contributions are small since  $q_z = 0.036$ .

To calculate the Doppler shift contribution due to excess micromotion along the radial and axial directions, the RMS velocities of the Fourier components were added in quadrature and normalized by the amplitude of the secular-motion Fourier component. Thus, along the radial direction the maximum total velocity is a factor of 1.45 larger than the maximum secular velocity. As a check, we also included up to  $n = \pm 6$  for the axial direction and found an increase of less than 0.2%, which is consistent with a small  $q$ -parameter. Thus, the maximum velocity corresponded to a Doppler shift of  $< 42$  kHz along the axial direction

and  $< 158$  kHz along the radial direction. We include the total contribution of 200 kHz in the error budget for the linewidth (see Section (6.3.2)) to determine an uncertainty in our measured linewidth.

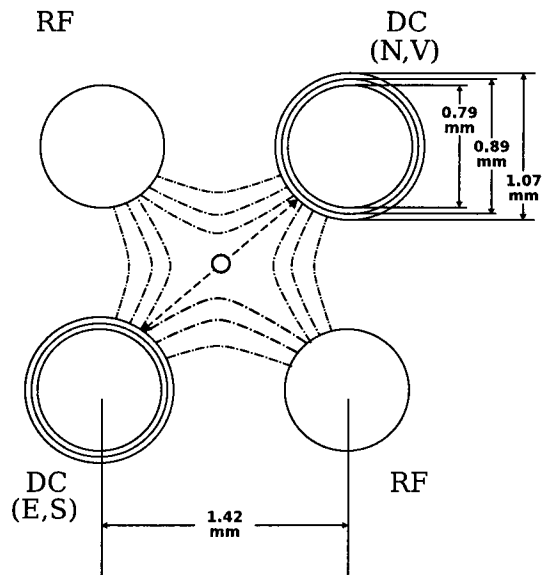


Figure 6.1: Schematic of pushing the ion along the radial direction to minimize micromotion. By inverting the voltages on tube electrodes Naomi and Vamp, we were able to increment the voltages of all four tube electrodes so that the ion was pushed along the radial direction (dashed line connecting the DC tube electrodes). The DC tube electrodes Naomi, Eva, Vamp and Snake are indicated by N, E, V, and S respectively. Exaggerated field lines due to the RF electrodes are also included, although the direction of field lines are omitted since the direction alternates with a frequency of  $\Omega_T$ .

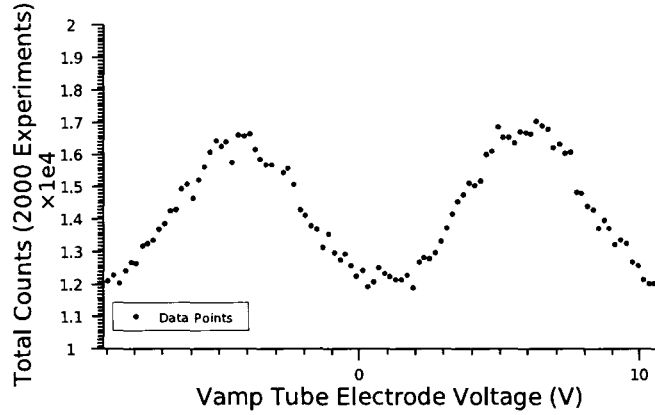


Figure 6.2: Absorption sidebands due to micromotion. The total number of photons in 2000 experiments is plotted as a function of voltage on one of the tube electrodes (Vamp), although all four tube electrode voltages were adjusted as discussed in Section (6.1.2). By intentionally introducing micromotion by pushing the ion along the radial direction we can determine where the fluorescence is a minimum, corresponding to the location of RF Null.

### 6.1.3 Power Saturation Parameter

In order to characterize power broadening of the lineshape we need to know the saturation parameter for the Probe beam. The information was determined from measurements made with  $^{24}\text{Mg}^+$  for the Probe beam. Power broadening in the Cyclor only affects detection and, to first order, has no effect on the measured linewidth.

To characterize the Probe laser, a single  $^{24}\text{Mg}^+$  ion was trapped and the number of photons detected was recorded as a function of probe laser detuning. Since  $I = 0$  for  $^{24}\text{Mg}^+$  there is no hyperfine splitting and so only a single laser beam is required to laser cool.

The isotope shift between  $^{24}\text{Mg}^+$  and  $^{25}\text{Mg}^+$  is  $1586 \text{ MHz}$  and so the  $I_2$  locking scheme for  $^{24}\text{Mg}^+$  was different from that described in Section (3.4.3).

Specifically, for  $^{24}\text{Mg}^+$  only a single double-pass AOM was used, and the frequency shift was positive relative to the undeflected beam. With this setup, feature  $b$  of iodine line #1599 (Figure (6.10)) is closest to ion resonance.

With a single  $^{24}\text{Mg}^+$  ion trapped, the PulseBlaster was programmed with a single-pulse sequence consisting of the Probe laser and the Detection Gate for a duration of  $500\ \mu\text{s}$ .

The Probe laser was locked to feature  $b$  of iodine line #1599 (Figure (6.10)) and the  $I_2$  double-pass AOM was scanned from  $70\ \text{MHz}$  to  $90\ \text{MHz}$ , with each data point summed over 2000 experiments to generate a single curve. The procedure was repeated for 9 different laser powers ranging from  $1.10 \pm 0.01\ \mu\text{W}$  to  $449 \pm 2\ \mu\text{W}$ . For each curve the laser power was measured upstream of the ion at a convenient location, between a pair of focusing lenses used to focus the beam at the ion.

The background counts, with no ion present, were also measured as a function of probe laser power and summed over 2000 experiments (see Figure (6.3)). This data was fit to a straight line since it was determined that the background counts were intensity-dependent (due to scattering from the electrodes) and the fit was subsequently used to subtract the background from the data.

The saturation parameter was obtained from the data in two different ways. In the first approach, each background-subtracted data set was fit to a

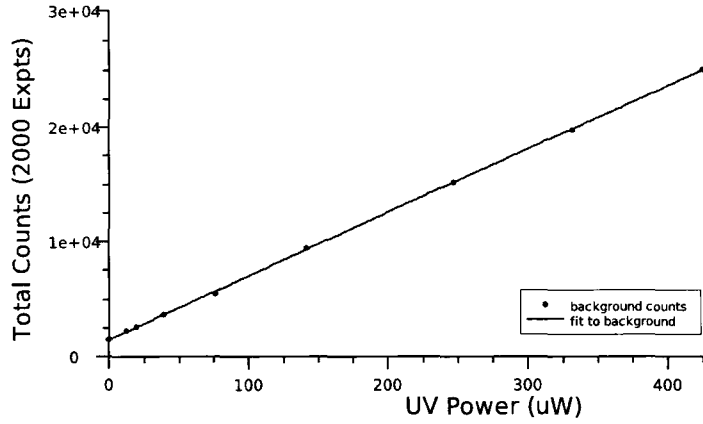


Figure 6.3: A plot of the measured background counts with no ion present, as the laser intensity is increased. The laser power was measured upstream from the trap. A fit to a straight line was used to interpolate the background count for each of the power-broadened spectra.

Lorentzian of the form:

$$y(\nu_L) = \frac{a}{1 + \left(\frac{4\pi(\nu_L - \nu_0)}{\Gamma'}\right)^2} \quad (6.2)$$

where  $a$  is the peak count,  $\nu_L$  is the laser frequency ( $MHz$ ),  $\nu_0$  is the resonant frequency ( $MHz$ ), and  $\Gamma'$  is the power broadened linewidth ( $\frac{rad}{s}$ ). Explicitly [50]:

$$\Gamma' = \Gamma \sqrt{1 + \frac{I}{I_s}} \quad (6.3)$$

where  $\Gamma$  is the natural linewidth,  $I$  is the laser intensity, and  $I_s$  is the saturation intensity. The power-broadened linewidth extracted from the fit to Equation (6.2) is plotted as a function of laser power in Figure (6.4). The error bars in the plot come from the statistical uncertainty of the Lorentzian fit. It was assumed that the standard deviation of each data point was  $\sqrt{N}$ , where  $N$

was the total number of photons detected.

The power-broadened linewidth was subsequently fit to:

$$\Gamma' = \Gamma \sqrt{1 + \frac{x}{b}} \quad (6.4)$$

Equation (6.4) has the same form as Equation (6.3) except that  $\frac{I}{I_s}$  is replaced with  $\frac{x}{b}$ , where  $x$  is the measured laser power between the pair of lenses upstream of the ion and  $b$  is the power saturation parameter. By comparing the two equations, it is clear that  $b$  is simply the power required to saturate the ion, extrapolated to the location between the pair of lenses where the power was measured.

A non-linear least-squares fit of the data to equation (6.4) returns  $\Gamma = 2\pi \cdot (42.8 \pm 1.1) \text{ MHz}$  and  $b = 36 \pm 3 \mu\text{W}$ ; the quoted uncertainties are from the fit alone. For data taking, we used the Lorentzian model to estimate the saturation parameter, the camera efficiency, and the linewidth. However, in fitting the data to a Lorentzian we have neglected the laser-detuning-dependent temperature. During the data analysis, we also fit to a laser-detuning-dependent Voigt profile and determined that, while the effect on the linewidth is not negligible, the saturation parameter obtained from the fit using a Voigt profile ( $35 \pm 3 \mu\text{W}$ ) was consistent with the saturation parameter obtained from the fit using a Lorentzian model (see Section (6.3.2)).

A second method to determine the power saturation parameter is to con-

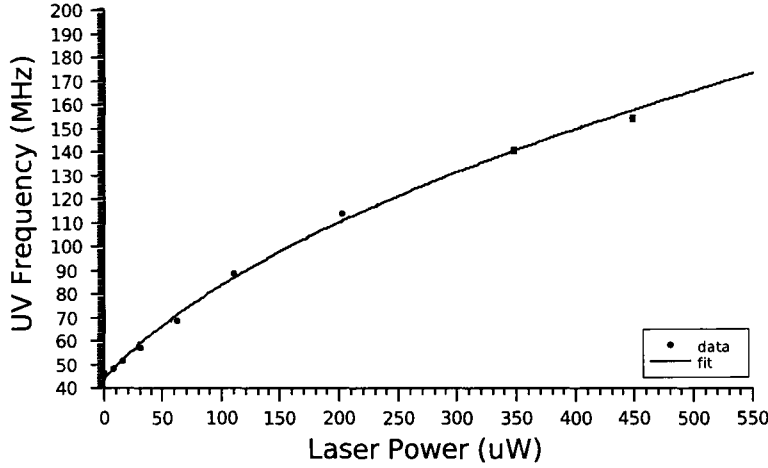


Figure 6.4: A plot of the measured linewidth as a function of laser power, showing broadening of the line. The measured linewidth at each power was determined by fitting the data to a Lorentzian, and subsequently plotted as a function of laser power. From the fit of the data to a power broadened model,  $b = 36 \pm 3$ . In this model we have neglected the laser-detuning-dependent temperature. In the full analysis (see Section (6.3.2)) the data was fit to a laser-detuning-dependent Voigt profile. From the Voigt fit,  $b = 35 \pm 3 \mu W$ , consistent with the value determined from this method.

sider the number of scattered photons at a fixed detuning as a function of laser power. Taking into account the camera efficiency, detection time, and number of experiments summed over, we can write an expression for the total number of photons detected as [50]:

$$N_S = \left( \frac{s_0}{1 + s_0} \right) \left( \frac{\Gamma}{2} \right) \frac{\eta N_E \tau_D}{1 + \left( \frac{2\Delta_L}{\Gamma\sqrt{1+s_0}} \right)^2} \quad (6.5)$$

where  $N_E$  is the number of experiments,  $\tau_D$  is the detection time,  $\eta$  is the overall quantum efficiency,  $\Delta_L$  is the laser detuning from resonance, with  $x$ ,  $b$  and the natural linewidth  $\Gamma$  as previously defined.

To reduce the number of unknown parameters in the fit we can take the

ratio of equation (6.5) at two different detunings from resonance:

$$r = \frac{1 + \left(\frac{2\Delta_L}{\Gamma\sqrt{1+s_0}}\right)^2}{1 + \left(\frac{2(\Delta_L+\Delta')}{\Gamma\sqrt{1+s_0}}\right)^2} \quad (6.6)$$

where  $\Delta'$  is the relative detuning,  $\Gamma$  is the natural linewidth,  $s_0 = \frac{x}{b}$  and the only free parameters are  $\Delta$ , the absolute detuning from resonance, and  $b$ , the power saturation parameter.

A non-linear least squares fit to Equation (6.6) with  $\Delta' = 2\pi \cdot 20 \text{ MHz}$  and  $\Gamma = 2\pi \cdot 43 \text{ MHz}$  is shown in Figure (6.5). From the fit  $\Delta_L = 2\pi \cdot (6 \pm 1) \text{ MHz}$  and  $b = 38 \pm 5 \mu W$ . In fact, it was subsequently determined that the linewidth is  $2\pi \cdot (42.4 \pm 1.2) \text{ MHz}$ ; however, since this second method resulted in larger uncertainties than the previous method, we did not use it. For this reason, we did not refit the data with the corrected linewidth.

Both methods are consistent with one another, although the first method has a smaller uncertainty in the statistical fit. The larger uncertainty in the second method may be attributed to taking ratios of different data sets, which magnifies the uncertainties. As discussed in Section (6.3.2), the data were also fit to a laser-detuning-dependent Voigt profile and from that analysis a saturation parameter of  $35 \pm 3 \mu W$  was obtained. Since the lineshape is more appropriately represented by a laser-detuning-dependent Voigt profile we choose to use a value of  $b = 35 \pm 3 \mu W$  for the remainder of the analysis.

The quantum efficiency,  $\eta$ , of the PMT could also be obtained from equa-

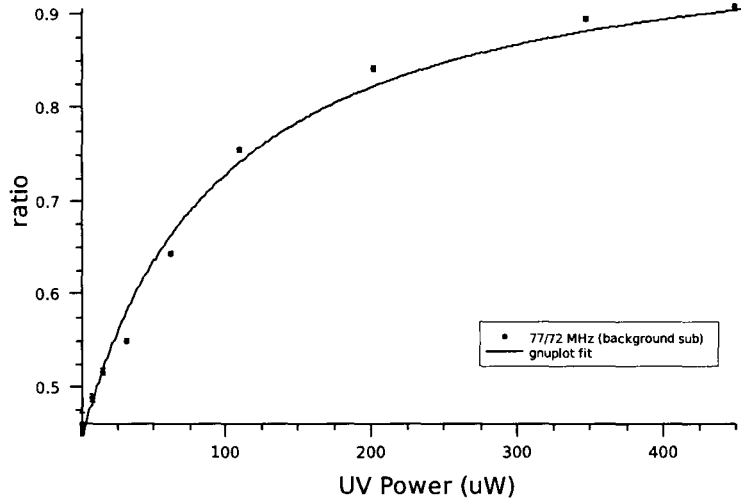


Figure 6.5: A plot of the ratio of the photon count at two detunings, separated by 20 MHz, as a function of laser power. From a fit to Equation (6.6),  $b = 38 \pm 5 \mu W$ .

tion (6.5). A plot of the total number of counts at a fixed detuning was fit to equation (6.5) using the values for line centre and for the power saturation parameter obtained from the previous two fits. From Figure (6.6),  $\eta = 0.27 \pm 0.01\%$  where the uncertainty in  $\eta$  was estimated by using the uncertainties in  $b$  and  $\Delta_L$ .

#### 6.1.4 Determining Probe Time

Determining the power saturation parameter allowed us to characterize power broadening of the linewidth. Another consideration we had to take into account was how long to probe the transition. Long probe times increased signal to noise at the cost of potentially broadening and pulling the line due to population of the other ground-state Zeeman sublevels (see Section (5.6)).

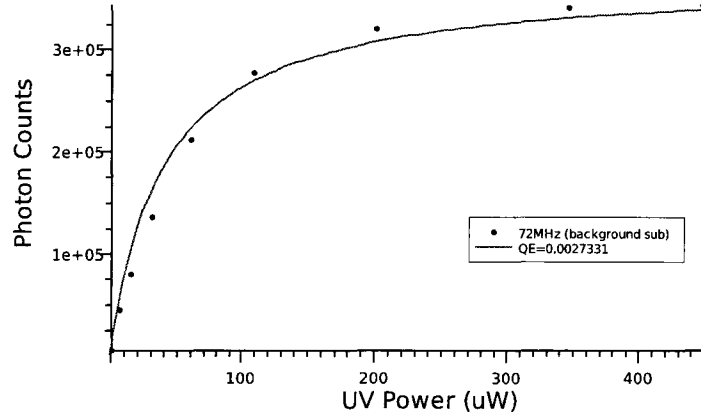


Figure 6.6: A plot of the total number of counts summed over 2000 experiments at a fixed detuning from resonance. An overall quantum efficiency of  $0.27 \pm 0.01\%$  is obtained from the fit.

Probe times for the  ${}^2S_{\frac{1}{2}} \rightarrow {}^2P_{\frac{1}{2}}$  transition were determined by preparing the ion in the  $(3, -3)$  ground state, probing for a variable time, and then turning on the detection laser.

A single  ${}^{25}\text{Mg}^+$  ion was trapped following the procedure outlined in section (6.1.1). The Probe power was attenuated to  $1 \mu\text{W}$  upstream of the trap corresponding to  $s_0 \simeq \frac{1}{35}$  (see Section (6.1.3)).

A curve of fixed probe time but varying Probe-laser detuning was taken with the laser locked to hyperfine feature  $n$  of iodine line #1599 (see Figure (6.10)). This was done to fix the laser frequency with respect to ion resonance since laser detuning from resonance affects the timescale on which pumping into the dark state occurs. The PulseBlaster was programmed with  $\tau_{OP} = 100 \mu\text{s}$  of optical pumping,  $\tau_P = 1 \mu\text{s}$  of probe time, and  $\tau_D = 250 \mu\text{s}$  of detection time.

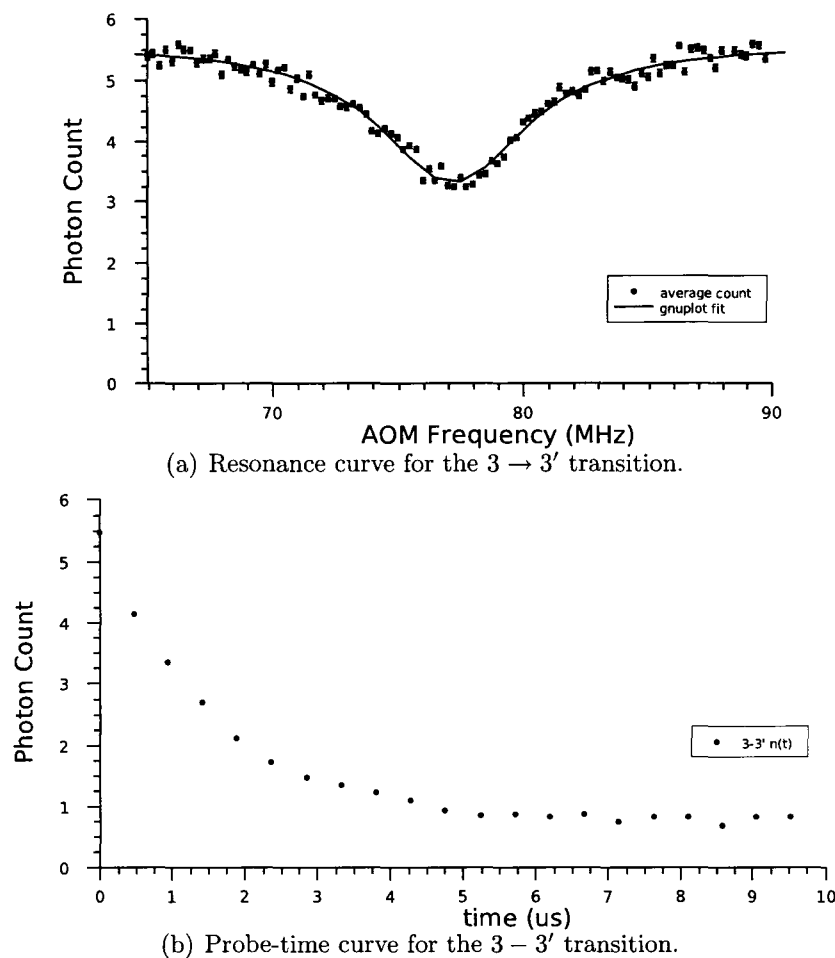


Figure 6.7: Probe-time and ion-resonance curves for the  $3 \rightarrow 3'$  transition. For both curves  $\tau_{OP} = 100 \mu s$  (optical-pumping time),  $\tau_D = 250 \mu s$  (detection time), and  $s_0 = \frac{1}{35}$  (saturation parameter). For the probe-time curve, the AOM frequency was fixed at  $77.61 \text{ MHz}$  (resonance was estimated by eye during the experiment), and each data point was averaged over 2000 experiments. For the ion-resonance curve, the probe time was fixed at  $1 \mu s$  and each data point was averaged over 5000 experiments. From a fit of the ion-resonance curve to a Lorentzian we determined line centre to be  $77.22 \pm 0.05 \text{ MHz}$ .

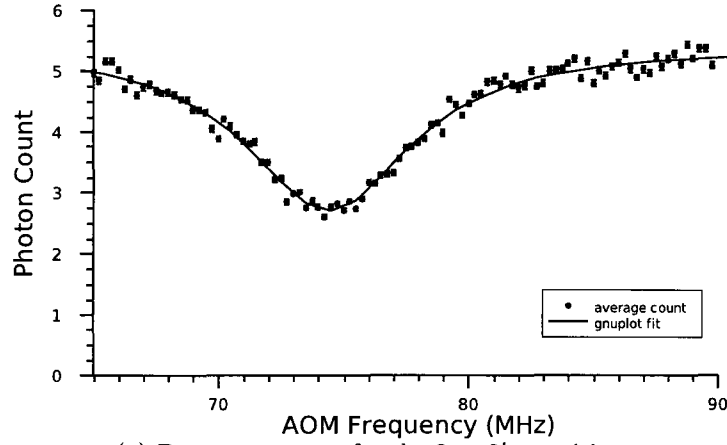
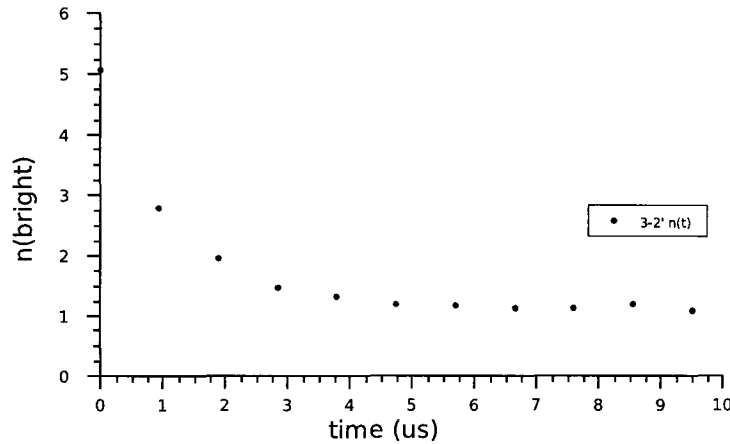
(a) Resonance curve for the  $3 \rightarrow 2'$  transition.(b) Probe-time curve for the  $3 \rightarrow 2'$  transition.

Figure 6.8: Probe-time and ion-resonance curves for the  $3 \rightarrow 2'$  transition. For both curves  $\tau_{OP} = 100 \mu s$  (optical-pumping time),  $\tau_D = 250 \mu s$  (detection time), and  $s_0 = \frac{1}{35}$  (saturation parameter). For the probe-time curve, the AOM frequency was fixed at  $74.557 \text{ MHz}$  (resonance was estimated by eye during the experiment), and each data point was averaged over 2000 experiments. For the ion-resonance curve, the probe time was fixed at  $1 \mu s$  and each data point was averaged over 5000 experiments.

The resulting curve is plotted in Figure (6.7(a)), where each data point is averaged over 2000 experiments. A line centre of  $77.22 \pm 0.05 \text{ MHz}$  was obtained from a weighted non-linear least-squares fit to an exponential of a Lorentzian to obtain a value for line centre. Here, each data point was weighted assuming a standard deviation of  $\sqrt{N}$  on the total number of counts.

The frequency of the AOM was set to  $77.61 \text{ MHz}$  (roughly on resonance) and the probe time was varied from  $0 - 10 \mu\text{s}$ . The data are plotted in Figure (6.7(b)). Each data point was averaged over 5000 experiments. Ion resonance was estimated by eye during the experiment, which is why the AOM frequency did not correspond exactly to what we obtained from the fit to ion resonance.

This procedure was repeated for the  $F = 3 \rightarrow F' = 2$  transition, with the same experimental parameters as the  $F = 3 \rightarrow F' = 3$  transition except the laser was locked to hyperfine feature  $r$  of the same iodine feature (see Figure (6.10)). The corresponding curves for laser detuning and variable probe time are plotted in Figures (6.8(a)) and (6.8(b)). For the probe-time curve, the AOM frequency was set to  $74.557 \text{ MHz}$ .

A line centre of  $74.43 \pm 0.05 \text{ MHz}$  was obtained from the fit, again assuming a standing deviation of  $\sqrt{N}$  on the total number of counts for each data point.

The time was chosen for the  $F = 3 \rightarrow F' = 2$  transition so that the on-resonance probability of being in the dark state was kept below 20%. For a saturation intensity of  $s_0 = \frac{1}{35}$  this corresponds (see Figure (6.8(b))) to a probe

time of  $0.25 \mu s$ . During the experiment, we reduced the probe laser intensity by a factor of four so that the probe time was  $1 \mu s$ .

For the  $F = 3 \rightarrow F' = 3$  transition, the effect of population dynamics is not as pronounced since the difference in the transition frequencies is less (see Appendix B). For this transition, the time chosen so that the probability of being in the dark state was kept below 50%. For a saturation intensity of  $s_0 = \frac{1}{35}$  this again corresponds to a probe time of  $1 \mu s$  (see Figure (6.7(b))). Due to the different Clebsch-Gordan coefficients for the two transitions, the probe time turns out to effectively be the same, although the probability of ending up in the  $F = 2$  manifold is different.

### 6.1.5 Determining Detection Time

We detected the final state of the ion after probing by driving the cycling transition, and counting the average number of photons detected by the PMT. The optimal detection time minimizes the overlap between the bright and dark states since the more separated they are, the easier it is distinguish between the two.

Naively, one would expect that longer detection times result in minimizing the overlap between bright and dark states; however, this is only true if the dark state ( $F = 2$  manifold) cannot scatter photons. Since hyperfine splitting of the  $^2S_{\frac{1}{2}}$  level is  $1.788 \text{ GHz}$  whereas  $\Gamma \simeq 2\pi \cdot 42 \text{ MHz}$ , approximately 1

scattering event from the dark state can occur for every 6917 scattering events from bright state. From the Clebsch-Gordan coefficients, if a scattering event occurs from the dark state, the ion will fall into the bright state  $\frac{2}{3}$  of the time and scatter photons for the remainder of the detection gate. The net effect on the dark state is that as the detection time increases, the probability that the ion scatters a photon from the dark state increases, resulting in a higher average photon number for the dark state.

To determine the optimal detection time, bright and dark histograms were taken for a series of different detection times and the overlap between the bright and dark states was calculated.

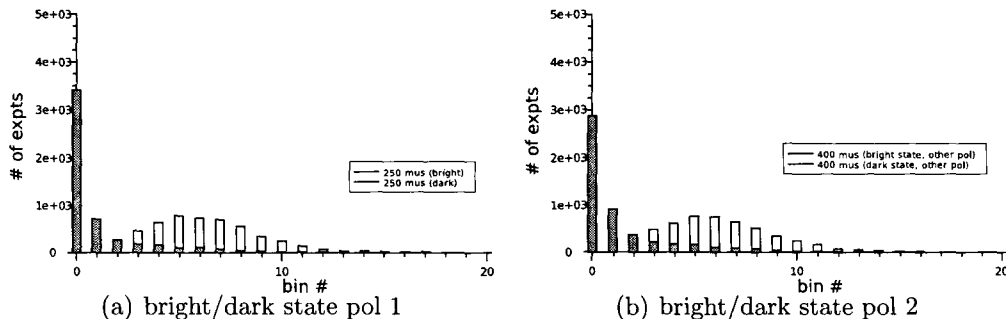


Figure 6.9: Bright- and dark-state histograms for both laser polarizations and for optimal detection times. For all four histograms  $\tau_{OP} = 100 \mu s$  (optical-pumping time),  $\tau_P = 1 \mu s$  (probe time). For dark-state histograms, the Probe laser power was increased to definitively drive the ion into the dark state.

A  $^{25}Mg^+$  ion was trapped following the procedure outlined in Section (6.1.1). The PulseBlaster was programmed with  $\tau_{OP} = 100 \mu s$  of optical pumping,  $\tau_P = 1 \mu s$  of probe time (long enough to reach a steady-state population predominantly in the dark state), and dark-state histograms were taken

for  $\tau_D = 200, 250, 300, 350 \mu s$  at one polarization and  $\tau_D = 200, 300, 400 \mu s$  at the other polarization. This pulse sequence was repeated with no probe pulse to obtain the bright-state histograms.

The overlap between bright and dark states was calculated from the histograms according to equation:

$$\chi = \frac{\sum B_i D_i}{\sqrt{\sum B_i \sum D_i}}, \quad (6.7)$$

where  $B_i$  and  $D_i$  are the number of experiments in the  $i^{th}$  photon bin of the bright and dark state, respectively. The detection time that minimized the overlap between bright and dark state histograms was selected as the optimal detection time. For the experiment  $\tau_D = 250 \mu s$  was chosen for one polarization and  $\tau_D = 400 \mu s$  was chosen for the other polarization (to minimize the overlap between bright and dark states in each case). The difference in detection time between the two polarizations is attributed to the change in laser detuning resulting from the shift in the Zeeman sublevels. The combined bright and dark state histograms for both polarizations are shown in Figures (6.9(a)) and (6.9(b)). The overlap between the bright and dark states calculated from equation (6.7) are 0.104 for  $\tau_D = 250 \mu s$  and 0.162 for  $\tau_D = 400 \mu s$ .

### 6.1.6 Determining Molecular Iodine Hyperfine Frequency Separation

To eliminate slow drifts in the laser frequency, and to calibrate the piezo-voltage tuning of the laser, the laser was locked to a hyperfine feature of iodine before taking each data curve. An additional advantage of locking to iodine is that we can tune the laser frequency by changing the frequency of the AOM in the iodine spectrometer – frequency changes are all done using RF sources which are highly stable and accurate. For each of the two transitions probed, the laser was locked to a different hyperfine feature of iodine. The frequency separation between the two hyperfine features of iodine was measured.

For reference, Figure (6.10) shows a curve of the iodine hyperfine features of line #1599 from the Iodine Atlas [69] for which the frequency of the laser was swept by changing the voltage driving the laser piezo. Hyperfine feature  $n$  was used to lock the laser for the ( $F = 3 \rightarrow F' = 3$ ) transition and feature  $r$  was used for the ( $F = 3 \rightarrow F' = 2$ ) transition. During the linewidth and  $\alpha$ -constant measurements, all laser tuning was done by changing the  $I_2$  double-pass AOM frequency while the laser was locked to iodine.

To measure the separation between the iodine features, the 560 nm output from the Probe LBO cavity was split into two beams and sent to two independent  $I_2$  cells, as shown in Figure (6.11). The original diagnostic beam in the Probe laser was used to lock the laser to the same hyperfine feature that

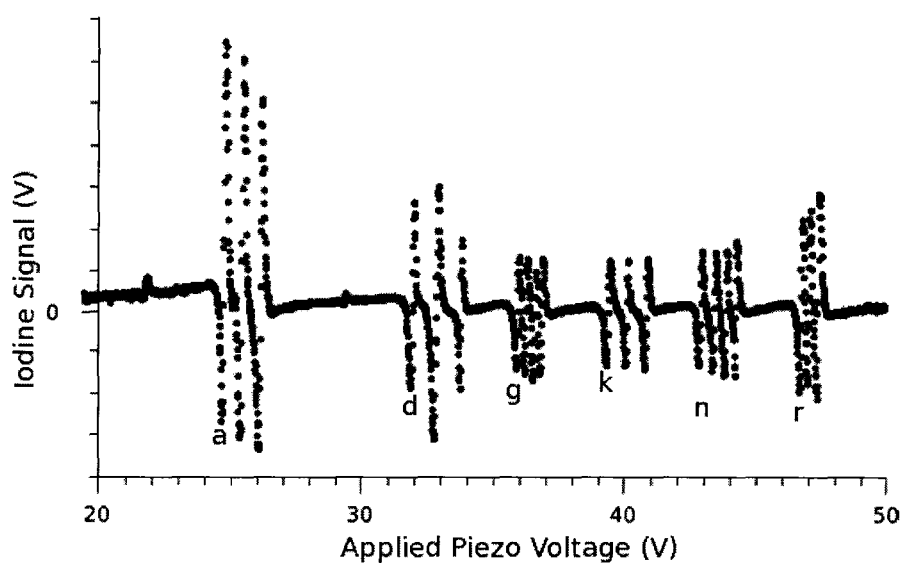


Figure 6.10: Doppler-free saturated absorption spectroscopy of Line #1599 from the Iodine Atlas [69]. It was not possible to tune over the entire range of the feature using the AOMs and so a voltage scan (driving the laser PZT) was taken to obtain the full feature. Hyperfine feature  $n$  and  $r$  were used to lock the laser to iodine for the ( $F = 3 \rightarrow F' = 3$ ) and ( $F = 3 \rightarrow F' = 2$ ) transitions, respectively, in  $^{25}\text{Mg}^+$ . Feature  $b$  was used to lock for  $^{24}\text{Mg}^+$ .

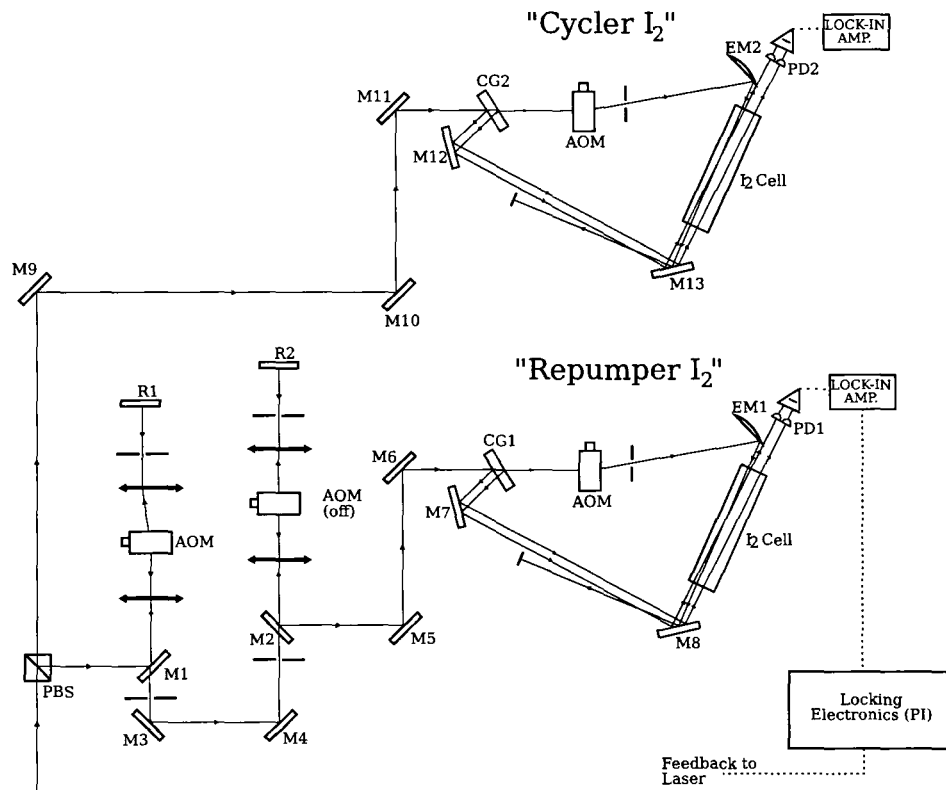


Figure 6.11: Schematic of the apparatus for the measurement of the separation between iodine hyperfine features  $n$  and  $r$ . The separation was measured by using the pre-existing Probe and Cycler iodine setups so as not to perturb the original setup. [Definition of labels: M1-13 = beam steering mirrors; R1-2 = retroreflector; CG1-2 = coated glass; EM1-2 = edge mirror; PD1-2 = photodetector]

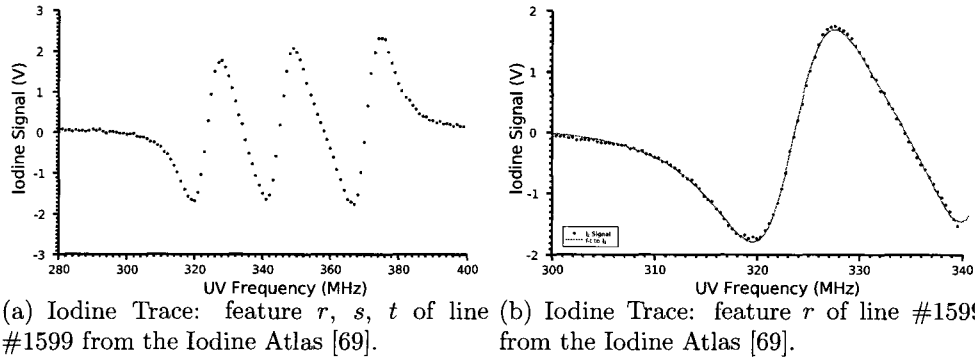


Figure 6.12: An iodine spectrum obtained by scanning the frequency of the double-pass AOM. The plots are shown giving the UV frequency, which is  $4\times$  the frequency of the signal generator (*HP 8662A*) used to drive the double-pass AOM.

was used when probing the  $F = 3 \rightarrow F' = 3'$  transition. The second  $I_2$  setup was shifted blue in frequency and scanned over a range to trace out the  $I_2$  hyperfine feature used to lock when probing the  $F = 3 \rightarrow F = 2'$  transition.

A mirror was placed at the input to the BBO cavity, steering the beam off to the iodine setup normally reserved for the Cyclor laser. The Probe beam was threaded through apertures located in the Cyclor  $I_2$  beam line where the AR-coated wedge split it into an  $I_2$  pump and weak probe and reference beams.

The pump beam in the Cyclor  $I_2$  beam line was sent through a modulating AOM driven by a *FLUKE 6061A* signal generator that was frequency modulated using a *HP 33120A* function generator. An aperture on the far side of the AOM isolated the first-order diffracted beam which was overlapped with, but counterpropagating to, the probe beam passing through the  $I_2$  cell. The pump beam power was  $25.6\text{ mW}$ . The probe and reference beam powers were  $150\text{ }\mu\text{W}$  each. After passing through the  $I_2$  cell both probe and reference

beams were detected on a auto-balancing photodetector [92] whose output was connected to a *Stanford Research Systems (SR830)* lock-in amplifier.

It was anticipated that the frequency separation between the hyperfine features used to lock was approximately  $160 \text{ MHz}$  and so one of the doublepass AOMs in the Probe beam line was turned off. After the single double-pass AOM, the beam was split into  $I_2$  pump, probe and reference beams with the pump beam modulated by the same source as in the Cyclor  $I_2$  setup. Due to differences in the  $I_2$  cells and beam sizes, and only  $13.6 \text{ mW}$  of power was in the pump beam and  $160 \text{ }\mu\text{W}$  were in the probe and reference beams. In this arrangement, the  $I_2$  feature separation is  $\Delta\nu_{I_2} = 4\nu_{AOM}$  (in UV  $\text{MHz}$ ).

The laser was locked to feature  $n$  in the Probe iodine setup and the frequency of the double-pass AOM was scanned from  $70 - 100 \text{ MHz}$  while the  $I_2$  signal from the Cyclor iodine setup was recorded. The scan was repeated for a smaller range, from  $75 - 85 \text{ MHz}$ , and both scans are plotted in Figure (6.12(a)) and Figure (6.12(b)). A fit of the data to the derivative of Lorentzians gives a zero-crossing of  $323.65 \pm 0.06 \text{ MHz}$  (in UV  $\text{MHz}$ ). Thus, the frequency separation between feature  $n$  and feature  $r$  is  $323.65 \pm 0.06 \text{ MHz}$  (in UV  $\text{MHz}$ ).

Incidentally, from Figure (6.10) we obtain a voltage separation of  $5.04 \pm 0.02 \text{ V}$ , corresponding to a tuning rate of  $64.3 \pm 0.3 \frac{\text{MHz}}{\text{V}}$  in the UV. We chose not to use voltage tuning to change the Probe-beam frequency for the experiment since we wanted to lock to iodine in order to keep the frequency

stable.

### 6.1.7 Taking Data Curves

Once we had characterized the saturation parameter and determined optimal probe times and detection times we were in a position to take data curves in order to determine the hyperfine  $a$  constant. Data curves tracing out the transition from  $^2S_{\frac{1}{2}} \rightarrow ^2P_{\frac{1}{2}}$  were taken at five different magnetic fields, so we could extrapolate to zero-field line centre. The five corresponding currents driving the Quantization Coil were 0.616 A, 1.042 A, 1.586 A, 2.074 A, and 2.560 A. At each magnetic field, the  $F = 3 \rightarrow F = 3'$  and the  $F = 3 \rightarrow F = 2'$  transitions were probed separately, locking to feature  $n$  and  $r$  of the iodine feature, respectively. A series of photon counts vs. Probe-laser detuning curves were taken with either the laser power or laser polarization varied for each data run. These curves, coupled with the iodine feature separation discussion in Section (6.1.6), allowed us to extract the  $a$  constant.

The laser pulse sequences were programmed into the PulseBlaster using the Labview interface (see Section (3.7.2)). In a single experiment, the pulse sequence consisted of 50  $\mu s$  of optical pumping followed by a probe time,  $\tau_P$ , that varied from 0.2  $\mu s$  to 4  $\mu s$  between data runs. The length of the probe time was set by the probe laser power, the Clebsch-Gordan coefficients, and the desired probability of driving into the dark state. This was determined

experimentally, as discussed in Section (6.1.4). A detection pulse followed, during which the Cyclor beam and the Detection Gate were turned on for 250  $\mu s$  or 400  $\mu s$ . The length of the detection pulse was chosen to minimize the overlap between the bright and dark state histograms and was determined experimentally as discussed in Section (6.1.5).

Data was collected for a single run using a separate Labview interface (see Section (3.7.3)) that swept the Probe frequency. (The Probe laser frequency was tuned by locking to  $I_2$  ( $\Delta\nu = 159$  Hz) and sweeping the  $I_2$  doublepass frequency.)

Before taking data for the  $F = 3 \rightarrow F' = 3$  transition, bright and dark histograms were recorded. The Probe power was measured at a convenient position far upstream from the trap and was converted into a corresponding saturation parameter during data analysis (see Section (6.1.3)).

The Probe laser was locked to hyperfine feature  $n$  of line #1599 (see Figure (6.10)) and was scanned during the data run by sweeping the frequency of the iodine doublepass AOMs. Both the iodine lock signal and the photon counts were monitored during the scan to ensure the laser remained locked to the appropriate hyperfine feature of iodine and that the sweep was well within the locking range of the frequency doubling cavities. At each probe saturation parameter a total of four curves were taken as a consistency check and to average over during analysis. We chose to take four separate curves instead of

a single curve in which more experiments were performed per data point. This was a compromise between obtaining enough data to average down technical noise and keeping the time for a single scan short enough that a perturbative occurrence (such as a laser going out of lock) did not waste a lot of time (since we would have to repeat the scan).

For the  $F = 3 \rightarrow F' = 2$  transition, the laser was locked to feature r of line #1599. Curves were taken for only one probe laser power. Originally we had anticipated determining the linewidth from the  $F = 3 \rightarrow F' = 3$  transition, and so taking fewer data curves for the  $F = 3 \rightarrow F' = 2$  transition reduced the total time to collect data. (However, population dynamics (see Section (5.6)) broadened the line and so we choose to extrapolate the natural linewidth from data taken with  $^{24}\text{Mg}^+$ , which has no hyperfine structure.) Bright and dark state histograms were taken for reference, and again, a minimum of four curves were taken at each magnetic field.

Once both transitions were probed, the polarization was changed from  $\sigma^+$  to  $\sigma^-$  by adjusting the half-wave plate upstream of the vacuum chamber by  $45^\circ$ . Both the half-wave plate and quarter-wave plate were then iteratively adjusted to re-optimize the polarization for optical pumping by maximizing the number of photons detected. The measurements for each transition were repeated at the new polarization.

Recall from Section (6.3.1) that the lineshape of the transition is not

Lorentzian because of Doppler shifts due to the ion's residual motion. However, a Lorentzian provided good enough fits to extract line centre and so each data curve was fit to a Lorentzian using Gnuplot [91] to determine this quantity. After examining the residuals it was realized that there was a nonzero varying background, although the difference between the Lorentzian and Voigt profiles would not give rise to the monotonically increasing background observed. The wings of the other Lorentzian contribute less than 1% to the amplitude, which is not enough to explain the background and results in a negligible shift of line centre ( $< 0.005\%$ ). The other Zeeman sublevels shift line centre (see Section (5.6)) and introduce asymmetry, but this does not result in a linear background. The shift due to population dynamics is not relevant to the final result since the Zeeman sublevels shift linearly with varying magnetic field and, in the data analysis, we extrapolated to zero-field or averaged over the two polarizations to determine the un-shifted line centre (see Section (6.2)). At zero field, all the Zeeman sublevels are degenerate. We used a power series to model the observed background, adding a term that was linearly dependent to the frequency and a term that was quadratically dependent to the frequency and each curve was subsequently refit. By examining the residuals we determined that a linear background was sufficient (no structure was observed in the residuals, and the coefficient of the quadratic term was consistent with zero).

## 6.2 Hyperfine $a$ Constant Of The $^2P_{\frac{1}{2}}$ State

During the experiment, we measured the UV double-pass AOM frequency corresponding to the transition frequency for the  $3 \rightarrow 3'$  transition and the  $3 \rightarrow 2'$  transition for varying magnetic fields and at both polarizations ( $\sigma^+$  and  $\sigma^-$ ). To determine the hyperfine  $a$  constant, we need to relate our measured frequency to the absolute transition frequency. As discussed in Section (3.4.3), a portion of the light from the visible doubling cavity was sent to iodine diagnostics. From Equation (3.3), relating the laser frequency to iodine, we obtain:

$$\nu_{(3,\pm 3) \rightarrow (3',\pm 2')}(B_0) = \nu_{I_2(\text{feature } n)} + 8\nu_{DP(3,\pm 3) \rightarrow (3',\pm 2')} + \nu_{MOD} \quad (6.8)$$

$$\nu_{(3,\pm 3) \rightarrow (2',\pm 2')}(B_0) = \nu_{I_2(\text{feature } r)} + 8\nu_{DP(3,\pm 3) \rightarrow (2',\pm 2')} + \nu_{MOD} \quad (6.9)$$

where  $B_0$  is the magnitude of the magnetic field,  $\nu_{I_2}$  is the iodine transition frequency (referred to the UV), and  $\nu_{DP}$  and  $\nu_{MOD}$  are the AOM frequencies for the double-passed and modulating AOMs. The transition frequency is in the UV. A transition driven from a positive  $m_F$  sublevel is driven by  $\sigma^-$  polarized light and a transition driven from a negative  $m_F$  sublevel is driven  $\sigma^+$  polarized light. The value of  $\nu_{DP}$  corresponding to line centre is different for varying magnetic fields since  $\nu_{I_2}$  and  $\nu_{MOD}$  are fixed.

In the low-field limit, the Zeeman sub-levels tune linearly with magnetic

field, and tune symmetrically about  $m_F = 0$  to better than 0.01% for the magnetic-field strengths used in our experiment. From Equation (5.20), which gives the shift in energy of a sublevel, we can calculate the shift in frequency for the transition driving from the ground state to the excited state. This is given by:

$$\nu_{(3,\pm 3)\rightarrow(3',\pm 2')}(B_0) = \nu_{(3,0)\rightarrow(3',0')} \mp (3g_{F=3} - 2g_{F'=3}) \frac{\mu_B}{h} B_0 \quad (6.10)$$

$$\nu_{(3,\pm 3)\rightarrow(2',\pm 2')}(B_0) = \nu_{(3,0)\rightarrow(2',0')} \mp (3g_{F=3} + 2g_{F'=2}) \frac{\mu_B}{h} B_0 \quad (6.11)$$

where  $g_F$  is the g-factor,  $\mu_B$  is the Bohr magneton,  $h$  is Planck's constant, and  $B_0$  is the magnitude of the magnetic field. The difference in sign between the  $(3, -3) \rightarrow (3', -2')$  and the  $(3, -3) \rightarrow (2', -2')$  equations results from the fact that the  $F = 3'$  manifold and the  $F = 3$  manifold tune together with increasing magnetic field whereas the  $F = 2'$  does not.

In taking data, we tuned the frequency sent to the double-pass AOM on the way to the iodine spectrometer. By isolating  $8\nu_{DP}$  (the double-pass AOM frequency in the UV) in Equations (6.8) and (6.9) and substituting in Equations (6.10) and (6.11) we obtain:

$$8\nu_{DP(3,\pm 3)\rightarrow(3',\pm 2')} = \nu_0 \mp (3g_{F=3} - 2g_{F'=3}) \frac{\mu_B}{h} B_0 \quad (6.12)$$

$$8\nu_{DP(3,\pm 3)\rightarrow(2',\pm 2')} = \nu'_0 \mp (3g_{F=3} + 2g_{F'=2}) \frac{\mu_B}{h} B_0. \quad (6.13)$$

Here we have combined the field-independent terms so that:

$$\nu_0 = \nu_{(3,0) \rightarrow (3',0')} - \nu_{I_2(\text{feature } n)} - \nu_{MOD} \quad (6.14)$$

$$\nu'_0 = \nu_{(3,0) \rightarrow (2',0')} - \nu_{I_2(\text{feature } r)} - \nu_{MOD}. \quad (6.15)$$

The frequencies  $\nu_0$  and  $\nu'_0$  are the actual field-independent component of the frequencies that were measured during the experiment.

Using the average counts per experiment, each data curve from the  $(3, \pm 3) \rightarrow (3', \pm 2')$  transition and the  $(3, -3) \rightarrow (2', \pm 2')$  transition was fit to a Lorentzian to determine line centre. For each different Quantization-Coil current, the measured transition frequency is related to the current (and hence magnetic field) by Equations (6.12) or (6.13). The line centres obtained from the fit are plotted as a function of Quantization-Coil current in Figure (6.13).

The data was analysed using three different methods that will be expanded upon in the following sections. In all three methods, we obtained  $\nu_0$  and  $\nu'_0$  which were used to calculate the hyperfine  $a$  constant. The first method involved simultaneously fitting both polarizations for a given transition while keeping the magnitude of the slope constrained to be the same. The constraint on the slope can be justified by noting that, at low magnetic field, the Zeeman sub-levels shift symmetrically about  $m_F = 0$ .

In the second method, the difference in frequency between two polarizations was calculated and plotted as a function of the magnetic field. Both transitions

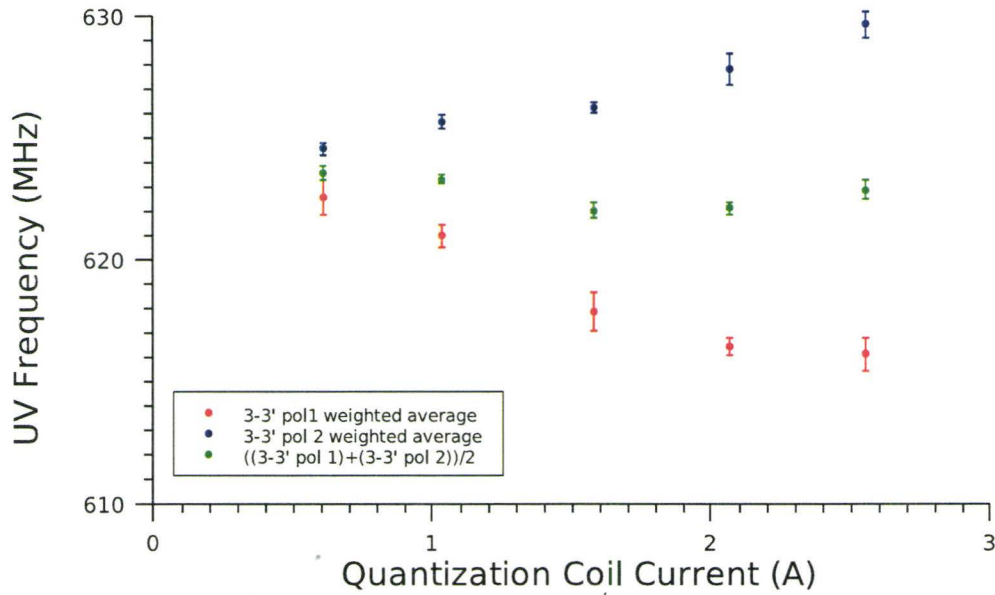
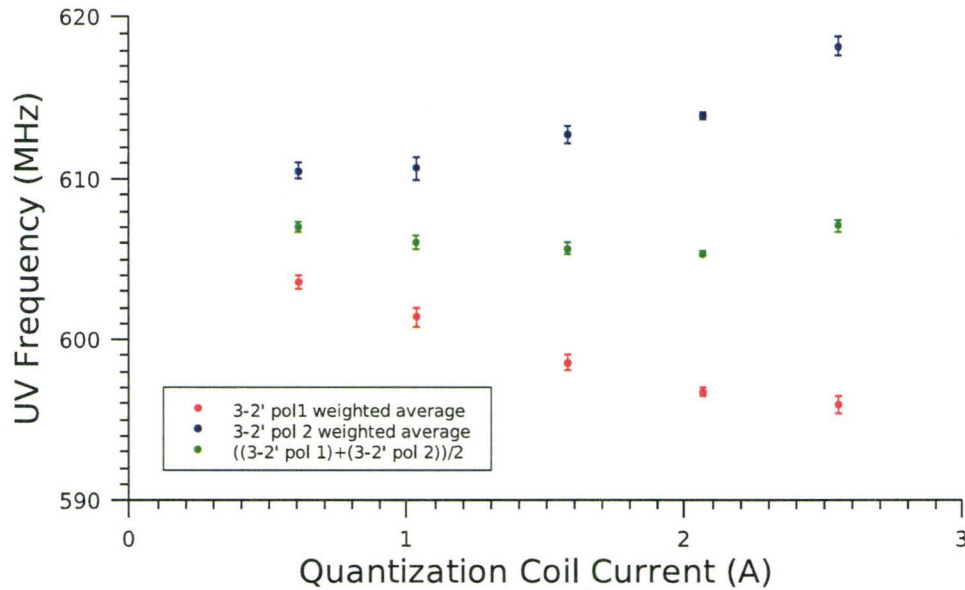
(a)  $(F = 3, m_F = \pm 3) \rightarrow (F' = 3, m'_F = \pm 2)$  transition.(b)  $(F = 3, m_F = \pm 3) \rightarrow (F' = 2, m'_F = \pm 2)$  transition.

Figure 6.13: Line centre is obtained from a fit of the counts vs. frequency data to a Lorentzian and is plotted as a function of magnetic field. At each different magnetic field the polarization of the Probe laser, Cyclor, and Repumper was reversed, corresponding to driving the transition with  $\sigma^+$  or  $\sigma^-$  polarized light. We can obtain the zero-field line centre by extrapolating to zero-field for each polarization or by averaging line centre for the two different polarizations at each magnetic field (since the Zeeman sublevels tune symmetrically about  $m_F = 0$ ).

were simultaneously fit with the constraint that the zero-field crossing should occur at the same coil current for both transitions. This need not necessarily occur at zero current because of possible background fields. This was followed by a simultaneous fit of both polarizations as was done in the first method, except with the additional constraint on the zero-field coil current.

In the third method the average over polarizations for a given transition was calculated and subsequently fit to a straight line with zero slope. All the three methods were compared and determined to be consistent with one another.

### 6.2.1 Constrained Slope Method

In the first approach, the slope of the linear fit was constrained to have the same magnitude for both polarizations in a given transition. This is justified because, at low magnetic field, the different Zeeman sub-levels tune symmetrically about  $m_F = 0$  (within 0.01% for the magnetic fields used). At one laser polarization, we optically pumped into the  $(3, -3)$  state and drove to  $(3', -2')$  or  $(2', -2')$  and at the other polarization we optically pumped into the  $(3, 3)$  state and drove to  $(3', 2')$  or  $(2', 2')$ . From Equations (6.12) and (6.13), the magnitude of the shift in transition frequency for transitions starting in the  $(3, -3)$  state is the same as transitions starting in the  $(3, 3)$  state.

Using Gnuplot [91], we simultaneously fit both polarizations to:

$$y_1(I_Q) = b_1 + mI_Q \quad (6.16)$$

$$y_2(I_Q) = b_2 - mI_Q \quad (6.17)$$

where  $m$ ,  $b_1$  and  $b_2$  were left as free parameters and  $I_Q$  was the coil current. A simultaneous fit was done by defining a dummy variable that switched between Equation (6.16) and Equation (6.17) for each data set during the course of an iteration. The resultant fits are shown in Figure (6.14) and the fitting results are summarized in Table (6.1).

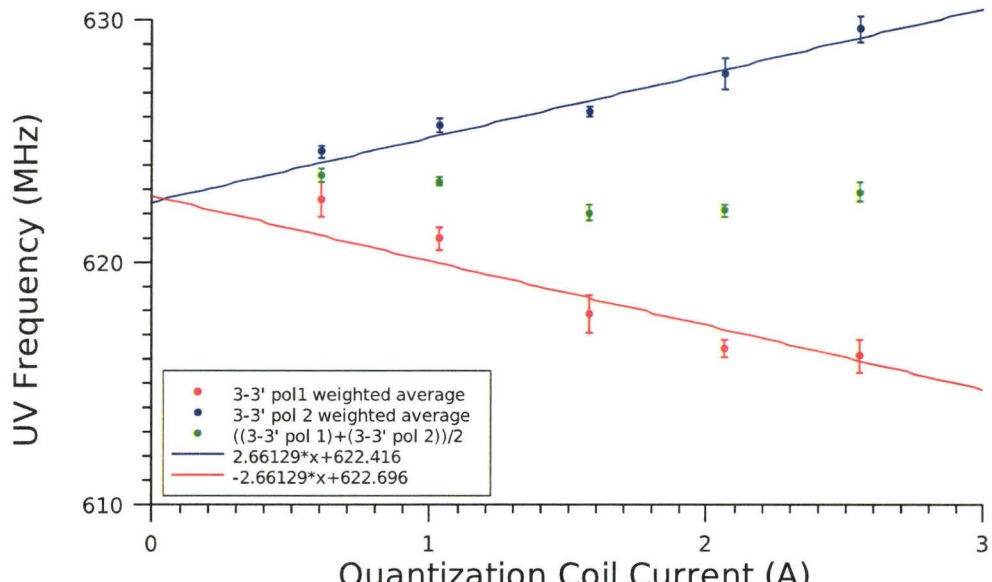
Table 6.1: Fitting results from the constrained-slope method

Transition	$m$	$b_1$	$b_2$
$(3 \rightarrow 3')$	$\pm 2.66 \pm 0.40 \frac{MHz}{A}$	$622.42 \pm 0.59 MHz$	$622.70 \pm 0.81 MHz$
$(3 \rightarrow 2')$	$\pm 3.69 \pm 0.48 \frac{MHz}{A}$	$606.69 \pm 0.95 MHz$	$604.77 \pm 0.91 MHz$

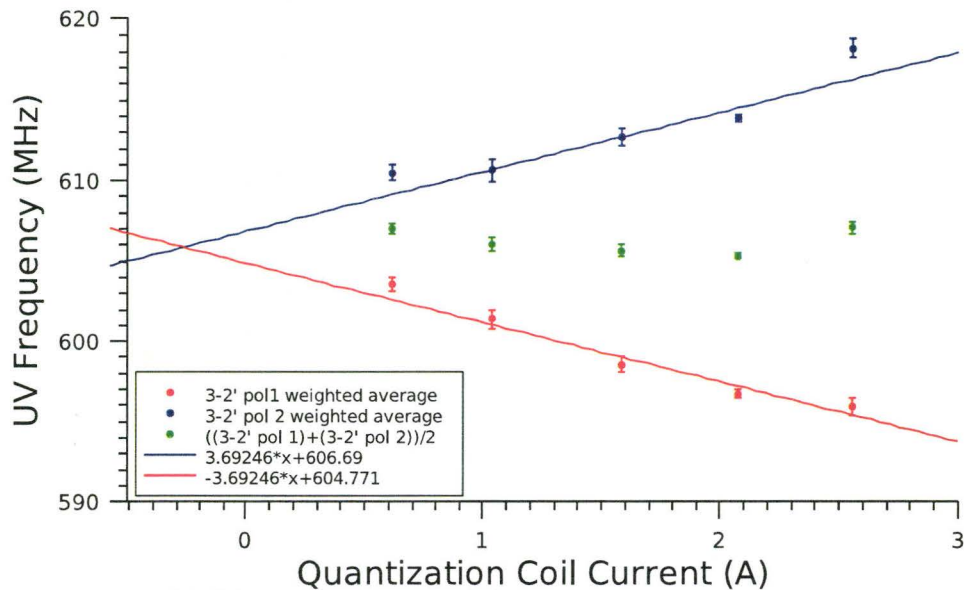
A zero-field crossing and line centre were calculated from the slopes and intercepts obtained from the fitting routine. From Equations (6.16) and (6.17) we obtain:

$$I_Q(B = 0) = \frac{b_2 - b_1}{2m} \quad (6.18)$$

$$\nu(B = 0) = \frac{b_1 + b_2}{2}. \quad (6.19)$$



(a)  $(F = 3, m_F = \pm 3) \rightarrow (F' = 3, m_{F'} = \pm 2)$  transition.



(b)  $(F = 3, m_F = \pm 3) \rightarrow (F' = 2, m_{F'} = \pm 2)$  transition.

Figure 6.14: The line centre vs. Quantization-Coil current was fit with the slope constrained to have the same magnitude for both polarizations. At low magnetic field, the different Zeeman sublevels tune symmetrically about  $m_F = 0$  and so we constrain the magnitude of the slope to be fixed for both polarizations. The results of the fit are summarized in Table (6.1) for both transitions.

Here,  $I_Q = 0.05_{-0.30}^{+0.32}$  A and  $\nu(B = 0)$  is  $\nu_0 = 622.56 \pm 0.70$  MHz in the case of the  $3 \rightarrow 3'$  transition (see Equation (6.14)). For the  $3 \rightarrow 2'$  transition,  $I_Q = 0.26_{-0.33}^{+0.25}$  A and  $\nu(B = 0)$  is  $\nu'_0 = 605.73 \pm 0.93$  MHz (see Equation (6.15)).

## 6.2.2 Constrained Slope and Zero-Field Method

An additional constraint on the fit was included in this second analysis. Specifically, the zero-field crossing for both the ( $3 \rightarrow 3'$ ) transition and the ( $3 \rightarrow 2'$ ) transition should occur at the same Quantization-Coil current. To include this constraint, the frequency difference between the transitions for the two polarizations in a given transition was calculated, and plotted as a function of increasing coil current. This is shown for both transitions in Figure (6.15). By taking the frequency difference, the dependence on the magnetic field (and hence the quantization coil current) is isolated. The frequency difference was simultaneously fit for both transitions to a straight line of the form:

$$\Delta\nu_{3 \rightarrow 3'}(I_Q) = m_{3 \rightarrow 3'}(I_Q - I_Q(B = 0)) \quad (6.20)$$

$$\Delta\nu_{3 \rightarrow 2'}(I_Q) = m_{3 \rightarrow 2'}(I_Q - I_Q(B = 0)) \quad (6.21)$$

where  $m_{3 \rightarrow 3'}$ ,  $m_{3 \rightarrow 2'}$ , and  $I_Q(B = 0)$  were left as free parameters. The original data shown in Figure (6.13) were re-fit requiring that the magnitudes of the slopes were equal for the two polarizations and that the zero-field Quantization

Coil current was  $-0.084 \pm 0.1197$  A. Explicitly we fit to:

$$y_1(I_Q) = m(I_Q - I_Q(B = 0)) + \nu(B = 0) \quad (6.22)$$

$$y_2(I_Q) = -m(I_Q - I_Q(B = 0)) + \nu(B = 0). \quad (6.23)$$

Again,  $\nu(B = 0)$  corresponds to  $\nu_0$  for the  $3 \rightarrow 3'$  transition and  $\nu'_0$  for the  $3 \rightarrow 2'$  transition. The results of the fit are summarized in Table (6.2).

Table 6.2: Fitting results from the constrained-slope and zero-field coil current

Transition	$m$	$\nu(B = 0)$
$(3 \rightarrow 3')$	$\pm 2.46^{+0.44}_{-0.15} \frac{MHz}{A}$	$622.49^{+0.15}_{-0.04} MHz$
$(3 \rightarrow 2')$	$\pm 4.01^{+0.65}_{-0.23} \frac{MHz}{A}$	$605.72^{+0.01}_{-0.03} MHz$

### 6.2.3 Average Polarization Method

By averaging between the two polarizations for a given transition at a given coil current, we determined  $\nu_0$  and  $\nu'_0$  (which we generically label as  $\nu(B = 0)$ , to be consistent with the previous analysis methods). The average data points were subsequently fit to a straight line, with zero slope and also fit to a straight line allowing the slope to vary. A weighted average of the five values was also calculated. The results are shown in Figure (6.16), and summarized in Table (6.3).

In the following section we compare the results from the different analysis

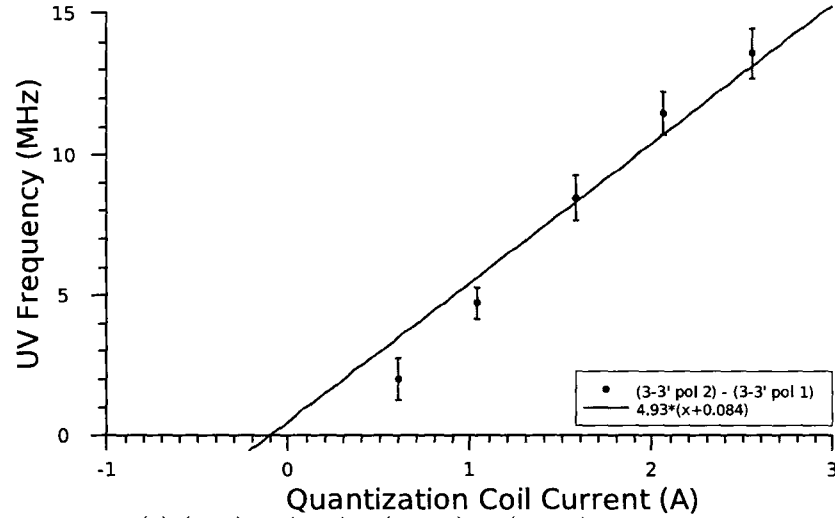
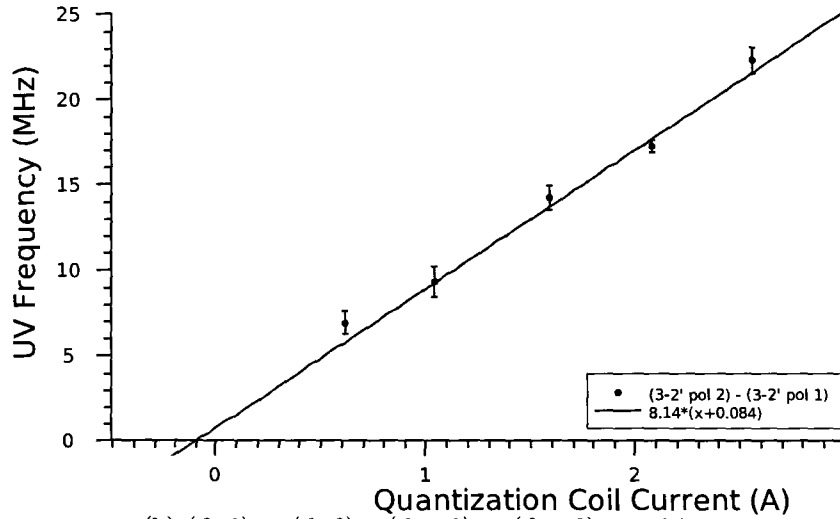
(a)  $(3, 3) \rightarrow (3, 2) - (3, -3) \rightarrow (3, -2)$  transition.(b)  $(3, 3) \rightarrow (2, 2) - (3, -3) \rightarrow (2, -2)$  transition.

Figure 6.15: For each transition, the difference in line centre for the two polarizations is plotted as a function of Quantization Coil current. The field dependence for both transitions was simultaneously fit with the constraint that the zero-field crossing occur at the same Quantization-Coil current for both transitions. The Quantization-Coil current corresponding to zero magnetic field ( $I_Q(B = 0) = 0.084 \pm 0.119$  A) was used to further constrain a fit of the original data (Figure (6.13)). The results of the fits are summarized in Table (6.2).

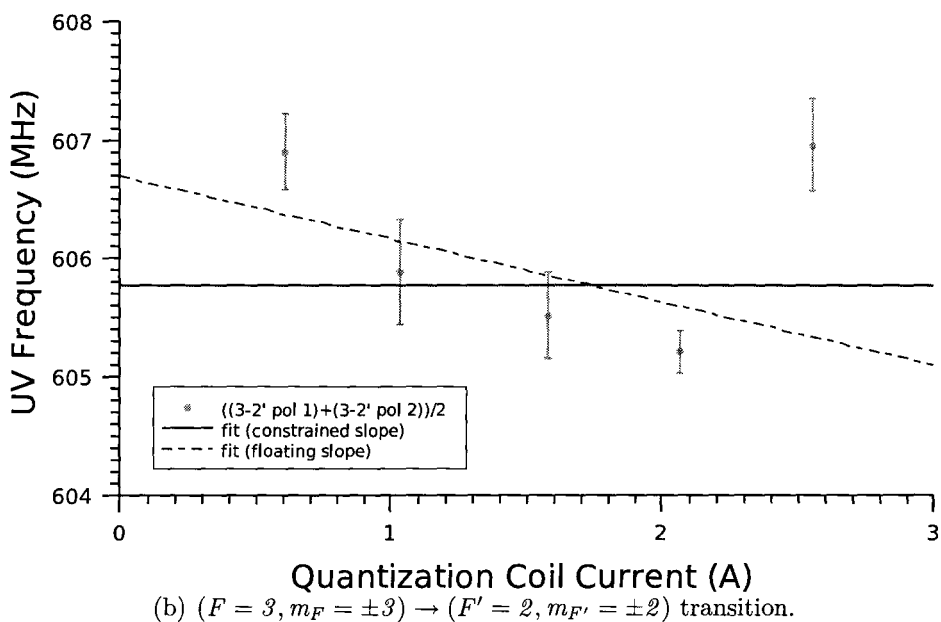
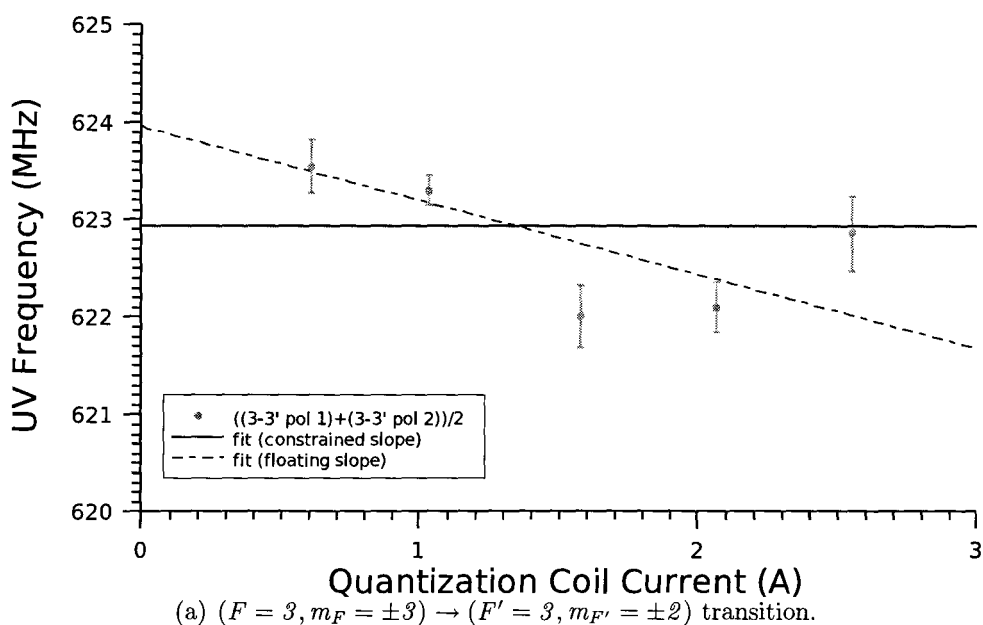


Figure 6.16: We obtain the field-free transition frequency by averaging between the two polarizations for a given transition at a given coil current. The average data points were subsequently fit to a straight line, with zero slope and also fit to a straight line allowing the slope to vary. A weighted average of the five values was also calculated. The results from the fit and weighted average are summarized in Table (6.3).

Table 6.3: Weighted average and fitting results from the average-polarization method

Method	Transition	$\nu(B = 0)$	slope
Fit (constrained slope)	$(3 \rightarrow 3')$	$622.93 \pm 0.29 \text{ MHz}$	$0 \frac{\text{MHz}}{\text{A}}$
Fit (constrained slope)	$(3 \rightarrow 2')$	$605.77 \pm 0.37 \text{ MHz}$	$0 \frac{\text{MHz}}{\text{A}}$
Fit (floating slope)	$(3 \rightarrow 3')$	$623.7 \pm 0.6 \text{ MHz}$	$-0.75 \pm 0.39 \frac{\text{MHz}}{\text{A}}$
Fit (floating slope)	$(3 \rightarrow 2')$	$606.7 \pm 1.1 \text{ MHz}$	$-0.53 \pm 0.61 \frac{\text{MHz}}{\text{A}}$
Weighted Average	$(3 \rightarrow 3')$	$622.93 \pm 0.11 \text{ MHz}$	N/A
Weighted Average	$(3 \rightarrow 2')$	$605.77 \pm 0.13 \text{ MHz}$	N/A

methods.

## 6.2.4 Summary of Analysis Methods

In each of the analysis methods we determined  $\nu(B = 0)$  (and hence  $\nu_0$  and  $\nu'_0$ ). In order to relate  $\nu_0$  and  $\nu'_0$  to the hyperfine  $a$  constant, we must first re-express them in terms of the field-free transition frequencies. Re-arranging Equations (6.14) and (6.15) we have:

$$\nu_{(3,0) \rightarrow (3',0')} = \nu_0 + \nu_{I_2(\text{feature } n)} + \nu_{MOD} \quad (6.24)$$

$$\nu_{(3,0) \rightarrow (2',0')} = \nu'_0 + \nu_{I_2(\text{feature } r)} + \nu_{MOD}. \quad (6.25)$$

Thus, the hyperfine  $a$  constant is:

$$a = \frac{\nu_{(3,0) \rightarrow (2',0')} - \nu_{(3,0) \rightarrow (3',0')}}{3} \quad (6.26)$$

$$= \frac{\nu'_0 - \nu_0 + \nu_{I_2(\text{feature } r)} - \nu_{I_2(\text{feature } n)}}{3} \quad (6.27)$$

$$= \frac{\nu'_0 - \nu_0 + \Delta\nu_{I_2}}{3} \quad (6.28)$$

where  $\Delta\nu_{I_2} = 323.65 \pm 0.06 \text{ MHz}$  is the frequency separation (in UV MHz) between iodine features  $n$  and  $r$  of line #1599 from the Iodine Atlas [69] (see Section (6.1.6)). The results from the different analysis methods are summarized in Table (6.4).

In the constrained slope method the zero-field current was obtained from the  $(3 \rightarrow 3')$  and the  $(3 \rightarrow 2')$  transition. A third value for the zero-field current was obtained from the constrained slope and constrained zero-field crossing method. All three values for the zero-field current fall within one standard deviation of one another and are consistent with a zero-field current of 0 A.

The ratio of the slope between the two transitions,  $R$ , is calculated from the measured values for the two applicable cases (see Table (6.4)). The measured values return a slope that is consistent between the two different analyses. The ratio was also calculated from theory assuming a linear Zeeman shift resulting in a ratio of 1.58. The calculated value falls within the uncertainty range for

both analysis methods; however, constraining both the slope and zero-field crossing reduces the uncertainty in the measured value.

In the constrained slope method, we obtained a value of  $102.28 \pm 0.39$  MHz for the hyperfine  $a$  constant. Constraining the slope is justified since the different Zeeman sublevels tune symmetrically about  $m_F = 0$  (to within 0.01%), and by constraining the slope we average out the pulling of line centre due to population dynamics (see Section (5.6)). In this method, we have allowed the zero-field current to vary between the two transitions and obtain two values for the zero-field current that are consistent with one another. This suggests that any variations in the magnetic field were not large enough to significantly effect our measured value, and so we added an additional constraint that zero-field cross be the same for both transitions.

For the constrained slope and constrained zero-field current method we determined that the hyperfine  $a$  constant is  $102.29 \pm 0.16$  MHz. Again, we justify constraining the slope because the different Zeeman sublevels tune symmetrically about  $m_F = 0$ .

By constraining the zero-field current we have implicitly assumed that variations in the magnetic field were negligible. Since line centres for the two transitions and two polarizations were measured on the same day, magnetic field variations occurring on slow time scales (day to day variation) would result in an overall shift of the zero-field value. While this effects our accuracy of the

measured zero-field current, it does not effect our measured value of line centre (since the relative magnitudes of the slope of both polarizations for a given transition are not affected).

Variations in the magnitude of the magnetic field on a given day would shift each data point. However, if such variations occurred, we would have seen a reduction in the quality of optical pumping because as the magnetic field changes we reduce the likelihood of preparing the ion in the  $(3, -3)$  state (see Section (6.1.1)).

In the average polarization method we obtained a hyperfine  $a$  constant of  $102.16 \pm 0.16$  MHz. No constraints were placed on the data to obtain the field-independent frequencies  $\nu_0$  and  $\nu'_0$ . The frequencies were subsequently fit to a straight line with zero slope to obtain an average value for the field-independent frequency. In this third method, we also allowed the slope to vary in the fit, and in both cases the slope was consistent to zero slope within two standard deviations. However, from Figure (6.16) we can see that the points lie on either side of the plot. Since no compelling evidence of a linear trend exists, we choose not to quote this value as our measured value. With this method we obtained a value for the hyperfine  $a$  constant that is consistent with all of the other analysis techniques discussed here. In addition to fitting the average values, we also calculated a weighted average of the frequencies for each transition. By calculating a weighted average we obtained a smaller

uncertainty in line centre; however, we choose not to quote this uncertainty in our final result since the scatter in the data points (see Figure (6.16)) is larger than uncertainty in the weighted average and so the fit uncertainty is more representative of what was experimentally observed.

The average method is consistent with the previous two methods discussed, although it does not require any assumptions on how the different Zeeman sublevels tune, nor does it make any assumption on the field-free current, since no extrapolation to zero-field is required. This results in a straightforward measurement of the hyperfine  $a$  constant. From this method, we determined that the hyperfine  $a$  constant is  $102.16 \pm 0.16$  MHz and that the other methods used to analyse our data are consistent with this measured value.

## 6.3 Linewidth of $Mg^+$

### 6.3.1 Contributions to Line Broadening

Recall that the measured magnesium linewidth is a convolution of the natural linewidth, the Doppler broadening, and the laser linewidth. In Section (2.2.3) we showed how ion motion results in sidebands in the absorption spectrum. In the resolved-sideband limit, the sideband spacing is much larger than the natural linewidth, and so the sidebands do not contribute to the measured linewidth. However, we are not in the resolved-sideband limit

Table 6.4: Hyperfine  $a$  Constant for  ${}^2P_{\frac{1}{2}}$ : Summary of Analysis

Method	$a$ (MHz)	$\nu_0$ (MHz)	$\nu'_0$ (MHz)	$I_Q(B=0)$ (A)	$R$
constrained slope, zero-field current from ( $3 \rightarrow 3'$ ) transition	$102.28 \pm 0.39$	$622.56 \pm 0.70$	$605.73 \pm 0.93$	$0.05^{+0.32}_{-0.30}$	$1.39 \pm 0.20$
constrained slope, zero-field current from ( $3 \rightarrow 2'$ ) transition	$102.28 \pm 0.39$	$622.56 \pm 0.70$	$605.73 \pm 0.93$	$-0.26^{+0.25}_{-0.33}$	$1.39 \pm 0.20$
constrained slope and constrained zero-field	$102.29 \pm 0.16$	$622.49^{+0.38}_{-0.29}$	$605.72^{+0.29}_{-0.38}$	$-0.09 \pm 0.12$	$1.63 \pm 0.07$
average of both polarizations (constrained slope)	$102.16 \pm 0.16$	$622.93 \pm 0.29$	$605.77 \pm 0.37$	N/A	N/A
average of both polarizations (floating slope)	$102.13 \pm 0.41$	$623.7 \pm 0.6$	$606.7 \pm 1.1$	N/A	N/A
average of both polarizations (weighted average)	$102.16 \pm 0.06$	$622.93 \pm 0.11$	$605.77 \pm 0.13$	N/A	N/A

( $\Gamma \simeq 2\pi \cdot 42 \text{ MHz}$ ,  $\omega_x \simeq 2\pi \cdot 4.7 \text{ MHz}$ ,  $\omega_y \simeq 2\pi \cdot 4.3 \text{ MHz}$ , and  $\omega_z \simeq 2\pi \cdot 0.421 \text{ MHz}$ ) and so these sidebands do contribute to the measured linewidth. By putting an upper limit on the ion temperature, we can estimate the contribution to the linewidth due to motional sidebands.

### Doppler Broadening

Broadening of the measured line results from Doppler effects since, at nonzero temperature, the ion has some residual motion. To determine the contribution to the linewidth, we estimated an upper limit to the ion temperature. In Section (2.3.3) we discussed the temporal dynamics of laser cooling. Following the analysis of Wesenberg *et al.* [48], we showed that the equilibrium mechanical energy can be calculated by numerically integrating Equation (2.73). (In fact, we can also calculate the equilibrium mechanical energy analytically [54].) We can subsequently use the ion's steady-state mechanical energy to assign a temperature to the ion.

In our previous analysis (see Section (2.3.3)), we neglected any possible heating due to background heating (eg. anomalous heating [51]). In the presence of anomalous heating, the ion equilibrates with a higher mechanical energy and hence a higher temperature. If we allow the ion to heat for a fixed period of time (by turning off the cooling lasers) and then laser cool while monitoring the time-dependent fluorescence, we can determine what the heating rate is, since we can determine the ion's average energy from the time-dependent

fluorescence [48]. This turns out not to be practical with our trap since a data run would require several days of continuous data-taking to complete. Even with enough people around so that we could monitor the experiment, the laser power would inevitably drift (usually due to polarization drifts in the laser), and we wouldn't be able to optimize them mid-experiment. Also, on these long timescales we would likely lose the ion and have to start over.

Instead, we attempted to set an upper limit on the heating rate. To do this, we trapped a single  $^{25}\text{Mg}^+$  ion, following the procedure outlined in Section (6.1.1). Wesenberg *et al.* showed that sensitivity to ion heating can be enhanced by first coherently driving the ion [48] and so the experiment consisted of a laser cooling pulse (so that the ion began each experiment at its equilibrium energy), a coherent drive pulse, possibly a heating pulse, and a detection/cooling pulse. If no statistical difference was observed between data curves where a heating pulse was applied and where a heating pulse wasn't applied, then we can use the uncertainty in the fit of the two data curves to put an upper limit on the heating rate (see below).

First, we coherently drove the ion by applying an AC voltage on the Vamp electrode ( $700\text{ mV}_{pp}$ ), near the trap frequency ( $398.663\text{ kHz}$ ), for a fixed period of time ( $500\text{ }\mu\text{s}$ ). Second, we coherently drove the ion with the same pulse, and allowed an additional wait time of  $300\text{ }\mu\text{s}$  (during which any fluctuating background fields could heat the ion [51]). Both data curves are shown in

Figure (6.17) along with a reference curve which consisted of a cooling pulse and a cooling/detection pulse.

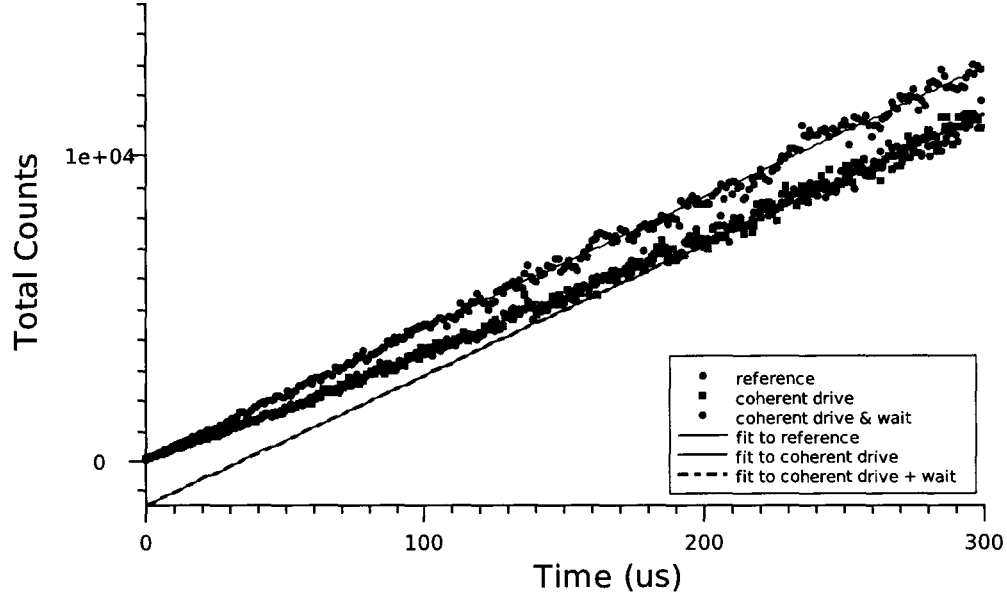


Figure 6.17: A plot of the time-dependent fluorescence for different initial ion energies. In the reference curve, no heating was applied (so the ion started at its equilibrium energy). In the second curve we coherently drove the ion by applying an AC voltage ( $700\text{ mV}_{pp}$ ,  $398.663\text{ kHz}$ ,  $500\text{ }\mu\text{s}$ ) to the Vamp electrode. At short times ( $t < 220\text{ }\mu\text{s}$ ) the ion is still “hot”, and so the scatter-rate is lower, resulting in fewer detected photons. After the ion has reached its equilibrium energy ( $t > 220\text{ }\mu\text{s}$ ) it scatters photons at the same rate as the reference curve. A similar trend is seen for the third curve, where we coherently drove the ion and waited an additional  $300\text{ }\mu\text{s}$ .

In the curve where we coherently drove the ion, we see a reduction in fluorescence compared to the reference curve. By approximately  $220\text{ }\mu\text{s}$ , the ion has been cooled to its equilibrium mechanical energy and scatters photons at the same rate as the reference curve. Similarly, in the curve where we coherently drove the ion and waited for  $300\text{ }\mu\text{s}$ , we see the same trend. In this case, appreciable heating would cause a further reduction in the total number

of photons detected. By fitting the linear region, and using the difference in the intercept between the curve in which we coherently drove the ion and the curve in which we coherently drove the ion and waited  $300 \mu s$  we can determine the difference in number of photons between the two curves (and hence the energy difference).

From a fit to the linear region we obtain an intercept of  $-1538 \pm 32$  photons in 1000 experiments for the curve where we coherently drove the ion, and  $-1539 \pm 27$  photons in 1000 experiments for the curve where we coherently drove the ion and waited an additional  $300 \mu s$ . Thus there is no significant difference in the initial ion temperature between the two curves. We varied the total number of points kept in the fit, and noticed no statistical difference between the two curves. We also allowed the slope to vary in each of the two curves (keeping only data points in the linear region). This increased the uncertainty in the intercept (although the slope in each curve where the ion was heated remained consistent with the slope obtained from the reference curve). We decided to constrain the slope, which is justified by the fact that the steady state fluorescence between the three curves is the same since the ion equilibrates to the same final energy.

Using the uncertainty in the intercept for the coherent drive curve and coherent drive with additional wait-time curve, we estimated a maximum difference of 60 photons detected over 1000 experiments. This corresponds to

a difference of 0.06 detected photons per experiment. Since the detection efficiency (see Section (6.1.3)) is  $0.27 \pm 0.01\%$ , a difference of 0.06 detected photons per experiment corresponds to a difference of 22 photons (on average) scattered per experiment. With a laser detuning of  $\frac{\Gamma}{2}$ , this corresponds to an energy of  $3 \cdot 10^{-25} J$  in  $300 \mu s$ . We stress that this corresponds to an upper limit on the heating rate. If our ion trap is typical, studies indicate that, with our trap size, the anomalous heating rate should be on the order of  $10^{-24} \frac{J}{s}$  [93].

Using our upper limit on the heating rate ( $1 \cdot 10^{-21} \frac{J}{s}$ ), we can obtain an upper limit on the ion temperature in one of two ways. We can numerically integrate Equation (2.73) to obtain the equilibrium mechanical energy. The disadvantage of this method is that it assumes no external heating mechanisms and that the spontaneous emission is isotropic. While it is possible to account for both of these effects, a more straightforward calculation of the equilibrium energy (and hence temperature) can be performed analytically and has been done by Itano and Wineland [54]. Ignoring background heating, they obtained:

$$T_{eq}(\Delta_L) = \frac{\hbar}{4k_B} \left( \frac{\Delta_L^2 + \left(\frac{\Gamma}{2}\right)^2}{\Delta_L} \right) \left( 1 + \frac{f_{si}}{f_i} \right). \quad (6.29)$$

Here we have introduced  $f_{si} = \frac{3}{10}$  and  $f_i = \frac{1}{2}$  (along the axial direction) and  $f_i = \frac{1}{4}$  (along the radial directions) to account for the absorption and emission pattern for a cooling transition in which  $\Delta m = \pm 1$  (which is the case for

all of the experiments described in this thesis). The Doppler cooling limit is obtained when  $\Delta_L = \frac{\Gamma}{2}$ . The minimum temperature is  $0.80 \text{ mK}$  along the axial direction and  $1.1 \text{ mK}$  along the radial directions.

To include the effect of background heating, we multiply the heating rate by the average scattering time ( $\frac{2}{\Gamma}$ ), resulting in an energy of  $\mathcal{E}_H = 4.8 \cdot 10^{-29} \text{ J}$ . We can re-express this energy as a frequency by dividing by Planck's constant, giving us  $11.6 \text{ kHz}$ . As reference, the recoil energy ( $\frac{\hbar^2 k^2}{2m}$ ), expressed in frequency units, is  $106 \text{ kHz}$ . Thus, we anticipate an increase on the order of 10% in the equilibrium temperature. Including background heating, the analytic expression for the equilibrium temperature is:

$$T'_{eq}(\Delta_L) = \frac{m \left[ \frac{\hbar^2 k^2}{2m} (f_i + f_{si}) + \mathcal{E}_H \right] \left[ \Delta_L^2 + \left( \frac{\Gamma}{2} \right)^2 \right]}{4k_b \Delta_L \hbar^2 f_i}, \quad (6.30)$$

which is minimized when  $\Delta_L = \frac{\Gamma}{2}$ . The minimum temperature is  $0.90 \text{ mK}$  along the axial direction and  $1.24 \text{ mK}$  along the radial direction.

In Section (6.3.2) we fit our measured linewidth data using the actual lineshape, accounting for the laser-detuning-dependent temperature. The actual lineshape is non-trivial, since Doppler broadening effects are complex. Recall from Section (2.2.3) that the effect of secular motion and micromotion results in sidebands in the absorption spectrum, separated by multiples of sums and differences of the secular and drive frequencies, whose amplitude is determined by Bessel functions. Things are further complicated since

the axial frequency ( $\omega_z \approx 2\pi \cdot 421 \text{ kHz}$ ) differed from the radial frequencies ( $\omega_x \approx 2\pi \cdot 4.7 \text{ MHz}$ ,  $\omega_y \approx 2\pi \cdot 4.3 \text{ MHz}$ ) in our experiment. Furthermore, since we are not in the resolved sideband limit, we do not observe distinct peaks.

Another way to think of how Doppler broadening effects the lineshape is to consider the RMS velocity associated with the ion's equilibrium mechanical energy. We can calculate the probability that the ion has some particular energy (and hence velocity, due to normal micromotion and secular motion) and determine the resultant lineshape. In Section (2.2.3) we explicitly treated the case for a harmonic probability distribution. In the case of a Maxwell-Boltzmann distribution, the lineshape is given by the Voigt profile [94]:

$$G = \frac{1}{\pi} \sqrt{\frac{m}{k_B T}} \int_{-\infty}^{\infty} \left( \frac{\frac{\Gamma'}{2}}{(\Delta_L + \vec{k}_L \cdot \vec{v})^2 + \left(\frac{\Gamma'}{2}\right)^2} \right) e^{-\left(\frac{mv^2}{2k_B T}\right)} dv \quad (6.31)$$

where  $m$  is the ion mass,  $k_B$  is Boltzmann's constant,  $T$  is the ion temperature,  $\Gamma'$  is the linewidth,  $\Delta_L$  is the laser detuning from resonance,  $\vec{k}_L$  is the laser wavevector and  $\vec{v}$  is the ion velocity. Examining the integrand, we see that the first term is simply a Lorentzian (including a term accounting for the first-order Doppler shift) and the second term is the probability that the ion has a particular velocity  $v$ . What we are doing, then, is summing over Lorentzians (whose line centres are Doppler shifted) weighted by the probability that the ion has that particular velocity. However, Equation (6.31) only accounts for the secular motion. In fact, the term  $\frac{k_B T}{m}$  corresponds to the maximum velocity

of the secular motion.

To account for the normal micromotion, we need to convolve multiple Gaussians, each with a width corresponding to the Fourier velocity component calculated by taking the derivative of the total ion motion (see Equation (2.21)). Furthermore, since the  $q_{x,y}$  parameters that we operated at were  $q_x = 0.783$  and  $q_y = 0.747$ , we need to consider higher order terms from Equation (2.21). During fitting, we included up to  $n = \pm 6$ . Thus, the resultant lineshape, including secular motion and normal micromotion is given by:

$$G_{tot} = \mathcal{N} \int_{-\infty}^{\infty} \left( \frac{\frac{\Gamma'}{2}}{(\Delta_L + \vec{k} \cdot \vec{v})^2 + \left(\frac{\Gamma'}{2}\right)^2} \right) e^{-\frac{v^2}{2v_{tot}^2}} \quad (6.32)$$

where  $\mathcal{N}$  is an overall normalization and  $v_{tot}^2 = \sum_{n=-6}^6 v_{n,\max}^2$ . Each of the  $n$  velocity components contributes to the Doppler width in quadrature. Although the normal micromotion is driven motion, its amplitude is proportional to the secular motion amplitude (but at a separate Fourier frequency) and so the probability distribution for micromotion velocities can be treated as an independent random variable which also has a Gaussian distribution. Furthermore, to account for motion in three dimensions, this must be repeated for each of the three directions and so the final  $v_{tot}$  includes 21 terms, 7 for each dimension.

If the ion was cooled to the same equilibrium energy at each detuning, then we would simply fit the data to the form given by Equation (6.32); however,

this was not the case in our experiment. The ion equilibrated at a different temperature for each different laser detuning because probing and detection was done with the same laser beam as the linewidth measurement (see Section (6.3.2)). We can still fit the data to a Voigt-like profile; however, we need to account for the laser-detuning-dependent equilibrium temperature:

$$G_{tot}(T) = \mathcal{N}(T) \int_{-\infty}^{\infty} \left( \frac{\frac{\Gamma'}{2}}{(\Delta_L + \vec{k} \cdot \vec{v})^2 + \left(\frac{\Gamma'}{2}\right)^2} \right) e^{-\frac{v^2}{2v_{tot}^2(T)}}. \quad (6.33)$$

By fitting the magnesium linewidth data to Equation (6.33) we determine the linewidth free of Doppler broadening. In practice, we fit our measured data assuming no heating and then re-fit the data assuming the maximum heating rate to obtain an upper and lower limit on the measured linewidth. From the fit we determined that the uncertainty in the measured linewidth is dominated by the fit uncertainty, with the uncertainty in ion temperature contributing less than 0.09%. In Section (6.3.2) we present the results of this method; however, before we can determine the natural linewidth of magnesium, we must first discuss our measurement of the laser linewidth, since it also contributes to the measured linewidth.

### Laser Linewidth

The contribution to the measured linewidth due to the laser linewidth was characterized by using a two-mirror cavity as a frequency discriminator for high

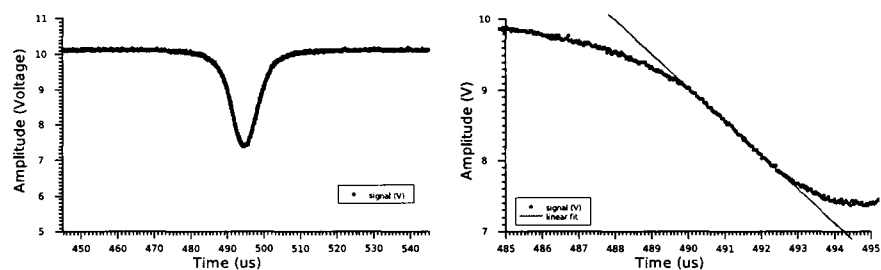
frequency noise and a hyperfine feature of iodine as a frequency discriminator for low frequency noise. In the cavity, changes in laser frequency result in changes in optical cavity length. By monitoring the reflected signal from the cavity on a photodetector, we can relate the changes in the signal amplitude directly to changes in the laser frequency. Alternatively, a hyperfine feature of iodine can be used as a frequency discriminator since changes in laser frequency are related to changes in absorption. In fact, each of these methods is suitable for different frequency ranges and so we used both to determine the laser linewidth, as we will discuss below.

At low frequencies the measured fluctuations are dominated by table vibrations and sound (when the cavity is used for the noise measurements); however, at high frequencies, the measured fluctuations are not. The advantage of using an iodine feature is that it is not sensitive to room vibrations (like the cavity is) and so the measured fluctuations are dominated by laser frequency fluctuations; however, we are not sensitive to high frequencies fluctuations (above the bandwidth of the lock-in amplifier) since the lock-in amplifier acts as a low-pass filter. Thus, we determined the laser linewidth by taking the total frequency noise as the sum of the low frequency noise (determined from the RMS frequency fluctuations of the iodine signal) and the high frequency noise (determined from the RMS frequency fluctuations of the cavity in a regime where cavity mechanical noise is negligible). In both cases, we locked to io-

dine with a time constant of 1 *ms* on the lock-in amplifier since this was the configuration with which we took data.

The cavity consisted of a high-reflectivity mirror ( $R > 99.9\%$ ,  $f = 37.5$  *mm*) that was epoxied to a Thorlabs PZT (*AE0505D08F*) and a flat input-coupler mirror ( $R > 99\%$ ). The two mirrors were separated by  $57 \pm 2$  *mm*, and beam height was 50.8 *mm* from the optical table. By keeping the cavity small, we increased the likelihood that table vibrations effected both mirrors similarly so as to reduce the contribution of table vibrations to our cavity noise spectrum.

The reflected light was monitored with a Thorlabs photodetector (*PDA400*) that had a bandwidth of 10 *MHz*. The signal from the photodetector was connected to a Techtronix digital oscilloscope (*TDS1000B*) that had a bandwidth of 40 *MHz*. A plot of a cavity fringe obtained from the digital oscilloscope is shown in Figure (6.18(a)).



(a) A plot of a single fringe of the cavity used to characterize laser linewidth. (b) A plot of the linear region of a single fringe of the cavity used to characterize laser linewidth.

Figure 6.18: An oscilloscope plot of a cavity fringe (single-shot) for the cavity used to characterize the laser linewidth at high frequencies. The linear portion of the fringe was fit to a straight line using 26 data points from 332.5  $\mu s$  to 333  $\mu s$ .

Fluctuations due to vibration, sound, laser intensity, and laser frequency

noise cause the cavity fringe to move, resulting in a change in the measured amplitude. We assumed that all signal fluctuations were due to laser frequency fluctuations. We can linearly relate changes in the measured amplitude to frequency deviations by tuning the laser frequency so that we are in the linear region of a cavity fringe (see Figure (6.18(b))). The laser frequency deviations are then given by:

$$\Delta\nu_L = \left(\frac{\Delta\nu_L}{\Delta V_L}\right) \left(\frac{\Delta V_L}{\Delta t_s}\right) \left(\frac{\Delta t_s}{\Delta V_s}\right) \Delta V_s \quad (6.34)$$

where  $\Delta\nu_L$  is a change in the laser frequency,  $\Delta V_L$  is a change in the voltage driving the piezo internal to the laser (to change laser frequency),  $\Delta t_s$  is a change in the measured time on the oscilloscope, and  $\Delta V_s$  is a change in the measured amplitude on the scope.

From Section (6.1.6), we determined  $\frac{\Delta\nu_L}{\Delta V_L} = 64.3 \pm 0.3 \frac{\text{MHz}}{\text{V}}$ . To calibrate the relationship between  $\Delta V_L$  and  $\Delta t_s$  we applied a difference of 31.4 V and measured how far the cavity fringe moved on the display oscilloscope, resulting in  $\frac{\Delta V_L}{\Delta t_s} = 0.0598 \pm 0.0006 \frac{\text{V}}{\mu\text{s}}$ . By fitting the linear region of the voltage vs. time data in Figure (6.18(b)) we obtained  $\frac{\Delta t_s}{\Delta V_s} = 2.94 \pm 0.06 \frac{\mu\text{s}}{\text{V}}$ . Combining this, we obtain  $\frac{\Delta\nu_L}{\Delta V_s} = 11.3 \pm 0.2 \frac{\text{MHz}}{\text{V}}$ .

We could only take 2500 data points in a single curve, and so it was not possible to take continuous data covering the entire frequency range in which we were interested. Instead, voltage vs. time curves were taken for a series of

different timebases on the scope and combined during analysis.

The upper limit of the frequency range for which we could reliably take data was set by the bandwidth of the detector (10 MHz). However, this was sufficient since the the noise contribution falls off rapidly with frequency (see Figure (6.20)).

An FFT was performed for each time trace obtained, and the amplitude was converted to frequency according to Equation (6.34). From the FFT, we obtained a noise power spectrum which was subsequently converted into a noise power spectral density by dividing each value in the power spectrum by the sampling frequency [95]. The noise power spectral density for different sampling intervals is plotted in Figure (6.20).

At low frequencies, the cavity signal is dominated by vibrations of the cavity itself. To determine the low frequency contributions to the laser linewidth, a second set of data was taken with the laser still locked to iodine (again with a time constant of 1 ms on the lock-in amplifier). Instead of using the output from the cavity photodetector to measure the time spectra, we used the output of the lock-in amplifier. Recall that in this case, we are using a hyperfine feature of iodine as a frequency discriminator since this method is insensitive to noise sources such as table vibrations. Figure (6.19) shows a scan of the hyperfine feature that was used to lock to iodine for the magnesium linewidth measurement discussed in Section (6.3). The linear portion of the

iodine signal was fit to a straight line to obtain a relationship between output voltage from the lock-in amplifier and frequency noise:

$$\Delta\nu_L = \left(\frac{\Delta V_L}{\Delta V_s}\right) \left(\frac{\Delta\nu_L}{\Delta V_L}\right) \Delta V_s. \quad (6.35)$$

This gives us  $\frac{\Delta\nu}{\Delta V_s} = 223 \pm 10 \frac{\text{kHz}}{\text{V}}$ , which can be used to convert the output of the lock-in amplifier to laser frequency fluctuations. The time constant of the lock-in amplifier was set to 1 *ms* (commensurate with experimental conditions, corresponding to a bandwidth of 159 *Hz*). Figure (6.21) shows the low frequency noise power spectral density obtained from this method. At 124 *Hz* we can see the amplitude of the noise starts to drop (approximately corresponding to the bandwidth of the lock-in amplifier). The lock-in amplifier acts as a low-pass filter and so this method is not suitable for measuring high frequency fluctuations.

By numerically integrating the spectral noise density obtained from the FFT [96], we determined the RMS frequency fluctuations to be  $36 \pm 2 \text{ kHz}$  (in the UV) for low frequencies ( $< 124 \text{ Hz}$ , corresponding to the bandwidth of our iodine lock). For high frequency noise ( $> 124 \text{ Hz}$ ), we used the noise power spectral density obtained from the cavity, shown in Figure (6.20). The high frequency contribution to the total RMS frequency fluctuation is  $16.0 \pm 0.3 \text{ kHz}$  (in the UV). Combining the low frequency (where iodine was used as our frequency discriminator) and high frequency (where the two-mirror cavity was

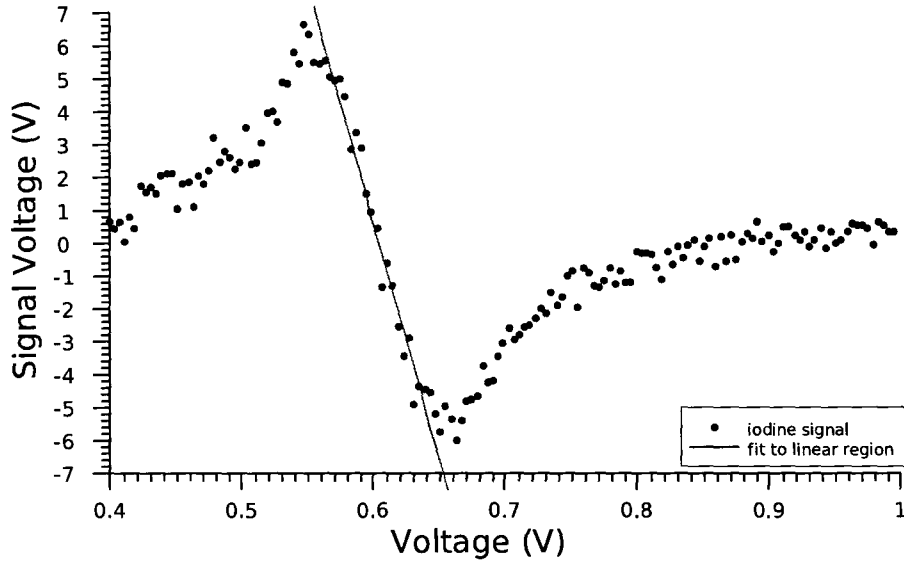


Figure 6.19: Calibration of the linear portion of the iodine signal.

used as a frequency discriminator) RMS frequency fluctuations we obtained a total of  $52 \pm 2$  kHz (in the UV). Since we were in the limit in which the noise is dominated by low frequency fluctuations, the laser linewidth is Gaussian [97], with a linewidth of  $122 \pm 4$  kHz (in the UV). To account for the laser linewidth contribution to our measured linewidth, we subtracted the laser linewidth from the measured linewidth (in quadrature) and we have included the uncertainty in the laser linewidth in the error budget (which we add in quadrature).

### 6.3.2 Measurement of the Linewidth of $Mg^+$

The effect of the population dynamics discussed in Section (5.6) is to increase the measured linewidth. It is possible to extract the linewidth from the  $^{25}Mg^+$  data by fitting to an analytic form of the full solution to the population dy-

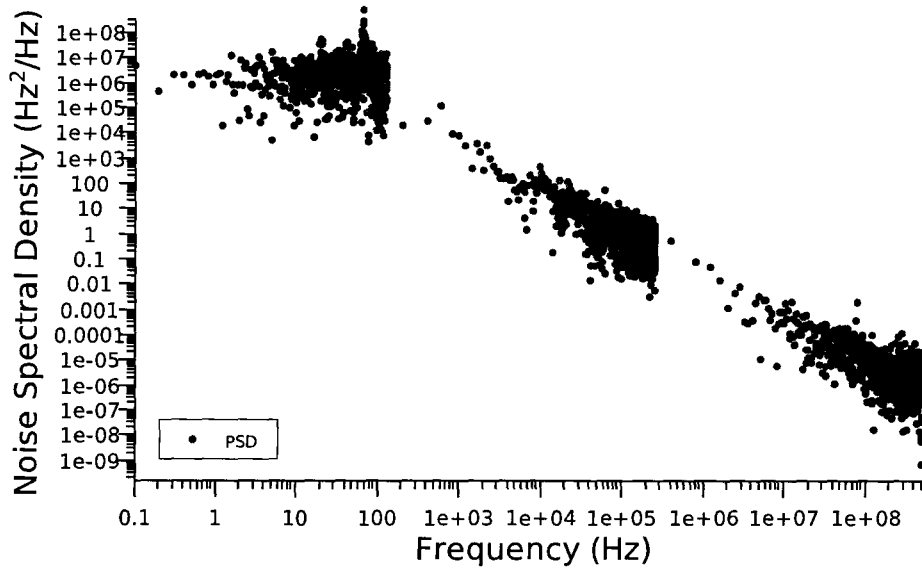


Figure 6.20: A plot of the noise power spectral density using a two-mirror cavity as a frequency discriminator. The laser was locked to iodine for all measurements. The high frequency ( $> 124 \text{ Hz}$ ) contribution to the total RMS frequency fluctuation is  $16.0 \pm 0.3 \text{ kHz}$  (in the UV).

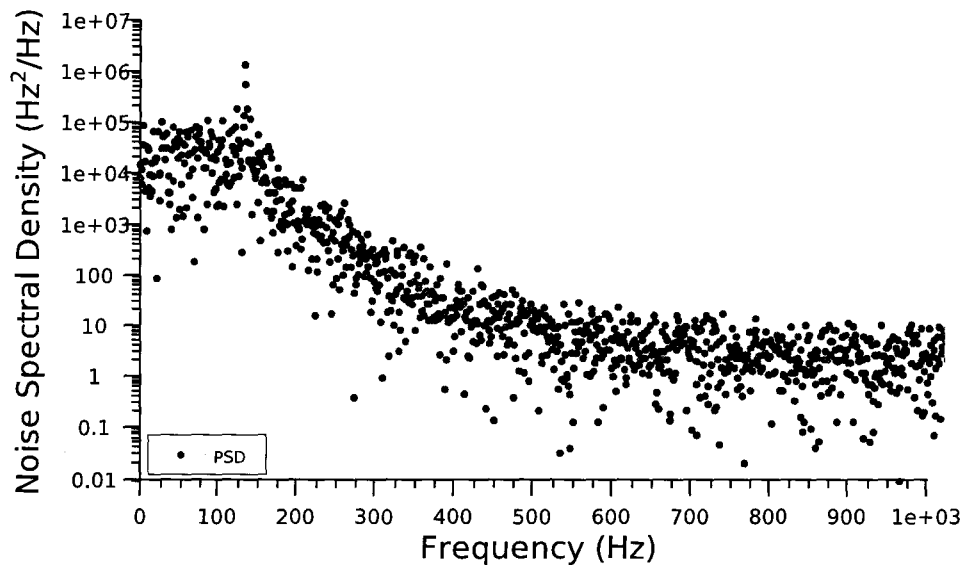


Figure 6.21: A plot of the noise power spectral density using iodine feature  $b$  as a frequency discriminator. The iodine feature allowed us to determine the low frequency contribution and was insensitive to mechanical noise. The laser was locked to iodine for all measurements. The low frequency ( $< 124 \text{ Hz}$ ) contribution to the total RMS frequency fluctuation is  $36 \pm 2 \text{ kHz}$  (in the UV).

namics. Alternatively, the linewidth can be measured using  $^{24}\text{Mg}^+$ , which has no hyperfine structure since  $I = 0$ . We elected to measure the linewidth using  $^{24}\text{Mg}^+$  since the analytic form obtained from the population dynamics would be difficult to fit.

A single  $^{24}\text{Mg}^+$  ion was trapped and the fluorescence was detected while the  $^2S_{\frac{1}{2}} \rightarrow ^2P_{\frac{1}{2}}$  was probed. By taking a series of data curves and varying the probe power for each curve we were able to extrapolate to the natural linewidth from a fit to the measured linewidth at each different laser power. We were able to do this using the probe power saturation data taken with  $^{24}\text{Mg}^+$  and discussed in Section (6.1.3). The apparatus and experimental setup have already been discussed in Section (6.1.3), and will only be summarized here.

A  $^{24}\text{Mg}^+$  ion was trapped and laser cooled using a single laser beam to drive the  $^2S_{\frac{1}{2}} \rightarrow ^2P_{\frac{1}{2}}$  transition. The isotope splitting between  $^{24}\text{Mg}^+$  and  $^{25}\text{Mg}^+$  is 1586 MHz and so the locking scheme for iodine was different from one used when we trapped  $^{25}\text{Mg}^+$ . In particular, one of the visible double-pass AOMs in the Probe laser iodine setup was turned off and the other one rotated, resulting in a positive frequency shift in the laser beam going to iodine. This AOM was subsequently tuned from 70 MHz to 90 MHz for each data curve.

Each experiment consisted of a single pulse that was 500  $\mu\text{s}$  long, during which the ion was simultaneously probed while the fluorescence was detected using the photomultiplier module. For a given data point, the experiment

was repeated 2000 times and the photon counts per experiment were summed. Typical data curves are shown in Figure (6.22) and Figure (6.23). Figure (6.22) was taken at low saturation intensity, and Figure (6.23) was taken at high saturation intensity and the resultant power broadening is evident in the data curve. An increase in the AOM frequency results in a decrease in the laser frequency because the shift in the double-pass AOM is positive (see Section (6.1.3)).

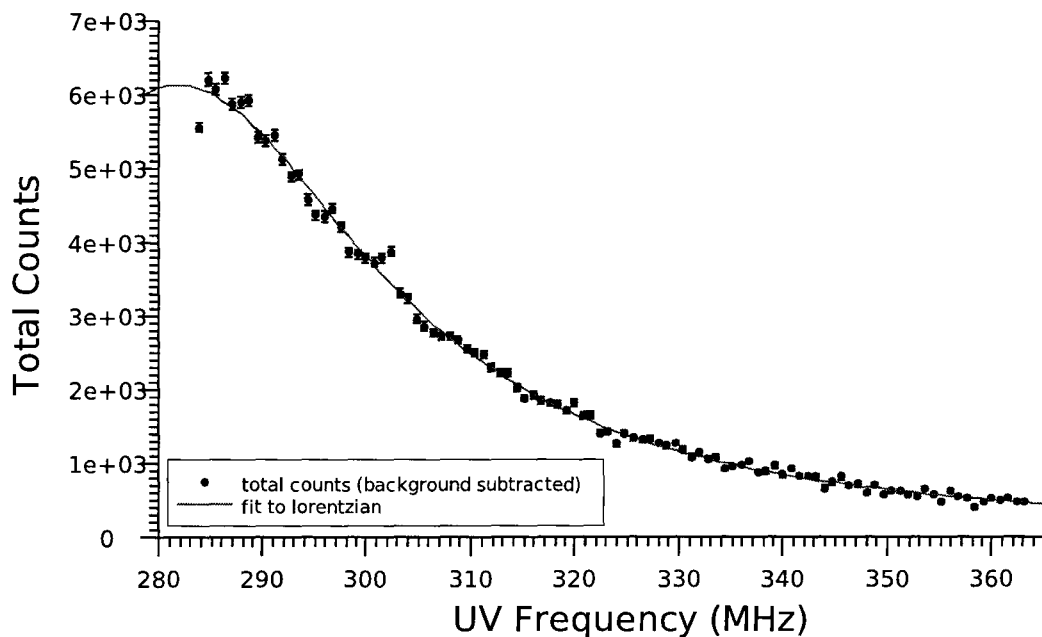


Figure 6.22: Total Counts vs. UV Frequency (low power): A data curve showing the total number of photons detected in  $500 \mu s$ , summed over 2000 experiments (background subtracted). The laser power corresponds to a saturation parameter of  $s \approx 0.03$ .

The ion was dumped after the data curves were taken and a background curve was taken. The laser power was varied across the full range over which that data was taken and the total number of photons counted over  $500 \mu s$  was

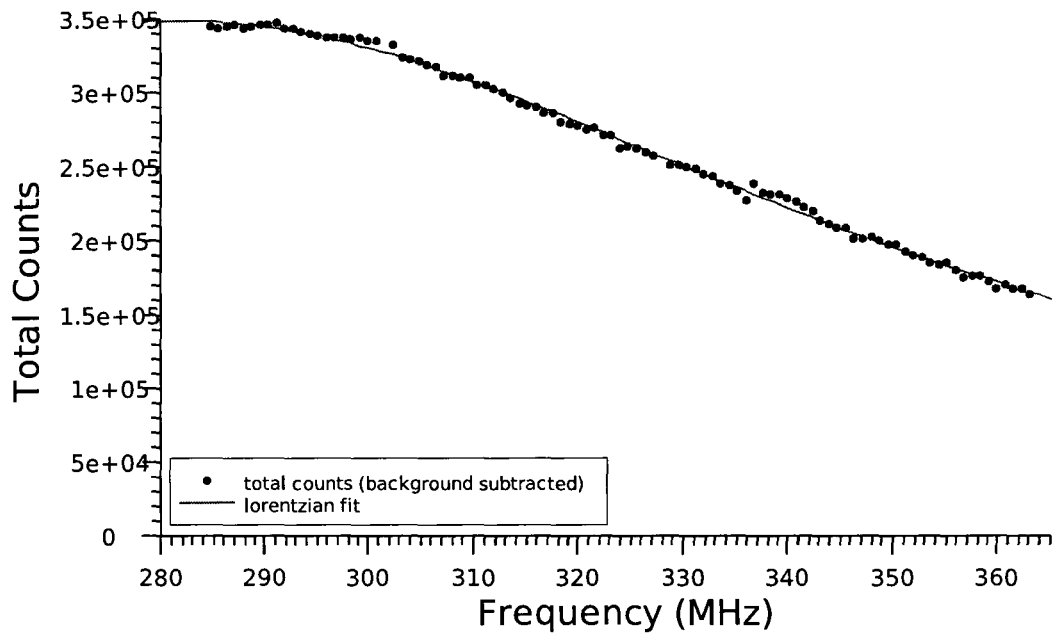


Figure 6.23: Total Counts vs. UV Frequency (high power): A data curve showing the total number of photons detected in  $500 \mu s$ , summed over 2000 experiments (background subtracted). The laser power corresponds to a saturation parameter of  $s \approx 12$ .

recorded.

At higher power, the background counts increased, suggesting that a fraction of the background counts resulted from laser light scattering off the electrodes. As the power increased, the number of scattered photons increased. The background counts vs. laser power was fit to straight line, and used to subtract the background counts from the data curves.

The background-subtracted data were fit to a Voigt profile:

$$G = \frac{A_0}{\sigma_{tot}(\Delta_L)} \int_{-\infty}^{\infty} \left( \frac{\frac{\Gamma'}{2}}{(\Delta_L + \vec{k}_L \cdot \vec{v})^2 + \left(\frac{\Gamma'}{2}\right)^2} \right) e^{-\left(\frac{v^2}{2\sigma_{tot}(\Delta_L)^2}\right)} dv. \quad (6.36)$$

Here  $\sigma_{tot}(\Delta_L)$  is the net laser-detuning-dependent Doppler width, accounting for the total ion motion in harmonics up to  $n = \pm 6$  (see Equation (2.21)). Terms of order higher than six contribute less than 0.1% to the Doppler width. Since we did not know what the actual temperature was, we used Equation (6.29) to calculate the lower limit of the ion temperature. For the upper limit of the ion temperature, we used Equation (6.30). For each laser power, we fit the data to a Voigt profile assuming first the lower limit, then the upper limit and obtained a power-broadened linewidth for each limiting case, which we will call  $\Gamma'_U$  and  $\Gamma'_L$ . We averaged the two values to obtain an absolute value for the power-broadened linewidth,  $\Gamma'_A$ . The uncertainty was determined by  $\Gamma'_U - \Gamma'_A$ , added in quadrature to the uncertainty in  $\Gamma'_L$  and  $\Gamma'_U$ . The fit uncertainty in the upper and lower limits were 1.1% – 1.2%, whereas the difference ( $\Gamma'_U - \Gamma'_A$ )

was between 0.05% – 0.09%. Thus, the net uncertainty was dominated by the fit uncertainty. This procedure was repeated for all nine laser powers and the resultant power-broadened linewidth was plotted as a function of laser power, as shown in Figure (6.24).

To obtain the linewidth, the data in Figure (6.24) were fit to a power-broadened linewidth model given by:

$$\Gamma'(x) = \Gamma \sqrt{1 + \frac{x}{b}} \quad (6.37)$$

where  $\Gamma$  is the linewidth,  $x$  is the laser power, and  $b$  is the power saturation parameter. From a fit of Equation (6.37) to the data we obtained a linewidth of  $\Gamma = 2\pi \cdot (42.4 \pm 1.2) \text{ MHz}$ . Note, only the statistical uncertainty in the fit is included. The laser linewidth (see Section (6.3.1)), and broadening due to Doppler effects also contribute to the measured linewidth (due to excess micromotion (see Section (2.2.3) and Section (6.1.2))). Recall that the measured laser linewidth is  $122 \pm 4 \text{ kHz}$ . Assuming the laser linewidth adds in quadrature to the natural linewidth, we can subtract the laser linewidth (adding its uncertainty in quadrature) from the measured linewidth. Since we have only placed upper limits on the broadening due to excess micromotion ( $< 200 \text{ kHz}$ ), we add it in quadrature to the uncertainty in the measured value. Secular motion, regular micromotion, and ion temperature are already accounted for in the Voigt model. In the Table (6.5) we list an error budget consisting of all the contri-

butions to the measured linewidth. Adding them in quadrature, we obtain the total uncertainty, giving us a natural linewidth of  $\Gamma = 2\pi \cdot (42.4 \pm 1.2) \text{ MHz}$ .

Table 6.5: Error Budget: factors contributing to the magnesium linewidth measurement

Source	$\frac{\Delta\omega}{2\pi}$ (MHz)	$\frac{\Delta\omega}{2\pi}$ (%)
fit uncertainty	1.2	2.8
laser linewidth	0.004	0.01
excess micromotion	0.2	0.47
total	1.2	2.8

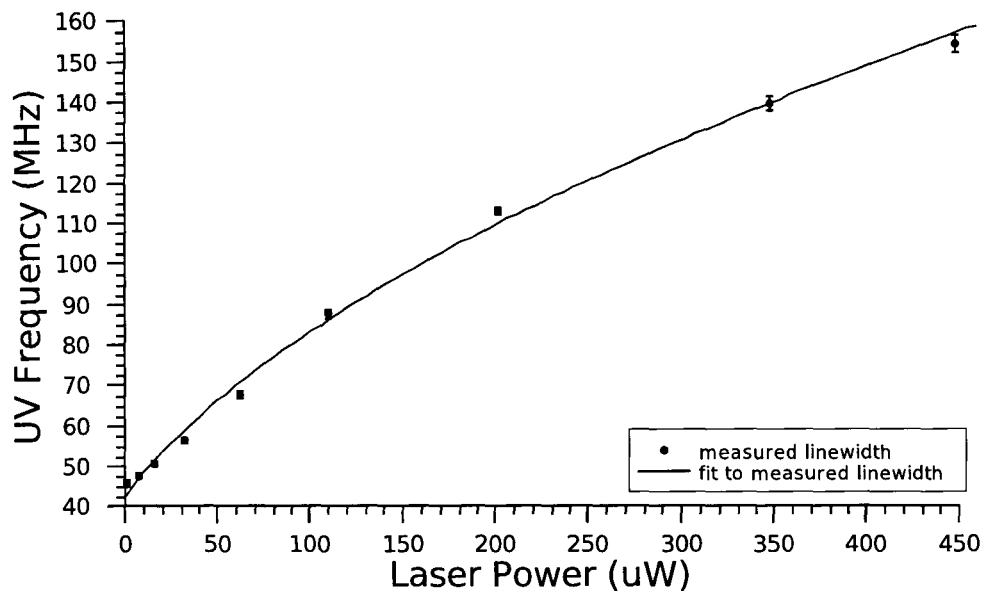


Figure 6.24: Natural Linewidth of  $Mg^+$ : The power-broadened linewidth was obtained for different powers of the Probe laser by fitting the data to a Voigt model, in which the laser-detuning-dependent temperature was accounted for by using an analytic form for the equilibrium temperature (see Section (6.3.1)). A natural linewidth was extrapolated from the data by fitting the power-broadened linewidth to Equation (6.37).



# Chapter 7

## Conclusions

Laser-cooled trapped ions serve as ideal candidates for spectroscopic measurements free of the usual limiting factors such as Doppler broadening, and other perturbations which limit the measurement. In this thesis, we have described our determination of the natural linewidth of magnesium, which had previously been measured [34] [35] [36] [37], and the hyperfine  $a$  constant of the  ${}^2P_{\frac{1}{2}}$  state of  ${}^{25}\text{Mg}^+$ , which had never been measured. The analysis and a detailed discussion of the measurements were presented in Chapter 6.

In advance of this measurement, we set up a complex apparatus used to laser cool and trap magnesium ions. We used a linear Paul trap to confine the ion and three laser systems for laser cooling and addressing the relevant transitions. The details of the apparatus were described in Chapter 3.

A significant part of setting up the apparatus was the construction of two

fibre-based laser systems designed to operate near 280 nm. Our laser systems frequency doubled the IR output in two separate stages, the details of which were discussed in Chapter 4. The overall efficiency of our laser system was limited by the second doubling stage (using BBO), whose peak efficiency was less than  $9 \frac{\%}{W}$  (limited by crystal quality), whereas the first stage had an efficiency of approximately  $25 \frac{\%}{W}$ . Friedenauer *et al.* concurrently developed their own fibre-based laser system [38] and obtained an efficiency of approximately  $30 \frac{\%}{W}$  for each stage. However, their cavities employed longer crystals than ours did. Accounting for the differences in crystal length, our LBO cavity out-performed theirs by a factor of 2 whereas their BBO cavity out-performed ours by a factor of  $> 3$ . These systems (along with the ones developed by Friedenauer *et al.*) were the first fibre-based systems at 280 nm.

## 7.1 Hyperfine $a$ Constant

To determine the hyperfine  $a$  constant we trapped and laser cooled a single  $^{25}\text{Mg}^+$  ion. The ion was optically pumped into ( $F = 3, m_F = \pm 3$ ) state to prepare the ion in the ground state before it was probed. If the probe beam successfully drove the ion out of the ground state, then it decayed into the  $F = 2$  manifold of the ground state some fraction of the time. Detection of the final state of the ion was accomplished by turning the Cyclor on and monitoring the fluorescence (or reduction therein).

The  ${}^2S_{\frac{1}{2}}|F = 3, m_F = \pm 3\rangle \rightarrow {}^2P_{\frac{1}{2}}|F' = 3, m_{F'} = \pm 2\rangle$  transition and the  ${}^2S_{\frac{1}{2}}|F = 3, m_F = \pm 3\rangle \rightarrow {}^2P_{\frac{1}{2}}|F' = 2, m_{F'} = \pm 2\rangle$  transition were separately probed to obtain a resonance curve corresponding to each transition. By varying the polarization and the magnetic field we were able to extrapolate to the frequency separation between the two transitions to zero magnetic field and thus obtain the hyperfine  $a$  constant. We determined that the best method was the average-polarization method, since no assumptions were made in determining the field-free transition frequencies for each of the two transitions. In particular, we choose to quote the hyperfine  $a$  constant obtained from the fit of the average polarization data to a line constrained to zero slope. Although the calculated uncertainty in the weighted average is smaller than the uncertainty in the fit, we choose to quote the fit uncertainty since it is more representative of the observed scatter in the data points (see Figure (6.16)) due to technical noise. From this we determine that the hyperfine  $a$  constant is  $102.16 \pm 0.16$  MHz. This quantity has not previously been measured, although theoretical calculations for the hyperfine  $a$  constant have been done by two different groups [26] [27]. Our measured value of  $102.16 \pm 0.16$  MHz lies between the calculated value of  $101.7$  MHz [27] and  $103.4$  MHz [26] corresponding to a 0.5% and 1% difference, respectively.

Both groups use a coupled cluster theory model, where the ground state energy is first calculated for the closed shell system of  ${}^{25}\text{Mg}^{2+}$  and then the

open shell is used coupled cluster method to calculate the ground and excited state energies for  $^{25}\text{Mg}^+$  [27]. The difference between the approach used by the two groups is that the more recent results of Sur et al. [27] include triple excitations in their calculations while the results of Safranova *et al.* [26] only include single and double excitations [27].

As a comparison, we look at the measured value of the ground state hyperfine  $a$  constant measured by Itano and Wineland [98] and compare the theoretically calculated values by the two groups against the measured value of  $596.254376(54)$   $\text{MHz}$ . The calculations of Sur *et al.* [27] give a value of  $592.86$   $\text{MHz}$  corresponding to a difference of 0.6%. The calculations of Safranova *et al.* [26], which only include single and double excitations, give a result of  $597.6$   $\text{MHz}$ . This corresponds to a difference of 0.23%. Interestingly, Sur et al. [27] include a series a calculations where only partial triple excitations were included resulting in an  $a$  value of  $597.45$   $\text{MHz}$  for the  $^2S_{\frac{1}{2}}$  state, and an  $a$  value of  $102.40$   $\text{MHz}$  for the  $^2P_{\frac{1}{2}}$  state, corresponding to a 0.2% difference from the measured values in both cases.

## 7.2 Linewidth of $^{24}\text{Mg}^+$

To obtain the linewidth, we monitored the fluorescence from a  $^{24}\text{Mg}^+$  ion while the laser was tuned near the resonant frequency driving the  $^2S_{\frac{1}{2}} \rightarrow ^2P_{\frac{1}{2}}$  transition. We repeated this for different laser intensities in order to extrapolate

to a natural linewidth of  $42.4 \pm 1.2$  MHz (2.8%) for  $Mg^+$ . In our measurement, probe and detection was done by the same laser beam and so a different steady-state temperature was reached for different laser detunings. We explicitly took this into account in our data analysis. This is consistent with previous measurements of the linewidth [34] [35] [36] [37].

The first measurement of the linewidth [34] was  $43.36 \pm 2.13$  MHz using the Hanle-effect method [99] [8]. Later, Nagourney *et al.* [35] used a similar method to one described in this thesis. After trapping a single  $^{24}Mg^+$  ion, Nagourney *et al.* scanned through the  $^2S_{\frac{1}{2}} \rightarrow ^2P_{\frac{1}{2}}$  transition, detecting fluorescence as the probing laser was scanned through resonance using a dye laser. By measuring the line profile for different laser intensities, they obtained a natural linewidth of  $45.7 \pm 5.9$  MHz.

Using a fast ion beam, a measurement of the linewidth to 1% was done by Ansbacher *et al.* [36] where they obtained a value of  $41.3 \pm 0.3$  MHz for the  $^2P_{\frac{3}{2}}$  level and  $41.8 \pm 0.4$  MHz for the  $^2P_{\frac{1}{2}}$  level.

A more recent measurement of the linewidth [37] of the  $^2P_{\frac{1}{2}}$  level involved trapping a chain of  $^{24}Mg^+$  ions in a linear Paul trap. One end of the chain was cooled, while a weak probe beam was used to probe an ion at the other end of the chain that was sympathetically cooled in the trap. A linewidth of  $41.4 \pm 1.1$  MHz was obtained, with an accuracy of 2.6%.

For comparison, we consider some theoretical results from groups who used

different approximation methods. First, we examine the calculations of Theodosiou and Federman [100], who calculated oscillator strengths for  $3s \rightarrow np$  transitions in  $Mg^+$ . Using a semiempirical method they calculated transition matrix elements assuming a central potential that required measured energy levels as well as ab initio calculations of the polarizability. They obtained an oscillator strength of  $f = 0.300 \pm 0.005$  for the  ${}^2S_{\frac{1}{2}} \rightarrow {}^2P_{\frac{1}{2}}$  transition, which corresponds to a linewidth of  $40.52 \pm 0.69$  MHz. The quoted uncertainty results from the sensitivity of the calculated value to the input parameters [100].

Mitroy and Safronova [101] calculated the line strengths using two different methods. The first method was semiempirical and similar to that of Theodosiou and Federman [100]. They obtained a line strength of  $5.602$  a.u., corresponding to a linewidth of  $40.99$  MHz. We believe that differences in the calculated linewidths of the two groups resulted from differences in the calculated polarizabilities that were used.

The second method employed an all-order many body perturbation theory method including single and double excitations of the Dirac-Fock wavefunction [101]. From this method they calculated a line strength of  $5.612$  a.u., corresponding to a linewidth of  $41.77$  MHz.

The calculated values of both groups are consistent with the measured values, although the more recent results of Mitroy and Safronova [101] are closer to the measured values. We believe this may be due to Mitroy and

Safranova [101] keeping higher order terms in their approximation method. It should also be noted that the results from the two methods calculated by Mitroy and Safranova [101] differ by only 0.18%, although the semiempirical method is computationally simpler.

### 7.3 Improvements on the Measurements

It is clear from our error budget for the linewidth measurement (see Section (6.3.2)) that the dominant source of error is the uncertainty in the fit. We could reduce the fit uncertainty by increasing the signal to noise with a higher detection efficiency or by using a discriminator. The Mitutoyo objective had a transmission of 60%, which is a considerable amount of loss if we compare it to the loss due to an AR coated lens (typically 0.25% per surface). Replacing the Mitutoyo objective with a UV-coated aspheric lens (Edmund Optics 49694,  $f = 15 \text{ mm}$ ) would result in an improvement in the ratio of signal to noise and would allow us to probe for shorter times. It would also improve our ability to distinguish between a dark and a bright state.

Being able to better distinguish between a dark and bright state would allow us to program a discriminator into the data acquisition VI that would distinguish between dark and bright states given some threshold value,  $k$ . By determining the overlap between the dark and bright histograms, we could choose the threshold value such that if fewer than  $k$  photons are counted, then

the ion is presumed to be in the dark state, and if greater than  $k$  photons are counted, then the ion is presumed to be in the bright state. By reducing the loss through the imaging system we can decrease the histogram overlap between the bright and dark states resulting in a near unit detection efficiency. However, setting up a discriminator would only improve the linewidth measurement if a  $^{25}\text{Mg}^+$  ion is probed (see below) since the discrimination method requires a dark state.

The increase in signal to noise resulting from the increased detection efficiency would have also allowed us to select shorter probe times, further minimizing the population effects discussed in Section (5.6) – this could lead to an improvement in the hyperfine  $a$  constant. For the linewidth measurement, we could minimize population effects would have been to use microwave transitions to prepare the ion in the  $(2, -2)$  state. From the  $(2, -2)$  state we could drive transitions to the  $(3', -3')$  with the probe laser, which would not have led to inadvertent population of the other Zeeman sublevels (since the ion can only decay into the  $(2, -2)$ ,  $(3, -3)$  or  $(3, -2)$ ). This would have allowed us determine the linewidth, free of broadening due to population dynamics. This would not have improved the hyperfine  $a$  constant measurement, since there is no  $(2', -3')$  sublevel to which the ion can be driven.

By measuring the background heating rate, we could determine the ion temperature and subsequently subtract it from our measured linewidth. This could

have been done using either a Raman technique [102], or by monitoring the temporal dynamics of fluorescence during laser cooling [48]. However, we did not have time to setup Raman beamlines prior to our linewidth measurement and, while the method of Wesenberg *et al.* allowed us to set an upper limit on the heating rate (see Section (6.3.1)), an actual measurement of the heating rate would have required several days of continuous data-taking to complete. Even with enough people around so that we could monitor the experiment, the laser power would inevitably drift (usually due to polarization drifts in the laser), and we wouldn't be able to optimize them mid-experiment. Also, on these long timescales we would likely lose the ion and have to start over. Incidentally, with better detection efficiency we could be sensitive to a smaller heating rate and hence reduce the uncertainty due to the ion temperature (this does not currently contribute to the net uncertainty, but an improvement in the fit uncertainty could result in this becoming more significant).

Another improvement to the measurement of the linewidth would be a further reduction of the excess radial micromotion, since it is the next largest contributor ( $< 200$  kHz). Recall from Section (6.1.2) that any background field can push the ion away from RF null, resulting in additional micromotion. Berkeland *et al.* suggest a “cross-correlation” method in which the modulation of the fluorescence due to the first-order Doppler shift is monitored [45]. However, the modulation of the fluorescence occurs at the RF drive frequency

( $\approx 14$  MHz for our trap) and we do not have access to a correlator with that bandwidth.

## 7.4 Measuring the ${}^2P_{\frac{3}{2}}$ Hyperfine Constants

An interesting spectroscopic measurement to make would be to determine the hyperfine constants of the  ${}^2P_{\frac{3}{2}}$  excited state of  ${}^{25}\text{Mg}^+$ , which also have not been previously measured. To make a measurement of the  $a$  and  $b$  hyperfine constants, we would have required a separate beam line to probe the different  $F$  manifolds of the  ${}^2P_{\frac{3}{2}}$  excited state.

Since  $J = \frac{3}{2}$  and  $I = \frac{5}{2}$  the allowed  $F$  values are  $F'' = (4, 3, 2, 1)$ . By optically pumping into the  $(F = 3, m_F = -3)$  sublevel of the ground state, we could only drive transitions into  $F'' = (4, 3, 2)$  since the transition selection rules are  $\Delta F = 0, \pm 1$ .

We would still need to use the cycler beam line and the repumper beam lines to laser cool and to optically pump the ion into the  $(F = 3, m_F = -3)$  sublevel of the ground state, but we would require a separate tunable probe beam to drive the  $(F = 3, m_F = -3)$  to the  $F''$  manifold.

To obtain the tunable probe beam, we could take the output from the Cyclor BBO cavity and split it into three separate beams which could each be passed through their own double-pass arrangement: two which increase the frequency (Probe and Cyclor), and one which decreases the frequency

(Repumper).

This setup would have allowed us to measure the hyperfine constants of the  ${}^2P_{\frac{3}{2}}$  excited state, although some careful consideration would be required to determine how to tune the probe laser independently of the other two beams. Although this measurement would have been interesting and relevant as a comparison for theoretical calculations, timing constraints have prevented us from attempting it.

In conclusion, we have successfully assembled the apparatus required for trapping of  $Mg^+$  ions. In particular, we designed one of the first fibre-based UV laser systems operating at 280 nm. With our apparatus, we made the first measurement of the hyperfine  $a$  constant  ${}^2P_{\frac{1}{2}}$ , and have also measured the linewidth of the  ${}^2S_{\frac{1}{2}} \rightarrow {}^2P_{\frac{1}{2}}$  transition.

The hyperfine  $a$  constant measurement compares well (within 1%) to the results of theoretical calculations [26] [27], although the results of Sur et al. [27] are more consistent (within 0.5%) with our measured values. By comparing the measured ground state hyperfine  $a$  constant [98] to the theoretical results of Sur et al. [27] we obtained a difference of 0.6% between the theory and experiment. This is consistent with the 0.5% difference between the results of Sur et al. [27] and our measured value of  $102.16 \pm 0.16$  MHz.

Our measurement of the linewidth of magnesium ( $42.4 \pm 1.2$  MHz) also compares well with the results of others who have measured it [34] [35] [36] [37].

The uncertainty in our measured linewidth is dominated by the uncertainty in our fit (1.2 MHz), larger than all the other sources combined.

# Appendix A

## Cavity Design Worksheet

### ▼ Cavity Parameters

We begin by defining the cavity g-parameters:

$$g_1^s := 1 - 2 \cdot \frac{a_s}{R_s} :$$

$$g_2^s := 1 - 2 \cdot \frac{X}{R_s} :$$

$$a_s := \frac{1}{2} \left( \frac{2 \cdot L}{1000} + \frac{l_{\text{crystal}}}{n_{\text{crystal}}} \right) :$$

$$g_1^t := 1 - 2 \cdot \frac{a_t}{R_t} :$$

$$g_2^t := 1 - 2 \cdot \frac{X}{R_t} :$$

$$a_t := \frac{1}{2} \left( \frac{2 \cdot L}{1000} + \frac{l_{\text{crystal}}}{n_{\text{crystal}}} \right) :$$

where  $R$  is the effective mirror radius of curvature (see below),  $X$  is the long distance between the curved mirrors,  $l_{\text{crystal}}$  is the crystal length,  $n_{\text{crystal}}$  is the crystal index of refraction and subscripts  $s, t$  correspond to the saggital and tangential planes respectively.

### ▼ Astigmatic Compensation Angle

The astigmatic compensation angle is given by solving the following:

$$\text{eqangle} := r \sin(\theta) \cdot \tan(\theta) = l_{\text{crystal}} \left( n_{\text{crystal}}^2 - 1 \right) / n_{\text{crystal}}^3 :$$

$$\text{solang} := \text{solve}(\text{eqangle}, \theta) :$$

$$\theta_a := \text{solang}[1] :$$

$$R_s := \frac{r}{\cos(\theta_a)} :$$

$$R_t := r \cdot \cos(\theta_a) :$$

where  $r$  is mirror radius of curvature, and  $\theta_a$  is the astigmatic-compensation angle.

### ▼ Cavity Waists

Using the g-parameters, we calculate the waists on the different mirrors:

$$w_{c_s} := \sqrt{\frac{\lambda \cdot R_s}{2 \pi} \cdot \sqrt{\frac{g_1^s \cdot g_2^s \cdot (1 - g_1^s \cdot g_2^s)}{g_2^s}}} :$$

$$w_{a_s} := \sqrt{\frac{\lambda \cdot R_s}{2 \pi} \cdot \sqrt{\frac{g_1^s \cdot g_2^s \cdot (1 - g_1^s \cdot g_2^s)}{g_1^s}}} :$$

$$w_{m_s} := \sqrt{\frac{\lambda \cdot R_s}{2 \pi} \cdot \sqrt{\frac{(g_1^s + g_2^s - 2 \cdot g_1^s \cdot g_2^s)^2}{g_1^s g_2^s (1 - g_1^s \cdot g_2^s)}}} :$$

$$w_{c_t} := n_{\text{crystal}} \cdot \sqrt{\frac{\lambda \cdot R_t}{2 \pi} \cdot \sqrt{\frac{g_1^t \cdot g_2^t \cdot (1 - g_1^t \cdot g_2^t)}{g_2^t}}} :$$

$$w_{a_t} := \sqrt{\frac{\lambda \cdot R_t}{2 \pi}} \cdot \sqrt{\frac{g_1 \cdot g_2 \cdot (1 - g_1 g_2)}{g_1^2}} :$$

$$w_{m_t} := \sqrt{\frac{\lambda \cdot R_t}{2 \pi}} \cdot \sqrt{\frac{(g_1 + g_2 - 2 \cdot g_1 \cdot g_2)^2}{g_1 g_2 (1 - g_1 \cdot g_2)}} :$$

where  $w_c$  is the crystal waist,  $w_a$  is the secondary air waist, and  $w_m$  is the spotsize on the curved mirror.

### ▼ User Input

This section requires user input. You must enter the mirror radius of curvature, the index of refraction for the crystal, and the wavelength of operation. You must also enter the physical length of the crystal. In particular, we have used a values commensurate with the LBO cavity (doubling from the IR to VIS) that was built.

$$r := 0.075 :$$

$$n_{\text{crystal}} := 1.604 :$$

$$\lambda := 1120 \cdot 1e-9 :$$

$$l_{\text{crystal}} := 7 / 1000 :$$

$$L_{\text{min}} := \left( \frac{R_s}{2} - \frac{l_{\text{crystal}}}{2 \cdot n_{\text{crystal}}} \right) \cdot 1000 :$$

### ▼ Length Calculations

$$X$$

$$X := 'X' :$$

$$T := \frac{Z}{2 \cdot \cos(2 \cdot \theta_a)} :$$

$$S[\text{short}] := (L/1000 + l[\text{crystal}]/2 \cdot (\cos(\delta) - \sin(\delta)/\tan(2 \cdot \theta))) / \cos(2 \cdot \theta) ;$$

$$S[\text{long}] := (L/1000 + l[\text{crystal}]/2 \cdot (\cos(\delta) + \sin(\delta)/\tan(2 \cdot \theta))) / \cos(2 \cdot \theta) ;$$

$$Z := (2 \cdot X - S[\text{short}] - S[\text{long}]) / (1 + 1/\cos(2 \cdot \theta)) ;$$

### ▼ Cavity Parameters

$$L := 36.097 :$$

$$X := 3 :$$

$$\delta := \text{evalf}(28 \cdot \text{Pi}/180) :$$

$$\text{"Mirror Radius of Curvature (cm)"} = 100r ;$$

$$\text{"Distance from Curved Mirror to Crystal Face (mm)"} = L ;$$

$$\text{"Distance between flat mirrors (cm)"} = Z \cdot 100 ;$$

$$\text{"Incidence Angle (degrees)"} = \text{evalf}(\theta \cdot 180/\text{Pi}) ;$$

$$\text{"Tangential Crystal Waist (micron)"} = w_c[t] \cdot 1e6 ;$$

$$\text{"Sagittal Crystal Waist (micron)"} = w_c[s] \cdot 1e6 ;$$

$$\text{"Tangential Secondary Waist (mm)"} = w_s[t] \cdot 1000 ;$$

$$\text{"Sagittal Secondary Waist (mm)"} = w_s[s] \cdot 1000 ;$$

$$\text{"Tangential Curved Mirror Spotsize (mm)"} = w_m[t] \cdot 1000 ;$$

$$\text{"Sagittal Curved Mirror spotsize (mm)"} = w_m[s] \cdot 1000 ;$$

$$\text{"Longer Distance from Curved to Flat Mirror (cm)"} = (T + S[\text{long}]) \cdot 100 ;$$

$$\text{"Shorter Distance from Curved to Flat Mirror (cm)"} = (T + S[\text{short}]) \cdot 100 ;$$



**Appendix B**

**Population Dynamics**

**Worksheet**

Assume pure  $\sigma$ - polarization for the cycler beam:

Atomic constants: (Mg)

restart :

with(ScientificConstants) : with(DEtools, odeadvisor) :

$\Gamma_{\text{Mg}} := 43 \cdot 2 \cdot \pi :$

$\lambda := 279.635 \cdot 10^{-9} :$

$I_n := \frac{5}{2} :$

First (next two, hidden, sections) we define Maple versions of the Wigner 3-j and 6-j symbols

(taken from <http://www.mirror-service.org/sites/ftp.inf.ethz.ch/pub/software/maple/5.3/share/Wigner>)

► Wigner 3-j symbols

► Wigner 6-j symbols

Okay, if we wish to calculate probabilities we need dipole matrix elements! The appropriate formula is:

$$\mu_{eg} = \sqrt{\frac{3 \lambda^3 \Gamma_P}{2 \hbar c \pi^3 \omega^2}} (-1)^{2F'+1+2J+\max(J,J')+1-MF'} \sqrt{(2J'+1)(2F+1)(2F'+1)} \\ \times \text{Wigner\_6j}(J', 1, J, F, I, F') \text{Wigner\_3j}(F', 1, F, -MF', q, MF)$$

Define  $\mu_{red}$  to be  $\mu$  divided by the base Rabi frequency. This allows us to focus on the Clebsch-Gordon stuff:

$$\mu_{red} := (J_l, F_l, m_{F_l}, J_u, F_u, m_{F_u}, i, q) \rightarrow (-1)^{(2 \cdot F_u + i + 2 \cdot J_l + \max(J_l, J_u) + 1 - m_{F_u})} \\ \cdot \sqrt{(2 \cdot J_u + 1) \cdot (2 \cdot F_l + 1) \cdot (2 \cdot F_u + 1)} \cdot \text{Wigner\_6j}(J_u, 1, J_l, F_l, i, F_u) \\ \cdot \text{Wigner\_3j}(F_u, 1, F_l, -m_{F_u}, q, m_{F_l}) :$$

And the Rabi frequency is then given by  $\Omega = \sqrt{\frac{3 \lambda^3 \Gamma_P}{(4 \hbar \pi^3 \omega^2)}} \times \mu_{red}$ .

▼ Probe Dynamics

► Hyperfine Definitions

▼ F=3 Manifold

▼ Driving to the F = 3' intermediate level:

Assuming that we optically pump into F=3, mF=-3 turning the probe on means that we can drive the ion from the ground state into the 2P<sub>1/2</sub> level. First I'll consider the case where the laser is tuned to drive the F=3, mF=-3 of the 2S<sub>1/2</sub> to the F'=3 manifold. From the F=3, mF=-3 the probe laser can only drive the ion into the F'=3, mF'=-2 sublevel. From here, the ion can decay into the F=3, mF=-3, F=3, mF=-2, or F=3, mF=-1 which are bright, or the F=2, mF=-2 and F=2, mF=-1, which are dark to the probe. Because the ion has more than one bright state, we need to consider what happens when the ions is

pumped into one of the other bright groundstate zeeman sublevels. In particular, we get the following possible decay paths:

$$\begin{aligned}
 (3,-3) &\rightarrow (3',-2) \rightarrow (2,-2) \\
 &\quad \rightarrow (2,-1) \\
 &\quad \rightarrow (3,-3) \\
 &\quad \rightarrow (3,-2) \\
 &\quad \rightarrow (3,-1) \\
 (3,-2) &\rightarrow (3',-1) \rightarrow (2,-2) \\
 &\quad \rightarrow (2,-1) \\
 &\quad \rightarrow (2,0) \\
 &\quad \rightarrow (3,-2) \\
 &\quad \rightarrow (3,-1) \\
 &\quad \rightarrow (3,0) \\
 (3,-1) &\rightarrow (3',0) \rightarrow (2,-1) \\
 &\quad \rightarrow (2,0) \\
 &\quad \rightarrow (2,1) \\
 &\quad \rightarrow (3,-1) \\
 &\quad \rightarrow (3,0) \\
 &\quad \rightarrow (3,1) \\
 (3,0) &\rightarrow (3',1) \rightarrow (2,0) \\
 &\quad \rightarrow (2,1) \\
 &\quad \rightarrow (2,2) \\
 &\quad \rightarrow (3,0) \\
 &\quad \rightarrow (3,1) \\
 &\quad \rightarrow (3,2) \\
 (3,1) &\rightarrow (3',2) \rightarrow (2,1) \\
 &\quad \rightarrow (2,2) \\
 &\quad \rightarrow (3,1) \\
 &\quad \rightarrow (3,2) \\
 &\quad \rightarrow (3,3) \\
 (3,2) &\rightarrow (3',3) \rightarrow (2,2) \\
 &\quad \rightarrow (3,2) \\
 &\quad \rightarrow (3,3) \\
 (3,3) &\rightarrow \text{nowhere}
 \end{aligned}$$

We can eliminate the excited state and obtain equations for the probability of the populating the various ground state sublevels. To keep things somewhat straightforward,  $3n$  would correspond to an  $mF=-3$ , and a  $3p$  will correspond to an  $F=3'$ . So, considering probabilities by level we have:

▼ Intermediate State  $(3',-2)$ :

▼  $(3,-3) \rightarrow (2,-2)$ :

$$\begin{aligned}
 F3P33n32n22n := d \rightarrow & \frac{1}{1 + \left(\frac{2 \cdot d}{\Gamma M g}\right)^2} \cdot \mu_{\text{red}} \left( \frac{1}{2}, 3, -3, \frac{1}{2}, 3, -2, \frac{5}{2}, \right. \\
 & \left. 1 \right)^2 \cdot \mu_{\text{red}} \left( \frac{1}{2}, 2, -2, \frac{1}{2}, 3, -2, \frac{5}{2}, 0 \right)^2 :
 \end{aligned}$$

▼  $(3,-3) \rightarrow (2,-1)$ :

$$\text{F3P33n32n21n} := d \rightarrow \frac{1}{1 + \left( \frac{2 \cdot d}{\Gamma \text{Mg}} \right)^2} \cdot \mu \text{red} \left( \frac{1}{2}, 3, -3, \frac{1}{2}, 3, -2, \frac{5}{2}, 1 \right)^2 \cdot \mu \text{red} \left( \frac{1}{2}, 2, -1, \frac{1}{2}, 3, -2, \frac{5}{2}, -1 \right)^2 :$$

▼ (3,-3)→(3,-3) [no change!]:

$$\text{F3P33n32n33n} := d \rightarrow \frac{1}{1 + \left( \frac{2 \cdot d}{\Gamma \text{Mg}} \right)^2} \cdot \mu \text{red} \left( \frac{1}{2}, 3, -3, \frac{1}{2}, 3, -2, \frac{5}{2}, 1 \right)^2 \cdot \mu \text{red} \left( \frac{1}{2}, 3, -3, \frac{1}{2}, 3, -2, \frac{5}{2}, 1 \right)^2 :$$

▼ (3,-3)→(3,-2):

$$\text{F3P33n32n32n} := d \rightarrow \frac{1}{1 + \left( \frac{2 \cdot d}{\Gamma \text{Mg}} \right)^2} \cdot \mu \text{red} \left( \frac{1}{2}, 3, -3, \frac{1}{2}, 3, -2, \frac{5}{2}, 0 \right)^2 \cdot \mu \text{red} \left( \frac{1}{2}, 3, -2, \frac{1}{2}, 3, -2, \frac{5}{2}, 0 \right)^2 :$$

▼ (3,-3)→(3,-1):

$$\text{F3P33n32n31n} := d \rightarrow \frac{1}{1 + \left( \frac{2 \cdot d}{\Gamma \text{Mg}} \right)^2} \cdot \mu \text{red} \left( \frac{1}{2}, 3, -3, \frac{1}{2}, 3, -2, \frac{5}{2}, -1 \right)^2 \cdot \mu \text{red} \left( \frac{1}{2}, 3, -1, \frac{1}{2}, 3, -2, \frac{5}{2}, -1 \right)^2 :$$

▼ Intermediate State (3',-1):

▼ (3,-2)→(2,-2):

$$\text{F3P32n31n22n} := d \rightarrow \frac{1}{1 + \left( \frac{2 \cdot (d - \text{ZSU}[1] + \text{ZSL}[1])}{\Gamma \text{Mg}} \right)^2} \cdot \mu \text{red} \left( \frac{1}{2}, 3, -2, \frac{1}{2}, 3, -1, \frac{5}{2}, 1 \right)^2 \cdot \mu \text{red} \left( \frac{1}{2}, 2, -2, \frac{1}{2}, 3, -1, \frac{5}{2}, 1 \right)^2 :$$

▼ (3,-2)→(2,-1):

$$\text{F3P32n31n21n} := d \rightarrow \frac{1}{1 + \left( \frac{2 \cdot (d - \text{ZSU}[1] + \text{ZSL}[1])}{\Gamma \text{Mg}} \right)^2} \cdot \mu \text{red} \left( \frac{1}{2}, 3, -2, \frac{1}{2}, 3, -1, \frac{5}{2}, 1 \right)^2 \cdot \mu \text{red} \left( \frac{1}{2}, 2, -1, \frac{1}{2}, 3, -1, \frac{5}{2}, 1 \right)^2 :$$

$$\left. \frac{5}{2}, 0 \right)^2 :$$

print(); # input placeholder

▼ (3,-2)→(2, 0):

$$\begin{aligned} \text{F3P32n31n20} := d \rightarrow & \frac{1}{1 + \left( \frac{2 \cdot (d - \text{ZSU}[1] + \text{ZSL}[1])}{\Gamma \text{Mg}} \right)^2} \\ & \cdot \mu\text{red} \left( \frac{1}{2}, 3, -2, \frac{1}{2}, 3, -1, \frac{5}{2}, 1 \right)^2 \cdot \mu\text{red} \left( \frac{1}{2}, 2, 0, \frac{1}{2}, 3, -1, \frac{5}{2}, \right. \\ & \left. -1 \right)^2 : \end{aligned}$$

▼ (3,-2)→(3,-2) [no change!!]:

$$\begin{aligned} \text{F3P32n31n32n} := d \rightarrow & \frac{1}{1 + \left( \frac{2 \cdot (d - \text{ZSU}[1] + \text{ZSL}[1])}{\Gamma \text{Mg}} \right)^2} \\ & \cdot \mu\text{red} \left( \frac{1}{2}, 3, -2, \frac{1}{2}, 3, -1, \frac{5}{2}, 1 \right)^2 \cdot \mu\text{red} \left( \frac{1}{2}, 3, -2, \frac{1}{2}, 3, -1, \right. \\ & \left. \frac{5}{2}, 1 \right)^2 : \end{aligned}$$

▼ (3,-2)→(3,-1):

$$\begin{aligned} \text{F3P32n31n31n} := d \rightarrow & \frac{1}{1 + \left( \frac{2 \cdot (d - \text{ZSU}[1] + \text{ZSL}[1])}{\Gamma \text{Mg}} \right)^2} \\ & \cdot \mu\text{red} \left( \frac{1}{2}, 3, -2, \frac{1}{2}, 3, -1, \frac{5}{2}, 1 \right)^2 \cdot \mu\text{red} \left( \frac{1}{2}, 3, -1, \frac{1}{2}, 3, -1, \right. \\ & \left. \frac{5}{2}, 0 \right)^2 : \end{aligned}$$

▼ (3,-2)→(3, 0):

$$\begin{aligned} \text{F3P32n31n30} := d \rightarrow & \frac{1}{1 + \left( \frac{2 \cdot (d - \text{ZSU}[1] + \text{ZSL}[1])}{\Gamma \text{Mg}} \right)^2} \cdot \mu\text{red} \left( \frac{1}{2}, \right. \\ & \left. 3, -2, \frac{1}{2}, 3, -1, \frac{5}{2}, 1 \right)^2 \cdot \mu\text{red} \left( \frac{1}{2}, 3, 0, \frac{1}{2}, 3, -1, \frac{5}{2}, -1 \right)^2 : \end{aligned}$$

▼ Intermediate State (3', 0):

▼ (3,-1)→(2,-1):

$$\begin{aligned} \text{F3P31n3021n} := d \rightarrow & \frac{1}{1 + \left( \frac{2 \cdot (d - \text{ZSU}[2] + \text{ZSL}[2])}{\Gamma \text{Mg}} \right)^2} \cdot \mu\text{red} \left( \frac{1}{2}, \right. \\ & \left. 3, -1, \frac{1}{2}, 3, 0, \frac{5}{2}, 1 \right)^2 \cdot \mu\text{red} \left( \frac{1}{2}, 2, -1, \frac{1}{2}, 3, 0, \frac{5}{2}, 1 \right)^2 : \end{aligned}$$

▼ (3,-1)→(2, 0):

$$\text{F3P31n3020} := d \rightarrow \frac{1}{1 + \left( \frac{2 \cdot (d - \text{ZSU}[2] + \text{ZSL}[2])}{\Gamma \text{Mg}} \right)^2} \cdot \mu_{\text{red}} \left( \frac{1}{2}, 3, -1, \frac{1}{2}, 3, 0, \frac{5}{2}, 1 \right)^2 \cdot \mu_{\text{red}} \left( \frac{1}{2}, 2, 0, \frac{1}{2}, 3, 0, \frac{5}{2}, 0 \right)^2 :$$

▼ (3,-1)→(2, 1):

$$\text{F3P31n3021} := d \rightarrow \frac{1}{1 + \left( \frac{2 \cdot (d - \text{ZSU}[2] + \text{ZSL}[2])}{\Gamma \text{Mg}} \right)^2} \cdot \mu_{\text{red}} \left( \frac{1}{2}, 3, -1, \frac{1}{2}, 3, 0, \frac{5}{2}, 1 \right)^2 \cdot \mu_{\text{red}} \left( \frac{1}{2}, 2, 1, \frac{1}{2}, 3, 0, \frac{5}{2}, -1 \right)^2 :$$

▼ (3,-1)→(3,-1) [no change!!]:

$$\text{F3P31n3031n} := d \rightarrow \frac{1}{1 + \left( \frac{2 \cdot (d - \text{ZSU}[2] + \text{ZSL}[2])}{\Gamma \text{Mg}} \right)^2} \cdot \mu_{\text{red}} \left( \frac{1}{2}, 3, -1, \frac{1}{2}, 3, 0, \frac{5}{2}, 1 \right)^2 \cdot \mu_{\text{red}} \left( \frac{1}{2}, 3, -1, \frac{1}{2}, 3, 0, \frac{5}{2}, 1 \right)^2 :$$

▼ (3,-1)→(3, 0):

$$\text{F3P31n3030} := d \rightarrow \frac{1}{1 + \left( \frac{2 \cdot (d - \text{ZSU}[2] + \text{ZSL}[2])}{\Gamma \text{Mg}} \right)^2} \cdot \mu_{\text{red}} \left( \frac{1}{2}, 3, -1, \frac{1}{2}, 3, 0, \frac{5}{2}, 1 \right)^2 \cdot \mu_{\text{red}} \left( \frac{1}{2}, 3, 0, \frac{1}{2}, 3, 0, \frac{5}{2}, 0 \right)^2 :$$

▼ (3,-1)→(3, 1):

$$\text{F3P31n3031} := d \rightarrow \frac{1}{1 + \left( \frac{2 \cdot (d - \text{ZSU}[2] + \text{ZSL}[2])}{\Gamma \text{Mg}} \right)^2} \cdot \mu_{\text{red}} \left( \frac{1}{2}, 3, -1, \frac{1}{2}, 3, 0, \frac{5}{2}, 1 \right)^2 \cdot \mu_{\text{red}} \left( \frac{1}{2}, 3, 1, \frac{1}{2}, 3, 0, \frac{5}{2}, -1 \right)^2 :$$

▼ Intermediate State (3', 1):

▼ (3, 0)→(2, 0):

$$\text{F3P303120} := d \rightarrow \frac{1}{1 + \left( \frac{2 \cdot (d - \text{ZSU}[3] + \text{ZSL}[3])}{\Gamma \text{Mg}} \right)^2} \cdot \mu_{\text{red}} \left( \frac{1}{2}, 3, 0, \frac{1}{2}, 3, 1, \frac{5}{2}, 1 \right)^2 \cdot \mu_{\text{red}} \left( \frac{1}{2}, 2, 0, \frac{1}{2}, 3, 1, \frac{5}{2}, 1 \right)^2 :$$

▼ (3, 0) → (2, 1):

$$\text{F3P303121} := d \rightarrow \frac{1}{1 + \left( \frac{2 \cdot (d - \text{ZSU}[3] + \text{ZSL}[3])}{\Gamma \text{Mg}} \right)^2} \cdot \mu_{\text{red}} \left( \frac{1}{2}, 3, 0, \frac{1}{2}, 3, 1, \frac{5}{2}, 1 \right)^2 \cdot \mu_{\text{red}} \left( \frac{1}{2}, 2, 1, \frac{1}{2}, 3, 1, \frac{5}{2}, 0 \right)^2 :$$

▼ (3, 0) → (2, 2):

$$\text{F3P303122} := d \rightarrow \frac{1}{1 + \left( \frac{2 \cdot (d - \text{ZSU}[3] + \text{ZSL}[3])}{\Gamma \text{Mg}} \right)^2} \cdot \mu_{\text{red}} \left( \frac{1}{2}, 3, 0, \frac{1}{2}, 3, 1, \frac{5}{2}, 1 \right)^2 \cdot \mu_{\text{red}} \left( \frac{1}{2}, 2, 2, \frac{1}{2}, 3, 1, \frac{5}{2}, -1 \right)^2 :$$

▼ (3, 0) → (3, 0) [no change!!]:

$$\text{F3P303130} := d \rightarrow \frac{1}{1 + \left( \frac{2 \cdot (d - \text{ZSU}[3] + \text{ZSL}[3])}{\Gamma \text{Mg}} \right)^2} \cdot \mu_{\text{red}} \left( \frac{1}{2}, 3, 0, \frac{1}{2}, 3, 1, \frac{5}{2}, 1 \right)^2 :$$

▼ (3, 0) → (3, 1):

$$\text{F3P303131} := d \rightarrow \frac{1}{1 + \left( \frac{2 \cdot (d - \text{ZSU}[3] + \text{ZSL}[3])}{\Gamma \text{Mg}} \right)^2} \cdot \mu_{\text{red}} \left( \frac{1}{2}, 3, 0, \frac{1}{2}, 3, 1, \frac{5}{2}, 1 \right)^2 \cdot \mu_{\text{red}} \left( \frac{1}{2}, 3, 1, \frac{1}{2}, 3, 1, \frac{5}{2}, 0 \right)^2 :$$

▼ (3, 0) → (3, 2):

$$\text{F3P303132} := d \rightarrow \frac{1}{1 + \left( \frac{2 \cdot (d - \text{ZSU}[3] + \text{ZSL}[3])}{\Gamma \text{Mg}} \right)^2} \cdot \mu_{\text{red}} \left( \frac{1}{2}, 3, 0, \frac{1}{2}, 3, 1, \frac{5}{2}, 1 \right)^2 \cdot \mu_{\text{red}} \left( \frac{1}{2}, 3, 2, \frac{1}{2}, 3, 1, \frac{5}{2}, -1 \right)^2 :$$

▼ Intermediate State (3', 2):

▼ (3, 1) → (2, 1):

$$\text{F3P313221} := d \rightarrow \frac{1}{1 + \left( \frac{2 \cdot (d - \text{ZSU}[4] + \text{ZSL}[4])}{\Gamma \text{Mg}} \right)^2} \cdot \mu_{\text{red}} \left( \frac{1}{2}, 3, 1, \frac{1}{2}, 3, 1, \frac{5}{2}, 1 \right)^2 \cdot \mu_{\text{red}} \left( \frac{1}{2}, 2, 1, \frac{1}{2}, 3, 1, \frac{5}{2}, 0 \right)^2 :$$

$$1, \frac{1}{2}, 3, 2, \frac{5}{2}, 1)^2 \cdot \mu_{\text{red}} \left( \frac{1}{2}, 2, 1, \frac{1}{2}, 3, 2, \frac{5}{2}, 1 \right)^2 :$$

▼ (3, 1)→(2, 2):

$$\text{F3P313222} := d \rightarrow \frac{1}{1 + \left( \frac{2 \cdot (d - \text{ZSU}[4] + \text{ZSL}[4])}{\Gamma \text{Mg}} \right)^2} \cdot \mu_{\text{red}} \left( \frac{1}{2}, 3, 1, \frac{1}{2}, 3, 2, \frac{5}{2}, 1 \right)^2 \cdot \mu_{\text{red}} \left( \frac{1}{2}, 2, 2, \frac{1}{2}, 3, 2, \frac{5}{2}, 0 \right)^2 :$$

▼ (3, 1)→(3, 1) [no change!!]:

$$\text{F3P313231} := d \rightarrow \frac{1}{1 + \left( \frac{2 \cdot (d - \text{ZSU}[4] + \text{ZSL}[4])}{\Gamma \text{Mg}} \right)^2} \cdot \mu_{\text{red}} \left( \frac{1}{2}, 3, 1, \frac{1}{2}, 3, 2, \frac{5}{2}, 1 \right)^2 \cdot \mu_{\text{red}} \left( \frac{1}{2}, 3, 1, \frac{1}{2}, 3, 2, \frac{5}{2}, 1 \right)^2 :$$

▼ (3, 1)→(3, 2):

$$\text{F3P313232} := d \rightarrow \frac{1}{1 + \left( \frac{2 \cdot (d - \text{ZSU}[4] + \text{ZSL}[4])}{\Gamma \text{Mg}} \right)^2} \cdot \mu_{\text{red}} \left( \frac{1}{2}, 3, 1, \frac{1}{2}, 3, 2, \frac{5}{2}, 1 \right)^2 \cdot \mu_{\text{red}} \left( \frac{1}{2}, 3, 2, \frac{1}{2}, 3, 2, \frac{5}{2}, 0 \right)^2 :$$

▼ (3, 1)→(3, 3):

$$\text{F3P313233} := d \rightarrow \frac{1}{1 + \left( \frac{2 \cdot (d - \text{ZSU}[4] + \text{ZSL}[4])}{\Gamma \text{Mg}} \right)^2} \cdot \mu_{\text{red}} \left( \frac{1}{2}, 3, 1, \frac{1}{2}, 3, 2, \frac{5}{2}, 1 \right)^2 \cdot \mu_{\text{red}} \left( \frac{1}{2}, 3, 3, \frac{1}{2}, 3, 2, \frac{5}{2}, -1 \right)^2 :$$

▼ Intermediate State (3', 3):

▼ (3, 2)→(2, 2):

$$\text{F3P323322} := d \rightarrow \frac{1}{1 + \left( \frac{2 \cdot (d - \text{ZSU}[5] + \text{ZSL}[5])}{\Gamma \text{Mg}} \right)^2} \cdot \mu_{\text{red}} \left( \frac{1}{2}, 3, 2, \frac{1}{2}, 3, 3, \frac{5}{2}, 1 \right)^2 \cdot \mu_{\text{red}} \left( \frac{1}{2}, 2, 2, \frac{1}{2}, 3, 3, \frac{5}{2}, 1 \right)^2 :$$

▼ (3, 2)→(3, 2) [no change!!]:

$$F3P323332 := d \rightarrow \frac{1}{1 + \left( \frac{2 \cdot (d - ZSU[5] + ZSL[5])}{\Gamma M g} \right)^2} \cdot \mu_{\text{red}} \left( \frac{1}{2}, 3, 2, \frac{1}{2}, 3, 3, \frac{5}{2}, 1 \right)^2 \cdot \mu_{\text{red}} \left( \frac{1}{2}, 3, 2, \frac{1}{2}, 3, 3, \frac{5}{2}, 1 \right)^2 :$$

▼ (3, 2) → (3, 3):

$$F3P323333 := d \rightarrow \frac{1}{1 + \left( \frac{2 \cdot (d - ZSU[5] + ZSL[5])}{\Gamma M g} \right)^2} \cdot \mu_{\text{red}} \left( \frac{1}{2}, 3, 2, \frac{1}{2}, 3, 3, \frac{5}{2}, 0 \right)^2 \cdot \mu_{\text{red}} \left( \frac{1}{2}, 3, 3, \frac{1}{2}, 3, 3, \frac{5}{2}, 0 \right)^2 :$$

▼ Rate Equations for the 3' intermediate level:

▼ Rate Equations:

So we have the simplified level/transition diagram:

So we have:

$$d/dt(p33n(t)) = [(-P33n32n32n - P33n32n31n - P33n32n22n - P33n32n21n) \cdot p33n(t)]$$

$$d/dt(p32n(t)) = [(-P32n31n31n - P32n31n30 - P32n31n22n - P32n31n21n - P32n31n20) \cdot p32n(t) + P33n32n32n \cdot p33n(t)]$$

$$d/dt(p31n(t)) = [(-P31n3030 - P31n3031 - P31n3021n - P31n3020 - P31n3021) \cdot p31n(t) + P33n32n31n \cdot p33n(t) + P32n31n31n \cdot p32n(t)]$$

$$d/dt(p30(t)) = [(-P303131 - P303132 - P303120 - P303121 - P303122) \cdot p30(t) + P32n31n30 \cdot p32n(t) + P31n3030 \cdot p31n(t)]$$

$$d/dt(p31(t)) = [(-P313032 - P313033 - P313221 - P313222) \cdot p31(t) + P31n3031 \cdot p31n(t) + P303131n \cdot p30(t)]$$

$$d/dt(p32(t)) = [(-P323333 - P323322) \cdot p32(t) + P303132 \cdot p30(t) + P313232 \cdot p31(t)]$$

$$d/dt(p33(t)) = [P323333 \cdot p32(t) + P313233 \cdot p31(t)]$$

$$d/dt(p22n(t)) = P33n32n22n \cdot p33n(t) + P32n31n22n \cdot p32n(t)$$

$$d/dt(p21n(t)) = P33n32n21n \cdot p33n(t) + P32n31n21n \cdot p32n(t) + P31n3021n \cdot p31n(t)$$

$$d/dt(p20(t)) = P32n31n20 \cdot p32n(t) + P31n3020 \cdot p31n(t) + P303120 \cdot p30(t)$$

$$d/dt(p21(t)) = P31n3021 \cdot p31n(t) + P303121 \cdot p30(t) + P313221 \cdot p31(t)$$

$$d/dt(p22(t)) = P303122 \cdot p30(t) + P313222 \cdot p31(t) + P323222 \cdot p32(t)$$

Giving us:

$$F3Eq33n := d \rightarrow \frac{d}{dt} F3p33n(t) = ((-F3P33n32n32n(d) - F3P33n32n31n(d) - F3P33n32n22n(d) - F3P33n32n21n(d)) \cdot F3p33n(t)) :$$

$$\begin{aligned} \text{F3Eq32n} := d \rightarrow \frac{d}{dt} \text{F3p32n}(t) = & ((-\text{F3P32n31n31n}(d) \\ & - \text{F3P32n31n30}(d) - \text{F3P32n31n22n}(d) - \text{F3P32n31n21n}(d) \\ & - \text{F3P32n31n20}(d)) \cdot \text{F3p32n}(t) + \text{F3P33n32n32n}(d) \\ & \cdot \text{F3p33n}(t)) : \end{aligned}$$

$$\begin{aligned} \text{F3Eq31n} := d \rightarrow \frac{d}{dt} \text{F3p31n}(t) = & ((-\text{F3P31n3030}(d) \\ & - \text{F3P31n3031}(d) - \text{F3P31n3021n}(d) - \text{F3P31n3020}(d) \\ & - \text{F3P31n3021}(d)) \cdot \text{F3p31n}(t) + \text{F3P33n32n31n}(d) \cdot \text{F3p33n}(t) \\ & + \text{F3P32n31n31n}(d) \cdot \text{F3p32n}(t)) : \end{aligned}$$

$$\begin{aligned} \text{F3Eq30} := d \rightarrow \frac{d}{dt} \text{F3p30}(t) = & ((-\text{F3P303131}(d) - \text{F3P303132}(d) \\ & - \text{F3P303120}(d) - \text{F3P303121}(d) - \text{F3P303122}(d)) \cdot \text{F3p30}(t) \\ & + \text{F3P31n3030}(d) \cdot \text{F3p31n}(t) + \text{F3P32n31n30}(d) \cdot \text{F3p32n}(t)) : \end{aligned}$$

$$\begin{aligned} \text{F3Eq31} := d \rightarrow \frac{d}{dt} \text{F3p31}(t) = & ((-\text{F3P313232}(d) - \text{F3P313233}(d) \\ & - \text{F3P313221}(d) - \text{F3P313222}(d)) \cdot \text{F3p31}(t) + \text{F3P303131}(d) \\ & \cdot \text{F3p30}(t) + \text{F3P31n3031}(d) \cdot \text{F3p31n}(t)) \end{aligned}$$

$$\begin{aligned} \text{F3Eq32} := d \rightarrow \frac{d}{dt} \text{F3p32}(t) = & ((-\text{F3P323333}(d) - \text{F3P323322}(d)) \\ & \cdot \text{F3p32}(t) + \text{F3P313232}(d) \cdot \text{F3p31}(t) + \text{F3P303132}(d) \\ & \cdot \text{F3p30}(t)) : \end{aligned}$$

$$\begin{aligned} \text{F3Eq33} := d \rightarrow \frac{d}{dt} \text{F3p33}(t) = & (\text{F3P313233}(d) \cdot \text{F3p31}(t) \\ & + \text{F3P323333}(d) \cdot \text{F3p32}(t)) : \end{aligned}$$

$$\begin{aligned} \text{F3Eq22n} := d \rightarrow \frac{d}{dt} \text{F3p22n}(t) = & \text{F3P33n32n22n}(d) \cdot \text{F3p33n}(t) \\ & + \text{F3P32n31n22n}(d) \cdot \text{F3p32n}(t) : \end{aligned}$$

$$\begin{aligned} \text{F3Eq21n} := d \rightarrow \frac{d}{dt} \text{F3p21n}(t) = & \text{F3P33n32n21n}(d) \cdot \text{F3p33n}(t) \\ & + \text{F3P32n31n21n}(d) \cdot \text{F3p32n}(t) + \text{F3P31n3021n}(d) \\ & \cdot \text{F3p31n}(t) : \end{aligned}$$

$$\begin{aligned} \text{F3Eq20} := d \rightarrow \frac{d}{dt} \text{F3p20}(t) = & \text{F3P32n31n20}(d) \cdot \text{F3p32n}(t) \\ & + \text{F3P31n3020}(d) \cdot \text{F3p31n}(t) + \text{F3P303120}(d) \cdot \text{F3p30}(t) : \end{aligned}$$

$$\begin{aligned} \text{F3Eq21} := d \rightarrow \frac{d}{dt} \text{F3p21}(t) = & \text{F3P31n3021}(d) \cdot \text{F3p31n}(t) \\ & + \text{F3P303121}(d) \cdot \text{F3p30}(t) + \text{F3P313221}(d) \cdot \text{F3p31}(t) : \end{aligned}$$

$$\begin{aligned} \text{F3Eq22} := d \rightarrow \frac{d}{dt} \text{F3p22}(t) = & \text{F3P303122}(d) \cdot \text{F3p30}(t) \\ & + \text{F3P313222}(d) \cdot \text{F3p31}(t) + \text{F3P323322}(d) \cdot \text{F3p32}(t) : \end{aligned}$$



Solving the Rate Equations:

```
ThreePrimeProbeDynamics := proc(ProbeDetuning)
  global F3Solns, F3P33n, F3P32n, F3P31n, F3P30, F3P31, F3P32,
  F3P33, F3P22n, F3P21n, F3P20, F3P21, F3P22;
  local F3Eqs;
  F3Eqs := {F3Eq33n(ProbeDetuning), F3Eq32n(ProbeDetuning),
```

```

F3Eq31n(ProbeDetuning), F3Eq30(ProbeDetuning),
F3Eq31(ProbeDetuning), F3Eq32(ProbeDetuning),
F3Eq33(ProbeDetuning), F3Eq22n(ProbeDetuning),
F3Eq21n(ProbeDetuning), F3Eq20(ProbeDetuning),
F3Eq21(ProbeDetuning), F3Eq22(ProbeDetuning), F3p33(0)
= 0, F3p32(0) = 0, F3p31(0) = 0, F3p30(0) = 0, F3p31n(0)
= 0, F3p32n(0) = 0, F3p33n(0) = 1, F3p22n(0) = 0, F3p21n(0)
= 0, F3p20(0) = 0, F3p21(0) = 0, F3p22(0) = 0 } :
F3Solns := dsolve(F3Eqs, numeric, output = listprocedure) :
F3P33n := eval(F3p33n(t), F3Solns);
F3P32n := eval(F3p32n(t), F3Solns);
F3P31n := eval(F3p31n(t), F3Solns);
F3P30 := eval(F3p30(t), F3Solns);
F3P31 := eval(F3p31(t), F3Solns);
F3P32 := eval(F3p32(t), F3Solns);
F3P33 := eval(F3p33(t), F3Solns);
F3P22n := eval(F3p22n(t), F3Solns);
F3P21n := eval(F3p21n(t), F3Solns);
F3P20 := eval(F3p20(t), F3Solns);
F3P21 := eval(F3p21(t), F3Solns);
F3P22 := eval(F3p22(t), F3Solns);
end proc:

```

▼ F=2 Manifold

▼ Driving to the F =2' intermediate level:

Assuming that we optically pump into F=3, mF=-3 turning the probe on means that we can drive the ion from the ground state into the 2P1/2 level. Now I'll consider the case where the laser is tuned to drive the F=3, mF=-3 of the 2S1/2 to the F'=2 manifold. From the F=3, mF=-3 the probe laser can only drive the ion into the F'=2, mF'=-2 sublevel. From here, the ion can decay into the F=3, mF=-3, F=3, mF=-2, or F=3, mF=-1 which are bright, or the F=2, mF=-2 and F=2, mF=-1, which are dark to the probe. Because the ion has more than one bright state, we need to consider what happens when the ions is pumped into one of the other bright groundstate zeeman sublevels. In particular, we get the following possible decay paths:

```

(3,-3) → (2',-2) → (2,-2)
           → (2,-1)
           → (3,-3)
           → (3,-2)
           → (3,-1)
(3,-2) → (2',-1) → (2,-2)
           → (2,-1)
           → (2, 0)
           → (3,-2)
           → (3,-1)
           → (3, 0)
(3,-1) → (2', 0) → (2,-1)
           → (2, 0)
           → (2, 1)
           → (3,-1)
           → (3, 0)
           → (3, 1)
(3, 0) → (2', 1) → (2, 0)
           → (2, 1)

```

$$\begin{aligned}
& \rightarrow (2, 2) \\
& \rightarrow (3, 0) \\
& \rightarrow (3, 1) \\
& \rightarrow (3, 2) \\
(3, 1) & \rightarrow (2', 2) \rightarrow (2, 1) \\
& \rightarrow (2, 2) \\
& \rightarrow (3, 1) \\
& \rightarrow (3, 2) \\
& \rightarrow (3, 3)
\end{aligned}$$

(3, 2) → nowhere

(3, 3) → nowhere

We can eliminate the excited state and obtain equations for the probability of the populating the various ground state sublevels. To keep things somewhat straightforward, 3n would correspond to an  $mF=-3$ , and a 3p will correspond to an  $F = 3'$ . So, considering probabilities by level we have:

▼ Intermediate State (2', -2):

▼ (3, -3) → (2, -2):

$$\begin{aligned}
F2P33n22n22n := d \rightarrow & \frac{1}{1 + \left( \frac{2 \cdot (d - \text{EHFS})}{\Gamma M g} \right)^2} \cdot \mu_{\text{red}} \left( \frac{1}{2}, 3, -3, \frac{1}{2}, \right. \\
& \left. 2, -2, \frac{5}{2}, 1 \right)^2 \cdot \mu_{\text{red}} \left( \frac{1}{2}, 2, -2, \frac{1}{2}, 2, -2, \frac{5}{2}, 0 \right)^2 :
\end{aligned}$$

▼ (3, -3) → (2, -1):

$$\begin{aligned}
F2P33n22n21n := d \rightarrow & \frac{1}{1 + \left( \frac{2 \cdot (d - \text{EHFS})}{\Gamma M g} \right)^2} \cdot \mu_{\text{red}} \left( \frac{1}{2}, 3, -3, \frac{1}{2}, 2, \right. \\
& \left. -2, \frac{5}{2}, 1 \right)^2 \cdot \mu_{\text{red}} \left( \frac{1}{2}, 2, -1, \frac{1}{2}, 2, -2, \frac{5}{2}, -1 \right)^2 :
\end{aligned}$$

▼ (3, -3) → (3, -3) [no change!]:

$$\begin{aligned}
F2P33n22n33n := d \rightarrow & \frac{1}{1 + \left( \frac{2 \cdot (d - \text{EHFS})}{\Gamma M g} \right)^2} \cdot \mu_{\text{red}} \left( \frac{1}{2}, 3, -3, \frac{1}{2}, 2, \right. \\
& \left. -2, \frac{5}{2}, 1 \right)^2 \cdot \mu_{\text{red}} \left( \frac{1}{2}, 2, -2, \frac{1}{2}, 3, -3, \frac{5}{2}, -1 \right)^2 :
\end{aligned}$$

▼ (3, -3) → (3, -2):

$$\begin{aligned}
F2P33n22n32n := d \rightarrow & \frac{1}{1 + \left( \frac{2 \cdot (d - \text{EHFS})}{\Gamma M g} \right)^2} \cdot \mu_{\text{red}} \left( \frac{1}{2}, 3, -3, \frac{1}{2}, 2, \right. \\
& \left. -2, \frac{5}{2}, 1 \right)^2 \cdot \mu_{\text{red}} \left( \frac{1}{2}, 3, -2, \frac{1}{2}, 2, -2, \frac{5}{2}, 0 \right)^2 :
\end{aligned}$$

▼ (3, -3) → (3, -1):

$$\begin{aligned} \text{F2P33n22n31n} := d \rightarrow & \frac{1}{1 + \left( \frac{2 \cdot (d - \text{EHFS})}{\Gamma \text{Mg}} \right)^2} \cdot \mu \text{red} \left( \frac{1}{2}, 3, -3, \frac{1}{2}, 2, \right. \\ & \left. -2, \frac{5}{2}, 1 \right)^2 \cdot \mu \text{red} \left( \frac{1}{2}, 3, -1, \frac{1}{2}, 2, -2, \frac{5}{2}, -1 \right)^2 : \end{aligned}$$

▼ Intermediate State (2', -1):

▼ (3, -2) → (2, -2):

$$\text{F2P32n21n22n} := d$$

$$\begin{aligned} \rightarrow & \frac{1}{1 + \left( \frac{2 \cdot (d + \text{ZSU2}[1] + \text{ZSL}[1] - \text{EHFS})}{\Gamma \text{Mg}} \right)^2} \cdot \mu \text{red} \left( \frac{1}{2}, \right. \\ & \left. 3, -2, \frac{1}{2}, 2, -1, \frac{5}{2}, 1 \right)^2 \cdot \mu \text{red} \left( \frac{1}{2}, 2, -2, \frac{1}{2}, 2, -1, \frac{5}{2}, 1 \right)^2 : \end{aligned}$$

▼ (3, -2) → (2, -1):

$$\text{F2P32n21n21n} := d$$

$$\begin{aligned} \rightarrow & \frac{1}{1 + \left( \frac{2 \cdot (d + \text{ZSU2}[1] + \text{ZSL}[1] - \text{EHFS})}{\Gamma \text{Mg}} \right)^2} \cdot \mu \text{red} \left( \frac{1}{2}, \right. \\ & \left. 3, -2, \frac{1}{2}, 2, -1, \frac{5}{2}, 1 \right)^2 \cdot \mu \text{red} \left( \frac{1}{2}, 2, -1, \frac{1}{2}, 2, -1, \frac{5}{2}, 0 \right)^2 : \end{aligned}$$

▼ (3, -2) → (2, 0):

$$\begin{aligned} \text{F2P32n21n20} := d \rightarrow & \frac{1}{1 + \left( \frac{2 \cdot (d + \text{ZSU2}[1] + \text{ZSL}[1] - \text{EHFS})}{\Gamma \text{Mg}} \right)^2} \\ & \cdot \mu \text{red} \left( \frac{1}{2}, 3, -2, \frac{1}{2}, 2, -1, \frac{5}{2}, 1 \right)^2 \cdot \mu \text{red} \left( \frac{1}{2}, 2, 0, \frac{1}{2}, 2, -1, \frac{5}{2}, \right. \\ & \left. -1 \right)^2 : \end{aligned}$$

▼ (3, -2) → (3, -2) [no change!!]:

$$\text{F2P32n21n32n} := d$$

$$\begin{aligned} \rightarrow & \frac{1}{1 + \left( \frac{2 \cdot (d + \text{ZSU2}[1] + \text{ZSL}[1] - \text{EHFS})}{\Gamma \text{Mg}} \right)^2} \cdot \mu \text{red} \left( \frac{1}{2}, \right. \\ & \left. 3, -2, \frac{1}{2}, 2, -1, \frac{5}{2}, 1 \right)^2 \cdot \mu \text{red} \left( \frac{1}{2}, 3, -2, \frac{1}{2}, 2, -1, \frac{5}{2}, 1 \right)^2 : \end{aligned}$$

▼ (3, -2) → (3, -1):

$$\text{F2P32n21n31n} := d$$

$$\rightarrow \frac{1}{1 + \left( \frac{2 \cdot (d + \text{ZSU2}[1] + \text{ZSL}[1] - \text{EHFS})}{\Gamma \text{Mg}} \right)^2} \cdot \mu \text{red} \left( \frac{1}{2}, \right.$$

$$3, -2, \frac{1}{2}, 2, -1, \frac{5}{2}, 1)^2 \cdot \mu_{\text{red}}\left(\frac{1}{2}, 3, -1, \frac{1}{2}, 2, -1, \frac{5}{2}, 0\right)^2 :$$

▼ (3, -2) → (3, 0):

$$\begin{aligned} \text{F2P32n21n30} := d &\rightarrow \frac{1}{1 + \left( \frac{2 \cdot (d + \text{ZSU2}[1] + \text{ZSL}[1] - \text{EHFS})}{\Gamma \text{Mg}} \right)^2} \\ &\cdot \mu_{\text{red}}\left(\frac{1}{2}, 3, -2, \frac{1}{2}, 2, -1, \frac{5}{2}, 1\right)^2 \cdot \mu_{\text{red}}\left(\frac{1}{2}, 3, 0, \frac{1}{2}, 2, -1, \frac{5}{2}, \right. \\ &\left. -1\right)^2 : \end{aligned}$$

▼ Intermediate State (2', 0):

▼ (3, -1) → (2, -1):

$$\begin{aligned} \text{F2P31n2021n} := d &\rightarrow \frac{1}{1 + \left( \frac{2 \cdot (d + \text{ZSU2}[2] + \text{ZSL}[2] - \text{EHFS})}{\Gamma \text{Mg}} \right)^2} \\ &\cdot \mu_{\text{red}}\left(\frac{1}{2}, 3, -1, \frac{1}{2}, 2, 0, \frac{5}{2}, 1\right)^2 \cdot \mu_{\text{red}}\left(\frac{1}{2}, 2, -1, \frac{1}{2}, 2, 0, \frac{5}{2}, \right. \\ &\left. 1\right)^2 : \end{aligned}$$

▼ (3, -1) → (2, 0):

$$\begin{aligned} \text{F2P31n2020} := d &\rightarrow \frac{1}{1 + \left( \frac{2 \cdot (d + \text{ZSU2}[2] + \text{ZSL}[2] - \text{EHFS})}{\Gamma \text{Mg}} \right)^2} \\ &\cdot \mu_{\text{red}}\left(\frac{1}{2}, 3, -1, \frac{1}{2}, 2, 0, \frac{5}{2}, 1\right)^2 \cdot \mu_{\text{red}}\left(\frac{1}{2}, 2, 0, \frac{1}{2}, 2, 0, \frac{5}{2}, 0\right)^2 : \end{aligned}$$

▼ (3, -1) → (2, 1):

$$\begin{aligned} \text{F2P31n2021} := d &\rightarrow \frac{1}{1 + \left( \frac{2 \cdot (d + \text{ZSU2}[2] + \text{ZSL}[2] - \text{EHFS})}{\Gamma \text{Mg}} \right)^2} \\ &\cdot \mu_{\text{red}}\left(\frac{1}{2}, 3, -1, \frac{1}{2}, 2, 0, \frac{5}{2}, 1\right)^2 \cdot \mu_{\text{red}}\left(\frac{1}{2}, 2, 1, \frac{1}{2}, 2, 0, \frac{5}{2}, \right. \\ &\left. -1\right)^2 : \end{aligned}$$

▼ (3, -1) → (3, -1) [no change!!]:

$$\text{F2P31n2031n} := d \rightarrow \frac{1}{1 + \left( \frac{2 \cdot (d + \text{ZSU2}[2] + \text{ZSL}[2] - \text{EHFS})}{\Gamma \text{Mg}} \right)^2}$$

$$\cdot \mu_{\text{red}} \left( \frac{1}{2}, 3, -1, \frac{1}{2}, 2, 0, \frac{5}{2}, 1 \right)^2 \cdot \mu_{\text{red}} \left( \frac{1}{2}, 3, -1, \frac{1}{2}, 2, 0, \frac{5}{2}, 1 \right)^2 :$$

▼ (3, -1) → (3, 0):

$$\text{F2P31n2030} := d \rightarrow \frac{1}{1 + \left( \frac{2 \cdot (d + \text{ZSU2}[2] + \text{ZSL}[2] - \text{EHFS})}{\Gamma \text{Mg}} \right)^2} \cdot \mu_{\text{red}} \left( \frac{1}{2}, 3, -1, \frac{1}{2}, 2, 0, \frac{5}{2}, 1 \right)^2 \cdot \mu_{\text{red}} \left( \frac{1}{2}, 3, 0, \frac{1}{2}, 2, 0, \frac{5}{2}, 0 \right)^2 :$$

▼ (3, -1) → (3, 1):

$$\text{F2P31n2031} := d \rightarrow \frac{1}{1 + \left( \frac{2 \cdot (d + \text{ZSU2}[2] + \text{ZSL}[2] - \text{EHFS})}{\Gamma \text{Mg}} \right)^2} \cdot \mu_{\text{red}} \left( \frac{1}{2}, 3, -1, \frac{1}{2}, 2, 0, \frac{5}{2}, 1 \right)^2 \cdot \mu_{\text{red}} \left( \frac{1}{2}, 3, 1, \frac{1}{2}, 2, 0, \frac{5}{2}, -1 \right)^2 :$$

▼ Intermediate State (2', 1):

▼ (3, 0) → (2, 0):

$$\text{F2P302120} := d \rightarrow \frac{1}{1 + \left( \frac{2 \cdot (d + \text{ZSU2}[3] + \text{ZSL}[3] - \text{EHFS})}{\Gamma \text{Mg}} \right)^2} \cdot \mu_{\text{red}} \left( \frac{1}{2}, 3, 0, \frac{1}{2}, 2, 1, \frac{5}{2}, 1 \right)^2 \cdot \mu_{\text{red}} \left( \frac{1}{2}, 2, 0, \frac{1}{2}, 2, 1, \frac{5}{2}, 1 \right)^2 :$$

▼ (3, 0) → (2, 1):

$$\text{F2P302121} := d \rightarrow \frac{1}{1 + \left( \frac{2 \cdot (d + \text{ZSU2}[3] + \text{ZSL}[3] - \text{EHFS})}{\Gamma \text{Mg}} \right)^2} \cdot \mu_{\text{red}} \left( \frac{1}{2}, 3, 0, \frac{1}{2}, 2, 1, \frac{5}{2}, 1 \right)^2 \cdot \mu_{\text{red}} \left( \frac{1}{2}, 2, 1, \frac{1}{2}, 2, 1, \frac{5}{2}, 0 \right)^2 :$$

▼ (3, 0) → (2, 2):

$$\text{F2P302122} := d \rightarrow \frac{1}{1 + \left( \frac{2 \cdot (d + \text{ZSU2}[3] + \text{ZSL}[3] - \text{EHFS})}{\Gamma \text{Mg}} \right)^2} \cdot \mu_{\text{red}} \left( \frac{1}{2}, 3, 0, \frac{1}{2}, 2, 1, \frac{5}{2}, 1 \right)^2 \cdot \mu_{\text{red}} \left( \frac{1}{2}, 2, 2, \frac{1}{2}, 2, 1, \frac{5}{2}, -1 \right)^2 :$$

▼ (3, 0) → (3, 0) [no change!!]:

$$\text{F2P302130} := d \rightarrow \frac{1}{1 + \left( \frac{2 \cdot (d + \text{ZSU2}[3] + \text{ZSL}[3] - \text{EHFS})}{\Gamma \text{Mg}} \right)^2} \cdot \mu_{\text{red}} \left( \frac{1}{2}, 3, 0, \frac{1}{2}, 2, 1, \frac{5}{2}, 1 \right)^2 \cdot \mu_{\text{red}} \left( \frac{1}{2}, 3, 0, \frac{1}{2}, 2, 1, \frac{5}{2}, 1 \right)^2 :$$

▼ (3, 0) → (3, 1):

$$\text{F2P302131} := d \rightarrow \frac{1}{1 + \left( \frac{2 \cdot (d + \text{ZSU2}[3] + \text{ZSL}[3] - \text{EHFS})}{\Gamma \text{Mg}} \right)^2} \cdot \mu_{\text{red}} \left( \frac{1}{2}, 3, 0, \frac{1}{2}, 2, 1, \frac{5}{2}, 1 \right)^2 \cdot \mu_{\text{red}} \left( \frac{1}{2}, 3, 1, \frac{1}{2}, 2, 1, \frac{5}{2}, 0 \right)^2 :$$

▼ (3, 0) → (3, 2):

$$\text{F2P302132} := d \rightarrow \frac{1}{1 + \left( \frac{2 \cdot (d + \text{ZSU2}[3] + \text{ZSL}[3] - \text{EHFS})}{\Gamma \text{Mg}} \right)^2} \cdot \mu_{\text{red}} \left( \frac{1}{2}, 3, 0, \frac{1}{2}, 2, 1, \frac{5}{2}, 1 \right)^2 \cdot \mu_{\text{red}} \left( \frac{1}{2}, 3, 2, \frac{1}{2}, 2, 1, \frac{5}{2}, -1 \right)^2 :$$

▼ Intermediate State (2', 2):

▼ (3, 1) → (2, 1):

$$\text{F2P312221} := d \rightarrow \frac{1}{1 + \left( \frac{2 \cdot (d + \text{ZSU2}[4] + \text{ZSL}[4] - \text{EHFS})}{\Gamma \text{Mg}} \right)^2} \cdot \mu_{\text{red}} \left( \frac{1}{2}, 3, 1, \frac{1}{2}, 2, 2, \frac{5}{2}, 1 \right)^2 \cdot \mu_{\text{red}} \left( \frac{1}{2}, 2, 1, \frac{1}{2}, 2, 2, \frac{5}{2}, 1 \right)^2 :$$

▼ (3, 1) → (2, 2):

$$\text{F2P312222} := d \rightarrow \frac{1}{1 + \left( \frac{2 \cdot (d + \text{ZSU2}[4] + \text{ZSL}[4] - \text{EHFS})}{\Gamma \text{Mg}} \right)^2} \cdot \mu_{\text{red}} \left( \frac{1}{2}, 3, 1, \frac{1}{2}, 2, 2, \frac{5}{2}, 1 \right)^2 \cdot \mu_{\text{red}} \left( \frac{1}{2}, 2, 2, \frac{1}{2}, 2, 2, \frac{5}{2}, 0 \right)^2 :$$

▼ (3, 1) → (3, 1) [no change!!]:

$$\text{F2P312231} := d \rightarrow \frac{1}{1 + \left( \frac{2 \cdot (d + \text{ZSU2}[4] + \text{ZSL}[4] - \text{EHFS})}{\Gamma \text{Mg}} \right)^2} \cdot \mu_{\text{red}} \left( \frac{1}{2}, 3, 1, \frac{1}{2}, 2, 2, \frac{5}{2}, 1 \right)^2 \cdot \mu_{\text{red}} \left( \frac{1}{2}, 3, 1, \frac{1}{2}, 2, 2, \frac{5}{2}, 1 \right)^2 :$$

▼ (3, 1) → (3, 2):

$$\text{F2P312232} := d \rightarrow \frac{1}{1 + \left( \frac{2 \cdot (d + \text{ZSU2}[4] + \text{ZSL}[4] - \text{EHFS})}{\Gamma \text{Mg}} \right)^2}$$

$$\cdot \mu_{\text{red}}\left(\frac{1}{2}, 3, 1, \frac{1}{2}, 2, 2, \frac{5}{2}, 1\right)^2 \cdot \mu_{\text{red}}\left(\frac{1}{2}, 3, 2, \frac{1}{2}, 2, 2, \frac{5}{2}, 0\right)^2 :$$

▼ (3, 1) → (3, 3):

$$F2P312233 := d \rightarrow \frac{1}{1 + \left( \frac{2 \cdot (d + ZSU2[4] + ZSL[4] - EHFS)}{\Gamma M_g} \right)^2} \cdot \mu_{\text{red}}\left(\frac{1}{2}, 3, 1, \frac{1}{2}, 2, 2, \frac{5}{2}, 1\right)^2 \cdot \mu_{\text{red}}\left(\frac{1}{2}, 3, 3, \frac{1}{2}, 2, 2, \frac{5}{2}, -1\right)^2 :$$

▼ Rate Equations for the 2' intermediate level:

▼ Rate Equations:

$$F2Eq33n := d \rightarrow \frac{d}{dt} F2p33n(t) = ( (-F2P33n22n32n(d) - F2P33n22n31n(d) - F2P33n22n22n(d) - F2P33n22n21n(d)) \cdot F2p33n(t) ) :$$

$$F2Eq32n := d \rightarrow \frac{d}{dt} F2p32n(t) = ( (-F2P32n21n31n(d) - F2P32n21n30(d) - F2P32n21n22n(d) - F2P32n21n21n(d) - F2P32n21n20(d)) \cdot F2p32n(t) + F2P33n22n32n(d) \cdot F2p33n(t) ) :$$

$$F2Eq31n := d \rightarrow \frac{d}{dt} F2p31n(t) = ( (-F2P31n2030(d) - F2P31n2031(d) - F2P31n2021n(d) - F2P31n2020(d) - F2P31n2021(d)) \cdot F2p31n(t) + F2P33n22n31n(d) \cdot F2p33n(t) + F2P32n21n31n(d) \cdot F2p32n(t) ) :$$

$$F2Eq30 := d \rightarrow \frac{d}{dt} F2p30(t) = ( (-F2P302131(d) - F2P302132(d) - F2P302120(d) - F2P302121(d) - F2P302122(d)) \cdot F2p30(t) + F2P31n2030(d) \cdot F2p31n(t) + F2P32n21n30(d) \cdot F2p32n(t) ) :$$

$$F2Eq31 := d \rightarrow \frac{d}{dt} F2p31(t) = ( (-F2P312232(d) - F2P312233(d) - F2P312221(d) - F2P312222(d)) \cdot F2p31(t) + F2P302131(d) \cdot F2p30(t) + F2P31n2031(d) \cdot F2p31n(t) ) :$$

$$F2Eq32 := d \rightarrow \frac{d}{dt} F2p32(t) = F2P302132(d) \cdot F2p30(t) + F2P312232(d) \cdot F2p31(t) :$$

$$F2Eq33 := d \rightarrow \frac{d}{dt} F2p33(t) = F2P312233(d) \cdot F2p31(t) :$$

$$F2Eq22n := d \rightarrow \frac{d}{dt} F2p22n(t) = F2P33n22n22n(d) \cdot F2p33n(t) + F2P32n21n22n(d) \cdot F2p32n(t) :$$

$$F2Eq21n := d \rightarrow \frac{d}{dt} F2p21n(t) = F2P33n22n21n(d) \cdot F2p33n(t) + F2P32n21n21n(d) \cdot F2p32n(t) + F2P31n2021n(d) \cdot F2p31n(t) :$$

$$\begin{aligned} \text{F2Eq20} := d \rightarrow \frac{d}{dt} \text{F2p20}(t) &= \text{F2P32n21n20}(d) \cdot \text{F2p32n}(t) \\ &+ \text{F2P31n2020}(d) \cdot \text{F2p31n}(t) + \text{F2P302120}(d) \cdot \text{F2p30}(t) : \end{aligned}$$

$$\begin{aligned} \text{F2Eq21} := d \rightarrow \frac{d}{dt} \text{F2p21}(t) &= \text{F2P31n2021}(d) \cdot \text{F2p31n}(t) \\ &+ \text{F2P302121}(d) \cdot \text{F2p30}(t) + \text{F2P312221}(d) \cdot \text{F2p31}(t) : \end{aligned}$$

$$\begin{aligned} \text{F2Eq22} := d \rightarrow \frac{d}{dt} \text{F2p22}(t) &= \text{F2P302122}(d) \cdot \text{F2p30}(t) \\ &+ \text{F2P312222}(d) \cdot \text{F2p31}(t) : \end{aligned}$$



Solving the Rate Equations:

```
TwoPrimeProbeDynamics := proc(ProbeDetuning)
  global F2Solns, F2P33n, F2P32n, F2P31n, F2P30, F2P31, F2P32,
    F2P33, F2P22n, F2P21n, F2P20, F2P21, F2P22;
  local F2Eqs;
  F2Eqs := { F2Eq33n(ProbeDetuning), F2Eq32n(ProbeDetuning),
    F2Eq31n(ProbeDetuning), F2Eq30(ProbeDetuning),
    F2Eq31(ProbeDetuning), F2Eq32(ProbeDetuning),
    F2Eq33(ProbeDetuning), F2Eq22n(ProbeDetuning),
    F2Eq21n(ProbeDetuning), F2Eq20(ProbeDetuning),
    F2Eq21(ProbeDetuning), F2Eq22(ProbeDetuning), F2p33(0)
    = 0, F2p32(0) = 0, F2p31(0) = 0, F2p30(0) = 0, F2p31n(0)
    = 0, F2p32n(0) = 0, F2p33n(0) = 1, F2p22n(0) = 0, F2p21n(0)
    = 0, F2p20(0) = 0, F2p21(0) = 0, F2p22(0) = 0 } :
  F2Solns := dsolve(F2Eqs, numeric, output = listprocedure) :
  F2P33n := eval(F2p33n(t), F2Solns);
  F2P32n := eval(F2p32n(t), F2Solns);
  F2P31n := eval(F2p31n(t), F2Solns);
  F2P30 := eval(F2p30(t), F2Solns);
  F2P31 := eval(F2p31(t), F2Solns);
  F2P32 := eval(F2p32(t), F2Solns);
  F2P33 := eval(F2p33(t), F2Solns);
  F2P22n := eval(F2p22n(t), F2Solns);
  F2P21n := eval(F2p21n(t), F2Solns);
  F2P20 := eval(F2p20(t), F2Solns);
  F2P21 := eval(F2p21(t), F2Solns);
  F2P22 := eval(F2p22(t), F2Solns);
end proc;
```



Rate Equations Allowing Off-Resonant Driving to 3' and 2':



Rate Equations:

$$\begin{aligned} \text{F23Eq33n} := d \rightarrow \frac{d}{dt} \text{F23p33n}(t) &= ((-\text{F3P33n32n32n}(d) \\ &- \text{F3P33n32n31n}(d) - \text{F3P33n32n22n}(d) - \text{F3P33n32n21n}(d)) \\ &\cdot \text{F23p33n}(t)) + ((-\text{F2P33n22n32n}(d) - \text{F2P33n22n31n}(d) \\ &- \text{F2P33n22n22n}(d) - \text{F2P33n22n21n}(d)) \cdot \text{F23p33n}(t)) : \\ \text{F23Eq32n} := d \rightarrow \frac{d}{dt} \text{F23p32n}(t) &= ((-\text{F3P32n31n31n}(d) \\ &- \text{F3P32n31n30}(d) - \text{F3P32n31n22n}(d) - \text{F3P32n31n21n}(d) \\ &- \text{F3P32n31n20}(d)) \cdot \text{F23p32n}(t) + \text{F3P33n32n32n}(d) \end{aligned}$$

$$\begin{aligned}
& \cdot F23p33n(t) + ((-F2P32n21n31n(d) - F2P32n21n30(d) \\
& - F2P32n21n22n(d) - F2P32n21n21n(d) - F2P32n21n20(d)) \\
& \cdot F23p32n(t) + F2P33n22n32n(d) \cdot F23p33n(t)) : \\
F23Eq31n := d \rightarrow \frac{d}{dt} F23p31n(t) = & ((-F3P31n3030(d) \\
& - F3P31n3031(d) - F3P31n3021n(d) - F3P31n3020(d) \\
& - F3P31n3021(d)) \cdot F23p31n(t) + F3P33n32n31n(d) \cdot F23p33n(t) \\
& + F3P32n31n31n(d) \cdot F23p32n(t)) + ((-F2P31n2030(d) \\
& - F2P31n2031(d) - F2P31n2021n(d) - F2P31n2020(d) \\
& - F2P31n2021(d)) \cdot F23p31n(t) + F2P33n22n31n(d) \cdot F23p33n(t) \\
& + F2P32n21n31n(d) \cdot F23p32n(t)) : \\
F23Eq30 := d \rightarrow \frac{d}{dt} F23p30(t) = & ((-F3P303131(d) - F3P303132(d) \\
& - F3P303120(d) - F3P303121(d) - F3P303122(d)) \cdot F23p30(t) \\
& + F3P31n3030(d) \cdot F23p31n(t) + F3P32n31n30(d) \cdot F23p32n(t)) \\
& + ((-F2P302131(d) - F2P302132(d) - F2P302120(d) \\
& - F2P302121(d) - F2P302122(d)) \cdot F23p30(t) + F2P31n2030(d) \\
& \cdot F23p31n(t) + F2P32n21n30(d) \cdot F23p32n(t)) : \\
F23Eq31 := d \rightarrow \frac{d}{dt} F23p31(t) = & ((-F3P313232(d) - F3P313233(d) \\
& - F3P313221(d) - F3P313222(d)) \cdot F23p31(t) + F3P303131(d) \\
& \cdot F23p30(t) + F3P31n3031(d) \cdot F23p31n(t)) + ((-F2P312232(d) \\
& - F2P312233(d) - F2P312221(d) - F2P312222(d)) \cdot F23p31(t) \\
& + F2P302131(d) \cdot F23p30(t) + F2P31n2031(d) \cdot F23p31n(t)) : \\
F23Eq32 := d \rightarrow \frac{d}{dt} F23p32(t) = & ((-F3P323333(d) - F3P323322(d)) \\
& \cdot F23p32(t) + F3P313232(d) \cdot F23p31(t) + F3P303132(d) \\
& \cdot F23p30(t)) + F2P302132(d) \cdot F23p30(t) + F2P312232(d) \\
& \cdot F23p31(t) : \\
F23Eq33 := d \rightarrow \frac{d}{dt} F23p33(t) = & (F3P313233(d) \cdot F23p31(t) \\
& + F3P323333(d) \cdot F23p32(t)) + F2P312233(d) \cdot F23p31(t) : \\
F23Eq22n := d \rightarrow \frac{d}{dt} F23p22n(t) = & F3P33n32n22n(d) \cdot F23p33n(t) \\
& + F3P32n31n22n(d) \cdot F23p32n(t) + F2P33n22n22n(d) \cdot F23p33n(t) \\
& + F2P32n21n22n(d) \cdot F23p32n(t) \\
F23Eq21n := d \rightarrow \frac{d}{dt} F23p21n(t) = & F3P33n32n21n(d) \cdot F23p33n(t) \\
& + F3P32n31n21n(d) \cdot F23p32n(t) + F3P31n3021n(d) \cdot F23p31n(t) \\
& + F2P33n22n21n(d) \cdot F23p33n(t) + F2P32n21n21n(d) \cdot F23p32n(t) \\
& + F2P31n2021n(d) \cdot F23p31n(t) \\
F23Eq20 := d \rightarrow \frac{d}{dt} F23p20(t) = & F3P32n31n20(d) \cdot F23p32n(t) \\
& + F3P31n3020(d) \cdot F23p31n(t) + F3P303120(d) \cdot F23p30(t) \\
& + F2P32n21n20(d) \cdot F23p32n(t) + F2P31n2020(d) \cdot F23p31n(t) \\
& + F2P302120(d) \cdot F23p30(t) : \\
F23Eq21 := d \rightarrow \frac{d}{dt} F23p21(t) = & F3P31n3021(d) \cdot F23p31n(t) \\
& + F3P303121(d) \cdot F23p30(t) + F3P313221(d) \cdot F23p31(t) \\
& + F2P31n2021(d) \cdot F23p31n(t) + F2P302121(d) \cdot F23p30(t) \\
& + F2P312221(d) \cdot F23p31(t) : \\
F23Eq22 := d \rightarrow \frac{d}{dt} F23p22(t) = & F3P303122(d) \cdot F23p30(t) \\
& + F3P313222(d) \cdot F23p31(t) + F3P323322(d) \cdot F23p32(t)
\end{aligned}$$



$$(3,-3) \rightarrow (4',-4) \rightarrow (3,-3)$$

We can eliminate the excited state and obtain equations for the probability of the populating the various ground state sublevels. To keep things somewhat straightforward, 3n would correspond to an  $mF=-3$ , and a 3p will correspond to an  $F = 3'$ . So, considering probabilities by level we have (separated by what intermediate state we use):

▼ Intermediate State (4', 2):

▼ (3, 3) → (3, 3) (no change):

$$P334233 := d \rightarrow \frac{1}{1 + \left(\frac{2 \cdot d}{\Gamma M g}\right)^2} \cdot \mu_{\text{red}}\left(\frac{1}{2}, 3, 3, \frac{3}{2}, 4, 2, \frac{5}{2}, -1\right)^2 \\ \cdot \mu_{\text{red}}\left(\frac{1}{2}, 3, 3, \frac{3}{2}, 4, 2, \frac{5}{2}, -1\right)^2 :$$

▼ (3, 3) → (3, 2):

$$P334232 := d \rightarrow \frac{1}{1 + \left(\frac{2 \cdot d}{\Gamma M g}\right)^2} \cdot \mu_{\text{red}}\left(\frac{1}{2}, 3, 3, \frac{3}{2}, 4, 2, \frac{5}{2}, -1\right)^2 \\ \cdot \mu_{\text{red}}\left(\frac{1}{2}, 3, 2, \frac{3}{2}, 4, 2, \frac{5}{2}, 0\right)^2 :$$

▼ (3, 3) → (3, 1):

$$P334231 := d \rightarrow \frac{1}{1 + \left(\frac{2 \cdot d}{\Gamma M g}\right)^2} \cdot \mu_{\text{red}}\left(\frac{1}{2}, 3, 3, \frac{3}{2}, 4, 2, \frac{5}{2}, -1\right)^2 \\ \cdot \mu_{\text{red}}\left(\frac{1}{2}, 3, 1, \frac{3}{2}, 4, 2, \frac{5}{2}, 1\right)^2 :$$

▼ Intermediate State (4', 1):

▼ (3, 2) → (3, 2): (no change)

$$P324132 := d \rightarrow \frac{1}{1 + \left(\frac{2 \cdot d}{\Gamma M g}\right)^2} \cdot \mu_{\text{red}}\left(\frac{1}{2}, 3, 2, \frac{3}{2}, 4, 1, \frac{5}{2}, -1\right)^2 \\ \cdot \mu_{\text{red}}\left(\frac{1}{2}, 3, 2, \frac{3}{2}, 4, 1, \frac{5}{2}, -1\right)^2 :$$

▼ (3, 2) → (3, 1):

$$P324131 := d \rightarrow \frac{1}{1 + \left(\frac{2 \cdot d}{\Gamma M g}\right)^2} \cdot \mu_{\text{red}}\left(\frac{1}{2}, 3, 2, \frac{3}{2}, 4, 1, \frac{5}{2}, -1\right)^2 \\ \cdot \mu_{\text{red}}\left(\frac{1}{2}, 3, 1, \frac{3}{2}, 4, 1, \frac{5}{2}, 0\right)^2 :$$

▼ (3, 2) → (3, 0):

$$P324130 := d \rightarrow \frac{1}{1 + \left(\frac{2 \cdot d}{\Gamma M g}\right)^2} \cdot \mu_{\text{red}}\left(\frac{1}{2}, 3, 2, \frac{3}{2}, 4, 1, \frac{5}{2}, -1\right)^2$$

$$\cdot\mu_{\text{red}}\left(\frac{1}{2}, 3, 0, \frac{3}{2}, 4, 1, \frac{5}{2}, 1\right)^2 :$$

▼ Intermediate State (4', 0):

▼ (3, 1)→(3, 1): (no change)

$$\begin{aligned} \text{P314031} &:= d \rightarrow \frac{1}{1 + \left(\frac{2 \cdot d}{\Gamma M g}\right)^2} \cdot \mu_{\text{red}}\left(\frac{1}{2}, 3, 1, \frac{3}{2}, 4, 0, \frac{5}{2}, -1\right)^2 \\ &\cdot \mu_{\text{red}}\left(\frac{1}{2}, 3, 1, \frac{3}{2}, 4, 0, \frac{5}{2}, -1\right)^2 : \end{aligned}$$

▼ (3, 1)→(3, 0):

$$\begin{aligned} \text{P314030} &:= d \rightarrow \frac{1}{1 + \left(\frac{2 \cdot d}{\Gamma M g}\right)^2} \cdot \mu_{\text{red}}\left(\frac{1}{2}, 3, 1, \frac{3}{2}, 4, 0, \frac{5}{2}, -1\right)^2 \\ &\cdot \mu_{\text{red}}\left(\frac{1}{2}, 3, 0, \frac{3}{2}, 4, 0, \frac{5}{2}, 0\right)^2 : \end{aligned}$$

▼ (3, 1)→(3, -1):

$$\begin{aligned} \text{P314031n} &:= d \rightarrow \frac{1}{1 + \left(\frac{2 \cdot d}{\Gamma M g}\right)^2} \cdot \mu_{\text{red}}\left(\frac{1}{2}, 3, 1, \frac{3}{2}, 4, 0, \frac{5}{2}, -1\right)^2 \\ &\cdot \mu_{\text{red}}\left(\frac{1}{2}, 3, -1, \frac{3}{2}, 4, 0, \frac{5}{2}, 1\right)^2 : \end{aligned}$$

▼ Intermediate State (4', -1):

▼ (3, 0)→(3, 0): (no change)

$$\begin{aligned} \text{P3041n30} &:= d \rightarrow \frac{1}{1 + \left(\frac{2 \cdot d}{\Gamma M g}\right)^2} \cdot \mu_{\text{red}}\left(\frac{1}{2}, 3, 0, \frac{3}{2}, 4, -1, \frac{5}{2}, -1\right)^2 \\ &\cdot \mu_{\text{red}}\left(\frac{1}{2}, 3, 0, \frac{3}{2}, 4, -1, \frac{5}{2}, -1\right)^2 : \end{aligned}$$

▼ (3, 0)→(3, -1):

$$\begin{aligned} \text{P3041n31n} &:= d \rightarrow \frac{1}{1 + \left(\frac{2 \cdot d}{\Gamma M g}\right)^2} \cdot \mu_{\text{red}}\left(\frac{1}{2}, 3, 0, \frac{3}{2}, 4, -1, \frac{5}{2}, -1\right)^2 \\ &\cdot \mu_{\text{red}}\left(\frac{1}{2}, 3, -1, \frac{3}{2}, 4, -1, \frac{5}{2}, 0\right)^2 : \end{aligned}$$

▼ (3, 0)→(3, -2):

$$\text{P3041n32n} := d \rightarrow \frac{1}{1 + \left(\frac{2 \cdot d}{\Gamma M g}\right)^2} \cdot \mu_{\text{red}}\left(\frac{1}{2}, 3, 0, \frac{3}{2}, 4, -1, \frac{5}{2}, -1\right)^2$$

$$\cdot \mu_{\text{red}} \left( \frac{1}{2}, 3, -2, \frac{3}{2}, 4, -1, \frac{5}{2}, 1 \right)^2 :$$

▼ Intermediate State (4', -2):

▼ (3, -1) → (3, -1): (no change)

$$P31n42n31n := d \rightarrow \frac{1}{1 + \left( \frac{2 \cdot d}{\Gamma M g} \right)^2} \cdot \mu_{\text{red}} \left( \frac{1}{2}, 3, -1, \frac{3}{2}, 4, -2, \frac{5}{2}, -1 \right)^2$$

$$\cdot \mu_{\text{red}} \left( \frac{1}{2}, 3, -1, \frac{3}{2}, 4, -2, \frac{5}{2}, -1 \right)^2 :$$

▼ (3, -1) → (3, -2):

$$P31n42n32n := d \rightarrow \frac{1}{1 + \left( \frac{2 \cdot d}{\Gamma M g} \right)^2} \cdot \mu_{\text{red}} \left( \frac{1}{2}, 3, -1, \frac{3}{2}, 4, -2, \frac{5}{2}, -1 \right)^2$$

$$\cdot \mu_{\text{red}} \left( \frac{1}{2}, 3, -2, \frac{3}{2}, 4, -2, \frac{5}{2}, 0 \right)^2 :$$

▼ (3, -1) → (3, -3):

$$P31n42n33n := d \rightarrow \frac{1}{1 + \left( \frac{2 \cdot d}{\Gamma M g} \right)^2} \cdot \mu_{\text{red}} \left( \frac{1}{2}, 3, -1, \frac{3}{2}, 4, -2, \frac{5}{2}, -1 \right)^2$$

$$\cdot \mu_{\text{red}} \left( \frac{1}{2}, 3, -3, \frac{3}{2}, 4, -2, \frac{5}{2}, 1 \right)^2 :$$

▼ Intermediate State (4', -3):

▼ (3, -2) → (3, -2):

$$P32n43n32n := d \rightarrow \frac{1}{1 + \left( \frac{2 \cdot d}{\Gamma M g} \right)^2} \cdot \mu_{\text{red}} \left( \frac{1}{2}, 3, -2, \frac{3}{2}, 4, -3, \frac{5}{2}, -1 \right)^2$$

$$\cdot \mu_{\text{red}} \left( \frac{1}{2}, 3, -2, \frac{3}{2}, 4, -3, \frac{5}{2}, -1 \right)^2 :$$

print(); # input placeholder

▼ (3, -2) → (3, -3):

$$P32n43n33n := d \rightarrow \frac{1}{1 + \left( \frac{2 \cdot d}{\Gamma M g} \right)^2} \cdot \mu_{\text{red}} \left( \frac{1}{2}, 3, -2, \frac{3}{2}, 4, -3, \frac{5}{2}, -1 \right)^2$$

$$\cdot \mu_{\text{red}} \left( \frac{1}{2}, 3, -3, \frac{3}{2}, 4, -3, \frac{5}{2}, 0 \right)^2 :$$

▼ Intermediate State (4', -4):

▼ (3, -3) → (3, -3):



$$P333222 := d \rightarrow \frac{1}{1 + \left( \frac{2 \cdot (d + \Delta HF3P)}{\Gamma M g} \right)^2} \cdot \mu_{red} \left( \frac{1}{2}, 3, 3, \frac{3}{2}, 3, 2, \frac{5}{2}, -1 \right)^2 \cdot \mu_{red} \left( \frac{1}{2}, 2, 2, \frac{3}{2}, 3, 2, \frac{5}{2}, 0 \right)^2 :$$

▼ (3, 3) → (2, 1):

$$P333221 := d \rightarrow \frac{1}{1 + \left( \frac{2 \cdot (d + \Delta HF3P)}{\Gamma M g} \right)^2} \cdot \mu_{red} \left( \frac{1}{2}, 3, 3, \frac{3}{2}, 3, 2, \frac{5}{2}, -1 \right)^2 \cdot \mu_{red} \left( \frac{1}{2}, 2, 1, \frac{3}{2}, 3, 2, \frac{5}{2}, 1 \right)^2 :$$

▼ (3, 3) → (3, 3): (no change)

$$P333233 := d \rightarrow \frac{1}{1 + \left( \frac{2 \cdot (d + \Delta HF3P)}{\Gamma M g} \right)^2} \cdot \mu_{red} \left( \frac{1}{2}, 3, 3, \frac{3}{2}, 3, 2, \frac{5}{2}, -1 \right)^2 \cdot \mu_{red} \left( \frac{1}{2}, 3, 3, \frac{3}{2}, 3, 2, \frac{5}{2}, -1 \right)^2 :$$

▼ (3, 3) → (3, 2):

$$P333232 := d \rightarrow \frac{1}{1 + \left( \frac{2 \cdot (d + \Delta HF3P)}{\Gamma M g} \right)^2} \cdot \mu_{red} \left( \frac{1}{2}, 3, 3, \frac{3}{2}, 3, 2, \frac{5}{2}, -1 \right)^2 \cdot \mu_{red} \left( \frac{1}{2}, 3, 2, \frac{3}{2}, 3, 2, \frac{5}{2}, 0 \right)^2 :$$

▼ (3, 3) → (3, 1):

$$P333231 := d \rightarrow \frac{1}{1 + \left( \frac{2 \cdot (d + \Delta HF3P)}{\Gamma M g} \right)^2} \cdot \mu_{red} \left( \frac{1}{2}, 3, 3, \frac{3}{2}, 3, 2, \frac{5}{2}, -1 \right)^2 \cdot \mu_{red} \left( \frac{1}{2}, 3, 1, \frac{3}{2}, 3, 2, \frac{5}{2}, 1 \right)^2 :$$

▼ Intermediate State (3', 1):

▼ (3, 2) → (2, 2):

$$P323122 := d \rightarrow \frac{1}{1 + \left( \frac{2 \cdot (d + \Delta HF3P)}{\Gamma M g} \right)^2} \cdot \mu_{red} \left( \frac{1}{2}, 3, 2, \frac{3}{2}, 3, 1, \frac{5}{2}, -1 \right)^2 \cdot \mu_{red} \left( \frac{1}{2}, 2, 2, \frac{3}{2}, 3, 1, \frac{5}{2}, -1 \right)^2 :$$

▼ (3, 2) → (2, 1):

$$P323121 := d \rightarrow \frac{1}{1 + \left( \frac{2 \cdot (d + \Delta HF3P)}{\Gamma M g} \right)^2} \cdot \mu_{red} \left( \frac{1}{2}, 3, 2, \frac{3}{2}, 3, 1, \frac{5}{2}, -1 \right)^2 \cdot \mu_{red} \left( \frac{1}{2}, 2, 1, \frac{3}{2}, 3, 1, \frac{5}{2}, 0 \right)^2 :$$

▼ (3, 2) → (2, 0):

$$\begin{aligned} \text{P323120} := d \rightarrow & \frac{1}{1 + \left( \frac{2 \cdot (d + \Delta\text{HF3P})}{\Gamma\text{Mg}} \right)^2} \cdot \mu\text{red} \left( \frac{1}{2}, 3, 2, \frac{3}{2}, 3, 1, \right. \\ & \left. \frac{5}{2}, -1 \right)^2 \cdot \mu\text{red} \left( \frac{1}{2}, 2, 0, \frac{3}{2}, 3, 1, \frac{5}{2}, 1 \right)^2 : \end{aligned}$$

▼ (3, 2) → (3, 2): (no change)

$$\begin{aligned} \text{P323132} := d \rightarrow & \frac{1}{1 + \left( \frac{2 \cdot (d + \Delta\text{HF3P})}{\Gamma\text{Mg}} \right)^2} \cdot \mu\text{red} \left( \frac{1}{2}, 3, 2, \frac{3}{2}, 3, 1, \right. \\ & \left. \frac{5}{2}, -1 \right)^2 \cdot \mu\text{red} \left( \frac{1}{2}, 3, 2, \frac{3}{2}, 3, 1, \frac{5}{2}, -1 \right)^2 : \end{aligned}$$

▼ (3, 2) → (3, 1):

$$\begin{aligned} \text{P323131} := d \rightarrow & \frac{1}{1 + \left( \frac{2 \cdot (d + \Delta\text{HF3P})}{\Gamma\text{Mg}} \right)^2} \cdot \mu\text{red} \left( \frac{1}{2}, 3, 2, \frac{3}{2}, 3, 1, \right. \\ & \left. \frac{5}{2}, -1 \right)^2 \cdot \mu\text{red} \left( \frac{1}{2}, 3, 1, \frac{3}{2}, 3, 1, \frac{5}{2}, 0 \right)^2 : \end{aligned}$$

▼ (3, 2) → (3, 0):

$$\begin{aligned} \text{P323130} := d \rightarrow & \frac{1}{1 + \left( \frac{2 \cdot (d + \Delta\text{HF3P})}{\Gamma\text{Mg}} \right)^2} \cdot \mu\text{red} \left( \frac{1}{2}, 3, 2, \frac{3}{2}, 3, 1, \right. \\ & \left. \frac{5}{2}, -1 \right)^2 \cdot \mu\text{red} \left( \frac{1}{2}, 3, 0, \frac{3}{2}, 3, 1, \frac{5}{2}, 1 \right)^2 : \end{aligned}$$

▼ Intermediate State (3', 0):

▼ (3, 1) → (2, 1):

$$\begin{aligned} \text{P313021} := d \rightarrow & \frac{1}{1 + \left( \frac{2 \cdot (d + \Delta\text{HF3P})}{\Gamma\text{Mg}} \right)^2} \cdot \mu\text{red} \left( \frac{1}{2}, 3, 1, \frac{3}{2}, 3, 0, \right. \\ & \left. \frac{5}{2}, -1 \right)^2 \cdot \mu\text{red} \left( \frac{1}{2}, 2, 1, \frac{3}{2}, 3, 0, \frac{5}{2}, -1 \right)^2 : \end{aligned}$$

▼ (3, 1) → (2, 0):

$$\begin{aligned} \text{P313020} := d \rightarrow & \frac{1}{1 + \left( \frac{2 \cdot (d + \Delta\text{HF3P})}{\Gamma\text{Mg}} \right)^2} \cdot \mu\text{red} \left( \frac{1}{2}, 3, 1, \frac{3}{2}, 3, 0, \right. \\ & \left. \frac{5}{2}, -1 \right)^2 \cdot \mu\text{red} \left( \frac{1}{2}, 2, 0, \frac{3}{2}, 3, 0, \frac{5}{2}, 0 \right)^2 : \end{aligned}$$

▼ (3, 1) → (2, -1):

$$\begin{aligned} \text{P313021n} := d \rightarrow & \frac{1}{1 + \left( \frac{2 \cdot (d + \Delta\text{HF3P})}{\Gamma\text{Mg}} \right)^2} \cdot \mu\text{red} \left( \frac{1}{2}, 3, 1, \frac{3}{2}, 3, 0, \right. \\ & \left. \frac{5}{2}, -1 \right)^2 \cdot \mu\text{red} \left( \frac{1}{2}, 2, -1, \frac{3}{2}, 3, 0, \frac{5}{2}, 1 \right)^2 : \end{aligned}$$

▼ (3, 1) → (3, 1): (no change)

$$\text{P313031} := d \rightarrow \frac{1}{1 + \left( \frac{2 \cdot (d + \Delta\text{HF3P})}{\Gamma\text{Mg}} \right)^2} \cdot \mu\text{red} \left( \frac{1}{2}, 3, 1, \frac{3}{2}, 3, 0, \frac{5}{2}, -1 \right)^2 \cdot \mu\text{red} \left( \frac{1}{2}, 3, 1, \frac{3}{2}, 3, 0, \frac{5}{2}, -1 \right)^2 :$$

▼ (3, 1) → (3, 0):

$$\text{P313030} := d \rightarrow \frac{1}{1 + \left( \frac{2 \cdot (d + \Delta\text{HF3P})}{\Gamma\text{Mg}} \right)^2} \cdot \mu\text{red} \left( \frac{1}{2}, 3, 1, \frac{3}{2}, 3, 0, \frac{5}{2}, -1 \right)^2 \cdot \mu\text{red} \left( \frac{1}{2}, 3, 0, \frac{3}{2}, 3, 0, \frac{5}{2}, 0 \right)^2 :$$

▼ (3, 1) → (3, -1):

$$\text{P313031n} := d \rightarrow \frac{1}{1 + \left( \frac{2 \cdot (d + \Delta\text{HF3P})}{\Gamma\text{Mg}} \right)^2} \cdot \mu\text{red} \left( \frac{1}{2}, 3, 1, \frac{3}{2}, 3, 0, \frac{5}{2}, -1 \right)^2 \cdot \mu\text{red} \left( \frac{1}{2}, 3, -1, \frac{3}{2}, 3, 0, \frac{5}{2}, 1 \right)^2 :$$

▼ Intermediate State (3', -1):

▼ (3, 0) → (2, 0):

$$\text{P3031n20} := d \rightarrow \frac{1}{1 + \left( \frac{2 \cdot (d + \Delta\text{HF3P})}{\Gamma\text{Mg}} \right)^2} \cdot \mu\text{red} \left( \frac{1}{2}, 3, 0, \frac{3}{2}, 3, -1, \frac{5}{2}, -1 \right)^2 \cdot \mu\text{red} \left( \frac{1}{2}, 2, 0, \frac{3}{2}, 3, -1, \frac{5}{2}, -1 \right)^2 :$$

▼ (3, 0) → (2, -1):

$$\text{P3031n21n} := d \rightarrow \frac{1}{1 + \left( \frac{2 \cdot (d + \Delta\text{HF3P})}{\Gamma\text{Mg}} \right)^2} \cdot \mu\text{red} \left( \frac{1}{2}, 3, 0, \frac{3}{2}, 3, -1, \frac{5}{2}, -1 \right)^2 \cdot \mu\text{red} \left( \frac{1}{2}, 2, -1, \frac{3}{2}, 3, -1, \frac{5}{2}, 0 \right)^2 :$$

▼ (3, 0) → (2, -2):

$$\text{P3031n22n} := d \rightarrow \frac{1}{1 + \left( \frac{2 \cdot (d + \Delta\text{HF3P})}{\Gamma\text{Mg}} \right)^2} \cdot \mu\text{red} \left( \frac{1}{2}, 3, 0, \frac{3}{2}, 3, -1, \frac{5}{2}, -1 \right)^2 \cdot \mu\text{red} \left( \frac{1}{2}, 2, -2, \frac{3}{2}, 3, -1, \frac{5}{2}, 1 \right)^2 :$$

▼ (3, 0) → (3, 0): (no change)

$$\text{P3031n30} := d \rightarrow \frac{1}{1 + \left( \frac{2 \cdot (d + \Delta\text{HF3P})}{\Gamma\text{Mg}} \right)^2} \cdot \mu\text{red} \left( \frac{1}{2}, 3, 0, \frac{3}{2}, 3, -1, \frac{5}{2}, -1 \right)^2 \cdot \mu\text{red} \left( \frac{1}{2}, 3, 0, \frac{3}{2}, 3, -1, \frac{5}{2}, -1 \right)^2 :$$

▼ (3, 0) → (3, -1):

$$\text{P3031n31n} := d \rightarrow \frac{1}{1 + \left( \frac{2 \cdot (d + \Delta\text{HF3P})}{\Gamma\text{Mg}} \right)^2} \cdot \mu\text{red} \left( \frac{1}{2}, 3, 0, \frac{3}{2}, 3, -1, \frac{5}{2}, -1 \right)^2 \cdot \mu\text{red} \left( \frac{1}{2}, 3, -1, \frac{3}{2}, 3, -1, \frac{5}{2}, 0 \right)^2 :$$

▼ (3, 0) → (3, -2):

$$\text{P3031n32n} := d \rightarrow \frac{1}{1 + \left( \frac{2 \cdot (d + \Delta\text{HF3P})}{\Gamma\text{Mg}} \right)^2} \cdot \mu\text{red} \left( \frac{1}{2}, 3, 0, \frac{3}{2}, 3, -1, \frac{5}{2}, -1 \right)^2 \cdot \mu\text{red} \left( \frac{1}{2}, 3, -2, \frac{3}{2}, 3, -1, \frac{5}{2}, 1 \right)^2 :$$

▼ Intermediate State (3', -2):

▼ (3, -1) → (2, -2):

$$\text{P31n32n22n} := d \rightarrow \frac{1}{1 + \left( \frac{2 \cdot (d + \Delta\text{HF3P})}{\Gamma\text{Mg}} \right)^2} \cdot \mu\text{red} \left( \frac{1}{2}, 3, -1, \frac{3}{2}, 3, -2, \frac{5}{2}, -1 \right)^2 \cdot \mu\text{red} \left( \frac{1}{2}, 2, -2, \frac{3}{2}, 3, -2, \frac{5}{2}, 0 \right)^2 :$$

▼ (3, -1) → (2, -1):

$$\text{P31n32n21n} := d \rightarrow \frac{1}{1 + \left( \frac{2 \cdot (d + \Delta\text{HF3P})}{\Gamma\text{Mg}} \right)^2} \cdot \mu\text{red} \left( \frac{1}{2}, 3, -1, \frac{3}{2}, 3, -2, \frac{5}{2}, -1 \right)^2 \cdot \mu\text{red} \left( \frac{1}{2}, 2, -1, \frac{3}{2}, 3, -2, \frac{5}{2}, -1 \right)^2 :$$

▼ (3, -1) → (3, -3):

$$\text{P31n32n33n} := d \rightarrow \frac{1}{1 + \left( \frac{2 \cdot (d + \Delta\text{HF3P})}{\Gamma\text{Mg}} \right)^2} \cdot \mu\text{red} \left( \frac{1}{2}, 3, -1, \frac{3}{2}, 3, -2, \frac{5}{2}, -1 \right)^2 \cdot \mu\text{red} \left( \frac{1}{2}, 3, -3, \frac{3}{2}, 3, -2, \frac{5}{2}, 1 \right)^2 :$$

▼ (3, -1) → (3, -2):

$$\text{P31n32n32n} := d \rightarrow \frac{1}{1 + \left( \frac{2 \cdot (d + \Delta\text{HF3P})}{\Gamma\text{Mg}} \right)^2} \cdot \mu\text{red} \left( \frac{1}{2}, 3, -1, \frac{3}{2}, 3, -2, \frac{5}{2}, -1 \right)^2 \cdot \mu\text{red} \left( \frac{1}{2}, 3, -2, \frac{3}{2}, 3, -2, \frac{5}{2}, 0 \right)^2 :$$

▼ (3, -1) → (3, -1): (no change)

$$\text{P31n32n31n} := d \rightarrow \frac{1}{1 + \left( \frac{2 \cdot (d + \Delta\text{HF3P})}{\Gamma\text{Mg}} \right)^2} \cdot \mu\text{red} \left( \frac{1}{2}, 3, -1, \frac{3}{2}, 3, -2, \frac{5}{2}, -1 \right)^2 \cdot \mu\text{red} \left( \frac{1}{2}, 3, -1, \frac{3}{2}, 3, -2, \frac{5}{2}, -1 \right)^2 :$$

▼ Intermediate State (3', -3):

▼ (3, -2) → (2, -2):

$$P32n33n22n := d \rightarrow \frac{1}{1 + \left( \frac{2 \cdot (d + \Delta_{HF3P})}{\Gamma M g} \right)^2} \cdot \mu_{\text{red}} \left( \frac{1}{2}, 3, -2, \frac{3}{2}, 3, -3, \frac{5}{2}, -1 \right)^2 \cdot \mu_{\text{red}} \left( \frac{1}{2}, 2, -2, \frac{3}{2}, 3, -3, \frac{5}{2}, -1 \right)^2 :$$

▼ (3,-2)→(3,-3):

$$P32n33n33n := d \rightarrow \frac{1}{1 + \left( \frac{2 \cdot (d + \Delta_{HF3P})}{\Gamma M g} \right)^2} \cdot \mu_{\text{red}} \left( \frac{1}{2}, 3, -2, \frac{3}{2}, 3, -3, \frac{5}{2}, -1 \right)^2 \cdot \mu_{\text{red}} \left( \frac{1}{2}, 3, -3, \frac{3}{2}, 3, -3, \frac{5}{2}, 0 \right)^2 :$$

▼ (3,-2)→(3,-2): (no change)

$$P32n33n32n := d \rightarrow \frac{1}{1 + \left( \frac{2 \cdot (d + \Delta_{HF3P})}{\Gamma M g} \right)^2} \cdot \mu_{\text{red}} \left( \frac{1}{2}, 3, -2, \frac{3}{2}, 3, -3, \frac{5}{2}, -1 \right)^2 \cdot \mu_{\text{red}} \left( \frac{1}{2}, 3, -2, \frac{3}{2}, 3, -3, \frac{5}{2}, -1 \right)^2 :$$

▼ Driving to the F = 2' intermediate level:

Again, we assume that we start out in the (3,3) level to include all the possible levels that can be driven. We also include the detuning due to the hyperfine structure. Measured relative to the cycling transition, this transition adds an additional detuning of  $\Delta = -(66.8 + 60.5)\text{MHz} = -127.3\text{ MHz}$ .

$$\Delta_{HF2P} := -2 \cdot \pi \cdot 127.3 :$$

(3, 3) → (2', 2) → (2, 2)  
 → (2, 1)  
 → (3, 3)  
 → (3, 2)  
 → (3, 1)  
 (3, 2) → (2', 1) → (2, 2)  
 → (2, 1)  
 → (2, 0)  
 → (3, 2)  
 → (3, 1)  
 → (3, 0)  
 (3, 1) → (2', 0) → (2, 1)  
 → (2, 0)  
 → (2, -1)  
 → (3, 1)  
 → (3, 0)  
 → (3, -1)  
 (3, 0) → (2', -1) → (2, 0)  
 → (2, -1)  
 → (2, -2)  
 → (3, 0)  
 → (3, -1)  
 → (3, -2)  
 (3, -1) → (2', -2) → (2, -2)  
 → (2, -1)  
 → (3, -1)  
 → (3, -2)

→ (3,-3)

We can eliminate the excited state and obtain equations for the probability of the populating the various ground state sublevels. To keep things somewhat straightforward, 3n would correspond to an  $mF=-3$ , and a 3p will correspond to an  $F = 3'$ . So, considering probabilities by level we have:

▼ Intermediate State (2',2):

▼ (3, 3)→(2, 2):

$$P332222 := d \rightarrow \frac{1}{1 + \left( \frac{2 \cdot (d + \Delta HF2P)}{\Gamma M_g} \right)^2} \cdot \mu_{red} \left( \frac{1}{2}, 3, 3, \frac{3}{2}, 2, 2, \frac{5}{2}, -1 \right)^2 \cdot \mu_{red} \left( \frac{1}{2}, 2, 2, \frac{3}{2}, 2, 2, \frac{5}{2}, 0 \right)^2 :$$

▼ (3, 3)→(2, 1):

$$P332221 := d \rightarrow \frac{1}{1 + \left( \frac{2 \cdot (d + \Delta HF2P)}{\Gamma M_g} \right)^2} \cdot \mu_{red} \left( \frac{1}{2}, 3, 3, \frac{3}{2}, 2, 2, \frac{5}{2}, -1 \right)^2 \cdot \mu_{red} \left( \frac{1}{2}, 2, 1, \frac{3}{2}, 2, 2, \frac{5}{2}, 1 \right)^2 :$$

▼ (3, 3)→(3,3): (no change)

$$P332233 := d \rightarrow \frac{1}{1 + \left( \frac{2 \cdot (d + \Delta HF2P)}{\Gamma M_g} \right)^2} \cdot \mu_{red} \left( \frac{1}{2}, 3, 3, \frac{3}{2}, 2, 2, \frac{5}{2}, -1 \right)^2 \cdot \mu_{red} \left( \frac{1}{2}, 3, 3, \frac{3}{2}, 2, 2, \frac{5}{2}, -1 \right)^2 :$$

▼ (3, 3)→(3, 2):

$$P332232 := d \rightarrow \frac{1}{1 + \left( \frac{2 \cdot (d + \Delta HF2P)}{\Gamma M_g} \right)^2} \cdot \mu_{red} \left( \frac{1}{2}, 3, 3, \frac{3}{2}, 2, 2, \frac{5}{2}, -1 \right)^2 \cdot \mu_{red} \left( \frac{1}{2}, 3, 2, \frac{3}{2}, 2, 2, \frac{5}{2}, 0 \right)^2 :$$

▼ (3, 3)→(3, 1):

$$P332231 := d \rightarrow \frac{1}{1 + \left( \frac{2 \cdot (d + \Delta HF2P)}{\Gamma M_g} \right)^2} \cdot \mu_{red} \left( \frac{1}{2}, 3, 3, \frac{3}{2}, 2, 2, \frac{5}{2}, -1 \right)^2 \cdot \mu_{red} \left( \frac{1}{2}, 3, 1, \frac{3}{2}, 2, 2, \frac{5}{2}, 1 \right)^2 :$$

▼ Intermediate State (2',1):

▼ (3, 2)→(2, 2):

$$P322122 := d \rightarrow \frac{1}{1 + \left( \frac{2 \cdot (d + \Delta HF2P)}{\Gamma M_g} \right)^2} \cdot \mu_{red} \left( \frac{1}{2}, 3, 2, \frac{3}{2}, 2, 1, \frac{5}{2}, -1 \right)^2 \cdot \mu_{red} \left( \frac{1}{2}, 2, 2, \frac{3}{2}, 2, 1, \frac{5}{2}, -1 \right)^2 :$$

▼ (3, 2)→(2, 1):

$$P322121 := d \rightarrow \frac{1}{1 + \left( \frac{2 \cdot (d + \Delta HF2P)}{\Gamma M_g} \right)^2} \cdot \mu_{red} \left( \frac{1}{2}, 3, 2, \frac{3}{2}, 2, 1, \frac{5}{2}, -1 \right)^2 \cdot \mu_{red} \left( \frac{1}{2}, 2, 1, \frac{3}{2}, 2, 1, \frac{5}{2}, 0 \right)^2 :$$

▼ (3, 2)→(2, 0):

$$P322120 := d \rightarrow \frac{1}{1 + \left( \frac{2 \cdot (d + \Delta HF2P)}{\Gamma M_g} \right)^2} \cdot \mu_{red} \left( \frac{1}{2}, 3, 2, \frac{3}{2}, 2, 1, \frac{5}{2}, -1 \right)^2 \cdot \mu_{red} \left( \frac{1}{2}, 2, 0, \frac{3}{2}, 2, 1, \frac{5}{2}, 1 \right)^2 :$$

▼ (3, 2)→(3, 2): (no change)

$$P322132 := d \rightarrow \frac{1}{1 + \left( \frac{2 \cdot (d + \Delta HF2P)}{\Gamma M_g} \right)^2} \cdot \mu_{red} \left( \frac{1}{2}, 3, 2, \frac{3}{2}, 2, 1, \frac{5}{2}, -1 \right)^2 \cdot \mu_{red} \left( \frac{1}{2}, 3, 2, \frac{3}{2}, 2, 1, \frac{5}{2}, -1 \right)^2 :$$

▼ (3, 2)→(3, 1):

$$P322131 := d \rightarrow \frac{1}{1 + \left( \frac{2 \cdot (d + \Delta HF2P)}{\Gamma M_g} \right)^2} \cdot \mu_{red} \left( \frac{1}{2}, 3, 2, \frac{3}{2}, 2, 1, \frac{5}{2}, -1 \right)^2 \cdot \mu_{red} \left( \frac{1}{2}, 3, 1, \frac{3}{2}, 2, 1, \frac{5}{2}, 0 \right)^2 :$$

▼ (3, 2)→(3, 0):

$$P322130 := d \rightarrow \frac{1}{1 + \left( \frac{2 \cdot (d + \Delta HF2P)}{\Gamma M_g} \right)^2} \cdot \mu_{red} \left( \frac{1}{2}, 3, 2, \frac{3}{2}, 2, 1, \frac{5}{2}, -1 \right)^2 \cdot \mu_{red} \left( \frac{1}{2}, 3, 0, \frac{3}{2}, 2, 1, \frac{5}{2}, 1 \right)^2 :$$

▼ Intermediate State (2', 0):

▼ (3, 1)→(2, 1):

$$P312021 := d \rightarrow \frac{1}{1 + \left( \frac{2 \cdot (d + \Delta HF2P)}{\Gamma M_g} \right)^2} \cdot \mu_{red} \left( \frac{1}{2}, 3, 1, \frac{3}{2}, 2, 0, \frac{5}{2}, -1 \right)^2 \cdot \mu_{red} \left( \frac{1}{2}, 2, 1, \frac{3}{2}, 2, 0, \frac{5}{2}, -1 \right)^2 :$$

▼ (3, 1)→(2, 0):

$$P312020 := d \rightarrow \frac{1}{1 + \left( \frac{2 \cdot (d + \Delta HF2P)}{\Gamma M_g} \right)^2} \cdot \mu_{red} \left( \frac{1}{2}, 3, 1, \frac{3}{2}, 2, 0, \frac{5}{2}, -1 \right)^2 \cdot \mu_{red} \left( \frac{1}{2}, 2, 0, \frac{3}{2}, 2, 0, \frac{5}{2}, 1 \right)^2 :$$

$$\left(\frac{5}{2}, -1\right)^2 \cdot \mu_{\text{red}}\left(\frac{1}{2}, 2, 0, \frac{3}{2}, 2, 0, \frac{5}{2}, 0\right)^2 :$$

▼ (3, 1)→(2, -1):

$$\text{P312021n} := d \rightarrow \frac{1}{1 + \left(\frac{2 \cdot (d + \Delta\text{HF2P})}{\Gamma\text{Mg}}\right)^2} \cdot \mu_{\text{red}}\left(\frac{1}{2}, 3, 1, \frac{3}{2}, 2, 0,$$

$$\frac{5}{2}, -1\right)^2 \cdot \mu_{\text{red}}\left(\frac{1}{2}, 2, -1, \frac{3}{2}, 2, 0, \frac{5}{2}, 1\right)^2 :$$

▼ (3, 1)→(3, 1): (no change)

$$\text{P312031} := d \rightarrow \frac{1}{1 + \left(\frac{2 \cdot (d + \Delta\text{HF2P})}{\Gamma\text{Mg}}\right)^2} \cdot \mu_{\text{red}}\left(\frac{1}{2}, 3, 1, \frac{3}{2}, 2, 0,$$

$$\frac{5}{2}, -1\right)^2 \cdot \mu_{\text{red}}\left(\frac{1}{2}, 3, 1, \frac{3}{2}, 2, 0, \frac{5}{2}, -1\right)^2 :$$

▼ (3, 1)→(3, 0):

$$\text{P312030} := d \rightarrow \frac{1}{1 + \left(\frac{2 \cdot (d + \Delta\text{HF2P})}{\Gamma\text{Mg}}\right)^2} \cdot \mu_{\text{red}}\left(\frac{1}{2}, 3, 1, \frac{3}{2}, 2, 0,$$

$$\frac{5}{2}, -1\right)^2 \cdot \mu_{\text{red}}\left(\frac{1}{2}, 3, 0, \frac{3}{2}, 2, 0, \frac{5}{2}, 0\right)^2 :$$

▼ (3, 1)→(3, -1):

$$\text{P312031n} := d \rightarrow \frac{1}{1 + \left(\frac{2 \cdot (d + \Delta\text{HF2P})}{\Gamma\text{Mg}}\right)^2} \cdot \mu_{\text{red}}\left(\frac{1}{2}, 3, 1, \frac{3}{2}, 2, 0,$$

$$\frac{5}{2}, -1\right)^2 \cdot \mu_{\text{red}}\left(\frac{1}{2}, 3, -1, \frac{3}{2}, 2, 0, \frac{5}{2}, 1\right)^2 :$$

▼ Intermediate State (2', -1):

▼ (3, 0)→(2, 0):

$$\text{P3021n20} := d \rightarrow \frac{1}{1 + \left(\frac{2 \cdot (d + \Delta\text{HF2P})}{\Gamma\text{Mg}}\right)^2} \cdot \mu_{\text{red}}\left(\frac{1}{2}, 3, 0, \frac{3}{2}, 2, -1,$$

$$\frac{5}{2}, -1\right)^2 \cdot \mu_{\text{red}}\left(\frac{1}{2}, 2, 0, \frac{3}{2}, 2, -1, \frac{5}{2}, -1\right)^2 :$$

▼ (3, 0)→(2, -1):

$$\text{P3021n21n} := d \rightarrow \frac{1}{1 + \left(\frac{2 \cdot (d + \Delta\text{HF2P})}{\Gamma\text{Mg}}\right)^2} \cdot \mu_{\text{red}}\left(\frac{1}{2}, 3, 0, \frac{3}{2}, 2,$$

$$-1, \frac{5}{2}, -1\right)^2 \cdot \mu_{\text{red}}\left(\frac{1}{2}, 2, -1, \frac{3}{2}, 2, -1, \frac{5}{2}, 0\right)^2 :$$

▼ (3, 0)→(2, -2):

$$P3021n22n := d \rightarrow \frac{1}{1 + \left( \frac{2 \cdot (d + \Delta HF2P)}{\Gamma Mg} \right)^2} \cdot \mu_{red} \left( \frac{1}{2}, 3, 0, \frac{3}{2}, 2, -1, \frac{5}{2}, -1 \right)^2 \cdot \mu_{red} \left( \frac{1}{2}, 2, -2, \frac{3}{2}, 2, -1, \frac{5}{2}, 1 \right)^2 :$$

▼ (3, 0) → (3, 0): (no change)

$$P3021n30 := d \rightarrow \frac{1}{1 + \left( \frac{2 \cdot (d + \Delta HF2P)}{\Gamma Mg} \right)^2} \cdot \mu_{red} \left( \frac{1}{2}, 3, 0, \frac{3}{2}, 2, -1, \frac{5}{2}, -1 \right)^2 \cdot \mu_{red} \left( \frac{1}{2}, 3, 0, \frac{3}{2}, 2, -1, \frac{5}{2}, -1 \right)^2 :$$

▼ (3, 0) → (3, -1):

$$P3021n31n := d \rightarrow \frac{1}{1 + \left( \frac{2 \cdot (d + \Delta HF2P)}{\Gamma Mg} \right)^2} \cdot \mu_{red} \left( \frac{1}{2}, 3, 0, \frac{3}{2}, 2, -1, \frac{5}{2}, -1 \right)^2 \cdot \mu_{red} \left( \frac{1}{2}, 3, -1, \frac{3}{2}, 2, -1, \frac{5}{2}, 0 \right)^2 :$$

▼ (3, 0) → (3, -2):

$$P3021n32n := d \rightarrow \frac{1}{1 + \left( \frac{2 \cdot (d + \Delta HF2P)}{\Gamma Mg} \right)^2} \cdot \mu_{red} \left( \frac{1}{2}, 3, 0, \frac{3}{2}, 2, -1, \frac{5}{2}, -1 \right)^2 \cdot \mu_{red} \left( \frac{1}{2}, 3, -2, \frac{3}{2}, 2, -1, \frac{5}{2}, 1 \right)^2 :$$

▼ Intermediate State (2', -2):

▼ (3, -1) → (2, -2):

$$P31n22n22n := d \rightarrow \frac{1}{1 + \left( \frac{2 \cdot (d + \Delta HF2P)}{\Gamma Mg} \right)^2} \cdot \mu_{red} \left( \frac{1}{2}, 3, -1, \frac{3}{2}, 2, -2, \frac{5}{2}, -1 \right)^2 \cdot \mu_{red} \left( \frac{1}{2}, 2, -2, \frac{3}{2}, 2, -2, \frac{5}{2}, 0 \right)^2 :$$

▼ (3, -1) → (2, -1):

$$P31n22n21n := d \rightarrow \frac{1}{1 + \left( \frac{2 \cdot (d + \Delta HF2P)}{\Gamma Mg} \right)^2} \cdot \mu_{red} \left( \frac{1}{2}, 3, -1, \frac{3}{2}, 2, -2, \frac{5}{2}, -1 \right)^2 \cdot \mu_{red} \left( \frac{1}{2}, 2, -1, \frac{3}{2}, 2, -2, \frac{5}{2}, -1 \right)^2 :$$

▼ (3, -1) → (3, -3):

$$P31n22n33n := d \rightarrow \frac{1}{1 + \left( \frac{2 \cdot (d + \Delta HF2P)}{\Gamma Mg} \right)^2} \cdot \mu_{red} \left( \frac{1}{2}, 3, -1, \frac{3}{2}, 2, -2, \frac{5}{2}, -1 \right)^2 \cdot \mu_{red} \left( \frac{1}{2}, 3, -3, \frac{3}{2}, 2, -2, \frac{5}{2}, 1 \right)^2 :$$

▼ (3,-1)→(3,-2):

$$P31n22n32n := d \rightarrow \frac{1}{1 + \left( \frac{2 \cdot (d + \Delta HF2P)}{\Gamma M g} \right)^2} \cdot \mu_{red} \left( \frac{1}{2}, 3, -1, \frac{3}{2}, 2, -2, \frac{5}{2}, -1 \right)^2 \cdot \mu_{red} \left( \frac{1}{2}, 3, -2, \frac{3}{2}, 2, -2, \frac{5}{2}, 0 \right)^2 :$$

▼ (3,-1)→(3,-1): (no change)

$$P31n22n31n := d \rightarrow \frac{1}{1 + \left( \frac{2 \cdot (d + \Delta HF2P)}{\Gamma M g} \right)^2} \cdot \mu_{red} \left( \frac{1}{2}, 3, -1, \frac{3}{2}, 2, -2, \frac{5}{2}, -1 \right)^2 :$$

▼ Starting in the F=2 Manifold:

The F=2 manifold is separated from the F=3 manifold by 1788MHz (hyperfine splitting). In addition to this we need to account for the hyperfine splitting of the excited state.

$$\Delta HFGS := 2 \cdot \pi \cdot 1788 :$$

We also include the detuning due to the hyperfine structure. Measured relative to the cycling transition, this transition adds an additional detuning of:

$$F=3: \Delta = -(66.8 - 7.5) \text{MHz} = -66.3 \text{MHz}.$$

$$F=2: \Delta = -(66.8 + 60.5) \text{MHz} = -127.3 \text{MHz}.$$

$$F=1: \Delta = -(66.8 + 116.9) \text{MHz} = -183.7 \text{MHz}.$$

▼ Driving to the F=3' intermediate level:

Assuming that we start out in the (2,m) level, turning the cyclor on means that we can drive the ion from the ground state into the 2P3/2 level. Assuming that we drive with  $\sigma^-$  polarized light, we get the following possible decay paths:

$$\begin{aligned} (2, -2) &\rightarrow (3', -3) \rightarrow (3, -3) \\ &\quad \rightarrow (3, -2) \\ &\quad \rightarrow (3, -1) \\ &\quad \rightarrow (2, -2) \quad \text{NC} \\ (2, -1) &\rightarrow (3', -2) \rightarrow (3, -3) \\ &\quad \rightarrow (3, -2) \\ &\quad \rightarrow (3, -1) \\ &\quad \rightarrow (2, -2) \\ &\quad \rightarrow (2, -1) \quad \text{NC} \\ (2, 0) &\rightarrow (3', -1) \rightarrow (3, -2) \\ &\quad \rightarrow (3, -1) \\ &\quad \rightarrow (3, 0) \\ &\quad \rightarrow (2, -2) \\ &\quad \rightarrow (2, -1) \\ &\quad \rightarrow (2, 0) \quad \text{NC} \\ (2, 1) &\rightarrow (3', 0) \rightarrow (3, -1) \\ &\quad \rightarrow (3, 0) \\ &\quad \rightarrow (3, 1) \\ &\quad \rightarrow (2, -1) \\ &\quad \rightarrow (2, 0) \\ &\quad \rightarrow (2, 1) \quad \text{NC} \\ (2, 2) &\rightarrow (3', 1) \rightarrow (3, 0) \\ &\quad \rightarrow (3, 1) \\ &\quad \rightarrow (3, 2) \end{aligned}$$

- (2, 0)
- (2, 1)
- (2, 2) NC

We can eliminate the excited state and obtain equations for the probability of the populating the various ground state sublevels. By level we have (separated by what intermediate state we use):

▼ Intermediate State (3', -3):

▼ (2, -2) → (3, -3):

$$P_{22n33n33n} := d \rightarrow \frac{1}{1 + \left( \frac{2 \cdot (d + \Delta_{HF3P} + \Delta_{HF3S})}{\Gamma_{Mg}} \right)^2} \cdot \mu_{red} \left( \frac{1}{2}, 2, -2, \frac{3}{2}, 3, -3, \frac{5}{2}, -1 \right)^2 \cdot \mu_{red} \left( \frac{1}{2}, 3, -3, \frac{3}{2}, 3, -3, \frac{5}{2}, 0 \right)^2 :$$

▼ (2, -2) → (3, -2):

$$P_{22n33n32n} := d \rightarrow \frac{1}{1 + \left( \frac{2 \cdot (d + \Delta_{HF3P} + \Delta_{HF3S})}{\Gamma_{Mg}} \right)^2} \cdot \mu_{red} \left( \frac{1}{2}, 2, -2, \frac{3}{2}, 3, -3, \frac{5}{2}, -1 \right)^2 \cdot \mu_{red} \left( \frac{1}{2}, 3, -2, \frac{3}{2}, 3, -3, \frac{5}{2}, -1 \right)^2 :$$

▼ (2, -2) → (2, -2): no change!!

$$P_{22n33n22n} := d \rightarrow \frac{1}{1 + \left( \frac{2 \cdot (d + \Delta_{HF3P} + \Delta_{HF3S})}{\Gamma_{Mg}} \right)^2} \cdot \mu_{red} \left( \frac{1}{2}, 2, -2, \frac{3}{2}, 3, -3, \frac{5}{2}, -1 \right)^2 :$$

▼ Intermediate State (3', -2):

▼ (2, -1) → (3, -3):

$$P_{21n32n33n} := d \rightarrow \frac{1}{1 + \left( \frac{2 \cdot (d + \Delta_{HF3P} + \Delta_{HF3S})}{\Gamma_{Mg}} \right)^2} \cdot \mu_{red} \left( \frac{1}{2}, 2, -1, \frac{3}{2}, 3, -2, \frac{5}{2}, -1 \right)^2 \cdot \mu_{red} \left( \frac{1}{2}, 3, -3, \frac{3}{2}, 3, -2, \frac{5}{2}, 1 \right)^2 :$$

▼ (2, -1) → (3, -2):

$$P_{21n32n32n} := d \rightarrow \frac{1}{1 + \left( \frac{2 \cdot (d + \Delta_{HF3P} + \Delta_{HF3S})}{\Gamma_{Mg}} \right)^2} \cdot \mu_{red} \left( \frac{1}{2}, 2, -1, \frac{3}{2}, 3, -2, \frac{5}{2}, -1 \right)^2 \cdot \mu_{red} \left( \frac{1}{2}, 3, -2, \frac{3}{2}, 3, -2, \frac{5}{2}, 0 \right)^2 :$$

▼ (2, -1) → (3, -1):

$$P_{21n32n31n} := d \rightarrow \frac{1}{1 + \left( \frac{2 \cdot (d + \Delta_{HF3P} + \Delta_{HF3S})}{\Gamma_{Mg}} \right)^2} \cdot \mu_{red} \left( \frac{1}{2}, 2, -1, \frac{3}{2}, 3, -2, \frac{5}{2}, -1 \right)^2 \cdot \mu_{red} \left( \frac{1}{2}, 3, -1, \frac{3}{2}, 3, -2, \frac{5}{2}, -1 \right)^2 :$$

▼ (2,-1)→(2,-2):

$$P21n32n22n := d \rightarrow \frac{1}{1 + \left( \frac{2 \cdot (d + \Delta HF3P + \Delta HFGS)}{\Gamma M g} \right)^2} \cdot \mu_{\text{red}} \left( \frac{1}{2}, 2, -1, \frac{3}{2}, 3, -2, \frac{5}{2}, -1 \right)^2 \cdot \mu_{\text{red}} \left( \frac{1}{2}, 2, -2, \frac{3}{2}, 3, -2, \frac{5}{2}, 0 \right)^2 :$$

▼ (2,-1)→(2,-1): no change

$$P21n32n21n := d \rightarrow \frac{1}{1 + \left( \frac{2 \cdot (d + \Delta HF3P + \Delta HFGS)}{\Gamma M g} \right)^2} \cdot \mu_{\text{red}} \left( \frac{1}{2}, 2, -1, \frac{3}{2}, 3, -2, \frac{5}{2}, -1 \right)^2 :$$

▼ Intermediate State (3',-1):

▼ (2, 0)→(3,-2):

$$P2031n32n := d \rightarrow \frac{1}{1 + \left( \frac{2 \cdot (d + \Delta HF3P + \Delta HFGS)}{\Gamma M g} \right)^2} \cdot \mu_{\text{red}} \left( \frac{1}{2}, 2, 0, \frac{3}{2}, 3, -1, \frac{5}{2}, -1 \right)^2 \cdot \mu_{\text{red}} \left( \frac{1}{2}, 3, -2, \frac{3}{2}, 3, -1, \frac{5}{2}, 1 \right)^2 :$$

▼ (2, 0)→(3,-1):

$$P2031n31n := d \rightarrow \frac{1}{1 + \left( \frac{2 \cdot (d + \Delta HF3P + \Delta HFGS)}{\Gamma M g} \right)^2} \cdot \mu_{\text{red}} \left( \frac{1}{2}, 2, 0, \frac{3}{2}, 3, -1, \frac{5}{2}, -1 \right)^2 \cdot \mu_{\text{red}} \left( \frac{1}{2}, 3, -1, \frac{3}{2}, 3, -1, \frac{5}{2}, 0 \right)^2 :$$

▼ (2, 0)→(3, 0):

$$P2031n30 := d \rightarrow \frac{1}{1 + \left( \frac{2 \cdot (d + \Delta HF3P + \Delta HFGS)}{\Gamma M g} \right)^2} \cdot \mu_{\text{red}} \left( \frac{1}{2}, 2, 0, \frac{3}{2}, 3, -1, \frac{5}{2}, -1 \right)^2 \cdot \mu_{\text{red}} \left( \frac{1}{2}, 3, 0, \frac{3}{2}, 3, -1, \frac{5}{2}, -1 \right)^2 :$$

▼ (2, 0)→(2,-2):

$$P2031n22n := d \rightarrow \frac{1}{1 + \left( \frac{2 \cdot (d + \Delta HF3P + \Delta HFGS)}{\Gamma M g} \right)^2} \cdot \mu_{\text{red}} \left( \frac{1}{2}, 2, 0, \frac{3}{2}, 3, -1, \frac{5}{2}, -1 \right)^2 \cdot \mu_{\text{red}} \left( \frac{1}{2}, 2, -2, \frac{3}{2}, 3, -1, \frac{5}{2}, 1 \right)^2 :$$

▼ (2, 0)→(2,-1):

$$P2031n21n := d \rightarrow \frac{1}{1 + \left( \frac{2 \cdot (d + \Delta HF3P + \Delta HFGS)}{\Gamma M g} \right)^2} \cdot \mu_{\text{red}} \left( \frac{1}{2}, 2, 0, \frac{3}{2}, 3, -1, \frac{5}{2}, -1 \right)^2 \cdot \mu_{\text{red}} \left( \frac{1}{2}, 2, -1, \frac{3}{2}, 3, -1, \frac{5}{2}, 0 \right)^2 :$$

▼ (2, 0)→(2, 0):

$$\begin{aligned} \text{P2031n20} := d \rightarrow & \frac{1}{1 + \left( \frac{2 \cdot (d + \Delta\text{HF3P} + \Delta\text{HF3S})}{\Gamma\text{Mg}} \right)^2} \cdot \mu\text{red} \left( \frac{1}{2}, 2, \right. \\ & \left. 0, \frac{3}{2}, 3, -1, \frac{5}{2}, -1 \right)^2 \cdot \mu\text{red} \left( \frac{1}{2}, 2, 0, \frac{3}{2}, 3, -1, \frac{5}{2}, -1 \right)^2 : \end{aligned}$$

▼ Intermediate State (3', 0):

▼ (2, 1) → (3, -1):

$$\begin{aligned} \text{P213031n} := d \rightarrow & \frac{1}{1 + \left( \frac{2 \cdot (d + \Delta\text{HF3P} + \Delta\text{HF3S})}{\Gamma\text{Mg}} \right)^2} \cdot \mu\text{red} \left( \frac{1}{2}, 2, \right. \\ & \left. 1, \frac{3}{2}, 3, 0, \frac{5}{2}, -1 \right)^2 \cdot \mu\text{red} \left( \frac{1}{2}, 3, -1, \frac{3}{2}, 3, 0, \frac{5}{2}, 1 \right)^2 : \end{aligned}$$

▼ (2, 1) → (3, 0):

$$\begin{aligned} \text{P213030} := d \rightarrow & \frac{1}{1 + \left( \frac{2 \cdot (d + \Delta\text{HF3P} + \Delta\text{HF3S})}{\Gamma\text{Mg}} \right)^2} \cdot \mu\text{red} \left( \frac{1}{2}, 2, 1, \right. \\ & \left. \frac{3}{2}, 3, 0, \frac{5}{2}, -1 \right)^2 \cdot \mu\text{red} \left( \frac{1}{2}, 3, 0, \frac{3}{2}, 3, 0, \frac{5}{2}, 0 \right)^2 : \end{aligned}$$

▼ (2, 1) → (3, 1):

$$\begin{aligned} \text{P213031} := d \rightarrow & \frac{1}{1 + \left( \frac{2 \cdot (d + \Delta\text{HF3P} + \Delta\text{HF3S})}{\Gamma\text{Mg}} \right)^2} \cdot \mu\text{red} \left( \frac{1}{2}, 2, 1, \right. \\ & \left. \frac{3}{2}, 3, 0, \frac{5}{2}, -1 \right)^2 \cdot \mu\text{red} \left( \frac{1}{2}, 3, 1, \frac{3}{2}, 3, 0, \frac{5}{2}, -1 \right)^2 : \end{aligned}$$

▼ (2, 1) → (2, -1):

$$\begin{aligned} \text{P213021n} := d \rightarrow & \frac{1}{1 + \left( \frac{2 \cdot (d + \Delta\text{HF3P} + \Delta\text{HF3S})}{\Gamma\text{Mg}} \right)^2} \cdot \mu\text{red} \left( \frac{1}{2}, 2, \right. \\ & \left. 1, \frac{3}{2}, 3, 0, \frac{5}{2}, -1 \right)^2 \cdot \mu\text{red} \left( \frac{1}{2}, 2, -1, \frac{3}{2}, 3, 0, \frac{5}{2}, 1 \right)^2 : \end{aligned}$$

▼ (2, 1) → (2, 0):

$$\begin{aligned} \text{P213020} := d \rightarrow & \frac{1}{1 + \left( \frac{2 \cdot (d + \Delta\text{HF3P} + \Delta\text{HF3S})}{\Gamma\text{Mg}} \right)^2} \cdot \mu\text{red} \left( \frac{1}{2}, 2, 1, \right. \\ & \left. \frac{3}{2}, 3, 0, \frac{5}{2}, -1 \right)^2 \cdot \mu\text{red} \left( \frac{1}{2}, 2, 0, \frac{3}{2}, 3, 0, \frac{5}{2}, 0 \right)^2 : \end{aligned}$$

▼ (2, 1) → (2, 1):

$$\begin{aligned} \text{P213021} := d \rightarrow & \frac{1}{1 + \left( \frac{2 \cdot (d + \Delta\text{HF3P} + \Delta\text{HF3S})}{\Gamma\text{Mg}} \right)^2} \cdot \mu\text{red} \left( \frac{1}{2}, 2, 1, \right. \\ & \left. \frac{3}{2}, 3, 0, \frac{5}{2}, -1 \right)^2 \cdot \mu\text{red} \left( \frac{1}{2}, 2, 1, \frac{3}{2}, 3, 0, \frac{5}{2}, -1 \right)^2 : \end{aligned}$$

▼ Intermediate State (3', 1):

▼ (2, 2)→(3, 0):

$$P223130 := d \rightarrow \frac{1}{1 + \left( \frac{2 \cdot (d + \Delta HF3P + \Delta HFGS)}{\Gamma Mg} \right)^2} \cdot \mu_{red} \left( \frac{1}{2}, 2, 2, \frac{3}{2}, 3, 1, \frac{5}{2}, -1 \right)^2 \cdot \mu_{red} \left( \frac{1}{2}, 3, 0, \frac{3}{2}, 3, 1, \frac{5}{2}, 1 \right)^2 :$$

▼ (2, 2)→(3, 1):

$$P223131 := d \rightarrow \frac{1}{1 + \left( \frac{2 \cdot (d + \Delta HF3P + \Delta HFGS)}{\Gamma Mg} \right)^2} \cdot \mu_{red} \left( \frac{1}{2}, 2, 2, \frac{3}{2}, 3, 1, \frac{5}{2}, -1 \right)^2 \cdot \mu_{red} \left( \frac{1}{2}, 3, 1, \frac{3}{2}, 3, 1, \frac{5}{2}, 0 \right)^2 :$$

▼ (2, 2)→(3, 2):

$$P223132 := d \rightarrow \frac{1}{1 + \left( \frac{2 \cdot (d + \Delta HF3P + \Delta HFGS)}{\Gamma Mg} \right)^2} \cdot \mu_{red} \left( \frac{1}{2}, 2, 2, \frac{3}{2}, 3, 1, \frac{5}{2}, -1 \right)^2 \cdot \mu_{red} \left( \frac{1}{2}, 3, 2, \frac{3}{2}, 3, 1, \frac{5}{2}, -1 \right)^2 :$$

▼ (2, 2)→(2, 0):

$$P223120 := d \rightarrow \frac{1}{1 + \left( \frac{2 \cdot (d + \Delta HF3P + \Delta HFGS)}{\Gamma Mg} \right)^2} \cdot \mu_{red} \left( \frac{1}{2}, 2, 2, \frac{3}{2}, 3, 1, \frac{5}{2}, -1 \right)^2 \cdot \mu_{red} \left( \frac{1}{2}, 2, 0, \frac{3}{2}, 3, 1, \frac{5}{2}, 1 \right)^2 :$$

▼ (2, 2)→(2, 1):

$$P223121 := d \rightarrow \frac{1}{1 + \left( \frac{2 \cdot (d + \Delta HF3P + \Delta HFGS)}{\Gamma Mg} \right)^2} \cdot \mu_{red} \left( \frac{1}{2}, 2, 2, \frac{3}{2}, 3, 1, \frac{5}{2}, -1 \right)^2 \cdot \mu_{red} \left( \frac{1}{2}, 2, 1, \frac{3}{2}, 3, 1, \frac{5}{2}, 0 \right)^2 :$$

▼ (2, 2)→(3, 0):

$$P223122 := d \rightarrow \frac{1}{1 + \left( \frac{2 \cdot (d + \Delta HF3P + \Delta HFGS)}{\Gamma Mg} \right)^2} \cdot \mu_{red} \left( \frac{1}{2}, 2, 2, \frac{3}{2}, 3, 1, \frac{5}{2}, -1 \right)^2 \cdot \mu_{red} \left( \frac{1}{2}, 2, 2, \frac{3}{2}, 3, 1, \frac{5}{2}, -1 \right)^2 :$$

▼ Driving to the F=2' intermediate level:

Assuming that we start out in the (2,m) level, turning the cyclor on means that we can drive the ion from the ground state into the 2P3/2 level. Assuming that we drive with  $\sigma^-$  polarized light, we get the following possible decay paths:

(2,-2) → goes nowhere  
 (2,-1) → (2',-2) → (3,-3)  
           → (3,-2)  
           → (3,-1)  
           → (2,-2)

$$\begin{aligned}
& \rightarrow (2,-1) \quad \text{NC} \\
(2, 0) & \rightarrow (2',-1) \rightarrow (3,-2) \\
& \rightarrow (3,-1) \\
& \rightarrow (3, 0) \\
& \rightarrow (2,-2) \\
& \rightarrow (2,-1) \\
& \rightarrow (2, 0) \quad \text{NC} \\
(2, 1) & \rightarrow (2', 0) \rightarrow (3,-1) \\
& \rightarrow (3, 0) \\
& \rightarrow (3, 1) \\
& \rightarrow (2,-1) \\
& \rightarrow (2, 0) \\
& \rightarrow (2, 1) \quad \text{NC} \\
(2, 2) & \rightarrow (2', 1) \rightarrow (3, 0) \\
& \rightarrow (3, 1) \\
& \rightarrow (3, 2) \\
& \rightarrow (2, 0) \\
& \rightarrow (2, 1) \\
& \rightarrow (2, 2) \quad \text{NC}
\end{aligned}$$

We can eliminate the excited state and obtain equations for the probability of the populating the various ground state sublevels. By level we have (separated by what intermediate state we use):

▼ Intermediate State (2',-2):

▼ (2,-1)→(3,-3):

$$\begin{aligned}
P_{21n22n33n} := d \rightarrow & \frac{1}{1 + \left( \frac{2 \cdot (d + \Delta_{\text{HF2P}} + \Delta_{\text{HFGS}})}{\Gamma_{\text{Mg}}} \right)^2} \cdot \mu_{\text{red}} \left( \frac{1}{2}, 2, \right. \\
& \left. -1, \frac{3}{2}, 2, -2, \frac{5}{2}, -1 \right)^2 \cdot \mu_{\text{red}} \left( \frac{1}{2}, 3, -3, \frac{3}{2}, 2, -2, \frac{5}{2}, 1 \right)^2 :
\end{aligned}$$

▼ (2,-1)→(3,-2):

$$\begin{aligned}
P_{21n22n32n} := d \rightarrow & \frac{1}{1 + \left( \frac{2 \cdot (d + \Delta_{\text{HF2P}} + \Delta_{\text{HFGS}})}{\Gamma_{\text{Mg}}} \right)^2} \cdot \mu_{\text{red}} \left( \frac{1}{2}, 2, \right. \\
& \left. -1, \frac{3}{2}, 2, -2, \frac{5}{2}, -1 \right)^2 \cdot \mu_{\text{red}} \left( \frac{1}{2}, 3, -2, \frac{3}{2}, 2, -2, \frac{5}{2}, 0 \right)^2 :
\end{aligned}$$

▼ (2,-1)→(3,-1):

$$\begin{aligned}
P_{21n22n31n} := d \rightarrow & \frac{1}{1 + \left( \frac{2 \cdot (d + \Delta_{\text{HF2P}} + \Delta_{\text{HFGS}})}{\Gamma_{\text{Mg}}} \right)^2} \cdot \mu_{\text{red}} \left( \frac{1}{2}, 2, \right. \\
& \left. -1, \frac{3}{2}, 2, -2, \frac{5}{2}, -1 \right)^2 \cdot \mu_{\text{red}} \left( \frac{1}{2}, 3, -1, \frac{3}{2}, 2, -2, \frac{5}{2}, -1 \right)^2 :
\end{aligned}$$

▼ (2,-1)→(2,-2):

$$\begin{aligned}
P_{21n22n22n} := d \rightarrow & \frac{1}{1 + \left( \frac{2 \cdot (d + \Delta_{\text{HF2P}} + \Delta_{\text{HFGS}})}{\Gamma_{\text{Mg}}} \right)^2} \cdot \mu_{\text{red}} \left( \frac{1}{2}, 2, \right. \\
& \left. -1, \frac{3}{2}, 2, -2, \frac{5}{2}, -1 \right)^2 \cdot \mu_{\text{red}} \left( \frac{1}{2}, 2, -2, \frac{3}{2}, 2, -2, \frac{5}{2}, 0 \right)^2 :
\end{aligned}$$

▼ (2, -1) → (2, -1):

$$P21n22n21n := d \rightarrow \frac{1}{1 + \left( \frac{2 \cdot (d + \Delta HF2P + \Delta HF GS)}{\Gamma M g} \right)^2} \cdot \mu red \left( \frac{1}{2}, 2, -1, \frac{3}{2}, 2, -2, \frac{5}{2}, -1 \right)^2 \cdot \mu red \left( \frac{1}{2}, 2, -1, \frac{3}{2}, 2, -2, \frac{5}{2}, -1 \right)^2 :$$

▼ Intermediate State (2', -1):

▼ (2, 0) → (3, -2):

$$P2021n32n := d \rightarrow \frac{1}{1 + \left( \frac{2 \cdot (d + \Delta HF2P + \Delta HF GS)}{\Gamma M g} \right)^2} \cdot \mu red \left( \frac{1}{2}, 2, 0, \frac{3}{2}, 2, -1, \frac{5}{2}, -1 \right)^2 \cdot \mu red \left( \frac{1}{2}, 3, -2, \frac{3}{2}, 2, -1, \frac{5}{2}, 1 \right)^2 :$$

▼ (2, 0) → (3, -1):

$$P2021n31n := d \rightarrow \frac{1}{1 + \left( \frac{2 \cdot (d + \Delta HF2P + \Delta HF GS)}{\Gamma M g} \right)^2} \cdot \mu red \left( \frac{1}{2}, 2, 0, \frac{3}{2}, 2, -1, \frac{5}{2}, -1 \right)^2 \cdot \mu red \left( \frac{1}{2}, 3, -1, \frac{3}{2}, 2, -1, \frac{5}{2}, 0 \right)^2 :$$

▼ (2, 0) → (3, 0):

$$P2021n30 := d \rightarrow \frac{1}{1 + \left( \frac{2 \cdot (d + \Delta HF2P + \Delta HF GS)}{\Gamma M g} \right)^2} \cdot \mu red \left( \frac{1}{2}, 2, 0, \frac{3}{2}, 2, -1, \frac{5}{2}, -1 \right)^2 \cdot \mu red \left( \frac{1}{2}, 3, 0, \frac{3}{2}, 2, -1, \frac{5}{2}, -1 \right)^2 :$$

▼ (2, 0) → (2, -2):

$$P2021n22n := d \rightarrow \frac{1}{1 + \left( \frac{2 \cdot (d + \Delta HF2P + \Delta HF GS)}{\Gamma M g} \right)^2} \cdot \mu red \left( \frac{1}{2}, 2, 0, \frac{3}{2}, 2, -1, \frac{5}{2}, -1 \right)^2 \cdot \mu red \left( \frac{1}{2}, 2, -2, \frac{3}{2}, 2, -1, \frac{5}{2}, 1 \right)^2 :$$

▼ (2, 0) → (2, -1):

$$P2021n21n := d \rightarrow \frac{1}{1 + \left( \frac{2 \cdot (d + \Delta HF2P + \Delta HF GS)}{\Gamma M g} \right)^2} \cdot \mu red \left( \frac{1}{2}, 2, 0, \frac{3}{2}, 2, -1, \frac{5}{2}, -1 \right)^2 \cdot \mu red \left( \frac{1}{2}, 2, -1, \frac{3}{2}, 2, -1, \frac{5}{2}, 0 \right)^2 :$$

▼ (2, 0) → (2, 0):

$$\text{P2021n20} := d \rightarrow \frac{1}{1 + \left( \frac{2 \cdot (d + \Delta\text{HF2P} + \Delta\text{HFGS})}{\Gamma\text{Mg}} \right)^2} \cdot \mu\text{red} \left( \frac{1}{2}, 2, 0, \frac{3}{2}, 2, -1, \frac{5}{2}, -1 \right)^2 \cdot \mu\text{red} \left( \frac{1}{2}, 2, 0, \frac{3}{2}, 2, -1, \frac{5}{2}, -1 \right)^2 :$$

▼ Intermediate State (2', 0):

▼ (2, 1) → (3, -1):

$$\text{P212031n} := d \rightarrow \frac{1}{1 + \left( \frac{2 \cdot (d + \Delta\text{HF2P} + \Delta\text{HFGS})}{\Gamma\text{Mg}} \right)^2} \cdot \mu\text{red} \left( \frac{1}{2}, 2, 1, \frac{3}{2}, 2, 0, \frac{5}{2}, -1 \right)^2 \cdot \mu\text{red} \left( \frac{1}{2}, 3, -1, \frac{3}{2}, 2, 0, \frac{5}{2}, 1 \right)^2 :$$

▼ (2, 1) → (3, 0):

$$\text{P212030} := d \rightarrow \frac{1}{1 + \left( \frac{2 \cdot (d + \Delta\text{HF2P} + \Delta\text{HFGS})}{\Gamma\text{Mg}} \right)^2} \cdot \mu\text{red} \left( \frac{1}{2}, 2, 1, \frac{3}{2}, 2, 0, \frac{5}{2}, -1 \right)^2 \cdot \mu\text{red} \left( \frac{1}{2}, 3, 0, \frac{3}{2}, 2, 0, \frac{5}{2}, 0 \right)^2 :$$

▼ (2, 1) → (3, 1):

$$\text{P212031} := d \rightarrow \frac{1}{1 + \left( \frac{2 \cdot (d + \Delta\text{HF2P} + \Delta\text{HFGS})}{\Gamma\text{Mg}} \right)^2} \cdot \mu\text{red} \left( \frac{1}{2}, 2, 1, \frac{3}{2}, 2, 0, \frac{5}{2}, -1 \right)^2 \cdot \mu\text{red} \left( \frac{1}{2}, 3, 1, \frac{3}{2}, 2, 0, \frac{5}{2}, -1 \right)^2 :$$

▼ (2, 1) → (2, -1):

$$\text{P212021n} := d \rightarrow \frac{1}{1 + \left( \frac{2 \cdot (d + \Delta\text{HF2P} + \Delta\text{HFGS})}{\Gamma\text{Mg}} \right)^2} \cdot \mu\text{red} \left( \frac{1}{2}, 2, 1, \frac{3}{2}, 2, 0, \frac{5}{2}, -1 \right)^2 \cdot \mu\text{red} \left( \frac{1}{2}, 2, -1, \frac{3}{2}, 2, 0, \frac{5}{2}, 1 \right)^2 :$$

▼ (2, 1) → (2, 0):

$$\text{P212020} := d \rightarrow \frac{1}{1 + \left( \frac{2 \cdot (d + \Delta\text{HF2P} + \Delta\text{HFGS})}{\Gamma\text{Mg}} \right)^2} \cdot \mu\text{red} \left( \frac{1}{2}, 2, 1, \frac{3}{2}, 2, 0, \frac{5}{2}, -1 \right)^2 \cdot \mu\text{red} \left( \frac{1}{2}, 2, 0, \frac{3}{2}, 2, 0, \frac{5}{2}, 0 \right)^2 :$$

▼ (2, 1) → (2, 1):

$$\text{P212021} := d \rightarrow \frac{1}{1 + \left( \frac{2 \cdot (d + \Delta\text{HF2P} + \Delta\text{HFGS})}{\Gamma\text{Mg}} \right)^2} \cdot \mu\text{red} \left( \frac{1}{2}, 2, 1, \frac{3}{2}, 2, 0, \frac{5}{2}, -1 \right)^2 \cdot \mu\text{red} \left( \frac{1}{2}, 2, 1, \frac{3}{2}, 2, 0, \frac{5}{2}, -1 \right)^2 :$$

$$\left(\frac{3}{2}, 2, 0, \frac{5}{2}, -1\right)^2 \cdot \mu_{\text{red}}\left(\frac{1}{2}, 2, 1, \frac{3}{2}, 2, 0, \frac{5}{2}, -1\right)^2 :$$

▼ Intermediate State (2', 1):

▼ (2, 2) → (3, 0):

$$\text{P222130} := d \rightarrow \frac{1}{1 + \left(\frac{2 \cdot (d + \Delta\text{HF2P} + \Delta\text{HFGS})}{\Gamma\text{Mg}}\right)^2} \cdot \mu_{\text{red}}\left(\frac{1}{2}, 2, 2, \frac{3}{2}, 2, 1, \frac{5}{2}, -1\right)^2 \cdot \mu_{\text{red}}\left(\frac{1}{2}, 3, 0, \frac{3}{2}, 2, 1, \frac{5}{2}, 1\right)^2 :$$

▼ (2, 2) → (3, 1):

$$\text{P222131} := d \rightarrow \frac{1}{1 + \left(\frac{2 \cdot (d + \Delta\text{HF2P} + \Delta\text{HFGS})}{\Gamma\text{Mg}}\right)^2} \cdot \mu_{\text{red}}\left(\frac{1}{2}, 2, 2, \frac{3}{2}, 2, 1, \frac{5}{2}, -1\right)^2 \cdot \mu_{\text{red}}\left(\frac{1}{2}, 3, 1, \frac{3}{2}, 2, 1, \frac{5}{2}, 0\right)^2 :$$

▼ (2, 2) → (3, 2):

$$\text{P222132} := d \rightarrow \frac{1}{1 + \left(\frac{2 \cdot (d + \Delta\text{HF2P} + \Delta\text{HFGS})}{\Gamma\text{Mg}}\right)^2} \cdot \mu_{\text{red}}\left(\frac{1}{2}, 2, 2, \frac{3}{2}, 2, 1, \frac{5}{2}, -1\right)^2 \cdot \mu_{\text{red}}\left(\frac{1}{2}, 3, 2, \frac{3}{2}, 2, 1, \frac{5}{2}, -1\right)^2 :$$

▼ (2, 2) → (2, 0):

$$\text{P222120} := d \rightarrow \frac{1}{1 + \left(\frac{2 \cdot (d + \Delta\text{HF2P} + \Delta\text{HFGS})}{\Gamma\text{Mg}}\right)^2} \cdot \mu_{\text{red}}\left(\frac{1}{2}, 2, 2, \frac{3}{2}, 2, 1, \frac{5}{2}, -1\right)^2 \cdot \mu_{\text{red}}\left(\frac{1}{2}, 2, 0, \frac{3}{2}, 2, 1, \frac{5}{2}, 1\right)^2 :$$

▼ (2, 2) → (2, 1):

$$\text{P222121} := d \rightarrow \frac{1}{1 + \left(\frac{2 \cdot (d + \Delta\text{HF2P} + \Delta\text{HFGS})}{\Gamma\text{Mg}}\right)^2} \cdot \mu_{\text{red}}\left(\frac{1}{2}, 2, 2, \frac{3}{2}, 2, 1, \frac{5}{2}, -1\right)^2 \cdot \mu_{\text{red}}\left(\frac{1}{2}, 2, 1, \frac{3}{2}, 2, 1, \frac{5}{2}, 0\right)^2 :$$

▼ (2, 2) → (2, 2):

$$\text{P222122} := d \rightarrow \frac{1}{1 + \left(\frac{2 \cdot (d + \Delta\text{HF2P} + \Delta\text{HFGS})}{\Gamma\text{Mg}}\right)^2} \cdot \mu_{\text{red}}\left(\frac{1}{2}, 2, 2, \frac{3}{2}, 2, 1, \frac{5}{2}, -1\right)^2 \cdot \mu_{\text{red}}\left(\frac{1}{2}, 2, 2, \frac{3}{2}, 2, 1, \frac{5}{2}, -1\right)^2 :$$

▼ Driving to the F=1' intermediate level:

$$\Delta\text{HF1P} := -2 \cdot \pi \cdot 183.7 :$$

Assuming that we start out in the (2,m) level, turning the cyclor on means that we can drive the ion from the ground state into the 2P3/2 level. Assuming that we drive with  $\sigma$ - polarized light, we get the following possible decay paths:

- (2,-2)  $\rightarrow$  goes nowhere
- (2,-1)  $\rightarrow$  goes nowhere
- (2, 0)  $\rightarrow$  (1',-1)  $\rightarrow$  (3,-2)
  - $\rightarrow$  (3,-1)
  - $\rightarrow$  (3, 0)
  - $\rightarrow$  (2,-2)
  - $\rightarrow$  (2,-1)
  - $\rightarrow$  (2, 0) NC
- (2, 1)  $\rightarrow$  (1', 0)  $\rightarrow$  (3,-1)
  - $\rightarrow$  (3, 0)
  - $\rightarrow$  (3, 1)
  - $\rightarrow$  (2,-1)
  - $\rightarrow$  (2, 0)
  - $\rightarrow$  (2, 1) NC
- (2, 2)  $\rightarrow$  (1', 1)  $\rightarrow$  (3, 0)
  - $\rightarrow$  (3, 1)
  - $\rightarrow$  (3, 2)
  - $\rightarrow$  (2, 0)
  - $\rightarrow$  (2, 1)
  - $\rightarrow$  (2, 2) NC

We can eliminate the excited state and obtain equations for the probability of the populating the various ground state sublevels. By level we have (separated by what intermediate state we use):

▼ Intermediate State (1', -1):

▼ (2, 0)  $\rightarrow$  (2,-2):

$$P_{2011n22n} := d \rightarrow \frac{1}{1 + \left( \frac{2 \cdot (d + \Delta HF1P + \Delta HF GS)}{\Gamma M_g} \right)^2} \cdot \mu_{red} \left( \frac{1}{2}, 2, 0, \frac{3}{2}, 1, -1, \frac{5}{2}, -1 \right)^2 \cdot \mu_{red} \left( \frac{1}{2}, 2, -2, \frac{3}{2}, 1, -1, \frac{5}{2}, 1 \right)^2 :$$

▼ (2, 0)  $\rightarrow$  (2,-1):

$$P_{2011n21n} := d \rightarrow \frac{1}{1 + \left( \frac{2 \cdot (d + \Delta HF1P + \Delta HF GS)}{\Gamma M_g} \right)^2} \cdot \mu_{red} \left( \frac{1}{2}, 2, 0, \frac{3}{2}, 1, -1, \frac{5}{2}, -1 \right)^2 \cdot \mu_{red} \left( \frac{1}{2}, 2, -1, \frac{3}{2}, 1, -1, \frac{5}{2}, 0 \right)^2 :$$

▼ (2, 0)  $\rightarrow$  (2, 0):

$$P_{2011n20} := d \rightarrow \frac{1}{1 + \left( \frac{2 \cdot (d + \Delta HF1P + \Delta HF GS)}{\Gamma M_g} \right)^2} \cdot \mu_{red} \left( \frac{1}{2}, 2, 0, \frac{3}{2}, 1, -1, \frac{5}{2}, -1 \right)^2 \cdot \mu_{red} \left( \frac{1}{2}, 2, 0, \frac{3}{2}, 1, -1, \frac{5}{2}, -1 \right)^2 :$$

▼ Intermediate State (1', 0):

▼ (2, 1)  $\rightarrow$  (2,-1):

$$P211021n := d \rightarrow \frac{1}{1 + \left( \frac{2 \cdot (d + \Delta HF1P + \Delta HF GS)}{\Gamma M g} \right)^2} \cdot \mu red \left( \frac{1}{2}, 2, 1, \frac{3}{2}, 1, 0, \frac{5}{2}, -1 \right)^2 \cdot \mu red \left( \frac{1}{2}, 2, -1, \frac{3}{2}, 1, 0, \frac{5}{2}, 1 \right)^2 :$$

▼ (2, 1) → (2, 0):

$$P211020 := d \rightarrow \frac{1}{1 + \left( \frac{2 \cdot (d + \Delta HF1P + \Delta HF GS)}{\Gamma M g} \right)^2} \cdot \mu red \left( \frac{1}{2}, 2, 1, \frac{3}{2}, 1, 0, \frac{5}{2}, -1 \right)^2 \cdot \mu red \left( \frac{1}{2}, 2, 0, \frac{3}{2}, 1, 0, \frac{5}{2}, 0 \right)^2 :$$

▼ (2, 1) → (2, 1):

$$P211021 := d \rightarrow \frac{1}{1 + \left( \frac{2 \cdot (d + \Delta HF1P + \Delta HF GS)}{\Gamma M g} \right)^2} \cdot \mu red \left( \frac{1}{2}, 2, 1, \frac{3}{2}, 1, 0, \frac{5}{2}, -1 \right)^2 \cdot \mu red \left( \frac{1}{2}, 2, 1, \frac{3}{2}, 1, 0, \frac{5}{2}, -1 \right)^2 :$$

▼ Intermediate State (1', 1):

▼ (2, 2) → (2, 0):

$$P221120 := d \rightarrow \frac{1}{1 + \left( \frac{2 \cdot (d + \Delta HF1P + \Delta HF GS)}{\Gamma M g} \right)^2} \cdot \mu red \left( \frac{1}{2}, 2, 2, \frac{3}{2}, 1, 1, \frac{5}{2}, -1 \right)^2 \cdot \mu red \left( \frac{1}{2}, 2, 0, \frac{3}{2}, 1, 1, \frac{5}{2}, 1 \right)^2 :$$

▼ (2, 2) → (2, 1):

$$P221121 := d \rightarrow \frac{1}{1 + \left( \frac{2 \cdot (d + \Delta HF1P + \Delta HF GS)}{\Gamma M g} \right)^2} \cdot \mu red \left( \frac{1}{2}, 2, 2, \frac{3}{2}, 1, 1, \frac{5}{2}, -1 \right)^2 \cdot \mu red \left( \frac{1}{2}, 2, 1, \frac{3}{2}, 1, 1, \frac{5}{2}, 0 \right)^2 :$$

▼ (2, 2) → (2, 2):

$$P221122 := d \rightarrow \frac{1}{1 + \left( \frac{2 \cdot (d + \Delta HF1P + \Delta HF GS)}{\Gamma M g} \right)^2} \cdot \mu red \left( \frac{1}{2}, 2, 2, \frac{3}{2}, 1, 1, \frac{5}{2}, -1 \right)^2 \cdot \mu red \left( \frac{1}{2}, 2, 2, \frac{3}{2}, 1, 1, \frac{5}{2}, -1 \right)^2 :$$

▼ Simplifying the Probabilities:

Rather than explicitly considering separate probabilities for each intermediate level, we can simplify things by combining the probabilities starting in one ground state zeeman sublevel and ending up in another regardless of what intermediate path they took:

## ▼ Initial Level (3,3):

Starting in the (3,3) level the cyclor can drive the ion into the (4',2'), (3',2') & (2',2'). From the excited state, we can decay into the following possible states:

$$\begin{aligned}
 (3,3) &\rightarrow (4',2') \rightarrow (3,1) \\
 &\quad \rightarrow (3,2) \\
 &\quad \rightarrow (3,3) \\
 (3,3) &\rightarrow (3',2') \rightarrow (3,1) \\
 &\quad \rightarrow (3,2) \\
 &\quad \rightarrow (3,3) \\
 &\quad \rightarrow (2,1) \\
 &\quad \rightarrow (2,2) \\
 (3,3) &\rightarrow (2',2') \rightarrow (3,1) \\
 &\quad \rightarrow (3,2) \\
 &\quad \rightarrow (3,3) \\
 &\quad \rightarrow (2,1) \\
 &\quad \rightarrow (2,2)
 \end{aligned}$$

This gives us the following equations for starting in the (3,3) and driving into one of the other Zeeman groundstate sublevels:

$$\begin{aligned}
 P3333 &:= d \rightarrow P334233(d) + P333233(d) + P332233(d) : \\
 P3332 &:= d \rightarrow P334232(d) + P333232(d) + P332232(d) : \\
 P3331 &:= d \rightarrow P334231(d) + P333231(d) + P332231(d) : \\
 P3322 &:= d \rightarrow P333222(d) + P332222(d) : \\
 P3321 &:= d \rightarrow P333221(d) + P332221(d) :
 \end{aligned}$$

## ▼ Initial Level (3,2):

Starting in the (3,2) level the cyclor can drive the ion into the (4',1'), (3',1') & (2',1'). From the excited state, we can decay into the following possible states:

$$\begin{aligned}
 (3,2) &\rightarrow (4',1') \rightarrow (3,0) \\
 &\quad \rightarrow (3,1) \\
 &\quad \rightarrow (3,2) \\
 (3,2) &\rightarrow (3',1') \rightarrow (3,0) \\
 &\quad \rightarrow (3,1) \\
 &\quad \rightarrow (3,2) \\
 &\quad \rightarrow (2,0) \\
 &\quad \rightarrow (2,1) \\
 &\quad \rightarrow (2,2) \\
 (3,2) &\rightarrow (2',1') \rightarrow (3,0) \\
 &\quad \rightarrow (3,1) \\
 &\quad \rightarrow (3,2) \\
 &\quad \rightarrow (2,0) \\
 &\quad \rightarrow (2,1) \\
 &\quad \rightarrow (2,2)
 \end{aligned}$$

This gives us the following equations for starting in the (3,2) and driving into one of the other Zeeman groundstate sublevels:

$$\begin{aligned}
 P3232 &:= d \rightarrow P324132(d) + P323132(d) + P322132(d) : \\
 P3231 &:= d \rightarrow P324131(d) + P323131(d) + P322131(d) : \\
 P3230 &:= d \rightarrow P324130(d) + P323130(d) + P322130(d) : \\
 P3222 &:= d \rightarrow P323122(d) + P322122(d) : \\
 P3221 &:= d \rightarrow P323121(d) + P322121(d) : \\
 P3220 &:= d \rightarrow P323120(d) + P322120(d) :
 \end{aligned}$$

## ▼ Initial Level (3,1):

Starting in the (3,1) level the cyclor can drive the ion into the (4',0'), (3',0') & (2',0'). From the excited state, we can decay into the following possible states:

$$(3,1) \rightarrow (4',0') \rightarrow (3,-1)$$

$$\begin{aligned}
& \rightarrow(3, 0) \\
& \rightarrow(3, 1) \\
(3,1) \rightarrow (3',0') \rightarrow & (3,-1) \\
& \rightarrow(3, 0) \\
& \rightarrow(3, 1) \\
& \rightarrow(2,-1) \\
& \rightarrow(2, 0) \\
& \rightarrow(2, 1) \\
(3,1) \rightarrow (2',0') \rightarrow & (3,-1) \\
& \rightarrow(3, 0) \\
& \rightarrow(3, 1) \\
& \rightarrow(2,-1) \\
& \rightarrow(2, 0) \\
& \rightarrow(2, 1)
\end{aligned}$$

This gives us the following equations for starting in the (3,1) and driving into one of the other Zeeman groundstate sublevels:

$$\begin{aligned}
P3131 &:= d \rightarrow P314031(d) + P313031(d) + P312031(d) : \\
P3130 &:= d \rightarrow P314030(d) + P313030(d) + P312030(d) : \\
P3131n &:= d \rightarrow P314031n(d) + P313031n(d) + P312031n(d) : \\
P3121 &:= d \rightarrow P313021(d) + P312021(d) : \\
P3120 &:= d \rightarrow P313020(d) + P312020(d) : \\
P3121n &:= d \rightarrow P313021n(d) + P312021n(d) :
\end{aligned}$$

▼ Initial Level (3,0):

Starting in the (3,0) level the cyclor can drive the ion into the (4',-1'), (3',-1') & (2',-1'). From the excited state, we can decay into the following possible states:

$$\begin{aligned}
(3,0) \rightarrow (4',-1') \rightarrow & (3,-2) \\
& \rightarrow(3,-1) \\
& \rightarrow(3, 0) \\
(3,0) \rightarrow (3',-1') \rightarrow & (3,-2) \\
& \rightarrow(3,-1) \\
& \rightarrow(3, 0) \\
& \rightarrow(2,-2) \\
& \rightarrow(2,-1) \\
& \rightarrow(2, 0) \\
(3,0) \rightarrow (2',-1') \rightarrow & (3,-2) \\
& \rightarrow(3,-1) \\
& \rightarrow(3, 0) \\
& \rightarrow(2,-2) \\
& \rightarrow(2,-1) \\
& \rightarrow(2, 0)
\end{aligned}$$

This gives us the following equations for starting in the (3,0) and driving into one of the other Zeeman groundstate sublevels:

$$\begin{aligned}
P3030 &:= d \rightarrow P3041n30(d) + P3031n30(d) + P3021n30(d) : \\
P3031n &:= d \rightarrow P3041n31n(d) + P3031n31n(d) + P3021n31n(d) : \\
P3032n &:= d \rightarrow P3041n32n(d) + P3031n32n(d) + P3021n32n(d) : \\
P3020 &:= d \rightarrow P3031n20(d) + P3021n20(d) : \\
P3021n &:= d \rightarrow P3031n21n(d) + P3021n21n(d) : \\
P3022n &:= d \rightarrow P3031n22n(d) + P3021n22n(d) :
\end{aligned}$$

▼ Initial Level (3,-1):

Starting in the (3,-1) level the cyclor can drive the ion into the (4',-2'), (3',-2') & (2',-2'). From the excited state, we can decay into the following possible states:

$$\begin{aligned}
(3,-1) \rightarrow (4',-2') \rightarrow & (3,-3) \\
& \rightarrow(3,-2) \\
& \rightarrow(3,-1)
\end{aligned}$$

$$\begin{aligned}
 (3,-1) &\rightarrow (3',-2') \rightarrow (3,-3) \\
 &\quad \rightarrow (3,-2) \\
 &\quad \rightarrow (3,-1) \\
 &\quad \rightarrow (2,-2) \\
 &\quad \rightarrow (2,-1)
 \end{aligned}$$

$$\begin{aligned}
 (3,-1) &\rightarrow (2',-2') \rightarrow (3,-3) \\
 &\quad \rightarrow (3,-2) \\
 &\quad \rightarrow (3,-1) \\
 &\quad \rightarrow (2,-2) \\
 &\quad \rightarrow (2,-1)
 \end{aligned}$$

This gives us the following equations for starting in the (3,-1) and driving into one of the other Zeeman groundstate sublevels:

$$\begin{aligned}
 P31n31n &:= d \rightarrow P31n42n31n(d) + P31n32n31n(d) + P31n22n31n(d) : \\
 P31n32n &:= d \rightarrow P31n42n32n(d) + P31n32n32n(d) + P31n22n32n(d) : \\
 P31n33n &:= d \rightarrow P31n42n33n(d) + P31n32n33n(d) + P31n22n33n(d) :
 \end{aligned}$$

$$P31n21n := d \rightarrow P31n32n21n(d) + P31n22n21n(d) :$$

$$P31n22n := d \rightarrow P31n32n22n(d) + P31n22n22n(d) :$$

▼ Initial Level (3,-2):

Starting in the (3,-2) level the cyclor can drive the ion into the (4',-3'), (3',-3'). From the excited state, we can decay into the following possible states:

$$\begin{aligned}
 (3,-2) &\rightarrow (4',-3') \rightarrow (3,-2) \\
 &\quad \rightarrow (3,-3) \\
 (3,-2) &\rightarrow (3',-3') \rightarrow (3,-3) \\
 &\quad \rightarrow (3,-2) \\
 &\quad \rightarrow (2,-2)
 \end{aligned}$$

This gives us the following equations for starting in the (3,-2) and driving into one of the other Zeeman groundstate sublevels:

$$\begin{aligned}
 P32n32n &:= d \rightarrow P32n43n32n(d) + P32n33n32n(d) : \\
 P32n33n &:= d \rightarrow P32n43n33n(d) + P32n33n33n(d) : \\
 P32n22n &:= d \rightarrow P32n33n22n(d) :
 \end{aligned}$$

▼ Initial Level (3,-3):

Starting in the (3,-3) level the cyclor can drive the ion into the (4',-4'). This is just the cycling transition. From the excited state, we can decay into the following possible states:

$$\begin{aligned}
 (2,-1) &\rightarrow (3',-3') \rightarrow (3,-2) \\
 &\quad \rightarrow (3,-3) \\
 &\quad \rightarrow (2,-2)
 \end{aligned}$$

This gives us the following equations for starting in the (3,-3) and driving into one of the other Zeeman groundstate sublevels:

$$P33n33n := d \rightarrow P33n44n33n(d) :$$

▼ Initial Level (2,-2):

Starting in the (2,-2) level the cyclor can drive the ion into the (3',-3'). From the excited state, we can decay into the following possible states:

$$\begin{aligned}
 (2,-1) &\rightarrow (3',-3') \rightarrow (3,-2) \\
 &\quad \rightarrow (3,-3) \\
 &\quad \rightarrow (2,-2)
 \end{aligned}$$

This gives us the following equations for starting in the (2,-2) and driving into one of the other Zeeman groundstate sublevels:

$$\begin{aligned}
 P22n33n &:= d \rightarrow P22n33n33n(d) : \\
 P22n32n &:= d \rightarrow P22n33n32n(d) : \\
 P22n22n &:= d \rightarrow P22n33n22n(d) :
 \end{aligned}$$

▼ Initial Level (2,-1):

Starting in the (2,-1) level the cyclor can drive the ion into the (3',-2'),

(2', 2'). From the excited state, we can decay into the following possible states:

$$\begin{aligned}
 (2, -1) &\rightarrow (3', -2') \rightarrow (3, -1) \\
 &\quad \rightarrow (3, -2) \\
 &\quad \rightarrow (3, -3) \\
 &\quad \rightarrow (2, -1) \\
 &\quad \rightarrow (2, -2) \\
 (2, -1) &\rightarrow (2', -2') \rightarrow (3, -1) \\
 &\quad \rightarrow (3, -2) \\
 &\quad \rightarrow (3, -3) \\
 &\quad \rightarrow (2, -1) \\
 &\quad \rightarrow (2, -2)
 \end{aligned}$$

This gives us the following equations for starting in the (2, -1) and driving into one of the other Zeeman groundstate sublevels:

$$\begin{aligned}
 P21n33n &:= d \rightarrow P21n32n33n(d) + P21n22n33n(d) : \\
 P21n32n &:= d \rightarrow P21n32n32n(d) + P21n22n32n(d) : \\
 P21n31n &:= d \rightarrow P21n32n31n(d) + P21n22n31n(d) : \\
 P21n22n &:= d \rightarrow P21n32n22n(d) + P21n22n22n(d) : \\
 P21n21n &:= d \rightarrow P21n32n21n(d) + P21n22n21n(d) :
 \end{aligned}$$

▼ Initial Level (2, 0):

Starting in the (2, 0) level the cyclor can drive the ion into the (3', -1'), (2', -1') & (1', -1'). From the excited state, we can decay into the following possible states:

$$\begin{aligned}
 (2, 0) &\rightarrow (3', -1') \rightarrow (3, 0) \\
 &\quad \rightarrow (3, -1) \\
 &\quad \rightarrow (3, -2) \\
 &\quad \rightarrow (2, 0) \\
 &\quad \rightarrow (2, -1) \\
 &\quad \rightarrow (2, -2) \\
 (2, 0) &\rightarrow (2', -1') \rightarrow (3, 0) \\
 &\quad \rightarrow (3, -1) \\
 &\quad \rightarrow (3, -2) \\
 &\quad \rightarrow (2, 0) \\
 &\quad \rightarrow (2, -1) \\
 &\quad \rightarrow (2, -2) \\
 (2, 0) &\rightarrow (1', -1') \rightarrow (2, 0) \\
 &\quad \rightarrow (2, -1) \\
 &\quad \rightarrow (2, -2)
 \end{aligned}$$

This gives us the following equations for starting in the (2, 0) and driving into one of the other Zeeman groundstate sublevels:

$$\begin{aligned}
 P2032n &:= d \rightarrow P2031n32n(d) + P2021n32n(d) : \\
 P2031n &:= d \rightarrow P2031n31n(d) + P2021n31n(d) : \\
 P2030 &:= d \rightarrow P2031n30(d) + P2021n30(d) : \\
 P2022n &:= d \rightarrow P2031n22n(d) + P2021n22n(d) + P2011n22n(d) : \\
 P2021n &:= d \rightarrow P2031n21n(d) + P2021n21n(d) + P2011n21n(d) : \\
 P2020 &:= d \rightarrow P2031n20(d) + P2021n20(d) + P2011n20(d) :
 \end{aligned}$$

▼ Initial Level (2, 1):

Starting in the (2, 1) level the cyclor can drive the ion into the (3', 0'), (2', 0') & (1', 0'). From the excited state, we can decay into the following possible states:

$$\begin{aligned}
 (2, 1) &\rightarrow (3', 0') \rightarrow (3, 1) \\
 &\quad \rightarrow (3, 0) \\
 &\quad \rightarrow (3, -1) \\
 &\quad \rightarrow (2, 1) \\
 &\quad \rightarrow (2, 0) \\
 &\quad \rightarrow (2, -1)
 \end{aligned}$$

$$\begin{aligned}
(2,1) &\rightarrow (2',0') \rightarrow (3,1) \\
&\quad \rightarrow (3,0) \\
&\quad \rightarrow (3,-1) \\
&\quad \rightarrow (2,1) \\
&\quad \rightarrow (2,0) \\
&\quad \rightarrow (2,-1) \\
(2,1) &\rightarrow (1',0') \rightarrow (2,1) \\
&\quad \rightarrow (2,0) \\
&\quad \rightarrow (2,-1)
\end{aligned}$$

This gives us the following equations for starting in the (2,1) and driving into one of the other Zeeman groundstate sublevels:

$$\begin{aligned}
P2131n &:= d \rightarrow P213031n(d) + P212031n(d) : \\
P2130 &:= d \rightarrow P213030(d) + P212030(d) : \\
P2131 &:= d \rightarrow P213031(d) + P212031(d) : \\
P2121n &:= d \rightarrow P213021n(d) + P212021n(d) + P211021n(d) : \\
P2120 &:= d \rightarrow P213020(d) + P212020(d) + P211020(d) : \\
P2121 &:= d \rightarrow P213021(d) + P212021(d) + P211021(d) :
\end{aligned}$$

▼ Initial Level (2, 2):

Starting in the (2,2) level the cyclor can drive the ion into the (3',1'), (2',1') & (1',1'). From the excited state, we can decay into the following possible states:

$$\begin{aligned}
(2,2) &\rightarrow (3',1') \rightarrow (3,2) \\
&\quad \rightarrow (3,1) \\
&\quad \rightarrow (3,0) \\
&\quad \rightarrow (2,2) \\
&\quad \rightarrow (2,1) \\
&\quad \rightarrow (2,0) \\
(2,2) &\rightarrow (2',1') \rightarrow (3,2) \\
&\quad \rightarrow (3,1) \\
&\quad \rightarrow (3,0) \\
&\quad \rightarrow (2,2) \\
&\quad \rightarrow (2,1) \\
&\quad \rightarrow (2,0) \\
(2,2) &\rightarrow (1',1') \rightarrow (2,2) \\
&\quad \rightarrow (2,1) \\
&\quad \rightarrow (2,0)
\end{aligned}$$

This gives us the following equations for starting in the (2,2) and driving into one of the other Zeeman groundstate sublevels:

$$\begin{aligned}
P2230 &:= d \rightarrow P223130(d) + P222130(d) : \\
P2231 &:= d \rightarrow P223131(d) + P222131(d) : \\
P2232 &:= d \rightarrow P223132(d) + P222132(d) : \\
P2220 &:= d \rightarrow P223120(d) + P222120(d) + P221120(d) : \\
P2221 &:= d \rightarrow P223121(d) + P222121(d) + P221121(d) : \\
P2222 &:= d \rightarrow P223122(d) + P222122(d) + P221122(d) :
\end{aligned}$$

▼ Rate Equations for the cycling laser:

▼ Rate Equations:

The rate equations are given by:

$$\begin{aligned}
Eq33 &:= d \rightarrow \frac{d}{dt} p33(t) = (-P3332(d) - P3331(d) - P3322(d) \\
&\quad - P3321(d)) \cdot p33(t) :
\end{aligned}$$

$$\begin{aligned}
Eq32 &:= d \rightarrow \frac{d}{dt} p32(t) = (-P3231(d) - P3230(d) - P3222(d) \\
&\quad - P3221(d) - P3220(d)) \cdot p32(t) + P3332(d) \cdot p33(t) + P2232(d)
\end{aligned}$$

$$\begin{aligned}
& \cdot p_{22}(t) : \\
\text{Eq31} & := d \rightarrow \frac{d}{dt} p_{31}(t) = (-P_{3130}(d) - P_{3131n}(d) - P_{3121}(d) \\
& \quad - P_{3120}(d) - P_{3121n}(d)) \cdot p_{31}(t) + P_{3231}(d) \cdot p_{32}(t) \\
& \quad + P_{3331}(d) \cdot p_{33}(t) + P_{2231}(d) \cdot p_{22}(t) + P_{2131}(d) \cdot p_{21}(t) : \\
\text{Eq30} & := d \rightarrow \frac{d}{dt} p_{30}(t) = (-P_{3031n}(d) - P_{3032n}(d) - P_{3020}(d) \\
& \quad - P_{3021n}(d) - P_{3022n}(d)) \cdot p_{30}(t) + P_{3130}(d) \cdot p_{31}(t) \\
& \quad + P_{3230}(d) \cdot p_{32}(t) + P_{2230}(d) \cdot p_{22}(t) + P_{2130}(d) \cdot p_{21}(t) \\
& \quad + P_{2030}(d) \cdot p_{20}(t) : \\
\text{Eq31n} & := d \rightarrow \frac{d}{dt} p_{31n}(t) = (-P_{31n32n}(d) - P_{31n33n}(d) \\
& \quad - P_{31n21n}(d) - P_{31n22n}(d)) \cdot p_{31n}(t) + P_{3031n}(d) \cdot p_{30}(t) \\
& \quad + P_{3131n}(d) \cdot p_{31}(t) + P_{2131n}(d) \cdot p_{21}(t) + P_{2031n}(d) \cdot p_{20}(t) \\
& \quad + P_{21n31n}(d) \cdot p_{21n}(t) : \\
\text{Eq32n} & := d \rightarrow \frac{d}{dt} p_{32n}(t) = (-P_{32n33n}(d) - P_{32n22n}(d)) \cdot p_{32n}(t) \\
& \quad + P_{31n32n}(d) \cdot p_{31n}(t) + P_{3032n}(d) \cdot p_{30}(t) + P_{2032n}(d) \cdot p_{20}(t) \\
& \quad + P_{21n32n}(d) \cdot p_{21n}(t) + P_{22n32n}(d) \cdot p_{22n}(t) : \\
\text{Eq33n} & := d \rightarrow \frac{d}{dt} p_{33n}(t) = P_{32n33n}(d) \cdot p_{32n}(t) + P_{31n33n}(d) \\
& \quad \cdot p_{31n}(t) + P_{21n33n}(d) \cdot p_{21n}(t) + P_{22n33n}(d) \cdot p_{22n}(t) : \\
\text{Eq22} & := d \rightarrow \frac{d}{dt} p_{22}(t) = P_{3322}(d) \cdot p_{33}(t) + P_{3222}(d) \cdot p_{32}(t) \\
& \quad - (P_{2230}(d) + P_{2231}(d) + P_{2232}(d) + P_{2220}(d) + P_{2221}(d)) \\
& \quad \cdot p_{22}(t) : \\
\text{Eq21} & := d \rightarrow \frac{d}{dt} p_{21}(t) = P_{3321}(d) \cdot p_{33}(t) + P_{3221}(d) \cdot p_{32}(t) \\
& \quad + P_{3121}(d) \cdot p_{31}(t) + P_{2221}(d) \cdot p_{22}(t) - (P_{2131n}(d) \\
& \quad + P_{2130}(d) + P_{2131}(d) + P_{2121n}(d) + P_{2120}(d)) \cdot p_{21}(t) : \\
\text{Eq20} & := d \rightarrow \frac{d}{dt} p_{20}(t) = P_{3220}(d) \cdot p_{32}(t) + P_{3120}(d) \cdot p_{31}(t) \\
& \quad + P_{3020}(d) \cdot p_{30}(t) + P_{2220}(d) \cdot p_{22}(t) + P_{2120}(d) \cdot p_{21}(t) \\
& \quad - (P_{2032n}(d) + P_{2031n}(d) + P_{2030}(d) + P_{2022n}(d) \\
& \quad + P_{2021n}(d)) \cdot p_{20}(t) : \\
\text{Eq21n} & := d \rightarrow \frac{d}{dt} p_{21n}(t) = P_{3121n}(d) \cdot p_{31}(t) + P_{3021n}(d) \cdot p_{30}(t) \\
& \quad + P_{31n21n}(d) \cdot p_{31n}(t) + P_{2121n}(d) \cdot p_{21}(t) + P_{2021n}(d) \cdot p_{20}(t) \\
& \quad - (P_{21n33n}(d) + P_{21n32n}(d) + P_{21n31n}(d) + P_{21n22n}(d)) \\
& \quad \cdot p_{21n}(t) : \\
\text{Eq22n} & := d \rightarrow \frac{d}{dt} p_{22n}(t) = P_{3022n}(d) \cdot p_{30}(t) + P_{31n22n}(d) \cdot p_{31n}(t) \\
& \quad + P_{32n22n}(d) \cdot p_{32n}(t) + P_{2022n}(d) \cdot p_{20}(t) + P_{21n22n}(d) \\
& \quad \cdot p_{21n}(t) - (P_{22n33n}(d) + P_{22n32n}(d)) \cdot p_{22n}(t)
\end{aligned}$$

▼ Determining Time Dependent Probabilities for Different Initial Conditions

▼ Population Driven into  $F'=3$  by Probe Laser

▼ Procedure to Calculate Cyclus Temporal Dynamics:

```

ThreePrimeCyclusDynamics := proc(ProbeDetuning, ProbeScatterings,
    CyclusDetuning, CyclusScatterings)
    global CF3Solns, CF3P33n, CF3P32n, CF3P31n, CF3P30, CF3P31,
    CF3P32, CF3P33, CF3P22n, CF3P21n, CF3P20, CF3P21, CF3P22,

```





$$\begin{aligned}
& + \frac{\mu_{\text{red}}\left(\frac{1}{2}, 3, 1, \frac{3}{2}, 3, 0, \frac{5}{2}, -1\right)^2}{1 + \left(\frac{2 \cdot (\text{CyclerDetuning} + \Delta\text{HF3P})}{\Gamma\text{Mg}}\right)^2} \\
& + \frac{\mu_{\text{red}}\left(\frac{1}{2}, 3, 1, \frac{3}{2}, 2, 0, \frac{5}{2}, -1\right)^2}{1 + \left(\frac{2 \cdot (\text{CyclerDetuning} + \Delta\text{HF2P})}{\Gamma\text{Mg}}\right)^2} \left. \right) \cdot \text{CF3P31}(t), t = 0 \dots 100 \\
& \left. \right) : \\
\text{CF3Photons32} := \text{evalf} & \left( \text{int} \left( \left( \frac{\mu_{\text{red}}\left(\frac{1}{2}, 3, 2, \frac{3}{2}, 4, 1, \frac{5}{2}, -1\right)^2}{1 + \left(\frac{2 \cdot (\text{CyclerDetuning})}{\Gamma\text{Mg}}\right)^2} \right. \right. \right. \\
& + \frac{\mu_{\text{red}}\left(\frac{1}{2}, 3, 2, \frac{3}{2}, 3, 1, \frac{5}{2}, -1\right)^2}{1 + \left(\frac{2 \cdot (\text{CyclerDetuning} + \Delta\text{HF3P})}{\Gamma\text{Mg}}\right)^2} \\
& \left. \left. \left. + \frac{\mu_{\text{red}}\left(\frac{1}{2}, 3, 2, \frac{3}{2}, 2, 1, \frac{5}{2}, -1\right)^2}{1 + \left(\frac{2 \cdot (\text{CyclerDetuning} + \Delta\text{HF2P})}{\Gamma\text{Mg}}\right)^2} \right) \cdot \text{CF3P32}(t), t = 0 \dots 100 \right) \right) : \\
\text{CF3Photons33} := \text{evalf} & \left( \text{int} \left( \left( \frac{\mu_{\text{red}}\left(\frac{1}{2}, 3, 3, \frac{3}{2}, 4, 2, \frac{5}{2}, -1\right)^2}{1 + \left(\frac{2 \cdot (\text{CyclerDetuning})}{\Gamma\text{Mg}}\right)^2} \right. \right. \right. \\
& + \frac{\mu_{\text{red}}\left(\frac{1}{2}, 3, 3, \frac{3}{2}, 3, 2, \frac{5}{2}, -1\right)^2}{1 + \left(\frac{2 \cdot (\text{CyclerDetuning} + \Delta\text{HF3P})}{\Gamma\text{Mg}}\right)^2} \\
& \left. \left. \left. + \frac{\mu_{\text{red}}\left(\frac{1}{2}, 3, 3, \frac{3}{2}, 2, 2, \frac{5}{2}, -1\right)^2}{1 + \left(\frac{2 \cdot (\text{CyclerDetuning} + \Delta\text{HF2P})}{\Gamma\text{Mg}}\right)^2} \right) \cdot \text{CF3P33}(t), t = 0 \dots 100 \right) \right)
\end{aligned}$$

$$\left. \begin{aligned}
& \right\} : \\
& \text{CF3Photons22n} \\
& := \text{evalf} \left( \text{int} \left( \left( \frac{\mu_{\text{red}} \left( \frac{1}{2}, 2, -2, \frac{3}{2}, 3, -3, \frac{5}{2}, -1 \right)^2}{1 + \left( \frac{2 \cdot (\text{CyclerDetuning} + \Delta\text{HF3P})}{\Gamma\text{Mg}} \right)^2} \right) \right) \right. \\
& \left. \cdot \text{CF3P22n}(t), t = 0 \dots \text{CyclerScatterings} \right) : \\
& \text{CF3Photons21n} \\
& := \text{evalf} \left( \text{int} \left( \left( \frac{\mu_{\text{red}} \left( \frac{1}{2}, 2, -1, \frac{3}{2}, 3, -2, \frac{5}{2}, -1 \right)^2}{1 + \left( \frac{2 \cdot (\text{CyclerDetuning} + \Delta\text{HF3P})}{\Gamma\text{Mg}} \right)^2} \right) \right. \right. \\
& \left. \left. + \frac{\mu_{\text{red}} \left( \frac{1}{2}, 2, -1, \frac{3}{2}, 2, -2, \frac{5}{2}, -1 \right)^2}{1 + \left( \frac{2 \cdot (\text{CyclerDetuning} + \Delta\text{HF2P})}{\Gamma\text{Mg}} \right)^2} \right) \cdot \text{CF3P21n}(t), t = 0 \right. \\
& \left. \dots \text{CyclerScatterings} \right) : \\
& \text{CF3Photons20} := \text{evalf} \left( \text{int} \left( \left( \frac{\mu_{\text{red}} \left( \frac{1}{2}, 2, 0, \frac{3}{2}, 4, 2, \frac{5}{2}, -1 \right)^2}{1 + \left( \frac{2 \cdot (\text{CyclerDetuning} + \Delta\text{HF3P})}{\Gamma\text{Mg}} \right)^2} \right) \right. \right. \\
& \left. \left. + \frac{\mu_{\text{red}} \left( \frac{1}{2}, 2, 0, \frac{3}{2}, 2, -1, \frac{5}{2}, -1 \right)^2}{1 + \left( \frac{2 \cdot (\text{CyclerDetuning} + \Delta\text{HF2P})}{\Gamma\text{Mg}} \right)^2} \right) \right. \\
& \left. \left. + \frac{\mu_{\text{red}} \left( \frac{1}{2}, 2, 0, \frac{3}{2}, 1, -1, \frac{5}{2}, -1 \right)^2}{1 + \left( \frac{2 \cdot (\text{CyclerDetuning} + \Delta\text{HF1P})}{\Gamma\text{Mg}} \right)^2} \right) \cdot \text{CF3P20}(t), t = 0 \right. \\
& \left. \dots \text{CyclerScatterings} \right) :
\end{aligned}$$

$$\begin{aligned}
\text{CF3Photons21} := & \text{evalf} \left( \text{int} \left( \left( \frac{\mu_{\text{red}} \left( \frac{1}{2}, 2, 1, \frac{3}{2}, 3, 0, \frac{5}{2}, -1 \right)^2}{1 + \left( \frac{2 \cdot (\text{CyclerDetuning} + \Delta\text{HF3P})}{\Gamma\text{Mg}} \right)^2} \right. \right. \right. \\
& + \frac{\mu_{\text{red}} \left( \frac{1}{2}, 2, 1, \frac{3}{2}, 2, 0, \frac{5}{2}, -1 \right)^2}{1 + \left( \frac{2 \cdot (\text{CyclerDetuning} + \Delta\text{HF2P})}{\Gamma\text{Mg}} \right)^2} \\
& \left. \left. \left. + \frac{\mu_{\text{red}} \left( \frac{1}{2}, 2, 1, \frac{3}{2}, 1, 0, \frac{5}{2}, -1 \right)^2}{1 + \left( \frac{2 \cdot (\text{CyclerDetuning} + \Delta\text{HF1P})}{\Gamma\text{Mg}} \right)^2} \right) \cdot \text{CF3P21}(t), t = 0 \right. \right. \\
& \left. \left. \left. \cdot \text{CyclerScatterings} \right) \right) : \\
\text{CF3Photons22} := & \text{evalf} \left( \text{int} \left( \left( \frac{\mu_{\text{red}} \left( \frac{1}{2}, 2, 2, \frac{3}{2}, 2, 1, \frac{5}{2}, -1 \right)^2}{1 + \left( \frac{2 \cdot (\text{CyclerDetuning} + \Delta\text{HF3P})}{\Gamma\text{Mg}} \right)^2} \right. \right. \right. \\
& + \frac{\mu_{\text{red}} \left( \frac{1}{2}, 2, 2, \frac{3}{2}, 2, 1, \frac{5}{2}, -1 \right)^2}{1 + \left( \frac{2 \cdot (\text{CyclerDetuning} + \Delta\text{HF2P})}{\Gamma\text{Mg}} \right)^2} \\
& \left. \left. \left. + \frac{\mu_{\text{red}} \left( \frac{1}{2}, 2, 2, \frac{3}{2}, 1, 1, \frac{5}{2}, -1 \right)^2}{1 + \left( \frac{2 \cdot (\text{CyclerDetuning} + \Delta\text{HF1P})}{\Gamma\text{Mg}} \right)^2} \right) \cdot \text{CF3P22}(t), t = 0 \right. \right. \\
& \left. \left. \left. \cdot \text{CyclerScatterings} \right) \right) : \\
\text{CF3TotalCounts} := & \text{CF3Photons33n} + \text{CF3Photons32n} \\
& + \text{CF3Photons31n} + \text{CF3Photons30} + \text{CF3Photons31} \\
& + \text{CF3Photons32} + \text{CF3Photons33} + \text{CF3Photons22n} \\
& + \text{CF3Photons21n} + \text{CF3Photons20} + \text{CF3Photons21} \\
& + \text{CF3Photons22} :
\end{aligned}$$

end proc:

▼ Procedure to Calculate Total Counts as a function of Probe Laser Detuning:

```

ThreePrimeLineShape := proc(ProbeFrequencyFromResonance,
  ProbeScatterings, CyclerDetuning, CyclerScatterings, name)
  local stepsize, freq, ProbeFrequency;
  writeto(name) :
  writeto(terminal) :
  stepsize := 2 :

```

```

ProbeFrequency := -ProbeFrequencyFromResonance;
#Initialize first point
for ProbeFrequency from -ProbeFrequencyFromResonance
  by stepsize to ProbeFrequencyFromResonance do
  ThreePrimeCyclerDynamics(2· $\pi$ ·ProbeFrequency, ProbeScatterings,
  CyclerDetuning, CyclerScatterings) :
  appendto(name) :
  print(ProbeFrequency, CF3TotalCounts);
  writeto(terminal) :
  end do
end proc:

```

▼ Procedure to Calculate Total Counts as a function of Probe Time:

```

ThreePrimeProbeTime := proc(ProbeFrequencyFromResonance,
  ProbeMaxScatterings, CyclerDetuning, CyclerScatterings, name)
  local stepsize, freq, ProbeTime;
  writeto(name) :
  writeto(terminal) :
  stepsize := 1 :
  ProbeTime := 0; #initialize first probe time
  for ProbeTime from 0 by stepsize to ProbeMaxScatterings do
    ThreePrimeCyclerDynamics(2· $\pi$ ·ProbeFrequencyFromResonance,
    ProbeTime, CyclerDetuning, CyclerScatterings) :
    appendto(name) :
    print(ProbeTime, CF3TotalCounts);
    writeto(terminal) :
  end do
end proc:

```

▼ Population Driven into  $F'=2$  by Probe Laser

▼ Procedure to Calculate Cycler Temporal Dynamics:

```

TwoPrimeCyclerDynamics := proc(ProbeDetuning, ProbeScatterings,
  CyclerDetuning, CyclerScatterings)
  global CF2Solns, CF2P33n, CF2P32n, CF2P31n, CF2P30, CF2P31,
  CF2P32, CF2P33, CF2P22n, CF2P21n, CF2P20, CF2P21, CF2P22,
  CF2Photons33n, CF2Photons32n, CF2Photons31n, CF2Photons30,
  CF2Photons31, CF2Photons32, CF2Photons33, CF2Photons22n,
  CF2Photons21n, CF2Photons20, CF2Photons21, CF2Photons22,
  CF2TotalCounts;
  local CF2Eqs;
  #setup ProbeDynamics:
  TwoPrimeProbeDynamics(ProbeDetuning) :
  #setup system of equations and numerically solve using dsolve:
  CF2Eqs := {Eq33n(CyclerDetuning), Eq32n(CyclerDetuning),
  Eq31n(CyclerDetuning), Eq30(CyclerDetuning),
  Eq31(CyclerDetuning), Eq32(CyclerDetuning),
  Eq33(CyclerDetuning), Eq22n(CyclerDetuning),
  Eq21n(CyclerDetuning), Eq20(CyclerDetuning),
  Eq21(CyclerDetuning), Eq22(CyclerDetuning), p33(0)
  = F2P33(ProbeScatterings), p32(0) = F2P32(ProbeScatterings),
  p31(0) = F2P31(ProbeScatterings), p30(0)
  = F2P30(ProbeScatterings), p31n(0)
  = F2P31n(ProbeScatterings), p32n(0)
  = F2P32n(ProbeScatterings), p33n(0)
  = F2P33n(ProbeScatterings), p22n(0)
  = F2P22n(ProbeScatterings), p21n(0)

```





$$\begin{aligned}
 & \left. \begin{aligned}
 & + \frac{\mu_{\text{red}}\left(\frac{1}{2}, 3, 2, \frac{3}{2}, 3, 1, \frac{5}{2}, -1\right)^2}{1 + \left(\frac{2 \cdot (\text{CyclerDetuning} + \Delta\text{HF3P})}{\Gamma\text{Mg}}\right)^2} \\
 & + \frac{\mu_{\text{red}}\left(\frac{1}{2}, 3, 2, \frac{3}{2}, 2, 1, \frac{5}{2}, -1\right)^2}{1 + \left(\frac{2 \cdot (\text{CyclerDetuning} + \Delta\text{HF2P})}{\Gamma\text{Mg}}\right)^2} \cdot \text{CF2P32}(t), t = 0 \dots 100
 \end{aligned} \right\} \\
 & \left. \begin{aligned}
 & \text{CF2Photons33} := \text{evalf} \left( \text{int} \left( \left( \frac{\mu_{\text{red}}\left(\frac{1}{2}, 3, 3, \frac{3}{2}, 4, 2, \frac{5}{2}, -1\right)^2}{1 + \left(\frac{2 \cdot (\text{CyclerDetuning})}{\Gamma\text{Mg}}\right)^2} \right. \right. \right. \\
 & \left. \left. \left. + \frac{\mu_{\text{red}}\left(\frac{1}{2}, 3, 3, \frac{3}{2}, 3, 2, \frac{5}{2}, -1\right)^2}{1 + \left(\frac{2 \cdot (\text{CyclerDetuning} + \Delta\text{HF3P})}{\Gamma\text{Mg}}\right)^2} \right. \right. \right. \\
 & \left. \left. \left. + \frac{\mu_{\text{red}}\left(\frac{1}{2}, 3, 3, \frac{3}{2}, 2, 2, \frac{5}{2}, -1\right)^2}{1 + \left(\frac{2 \cdot (\text{CyclerDetuning} + \Delta\text{HF2P})}{\Gamma\text{Mg}}\right)^2} \right) \cdot \text{CF2P33}(t), t = 0 \dots 100 \right) \right) \\
 & \left. \begin{aligned}
 & \text{CF2Photons22n} \\
 & := \text{evalf} \left( \text{int} \left( \left( \frac{\mu_{\text{red}}\left(\frac{1}{2}, 2, -2, \frac{3}{2}, 3, -3, \frac{5}{2}, -1\right)^2}{1 + \left(\frac{2 \cdot (\text{CyclerDetuning} + \Delta\text{HF3P})}{\Gamma\text{Mg}}\right)^2} \right) \right. \right. \right. \\
 & \left. \left. \left. \cdot \text{CF2P22n}(t), t = 0 \dots \text{CyclerScatterings} \right) \right) : \\
 & \text{CF2Photons21n} \\
 & := \text{evalf} \left( \text{int} \left( \left( \frac{\mu_{\text{red}}\left(\frac{1}{2}, 2, -1, \frac{3}{2}, 3, -2, \frac{5}{2}, -1\right)^2}{1 + \left(\frac{2 \cdot (\text{CyclerDetuning} + \Delta\text{HF3P})}{\Gamma\text{Mg}}\right)^2} \right) \right. \right. \right.
 \end{aligned} \right)
 \end{aligned}$$

$$\begin{aligned}
& \left. \begin{aligned}
& + \frac{\mu_{\text{red}}\left(\frac{1}{2}, 2, -1, \frac{3}{2}, 2, -2, \frac{5}{2}, -1\right)^2}{1 + \left(\frac{2 \cdot (\text{CyclorDetuning} + \Delta\text{HF2P})}{\Gamma\text{Mg}}\right)^2} \cdot \text{CF2P21n}(t), t = 0 \\
& \text{..CyclorScatterings}
\end{aligned} \right\} : \\
\text{CF2Photons20} := \text{evalf} \left( \int \left( \left( \frac{\mu_{\text{red}}\left(\frac{1}{2}, 2, 0, \frac{3}{2}, 4, 2, \frac{5}{2}, -1\right)^2}{1 + \left(\frac{2 \cdot (\text{CyclorDetuning} + \Delta\text{HF3P})}{\Gamma\text{Mg}}\right)^2} \right. \right. \right. \\
& + \frac{\mu_{\text{red}}\left(\frac{1}{2}, 2, 0, \frac{3}{2}, 2, -1, \frac{5}{2}, -1\right)^2}{1 + \left(\frac{2 \cdot (\text{CyclorDetuning} + \Delta\text{HF2P})}{\Gamma\text{Mg}}\right)^2} \\
& \left. \left. \left. + \frac{\mu_{\text{red}}\left(\frac{1}{2}, 2, 0, \frac{3}{2}, 1, -1, \frac{5}{2}, -1\right)^2}{1 + \left(\frac{2 \cdot (\text{CyclorDetuning} + \Delta\text{HF1P})}{\Gamma\text{Mg}}\right)^2} \right) \cdot \text{CF2P20}(t), t = 0 \right. \right. \\
& \left. \left. \left. \text{..CyclorScatterings} \right) \right) : \\
\text{CF2Photons21} := \text{evalf} \left( \int \left( \left( \frac{\mu_{\text{red}}\left(\frac{1}{2}, 2, 1, \frac{3}{2}, 3, 0, \frac{5}{2}, -1\right)^2}{1 + \left(\frac{2 \cdot (\text{CyclorDetuning} + \Delta\text{HF3P})}{\Gamma\text{Mg}}\right)^2} \right. \right. \right. \\
& + \frac{\mu_{\text{red}}\left(\frac{1}{2}, 2, 1, \frac{3}{2}, 2, 0, \frac{5}{2}, -1\right)^2}{1 + \left(\frac{2 \cdot (\text{CyclorDetuning} + \Delta\text{HF2P})}{\Gamma\text{Mg}}\right)^2} \\
& \left. \left. \left. + \frac{\mu_{\text{red}}\left(\frac{1}{2}, 2, 1, \frac{3}{2}, 1, 0, \frac{5}{2}, -1\right)^2}{1 + \left(\frac{2 \cdot (\text{CyclorDetuning} + \Delta\text{HF1P})}{\Gamma\text{Mg}}\right)^2} \right) \cdot \text{CF2P21}(t), t = 0 \right. \right. \\
& \left. \left. \left. \text{..CyclorScatterings} \right) \right) :
\end{aligned}$$

$$\begin{aligned}
\text{CF2Photons22} := & \text{evalf} \left( \text{int} \left( \left( \frac{\mu_{\text{red}} \left( \frac{1}{2}, 2, 2, \frac{3}{2}, 2, 1, \frac{5}{2}, -1 \right)^2}{1 + \left( \frac{2 \cdot (\text{CyclersDetuning} + \Delta\text{HF3P})}{\Gamma\text{Mg}} \right)^2} \right. \right. \right. \\
& + \frac{\mu_{\text{red}} \left( \frac{1}{2}, 2, 2, \frac{3}{2}, 2, 1, \frac{5}{2}, -1 \right)^2}{1 + \left( \frac{2 \cdot (\text{CyclersDetuning} + \Delta\text{HF2P})}{\Gamma\text{Mg}} \right)^2} \\
& \left. \left. \left. + \frac{\mu_{\text{red}} \left( \frac{1}{2}, 2, 2, \frac{3}{2}, 1, 1, \frac{5}{2}, -1 \right)^2}{1 + \left( \frac{2 \cdot (\text{CyclersDetuning} + \Delta\text{HF1P})}{\Gamma\text{Mg}} \right)^2} \right) \cdot \text{CF2P22}(t), t = 0 \right. \right. \\
& \left. \left. \left. \cdot \text{CyclersScatterings} \right) \right) : \right. \\
\text{CF2TotalCounts} := & \text{CF2Photons33n} + \text{CF2Photons32n} \\
& + \text{CF2Photons31n} + \text{CF2Photons30} + \text{CF2Photons31} \\
& + \text{CF2Photons32} + \text{CF2Photons33} + \text{CF2Photons22n} \\
& + \text{CF2Photons21n} + \text{CF2Photons20} + \text{CF2Photons21} \\
& + \text{CF2Photons22} : \\
& \text{print("done");} \\
& \text{end proc;}
\end{aligned}$$

▼ Procedure to Calculate Total Counts as a function of Probe Laser Detuning:

```

TwoPrimeLineShape := proc(ProbeFrequencyFromResonance,
    ProbeScatterings, CyclersDetuning, CyclersScatterings, name)
    local stepsize, freq, ProbeFrequency;
    writeto(name) :
    writeto(terminal) :
    stepsize := 2 :
    ProbeFrequency := -ProbeFrequencyFromResonance;
    #Initialize first point
    for ProbeFrequency from -ProbeFrequencyFromResonance
        by stepsize to ProbeFrequencyFromResonance do
            TwoPrimeCyclersDynamics(2·π·ProbeFrequency, ProbeScatterings,
                CyclersDetuning, CyclersScatterings) :
            appendto(name) :
            print(ProbeFrequency, CF2TotalCounts);
            writeto(terminal) :
        end do
    end proc;

```

▼ Procedure to Calculate Total Counts as a function of Probe Time:

```

TwoPrimeProbeTime := proc(ProbeFrequencyFromResonance,
    ProbeMaxScatterings, CyclersDetuning, CyclersScatterings, name)
    local stepsize, freq, ProbeTime;
    writeto(name) :
    writeto(terminal) :
    stepsize := 1 :
    ProbeTime := 0; #initialize first probe time
    for ProbeTime from 0 by stepsize to ProbeMaxScatterings do

```

```

TwoPrimeCyclerDynamics(2·π·ProbeFrequencyFromResonance,
ProbeTime, CyclerDetuning, CyclerScatterings) :
appendto(name) :
print(ProbeTime, CF2TotalCounts);
writeto(terminal) :
end do
end proc:

```

### ▼ Full Population Dynamics

#### ▼ Procedure to Calculate Cycler Temporal Dynamics

```

FullCyclerDynamics := proc(ProbeDetuning, ProbeScatterings,
CyclerDetuning, CyclerScatterings)
global CF23Solns, CF23P33n, CF23P32n, CF23P31n, CF23P30,
CF23P31, CF23P32, CF23P33, CF23P22n, CF23P21n, CF23P20,
CF23P21, CF23P22, CF23Photons33n, CF23Photons32n,
CF23Photons31n, CF23Photons30, CF23Photons31,
CF23Photons32, CF23Photons33, CF23Photons22n,
CF23Photons21n, CF23Photons20, CF23Photons21,
CF23Photons22, CF23TotalCounts;
local CF23Eqs;
#setup ProbeDynamics:
print(ProbeDetuning) :
FullProbeDynamics(ProbeDetuning) :
#setup system of equations and numerically solve using dsolve:
CF23Eqs := {Eq33n(CyclerDetuning), Eq32n(CyclerDetuning),
Eq31n(CyclerDetuning), Eq30(CyclerDetuning),
Eq31(CyclerDetuning), Eq32(CyclerDetuning),
Eq33(CyclerDetuning), Eq22n(CyclerDetuning),
Eq21n(CyclerDetuning), Eq20(CyclerDetuning),
Eq21(CyclerDetuning), Eq22(CyclerDetuning), p33(0)
= F23P33(ProbeScatterings), p32(0)
= F23P32(ProbeScatterings), p31(0)
= F23P31(ProbeScatterings), p30(0)
= F23P30(ProbeScatterings), p31n(0)
= F23P31n(ProbeScatterings), p32n(0)
= F23P32n(ProbeScatterings), p33n(0)
= F23P33n(ProbeScatterings), p22n(0)
= F23P22n(ProbeScatterings), p21n(0)
= F23P21n(ProbeScatterings), p20(0)
= F23P20(ProbeScatterings), p21(0)
= F23P21(ProbeScatterings), p22(0)
= F23P22(ProbeScatterings)} :
CF23Solns := dsolve(CF23Eqs, numeric, output = listprocedure) :
CF23P33n := eval(p33n(t), CF23Solns) :
CF23P32n := eval(p32n(t), CF23Solns) :
CF23P31n := eval(p31n(t), CF23Solns) :
CF23P30 := eval(p30(t), CF23Solns) :
CF23P31 := eval(p31(t), CF23Solns) :
CF23P32 := eval(p32(t), CF23Solns) :
CF23P33 := eval(p33(t), CF23Solns) :
CF23P22n := eval(p22n(t), CF23Solns) :
CF23P21n := eval(p21n(t), CF23Solns) :
CF23P20 := eval(p20(t), CF23Solns) :
CF23P21 := eval(p21(t), CF23Solns) :
CF23P22 := eval(p22(t), CF23Solns) :
#integrate!

```

$$\begin{aligned}
\text{CF23Photons33n} &:= \text{evalf} \left( \text{int} \left( \left( \frac{1}{1 + \left( \frac{2 \cdot (\text{CyclerDetuning})}{\Gamma \text{Mg}} \right)^2} \right) \right. \right. \\
&\quad \left. \left. \cdot \text{CF23P33n}(t), t = 0 \dots \text{CyclerScatterings} \right) \right) : \\
\text{CF23Photons32n} &:= \text{evalf} \left( \left( \frac{\mu_{\text{red}} \left( \frac{1}{2}, 3, -2, \frac{3}{2}, 4, -3, \frac{5}{2}, -1 \right)^2}{1 + \left( \frac{2 \cdot (\text{CyclerDetuning})}{\Gamma \text{Mg}} \right)^2} \right. \right. \\
&\quad \left. \left. + \frac{\mu_{\text{red}} \left( \frac{1}{2}, 3, -2, \frac{3}{2}, 3, -3, \frac{5}{2}, -1 \right)^2}{1 + \left( \frac{2 \cdot (\text{CyclerDetuning} + \Delta \text{HF3P})}{\Gamma \text{Mg}} \right)^2} \right) \cdot \text{int}(\text{CF23P32n}(t), t = 0 \dots 100) \right) : \\
\text{CF23Photons31n} &:= \text{evalf} \left( \text{int} \left( \left( \frac{\mu_{\text{red}} \left( \frac{1}{2}, 3, -1, \frac{3}{2}, 4, -2, \frac{5}{2}, -1 \right)^2}{1 + \left( \frac{2 \cdot (\text{CyclerDetuning})}{\Gamma \text{Mg}} \right)^2} \right. \right. \right. \\
&\quad \left. \left. + \frac{\mu_{\text{red}} \left( \frac{1}{2}, 3, -1, \frac{3}{2}, 3, -2, \frac{5}{2}, -1 \right)^2}{1 + \left( \frac{2 \cdot (\text{CyclerDetuning} + \Delta \text{HF3P})}{\Gamma \text{Mg}} \right)^2} \right. \right. \\
&\quad \left. \left. + \frac{\mu_{\text{red}} \left( \frac{1}{2}, 3, -1, \frac{3}{2}, 2, -2, \frac{5}{2}, -1 \right)^2}{1 + \left( \frac{2 \cdot (\text{CyclerDetuning} + \Delta \text{HF2P})}{\Gamma \text{Mg}} \right)^2} \right) \cdot \text{CF23P31n}(t), t = 0 \dots 100 \right) : \\
\text{CF23Photons30} &:= \text{evalf} \left( \text{int} \left( \left( \frac{\mu_{\text{red}} \left( \frac{1}{2}, 3, 0, \frac{3}{2}, 4, -1, \frac{5}{2}, -1 \right)^2}{1 + \left( \frac{2 \cdot (\text{CyclerDetuning})}{\Gamma \text{Mg}} \right)^2} \right. \right. \right. \\
&\quad \left. \left. + \frac{\mu_{\text{red}} \left( \frac{1}{2}, 3, 0, \frac{3}{2}, 3, -1, \frac{5}{2}, -1 \right)^2}{1 + \left( \frac{2 \cdot (\text{CyclerDetuning} + \Delta \text{HF3P})}{\Gamma \text{Mg}} \right)^2} \right) \right) :
\end{aligned}$$



$$\begin{aligned}
& \text{CF23Photons33} := \text{evalf} \left( \text{int} \left( \left( \frac{\mu_{\text{red}} \left( \frac{1}{2}, 3, 3, \frac{3}{2}, 4, 2, \frac{5}{2}, -1 \right)^2}{1 + \left( \frac{2 \cdot (\text{CyclersDetuning})}{\Gamma \text{Mg}} \right)^2} \right. \right. \right. \\
& \quad + \frac{\mu_{\text{red}} \left( \frac{1}{2}, 3, 3, \frac{3}{2}, 3, 2, \frac{5}{2}, -1 \right)^2}{1 + \left( \frac{2 \cdot (\text{CyclersDetuning} + \Delta \text{HF3P})}{\Gamma \text{Mg}} \right)^2} \\
& \quad \left. \left. \left. + \frac{\mu_{\text{red}} \left( \frac{1}{2}, 3, 3, \frac{3}{2}, 2, 2, \frac{5}{2}, -1 \right)^2}{1 + \left( \frac{2 \cdot (\text{CyclersDetuning} + \Delta \text{HF2P})}{\Gamma \text{Mg}} \right)^2} \right) \cdot \text{CF23P33}(t), t = 0 \right. \right. \\
& \quad \left. \left. \left. \cdot 100 \right) \right) : \right. \\
& \text{CF23Photons22n} \\
& := \text{evalf} \left( \text{int} \left( \left( \frac{\mu_{\text{red}} \left( \frac{1}{2}, 2, -2, \frac{3}{2}, 3, -3, \frac{5}{2}, -1 \right)^2}{1 + \left( \frac{2 \cdot (\text{CyclersDetuning} + \Delta \text{HF3P})}{\Gamma \text{Mg}} \right)^2} \right) \right. \right. \\
& \quad \left. \left. \left. \cdot \text{CF23P22n}(t), t = 0 \cdot \text{CyclersScatterings} \right) \right) : \right. \\
& \text{CF23Photons21n} \\
& := \text{evalf} \left( \text{int} \left( \left( \frac{\mu_{\text{red}} \left( \frac{1}{2}, 2, -1, \frac{3}{2}, 3, -2, \frac{5}{2}, -1 \right)^2}{1 + \left( \frac{2 \cdot (\text{CyclersDetuning} + \Delta \text{HF3P})}{\Gamma \text{Mg}} \right)^2} \right. \right. \right. \\
& \quad + \frac{\mu_{\text{red}} \left( \frac{1}{2}, 2, -1, \frac{3}{2}, 2, -2, \frac{5}{2}, -1 \right)^2}{1 + \left( \frac{2 \cdot (\text{CyclersDetuning} + \Delta \text{HF2P})}{\Gamma \text{Mg}} \right)^2} \left. \right) \cdot \text{CF23P21n}(t), t = 0 \\
& \quad \left. \left. \left. \cdot \text{CyclersScatterings} \right) \right) : \right. \\
& \text{CF23Photons20} \\
& := \text{evalf} \left( \text{int} \left( \left( \frac{\mu_{\text{red}} \left( \frac{1}{2}, 2, 0, \frac{3}{2}, 4, 2, \frac{5}{2}, -1 \right)^2}{1 + \left( \frac{2 \cdot (\text{CyclersDetuning} + \Delta \text{HF3P})}{\Gamma \text{Mg}} \right)^2} \right) \right. \right.
\end{aligned}$$



```

        ..CyclersScatterings } } :
    CF23TotalCounts := CF23Photons33n + CF23Photons32n
        + CF23Photons31n + CF23Photons30 + CF23Photons31
        + CF23Photons32 + CF23Photons33 + CF23Photons22n
        + CF23Photons21n + CF23Photons20 + CF23Photons21
        + CF23Photons22 :
    print("done");
end proc;
▼ Procedure to Calculate Total Counts as a function of Probe Laser
Detuning
FullLineShape := proc(ProbeFrequencyFromResonance,
    ProbeScatterings1, ProbeScatterings2, CyclersDetuning,
    CyclersScatterings, name1, name2)
    local stepsize, ProbeFrequency;
    writeto(name1) :
    writeto(name2) :
    writeto(terminal) :
    stepsize := 2 :
    ProbeFrequency := -ProbeFrequencyFromResonance;
    #Initialize first point
    for ProbeFrequency from -ProbeFrequencyFromResonance
        by stepsize to ProbeFrequencyFromResonance do
        FullCyclerDynamics(2·π·ProbeFrequency, ProbeScatterings1,
            CyclersDetuning, CyclersScatterings) :
        appendto(name1) :
        print(ProbeFrequency + 150, CF23TotalCounts);
        writeto(terminal) :
        FullCyclerDynamics((2·π·ProbeFrequency + EHFS),
            ProbeScatterings2, CyclersDetuning, CyclersScatterings) :
        appendto(name2) :
        print(ProbeFrequency + 150, CF23TotalCounts);
        writeto(terminal) :
    end do
end proc;
▼ Procedure to Calculate Total Counts as a function of Probe Time
FullProbeTime := proc(ProbeFrequencyFromResonance,
    ProbeMaxScatterings, CyclersDetuning, CyclersScatterings, name)
    local stepsize, freq ProbeTime;
    writeto(name) :
    writeto(terminal) :
    stepsize := 1 :
    ProbeTime := 0; #initialize first probe time
    for ProbeTime from 0 by stepsize to ProbeMaxScatterings do
        FullCyclerDynamics(2·π·ProbeFrequencyFromResonance,
            ProbeTime, CyclersDetuning, CyclersScatterings) :
        appendto(name) :
        print(ProbeTime, CF23TotalCounts);
        writeto(terminal) :
    end do
end proc;

```



# Bibliography

- [1] G. Herzberg and J. Spinks, *Atomic Spectra and Atomic Structure*, 2nd ed. (Dover Publications, New York, USA, 1944).
- [2] B. Waerden, *Sources of Quantum Mechanics*, 1st ed. (North-Holland Publishing Co., Amsterdam, The Netherlands, 1967).
- [3] I. I. Rabi and V. W. Cohen, *Phys. Rev.* **43**, 582 (1933).
- [4] N. F. Ramsey, *Phys. Rev.* **78**, 695 (1950).
- [5] W. E. Lamb and R. C. Retherford, *Phys. Rev.* **72**, 241 (1947).
- [6] T. H. Maiman, *Br. Commun. Electron.* **7**, 674 (1960).
- [7] P. A. Franken, A. E. Hill, C. W. Peters, and G. Weinreich, *Phys. Rev. Lett.* **7**, 118 (1961).
- [8] W. Demtroder, *Laser Spectroscopy*, 3rd ed. (Springer-Verlag, New York, USA, 2003).
- [9] R. Dicke, *Phys. Rev.* **89**, 472 (1953).

- [10] W. Paul, O. Osberghaus, and E. Fischer, *Forschungsber. des Wirtsch. Verkehrsminist. Nordrhein-Westfalen* **415**, (1958).
- [11] E. Fischer, *Z. Phys.* **156**, 1 (1959).
- [12] H. Shelton, R. Langmuir, and R. Wuerker, *J. Appl. Phys.* **30**, 342 (1959).
- [13] H. G. Dehmelt and F. L. Walls, *Phys. Rev. Lett.* **21**, 127 (1968).
- [14] F. G. Major and G. Werth, *Phys. Rev. Lett.* **30**, 1155 (1973).
- [15] W. H. Oskay, W. M. Itano, and J. C. Bergquist, *Phys. Rev. Lett.* **94**, 163001 (2005).
- [16] G. Graff, E. Klempt, and G. Werth, *Z. Phys.* **222**, 201 (1969).
- [17] H. G. Dehmelt, *Adv. Atom. Mol. Phys.* **3**, 53 (1967).
- [18] D. Wineland and H. Dehmelt, *Bull. Am. Phys. Soc.* **20**, 637 (1975).
- [19] T. Hansch and A. Schawlow, *Opt. Commun.* **13**, 68 (1975).
- [20] D. J. Wineland, R. E. Drullinger, and F. L. Walls, *Phys. Rev. Lett.* **40**, 1639 (1978).
- [21] W. Neuhauser, M. Hohenstatt, P. Toschek, and H. Dehmelt, *Phys. Rev. Lett.* **41**, 233 (1978).
- [22] W. D. Phillips and H. Metcalf, *Phys. Rev. Lett.* **48**, 596 (1982).

- [23] J. Berengut *et al.*, arXiv:physics/0408017v3 (2006).
- [24] K. Webb *et al.*, Phys. Rev. Lett. **82**, 884 (1999).
- [25] M. Zakova *et al.*, Hyperfine Interact. **171**, 189 (2006).
- [26] M. Safronova, A. Derevianko, and W. Johnson, Phys. Rev. A **58**, 1016 (1998).
- [27] C. Sur *et al.*, Eur. Phys. J. D **32**, 25 (2005).
- [28] CPIM, [http://www.bipm.org/en/si/si\\_brochure/chapter2/2-1/second.html](http://www.bipm.org/en/si/si_brochure/chapter2/2-1/second.html).
- [29] NRC FCs1 Cesium Fountain Clock, <http://www.nrc-cnrc.gc.ca/eng/projects/inms/fountain-clock.html>.
- [30] NIST-F1 Cesium Fountain Clock, <http://tf.nist.gov/timefreq/cesium/fountain.htm>.
- [31] T. Rosenband *et al.*, Phys. Rev. Lett. **98**, 220801 (2007).
- [32] A. D. Ludlow *et al.*, Science **319**, 1805 (2008).
- [33] T. Rosenband *et al.*, Science **319**, 1808 (2008).
- [34] W. Smith and A. Gallagher, Phys. Rev. **145**, 26 (1966).
- [35] W. Nagourney, G. Janik, and H. Dehmelt, Proc. Nat. Acad. Sci. **80**, 643 (1983).

- [36] W. Ansbacher, Y. Li, and E. H. Pinnington, *Phys. Lett. A* **139**, 165 (1989).
- [37] M. Herrmann *et al.*, *Phys. Rev. Lett.* **102**, 013006 (2009).
- [38] A. Friedenauer *et al.*, *Appl. Phys. B* **84**, 371 (2006).
- [39] G. Woodgate, *Elementary Atomic Structure*, 2nd ed. (Oxford University Press, Oxford, UK, 1983).
- [40] L. Féret and J. Pascale, *Phys. Rev. A* **58**, 3585 (1998).
- [41] D. N. Madsen and J. W. Thomsen, *J. Phys. B* **35**, 2173 (2002).
- [42] M. Abramowitz and I. Stegun, *Handbook of Mathematical Functions* (Dover Publications, New York, USA, 1972).
- [43] P. Kapitza, *Zh. Eksp. Teor. Fiz.* **34**, 242 (1951).
- [44] W. Neuhauser, M. Hohenstatt, P. Toschek, and H. Dehmelt, *Phys. Rev. Lett.* **41**, 233 (1978).
- [45] D. J. Berkeland *et al.*, *J. Appl. Phys.* **83**, 5025 (1998).
- [46] D. Leibfried, R. Blatt, C. Monroe, and D. Wineland, *Rev. Mod. Phys.* **75**, 281 (2003).
- [47] L. Bao and E. F. Redish, *Am. J. Phys.* **70**, 210 (2002).
- [48] J. H. Wesenberg *et al.*, *Phys. Rev. A* **76**, 053416 (2007).

- [49] Maple, <http://www.maplesoft.com/>.
- [50] H. J. Metcalf and P. van der Straten, *Laser Cooling and Trapping*, 2nd ed. (Springer, New York, USA, 2002).
- [51] Q. A. Turchette *et al.*, Phys. Rev. A **61**, 063418 (2000).
- [52] J. Sakurai, *Modern Quantum Mechanics* (Addison-Wesley Publishing Company, Massachusetts, USA, 1994).
- [53] C. Gerry and P. Knight, *Introductory Quantum Optics*, 1st ed. (Cambridge University Press, Cambridge, UK, 2005).
- [54] W. M. Itano and D. J. Wineland, Phys. Rev. A **25**, 35 (1982).
- [55] D. Wineland and H. Dehmelt, Bull. Am. Phys. Soc. **20**, 60 (1975).
- [56] J. Hasted, *Physics of Atomic Collisions* (Butterworths, London, UK, 1964).
- [57] J. Zhou, Building A Magnesium Ion Trap For Quantum Computation, MSc Thesis, McMaster University, 2007.
- [58] K. Odaka and S. Ueda, J. Vac. Sci. Technol. A **13**, 520 (1995).
- [59] Y. Ishikawa and T. Yoshimura, J. Vac. Sci. Technol. A **13**, 1847 (1995).
- [60] M. Bernardini *et al.*, J. Vac. Sci. Technol. A **16**, 188 (1998).
- [61] D. Berkeland, Rev. Sci. Instrum. **73**, 2856 (2002).

- [62] L. Topozini, personal communication.
- [63] W. Macalpine and R. Schildknecht, Proc. IRE **47**, 2099 (1959).
- [64] F. Terman, *Electronic and Radio Engineering, Electrical and Electronic Engineering*, 4th ed. (McGraw-Hill, New York, USA, 1955).
- [65] M. Madsen, Advanced Ion Trap Development and Ultrafast Laser-Ion Interactions, PhD Thesis, University of Michigan, 2006.
- [66] G. A. Ball and W. W. Morey, Opt. Lett. **17**, 420 (1992).
- [67] T. Hansch and B. Couillaud, Opt. Commun. **35**, 441 (1980).
- [68] J. Hall *et al.*, Appl. Phys. B **31**, 97 (1983).
- [69] P. Luc and P. Gersrekorn, *Atlas du Spectre d'absorbtion de la molecule d'iode 14800-20000 cm-1* (Edition de Centre National de la Recherche Scientifique (CNRS), Orsay, France, 1978).
- [70] W. R. Bennett, Phys. Rev. **126**, 580 (1962).
- [71] B. E. King, Quantum State Engineering and Information Processing with Trapped Ions, PhD Thesis, University of Colorado, 1999.
- [72] T. Schaetz *et al.*, Phys. Rev. Lett. **94**, 010501 (2005).
- [73] A. Yariv, *Quantum Electronics* (John Wiley and Sons, New York, USA, 1975).

- [74] G. Boyd and D. Kleinman, *J. Appl. Phys.* **39**, 3597 (1968).
- [75] T. Gosnell, A. Nurmikko, and W. Risk, *Compact Blue-Green Lasers* (Cambridge University Press, Cambridge, UK, 2003).
- [76] SNLO, SNLO, <http://www.sandia.gov/imrl/XWEB1128/snloftp.htm>.
- [77] J. Nielson, *Opt. Lett.* **20**, 840 (1995).
- [78] E. Ippen, A. Dienes, H. Kogelnik, and C. Shank, *IEEE J. Quantum Electron.* **QE-8**, 373 (1972).
- [79] A. Siegman, *Lasers* (University Science Books, California, USA, 1986).
- [80] H. Kogelnik and T. Li, *Appl. Opt.* **5**, 1550 (1966).
- [81] P. Miloni and J. Eberly, *Lasers* (John Wiley and Sons, New York, USA, 1988).
- [82] M. Dunn and A. Ferguson, *Opt. Commun.* **20**, 214 (1977).
- [83] D. Hanna, *IEEE J. Quantum Electron.* **QE-5**, 483 (1969).
- [84] D. Metcalf, P. de Giovanni, J. Zachorowski, and M. Leduc, *Appl. Opt.* **26**, 4508 (1987).
- [85] A. Douillet *et al.*, *J. Opt. Soc. Am. B* **16**, 1481 (1999).
- [86] R. L. Targat, J.-J. Zondy, and P. Lemonde, *Opt. Commun.* **247**, 471 (2005).

- [87] H. Kopfermann, *Nuclear Moments* (Academic Press Inc., New York, USA, 1958).
- [88] N. F. Ramsey, *Molecular Beams* (Oxford University Press, London, UK, 1956).
- [89] L. Topozini, Trapped- $Mg^+$  Apparatus For Control and Structure Studies, MSc Thesis, McMaster University, 2006.
- [90] H. Kuhn, *Atomic Spectra*, 2nd ed. (Academic Press Inc., New York, USA, 1969).
- [91] Gnuplot, <http://www.gnuplot.info/>.
- [92] P. Hobbs, *Building Electro-Optical Systems: Making It All Work* (John Wiley and Sons, New York, USA, 2000).
- [93] R. J. Epstein *et al.*, Phys. Rev. A **76**, 033411 (2007).
- [94] J. Verdeyen, *Laser Electronics*, 2nd ed. (Prentice Hall, New Jersey, USA, 1989).
- [95] G. Heinzl, A. Rudiger, and R. Schilling, Technical report, Max-Planck-Institut fur Gravitationsphysik, <http://edoc.mpg.de/395068>.
- [96] L. D. Turner, K. P. Weber, C. J. Hawthorn, and R. E. Scholten, Opt. Commun. **201**, 391 (2002).

- [97] M. Zhu and J. L. Hall, *J. Opt. Soc. Am. B* **10**, 802 (1993).
- [98] W. M. Itano and D. J. Wineland, *Phys. Rev. A* **24**, 1364 (1981).
- [99] W. Hanle, *Z. Physik* **30**, 93 (1924).
- [100] C. E. Theodosiou and S. R. Federman, *Astrophys. J.* **527**, 470 (1999).
- [101] J. Mitroy and M. S. Safronova, *Phys. Rev. A* **79**, 012513 (2009).
- [102] D. M. Meekhof *et al.*, *Phys. Rev. Lett.* **76**, 1796 (1996).

